Bimolecular chemistry at sub-microkelvin temperatures

Share Your Story

The Harvard community has made this article openly available.
Please share how this access benefits you. Submit a story .

Accessibility

HARVARD UNIVERSITY
Graduate School of Arts and Sciences

DISSERTATION ACCEPTANCE CERTIFICATE

The undersigned, appointed by the

Department of Physics

have examined a dissertation entitled

Bimolecular chemistry at sub-mirokelvin temperatures

presented by   Yu Liu

candidate for the degree of Doctor of Philosophy and hereby
certify that it is worthy of acceptance.

Signature _____

Typed name: Professor Kang-Kuen Ni, Chair

Signature _____

Typed name: Professor Markus Greiner

Signature _____

Typed name: Professor Eric Heller

Date: August 7, 2020

Bimolecular chemistry at sub-microkelvin temperatures

a dissertation presented
by
Yu Liu
to
The Department of Physics

in partial fulfillment of the requirements
for the degree of
Doctor of Philosophy
in the subject of
Physics

Harvard University
Cambridge, Massachusetts
August 2020

Bimolecular chemistry at sub-microkelvin temperatures

Abstract

Advances in AMO techniques lead to the creation of ultracold samples of molecular species and opened opportunities to explore chemistry in the ultralow temperature regime. While many prior studies investigated how long-range forces influence ultracold reactions, we aim to extend the exploration into the short-range where chemistry actually takes place. To this end, we developed a new experimental apparatus that combines the production of quantum-state-selected ultracold molecules with ion mass and kinetic energy spectrometry. Using such an apparatus, we were able to probe the exchange reaction between ultracold potassium-rubidium (KRb) molecules in its entirety, detecting both the reaction intermediates and the products. Such direct signals allowed us to further investigate this reaction, and eventually gain control over its various aspects. This thesis will describe the identification of an unusually long-lived reaction intermediate and a direct measurement of its lifetime, steering the pathway of the reaction with light, and controlling the quantum state distribution of the reaction products via an external magnetic field. The techniques we have developed here open up the exciting possibility to understand and manipulate state-to-state chemistry in the ultracold regime.

Contents

For my parents, my fiancée, and all my teachers.

Citations to Previously Published Work

Parts of this thesis have been previously reported in the following papers.

1. Hu, M. G.*, Liu, Y.*, Nichols, M. A., Zhu, L., Quéméner, G., Dulieu, O., & Ni, K. K. (2020). Product-state control of ultracold reactions via conserved nuclear spins. arXiv preprint arXiv:2005.10820.

2. Liu, Y.*, Hu, M. G.*, Nichols, M. A., Grimes, D. D., Karman, T., Guo, H., & Ni, K. K. (2020). Photo-excitation of long-lived transient intermediates in ultracold reactions. *Nature Physics*, 1-5.

3. Liu, Y.*, Grimes, D. D.*, Hu, M. G.*, & Ni, K. K. (2020). Probing ultracold chemistry using ion spectrometry. *Physical Chemistry Chemical Physics*, 22(9), 4861-4874.

4. Hu, M. G.*, Liu, Y.*, Grimes, D. D., Lin, Y. W., Gheorghe, A. H., Vexiau, R., … & Ni, K. K. (2019). Direct observation of bimolecular reactions of ultracold KRb molecules. *Science*, 366(6469), 1111-1115.

---

*These authors contributed equally to this work.

Acknowledgments

First and foremost, I would like to thank my thesis advisor Kang-Kuen Ni for her constant guidance and support over the past six years. Building up an experimental apparatus from scratch is as rewarding as it is challenging. Along the way, I have benefited not only from Kang-Kuen's vast knowledge of experimental AMO physics, but also her infectious excitement about scientific discovery. As an advisor, she always made me feel that my efforts and ideas are appreciated, creating positive reinforcements that motivated me throughout the journey, including some of the more frustrating parts. At the same time, she is uncompromising – pushing for robustness in the experimental systems I build and quality in the research that I conduct. Learning from and working with her over the last few years have made me a better presenter, a better writer, a better scientist, and a better person. I will carry the many lessons from her into my career and the rest of my life.

I am also very fortunate to have had Prof. Rick Heller and Prof. Markus Greiner as my co-advisors for this thesis. Prof. Heller provided wonderful physical insights to many of the scientific problems I had struggled with over my PhD, and is a delightful conversationalist. Prof. Greiner's technical expertise have helped us through many of the challenges that came with building a new apparatus. I also had a great experience as the teaching fellow for Prof. Greiner's undergraduate optics course, which has helped me strengthen my optics knowledge base and

gave me new perspectives on old problems.

The completion of this thesis work would not have been possible without the many teammates whom I've had the privilege to work with. I'd like to first acknowledge my postdoc, Ming-Guang – the person who I worked the longest and most closely with over the last few years. He is as hardworking as he is efficient, and played an important part in keeping the experiment on a reasonable schedule. His expertise in experimental AMO physics helped us push through the many technical hurdles that threatened to stop the experiment in its tracks. As someone with a perfectionist tendency, I learned from him the valuable lesson of making smart compromises. He always brought positive energies to the lab, and is a lot of fun to work with for that reason. David Grimes, another postdoc on our experiment, brought the much needed chemistry expertise to a lab composed entirely of physicists. Conversations with him have help me develop an appreciation for the wider field of physical chemistry research. I am also grateful for my fellow grad students, Hyunmok, Yu-Ting, Andrei, Lee, Yichao, Jessie, and Kenneth, with whom I have shared friendship and comradery.

My preparation as an undergraduate played a vital part in my completion of this PhD. For this, I have my research advisors Dr. Michael Pravica and Dr. David Shelton to thank. Dr. Pravica gave me an opportunity to work in his research lab at UNLV since when I was a high school senior. His enthusiastic personality convinced me that physics was fun, and he turned out to be right! Dr. Shelton was my teacher for the intermediate laboratory courses – a kind of "rite of passage" course for experimentalists that exist in most physics programs. From him, I learned how to ask the right questions about a physical problem, how to design experiments to address those questions, and how to deal with experimental uncertainties. To this day, I still find myself actively implementing his many teachings in my own research. He has also patiently supervised my senior project – construction of a rubidium MOT – one that had a direct impact on my developing an interest in AMO physics.

My family has been a constant source of moral support throughout grad school, despite their distance. I am indebted to my father for the many hardships he endured to bring me to the US for education. As someone who pursued and obtained a PhD in his 50s, he is a walking example of the phrase "it's never too old to learn". His unrelenting passion as an academic and a teacher has inspired me to pursue a career in academia. My mother has provided me with positive energy in life and continually encourages me to become a better person by helping those around me. I am also grateful for my cousin Sirui, for sharing the PhD experience with me as he is on track to becoming one himself!

Last but not least, I'd like to thank my fiancée, Xiao, for her unwavering support over the past three years. I'm glad to have shared a very special period of my life with her, and look forward to a journey with her as my partner in life.

Chapter 1

Introduction

1.1 Reaction dynamics

The burning of wood, the browning of an apple, and the depletion of the ozone layer – these macroscopically observable chemical changes are all manifestations of microscopic reaction events – the transformation of molecules from one configuration (the reactants) into another (the products). Such an understanding, first developed in the late nineteenth century, gave rise to the study of reaction dynamics [129], the central theme of which is to gain molecular level understanding and even control of chemical changes. The fundamental guiding forces for molecular level changes in a reaction are the electrostatic (Coulomb) interactions between the elementary components* of molecules – the electrons and the nuclei. For a given arrangement of electrons and nuclei $\{\mathbf{r}_i\}$ and $\{\mathbf{R}_j\}$, which respectively represent the sets of coordinates for all electrons and nuclei involved in a reaction, the potential energy of the reactive system arising from these

---

*Elementary in a chemistry sense, not physics.

interactions is given by

$$U(\{\mathbf{r}_i\}, \{\mathbf{R}_j\}) = U_{ee}(\{\mathbf{r}_i\}) + U_{NN}(\{\mathbf{R}_j\}) + U_{eN}(\{\mathbf{r}_i\}, \{\mathbf{R}_j\}), \qquad (1.1)$$

where the three terms represent electron-electron, nucleus-nucleus, and electron-nucleus inter-actions, respectively. The dynamics of the system, *i.e.* configurations of all particles at a given time t during the reaction, is then determined by its Hamiltonian

$$H(\{\mathbf{r}_i(t)\}, \{\mathbf{R}_j(t)\}) = \sum_i \frac{\mathbf{p}_i^2(t)}{2m_e} + \sum_j \frac{\mathbf{P}_j^2(t)}{2M_j} + U(\{\mathbf{r}_i(t)\}, \{\mathbf{R}_j(t)\}), \qquad (1.2)$$

where $\mathbf{p}, \mathbf{P}, m_e$, and M represent the momenta and masses of the electrons and the nuclei, respectively.

Solving Eq. 1.2 under the framework of quantum mechanics*, however, is a daunting task for all but the simplest molecular systems (e.g. H_2^+ [89]). One of the obstacles lies in the fact that the motions of the electrons and the nuclei are not independent of each other. To this end, the Born-Oppenheimer approximation [197] (BO) introduces significant simplifications to the problem by assuming that their motions can be decoupled, on the basis that electrons typically move much faster than the nuclei due to its lighter mass. This effectively allows the problem of reaction dynamics to be divided into two: an electronic structure one, and a nuclear dynamics one. Under BO, electronic part of the problem can be tackled for one nuclear configuration, $\{\mathbf{R}_j'\}$, at a time, by solving the time-independent Schrödinger equation

$$\left[\sum_i \frac{\mathbf{p}_i^2}{2m_e} + U(\{\mathbf{r}_i\}, \{\mathbf{R}_j'\}) \right] \Psi(\{\mathbf{r}_i\}) = V(\{\mathbf{R}_j'\}) \Psi(\{\mathbf{r}_i\}, \{\mathbf{R}_j'\}), \qquad (1.3)$$

where Ψ represents the properly antisymmetrized electronic wave function, and $V(\{\mathbf{R}_j'\})$ rep-

---

*Electrons and nuclei are, after all, quantum mechanical objects.

resents the potential energy experienced by the system at $\{\mathbf{R}'_j\}$. Solving Eq. 1.3 for all nuclear configurations that can potentially be sampled by the reaction allows one to construct $V(\{\mathbf{R}_j\})$, also known as the potential energy surface (PES) for the reaction. The rest of the problem is then determining the motions of the nuclei, which are governed by the time-dependent Schrödinger equation

$$\left[\sum_j \frac{\mathbf{P}_j^2(t)}{2M_j} + V(\{\mathbf{R}_j(t)\})\right] \Phi(\{\mathbf{R}_j(t)\}) = E\Phi(\{\mathbf{R}_j(t)\}), \qquad (1.4)$$

where Φ represents the nuclear wave function, and E is the total energy of the system. The solution to Eq. 1.4, $\Phi(\{\mathbf{R}_j(t)\})$, which describes the distribution of all nuclei within the system at all times, completely characterizes the reaction dynamics.

The PES is a powerful concept for visualizing the reaction dynamics – it allows one to picture a chemical reaction as the constituent nuclei moving through an energy landscape from reactants to products. As a pedagogical example, Fig. 1.1 shows the PES for a prototypical reaction AB + C → A + BC. The approach between AB and C is restricted to a co-linear geometry (see inset), such that the only relevant degrees of freedom are the r_{AB} and r_{BC} – the distance between A and B and that between B and C. The red curve represents the *minimum energy path* (MEP) for the reaction, which is the path of least resistance from reactants to products. The position along the MEP is the *reaction coordinate* (RC). In this particular example, we have chosen for the reactants and products to be connected by an attractive well, which supports the formation of a transient intermediate complex ABC*. As such, this is a *complex-forming* reaction. Another class of reactions feature instead a repulsive barrier, and are known as *direct* reactions.

The discussions above describe how the problem of reaction dynamics is approached from a theoretical point of view – first calculate the PES, then solve for the nuclear dynamics. Experimentally, on the other hand, the approach is usually the opposite – first probe the nuclear motion at certain stages of the reaction, then from the results determine the PES and the dynam-

3
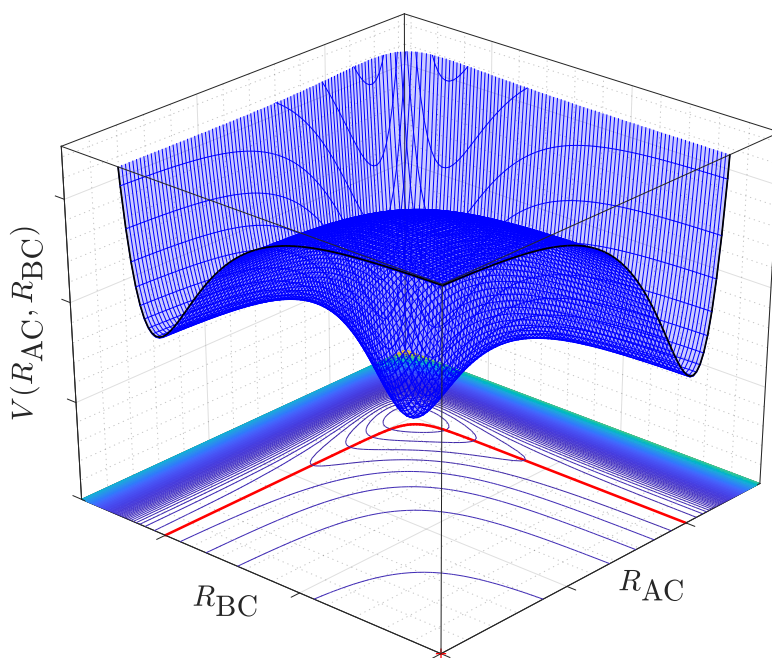
Figure 1.1: Potential energy surface (PES) for a prototypical complex-forming reaction AB + C → A + BC.

ics thereon. This requires suitable experimental observables that related to various aspects of the PES, which can be found in the reactants, the transition state or intermediate complex, and the products. For example, whether a reaction proceeds more efficiently with vibrationally or translationally excited reactants tells us whether the chemical barrier occurs early or late along the MEP[168]; the rate at which a reaction crosses its barrier can be related to how tight the potential is in directions orthogonal to the MEP[41]; the lifetime of the intermediate complex in a barrierless reaction can inform on the depth of the potential well as well as the complexity of the nuclear motions therein[200]; and the product state resolved rates in certain reactions can reveal the existence of conical intersections along the reaction pathway and effects of quantum

interference[116].

In order to gain access to relevant dynamical observables, a variety of experimental techniques have been developed and continually refined over the last half century. Techniques such as laser-induced fluorescence[86] and state-selective ionization[225] provided sensitive probes for the internal (*e.g.* rotational, vibrational, and electronic) excitations of the product molecules, while ion imaging[15] enabled measurements of their translational energies and angular distributions. Even the transition state or intermediate complex of the reaction, which are highly transient objects, can be directly accessed. For example, timescales for barrier crossing or complex dissociation can be probed using ultrafast lasers[223], while structures of the transition state or complex can be obtained using photodetachment[79,50], photoabsorption[194], photodissociation[180], or Coulomb explosion[205].

Besides the ability to probe a reaction with high degrees of sensitivity, an equally important ingredient to unraveling the complexity of reaction dynamics is to initiate a reaction with high degrees of control. This means experimentally defining the state of the reactants, which include their relative motion, as well as quantum states associated with their orbital, electronic, rotation, vibration, and spin degrees of freedom. At finite temperature, however, molecules exist as thermal ensembles, with the populations among different velocity classes and quantum states given by Boltzmann distributions. As a result, any observations will be subject to certain degrees of ensemble averaging, which can obscure important effects such as quantum interference between difference reactive pathways[17], and in general complicate the process of determining the reaction PES and the dynamics thereon.

In order to overcome the thermal distribution and localize the reactant populations in selected states, we need to cool down the reactant samples. But how cold? The answer depends on the degrees of freedom one seeks to control and their corresponding energy scales*, which are

---

*Throughout this thesis and depending on the context, we will express energy in terms of different
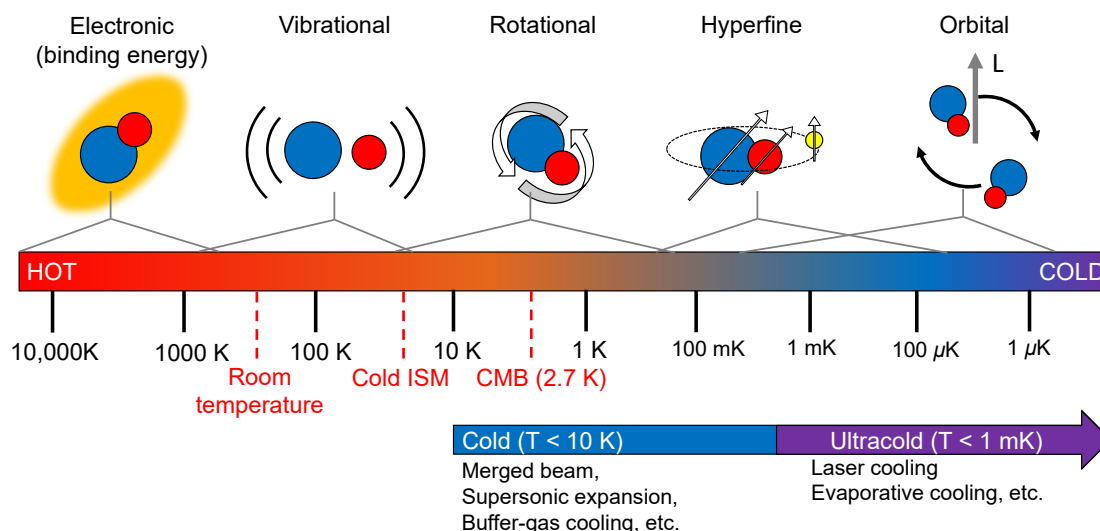
Figure 1.2: Characteristic energy scales of various molecular degrees of freedom expressed in temperature units (K). ISM: interstellar medium. CMB: cosmic microwave background.

shown in rough orders of magnitude as markings on a "molecular thermometer" in Fig. 1.2*. The translational energy lacks its own characteristic scale, but simply follows the temperature in a thermally equilibrated sample. The figure makes clear that while most molecules already exist in their ground electronic and vibrational states at room temperature ($\sim$300 K), gaining control over molecular rotations as well as translations both require going much lower on the scale. To this end, techniques like cryogenic buffer gas cooling[67] and supersonic expansion[184], typically used in molecular beam settings, enabled the creation of reactant samples that are both translationally and rotationally cold. More recently, merged beam[100] and Stark deceleration[110] have pushed the limit of the lowest achievable translational energy in molecular beam setups, enabling control over the orbital motion of the reactants – one of the lowest energy scales on the

---

equivalent physical quantities, including temperature, frequency, and wave number. For a conversion between these units, as well as those more commonly used in the chemistry literature, see Tab. 1.1

*In this example, we consider a relatively heavy diatomic molecule, such as the potassium rubidium molecule or KRb, which is the main subject of our investigation. For lighter molecules that are more typically encountered in gas-phase chemistry, *e.g.* H_2, CO, NO, CH_4, the rotational, vibrational, and orbital energy scales can be higher by one to two orders of magnitude

Table 1.1: Energy conversion factors between different units used in a variety of chemical and physical disciplines.

to/from	eV	cm^{-1} [†]	GHz[‡]	K[*]	a.u.[§]	kJ/mol	kcal/mol
eV	1	1.240E-4	4.136E-6	8.617E-5	27.21	0.01036	0.04336
cm^{-1} [†]	8066	1	0.03336	0.6950	2.195E5	83.60	349.8
GHz[‡]	2.418E5	29.98	1	20.84	6.580E6	2506	1.049E4
K[*]	1.161E4	1.439	0.04799	1	3.158E4	120.3	503.2
a.u.[§]	0.03675	4.556E-6	1.520E-7	3.167E-6	1	3.806E-4	1.594E-3
kJ/mol	96.55	0.01197	3.990E-4	8.320E-3	2627	1	4.187
kcal/mol	23.06	2.860E-3	9.537E-5	1.987E-3	627.5	0.2390	1

[†] $E = h\tilde{\nu}$, where $h = 6.626 \times 10^{-34}$ J $\cdot$ s is Planck's constant, and $\tilde{\nu}$ is wave number in units of inverse centimeters.

[‡] $E = h\nu$, where ν is frequency in units of gigahertz.

[*] $E = k_B T$, where $k_B = 1.381 \times 10^{-23}$ J/K is the Boltzmann constant, and T is temperature in units of Kelvin.

[§] Atomic units, or Hartree.

thermometer. This allowed studies of molecular collisions involving only a handful of partial waves, revealing resonant features in the scattering cross section that are typically washed out when too many partial waves participate [126,59].

Once a sample is prepared in the quantum ground states of the target degree(s) of freedom, the reaction can either be studied as is, or with controlled amounts of energy added back in to probe effects of excitation on the reaction pathway and outcome. Raman adiabatic passage techniques, including STIRAP[207] and SARP[149], allows highly efficient creations of molecular samples in targeted rotational and/or vibrational excited states. By preparing HD molecules in well-defined rotational states at a temperature of 1 K, Perreault *et al.*[167] studied effects of molecular alignment on the scattering between HD and D_2, and demonstrated a dramatic stereodynamic preference for one alignment over the other. Using HD molecules in the $v = 1$ vibrational state as precursors to the reaction HD + F $\rightarrow$ HF + D, Wang *et al.*[208] discovered dynamical resonances that are only accessible with vibrationally excited molecules, which helped better understand the shape of the underlying PES.

Given the significant improvements in controllability that cold techniques have brought to the field of reaction dynamics, natural questions arise: is it possible to reach below the millikelvin scale in a molecular sample, and gain total control over all quantum degrees of freedom within the molecules, including the orbital as well as the often neglected hyperfine degrees of freedom? And if so, what would chemistry look like under this new temperature regime? This is where the story of this thesis begins. In the next section (1.2), we discuss cooling techniques developed over the past decade that have allowed molecules to reach record low temperatures, in what is known as the "ultracold" regime; and in the subsequent section (1.3), we review current progress in the emerging field of ultracold chemistry, and discuss the motivations for our work.

1.2 Creating and manipulating ultracold molecules

An important precursor to the realization of colder molecular samples is the development and maturation of atom cooling over the past few decades. In the late 1980s, the invention of laser cooling techniques[48] allowed the temperature of selected atomic species to be brought below a milikelvin, and into what is known as the "ultracold" regime. Such a regime is characterized by single partial wave collisions, *i.e.* s-wave for identical bosons and distinguishable particles, p-wave for identical fermions. Later on, the addition of magnetic trapping[103] and evaporative cooling[102] enabled further cooling of the atoms as well as increases in their density, which led to the creations of the first Bose-Einstein condensates[13,58]. These days, the creation of ultracold atoms is routine in experiments around the world*, with applications ranging from precision measurements to quantum computation.

With the tremendous success of ultracold atoms, efforts began to also bring molecules into

---

*And above it[16].

8

this temperature regime[*]. The major appeal of molecules is that they display rich internal structures associated with their rotations and vibrations, which can be exploited to bring many of applications that have relied on ultracold atoms to their next levels. For example, the strong electric dipole-dipole interactions[155] between molecules make them suitable building blocks for quantum simulation[145,33,51] and quantum computation[62,221,157,111]; the rotation and vibrations for certain classes of molecules offer high sensitivity to fundamental quantities such as the electron electric dipole moment[19,38,14] and the electron-to-proton mass ratio[120,121]. Furthermore, and most importantly for the purpose of this thesis, ultracold molecules offer a platform to explore chemistry[17,199] with an unprecedented level of control.

When it comes to realizing ultracold molecules in the lab, the blessing that is their rich internal structure became somewhat of a curse. Virtually all ultracold atom experiments begin with laser cooling, a technique that relies on rapid and repeated scattering of photons between two levels within the atom – the ground state and an electronically excited state. While good photon-cycling properties can be found in many atom species, most notably alkali and alkaline earth atoms, they are in general not available in molecules. Molecules, once electronically excited, can decay (via spontaenous emission) into a wealth of rovibrational states on the ground electronic surface, thus rendering it unavailable for re-excitation. To circumvent this issue, two general classes of approaches emerged – one is to find molecules that can be laser-cooled, while the other is to associate molecules from laser-cooled atoms. For details on the prior approach, we refer the reader to the parallel thesis work of Loic Anderegg (Harvard University), which describes the realization of laser cooling and trapping of CaF molecules[10,9,43], and, more recently, loading these molecules into optical tweezers[11] and observing their collisions[44].

---

[*]Besides ultracold molecules, ultracold molecular ions were also a subject of major research interest, promising to play important roles in many of the same applications. For more information on this subject, which will be mostly omitted in the present discussion, we refer the readers to Ref.[64] and references therein.

In the rest of this section, we focus our discussion on the atom association approach, which is our method of choice. The basic idea is simple: first cool atomic species A and B to ultracold temperatures using established methods, then induce bonding between them to produce AB. The implementation of this procedure – in particular the second step – is far from straightforward. After all, atom pairs and molecules are fundamentally different objects – the typical distance between the atoms is 10^5 Å when they are free*, but only a few Å when inside a deeply-bound molecule; the free atoms experience no binding, while a molecule, when at or near its rovibrational ground state, is bound by an energy equivalent to $\sim 10^3 - 10^4$ K. Thus, effectively transforming one into another is met with the challenges of bridging the enormous gaps in both bond length and binding energy, all while not heating up the sample.

Stwalley and coworkers used photoassociation (PA) to address the binding energy mismatch in their pioneering work on ultracold molecules[193]. In this method, the atom pairs A and B are photoexcited, while on the collisional asymptote, to a bound excited state molecule AB*, which then decays via spontaneous emission to some rovibrational state on the ground PES, resulting in a deeply-bound molecule AB. There is, however, little to no control over the exact quantum state of AB, as the decay process will populate any ground vibrational state that has Franck-Condon overlap with the excited state. Thus while such a method produces molecules that are translationally as cold as the atoms from which they are formed, internally these molecules are still quite hot. Furthermore, efficient PA requires atom pairs to be reasonably close together, a condition that is not easily satisfied by the relatively dilute ultracold gases. Nevertheless, early experiments on PA demonstrate that binding ultracold atoms using photons is a viable path towards ultracold molecules.

Ultimately, the issues of both final state control and efficiency are resolved by the fully coherent scheme. First demonstrated on homonuclear molecules by Lang et $al.$[125] (Rb_2) and Danzl

---

*Assuming a typical atom number density of 10^{12} cm^{-3}

et al. [125] (Cs$_2$), and on heteronucler molecules by Ni *et al.* [154] (KRb), this technique allowed creation of deeply-bound, ultracold molecular samples that are close to the quantum degenerate regime. We take KRb [154] as an example to illustrate the basic ideas of this approach. In this case, pairs of ultracold Rb and K atoms are first magneto-associated into weakly-bond Feshbach (FB) molecules, then transferred into the rovibronic ground state via stimulated Raman adiabatic passage (STIRAP), a coherent two-photon transition. The FB molecule, which has a typical binding energy of several megahertz and a bond length of ~ 150 Å, acts an intermediary between the free atom pair and GS molecule during the transformation. Compared to the free atom pair, the FB molecules have much better Franck-Condon overlap with the GS molecule, making it possible to find an electronically excited intermediate state whose wavefunction has favorable overlaps to both, thus enabling the optical Raman transfer. In STIRAP, each FB molecule is coherently transferred into the GS, and the ~ 6000 K binding energy is carried away by the photons without additional heating to the sample. The end result is a gas of ultracold KRb molecules in which every molecule is identically prepared their quantum ground state, and collide via single (s or p) partial waves [154,162]. Furthermore, by changing the wavelengths and/or polarizations of the lasers used in the STIRAP scheme, different rotational, vibrational, and hyperfine states of molecule can be accessed.

The above experiments demonstrate that it is indeed possible to control all degrees of freedom within a molecule, as well as their collisions. This represents an important first step towards realizing the full potential of ultracold molecules outlined in the beginning of this section, including the main topic of this thesis – chemistry.

Since the creation of ultracold KRb, many other bialkali species were successively brought into the ultracold regime using similar schemes. These include RbCs [196,146], NaK [165], NaRb [96], and LiNa [176], with others like NaCs [136,224] and LiCs currently in the works. Owing to the high degree of maturity in cooling and manipulating alkali atoms, bialkali molecules, to this day,

remain the densest, coldest, and among the best quantum state controlled molecular samples. On the other hand, direct laser cooled molecules are quickly catching up on some of these fronts. Both of these established approaches, however, require molecules (or their atomic precursors) that have very specific properties, and therefore cannot be easily adapted to other species. To this end, improvements to the molecular beam technology, including new methods to slow and trap molecules[215,2], represent a promising path towards higher chemical diversity in the field of ultracold molecules.

1.3   Ultracold chemistry

The advent of ultracold molecules created a wave of interests in studying their chemical reactivity, both experimentally and theoretically. In this section, we discuss what makes ultracold reactions special and interesting, what the field has learned so far, and what we plan to explore. To understand low temperature reactions, it is helpful to divide the potential energy surface (PES) into different portions, as shown schematically in Fig 1.3. A pair of reactant molecules are set on a collision course starting from the *asymptotic* region, where they are far away and do not significantly interact. They then enter the *long-range* portion of the potential, where the interactions are dominated by relatively weak forces, including high-order electrostatic forces, such as van der Waals and dipole-dipole, as well as the centrifugal force arising from the orbital motion of the molecules. The energies of these interactions are typically on the micro to millikelvin scale. Once the molecules move past the long-range they enter the *short-range*, where rearrangements of the electron and nuclei occur, producing products in the end.

1.3.1 Long-range effects and scattering resonances

One of the defining features of ultracold reactions is the extremely low collision energy between reactants, which has two immediate implications for chemical reactivity in this temperature regime: 1. only reactions that are exothermic *and* lack a chemical barrier in the short-range are energetically allowed to proceed, implying the formation of intermediate complexes in all ultracold reactions; 2. Long-range interactions become comparable to or even higher than the collision energy. As a result, these weak forces that are typically ignored in higher temperature reactions can now significantly affect the approach between ultracold reactants. This led to a flurry of activities in studying the role of long-range interactions in ultracold reactions, which we will discuss next.

Ultracold chemical reactivity was first observed, fittingly, in a sample of KRb molecules – the first species to be brought into the new temperature regime. In a 2010 study, Ospelkaus *et al.* [161] observed rapid and unexpected losses in a gas of rovibronic ground state $^{40}K^{87}Rb$ molecules. These losses were attributed to the bimolecular reaction $KRb + KRb \rightarrow K_2 + Rb_2$. Remarkably, the reaction rate displayed dramatic dependence on whether the KRb molecules are prepared in identical hyperfine states or statistically-mixed hyperfine states, with a $10 - 100$ fold difference observed between the two cases. The explanation for this effect lies, interestingly, in quantum statistics. The fermionic nature of the $^{40}K^{87}Rb$ molecules demands the partial wave for their collisions to be odd in case where they are indistinguishable, *i.e.* in identical quantum states. This means that at ultralow temperatures, where collisions occur via the lowest few partial waves, identical KRbs react via $p-$wave collisions, with orbital angular momentum of $1\hbar$. In a statistically-mixed state, on the other hand, the molecules are distinguishable, and therefore allowed to collide via the lowest $s-$wave, with angular momentum of 0. In the $p-$wave case, the colliding KRb pair face a centrifugal barrier that is more than an order of magnitude higher than

their collision energy, and can only reach the short-range through the relatively slow process of quantum tunneling. In the $s-$wave case, however, no barriers are present, and the pair are guided directly into the short-range by the long-range attraction, resulting in the much higher observed loss rate.

The significance of the KRb study is the demonstration of quantum control over reaction rates through internal state control. It makes clear and exploits the fact that the long-range potential is directly tied to the internal quantum states of the reactants. In similar spirits, a number of studies demonstrated control over ultracold reactions by manipulating different degrees of freedom within the reactants. For example, a later study on KRb showed that introducing dipole-dipole interactions by polarizing the molecules in an electric field can significantly enhance their chemical reactivity[156], while confining polarized molecules in reduced dimensions can reduce reactivity[61]. Large dipolar interactions can lead to collisions with contributions from many partial waves, resulting in highly anisotropic interactions between molecules that lead to exotic behaviors in their loss rates[95]. Long-range interactions can be further modified by electronically exciting one of the reactants, in which case effects like the radiative lifetime[172] and orbital shape[97] of the excited state become significant to subsequent reaction rates.

Another important subject of research in cold and ultracold chemistry is scattering resonances, which arise when a scattering state of the reactants or products becomes strongly coupled to a bound or quasi-bound state of the intermediate complex (see Fig. 1.3 inset). Resonances involving quasi-bound states are known as "shape resonances", while those involving true bound states are known as "Feshbach resonances". The energies of the resonances depend sensitively on both long- and short-range interactions, making them excellent probes for the shape of the PES. While the observation of resonances in conventional temperature reactions is typically hindered by effects of thermal averaging, it becomes possible in cold reactions where collision energies are low and narrowly distributed. Observations of shape resonances have been made in
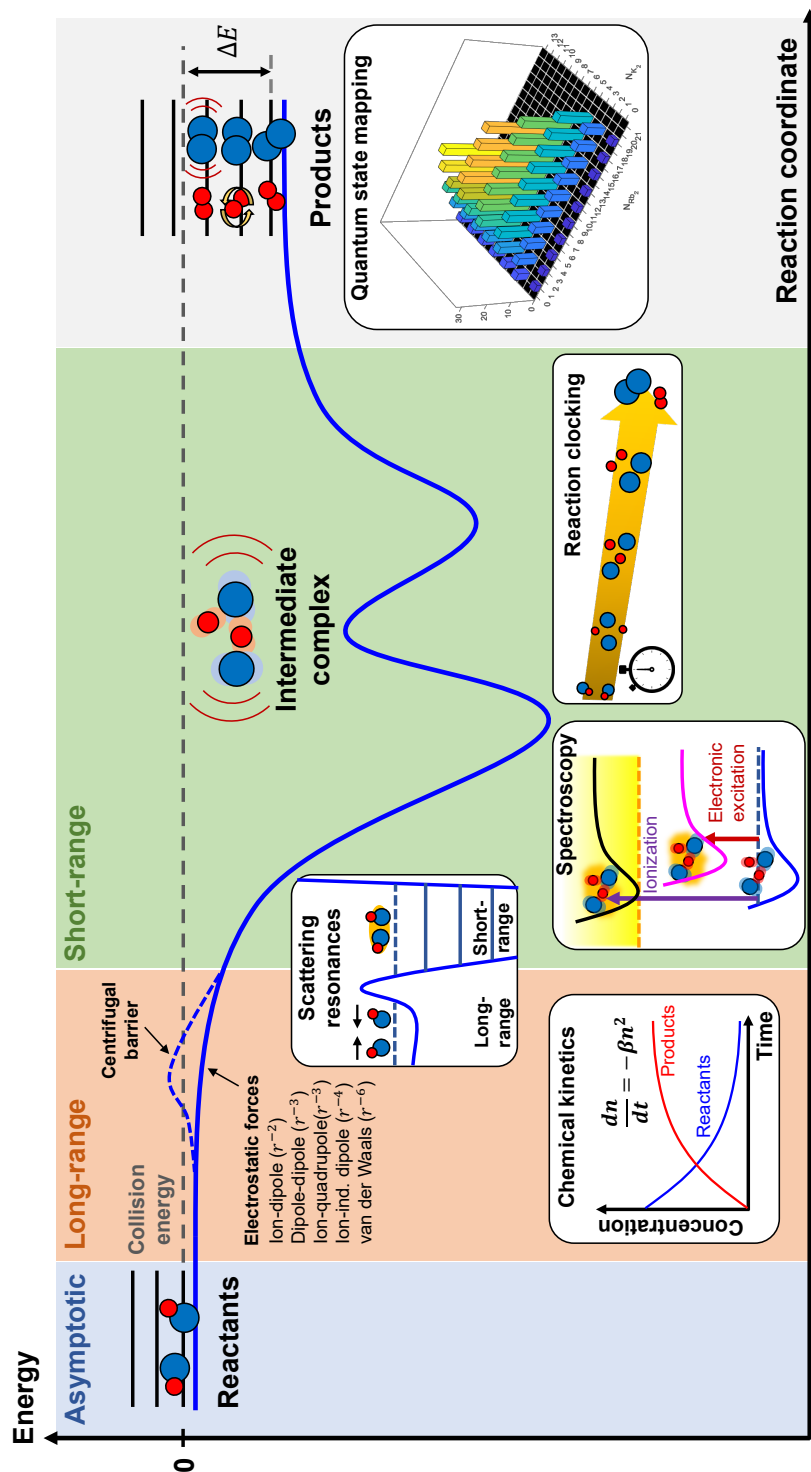
Figure 1.3: Schematic PES (not to scale) of a barrierless, exothermic cold reaction along some reaction coordinate, divided into asymptotic, long-range, and short-range portions. Experimental techniques that are sensitive to the different portions are illustrated in white boxes accordingly. Reactants are prepared with low collision energies and in well-defined quantum states in the asymptotic region. They approach each other under the influence of the long-range potential, characterized by centrifugal and electrostatic forces. The potential well in the short-range leads to the formation of a transient intermediate complex, which will proceed further to products in the case of exothermic reactions, or back to reactants in endothermic ones. Though cold reactions are overall barrierless, submerged barriers, such as illustrated above, are predicted to exist in many reactions [201,37,36,42].

photodissociation[141], Penning ionization reaction[119], as well as inelastic collisions[59], providing benchmark tests for the accuracy of the highest-level *ab initio* surfaces. Feshbach resonances play an important role in ultracold collisions of atoms[45], and have been predicted for both atom-molecule[140,113,77] and molecule-molecule[26,202] collisions. Magnetically tunable Feshbach resonances have been observed in ultracold NaK + K collisions[217], challenging quantum chemistry calculations for heavy atom systems.

1.3.2   Into the short-range

When this thesis work began in 2015, much has already been learned about the effects of long-range interactions on ultracold collisions. The short-range, where the "chemistry" actually happens, is nevertheless left mostly unexplored. As such, the potential for ultracold molecules as a highly controlled platform to study reaction dynamics is yet to be fulfilled. We decided to delve into this unknown regime. In this section, we consider chemical dynamics in the ultracold regime, drawing mostly on relevant knowledge gained from theoretical investigations of this subject.

The first question we should ask ourselves is: would the dynamics of ultracold reactions look significantly different from their higher temperature counterparts? Upon first glance, the answer seems to be no. After all, the binding energy in the short-range is typically $10^3 - 10^4$ K, and it does not seem like it would make a difference whether we launch a reaction at a microkelvin or a hundred kelvin. To properly answer this question, however, we need to consider the intermediate complex formed in the short-range. As we briefly mentioned in section 1.1, intermediate complexes are highly transient objects. Their lifetime, τ_c, is proportional to the density, ρ_c, of internal modes through which the energy of the complex can be re-distributed, and inversely proportional to number of exit channels, N_0, available for the complex to dissoci-

ate, either into products or back into reactants[129]. For reactions of small systems, τ_c is typically no more than on the order of a rotational period (10 ps), and a direct observation of the complex requires ultrafast techniques[181]. For larger systems the relatively large number of internal modes can extend the lifetime to as long as microseconds[158]. As one starts to lower the initial temperature of the reaction, however, N_0 start to decrease, pulling the lifetime to a lower value. Under ultracold conditions, N_0 can energetically minimized by preparing the reactants in their absolute quantum ground state. In such a case, it was predicted that collisions between bialkali molecules AB, the intermediate complex $A_2B_2^*$, consisting of merely four atoms, can live for several hundred nanoseconds to several hundred microseconds, depending on the exothermicity of the reaction[46]. Such an extraordinarily long lifetime, if turns out to be true, will open up the exciting possibility to directly probe the short-range dynamics without resorting to ultrafast lasers. In the time-domain, we can "clock" the reaction and make a direct and more precise measurement of complex lifetime. In the frequency-domain, we can learn more about the structure of the complex through high resolution spectroscopy, without the need to first stabilize the complex and interrupt its dynamics[213,24,34].

The short-range not only determines the dyanmics of the complex, but also guides the process of product formation. As such, studying the quantum states of the products and the population distribution among them can provide additional information about the short-range. To this end, the ability to initialize a reaction with complete quantum control over the reactants makes it possible to truly investigate chemistry on a state-to-state level – for reactants prepared in a given quantum state, what is the probability of of scattering into different product states? Such a capability promises to dramatically simplify the process extracting useful information about the dynamics from the experimentally measured state distribution – much like any black box problem, the simpler the input is, the easier it is to understand the mechanisms inside the box based on the output. As such, "the detection of product states" was recognized as one of the

"major milestones that need to be reached for the continued progress of this field" by an editorial on cold molecules in 2011[65].

Ultimately, investigating both the intermediate and products will provide the most comprehensive picture on the short-range dynamics of ultracold reactions, which may hold many more surprises beyond our expectations. Realizing such a goal, however, will require the design of a new experimental apparatus, which we will discuss in the next section.

Beyond understanding ultracold reactions lies the possibility for control. As was made clear by our discussion on the long-range behaviors of ultracold reactions (section 1.3.1), the ability to initialize reactions in well-defined quantum states of the reactants is vital to the realization of state-dependent chemistry. Given our goal of exploring the short-range, would it be possible to take advantage of the same controllability to influence the dynamics of the reaction, as well as how products form? As we will demonstrate in this thesis, the answers to both questions are yes.

1.4 Probing ultracold reactions

So far, the experimental observables in ultracold chemistry studies have mostly been limited to kinetic ones, *i.e.* the rates at which reactants disappear or products appear. Based on how the rate changes in response to different initial conditions, effects of long-range interactions and the presence of scattering resonances were inferred. Kinetic observables can be readily monitored using the existing infrastructure of ultracold experiments. In these experiments, the most common detection method is optical (fluorescence or absorption) imaging[117]. This technique provides powerful visualizations of the spatial configurations of particles and information such as their number, density, momentum, and temperature. Moreover, optical imaging is sensitive to the quantum states of the particles, a key capability for manipulating atoms and molecules

on a quantum-level. An essential requirement for imaging ultracold matter, where the typical density ranges from 10^8 to 10^{14} cm^{-3}, is that each particle can scatter many photons to provide sufficient signal for detection. This demands molecules prepared in a specific quantum state to repeatedly undergo "cycling" optical transition – the same as what is required laser cooling. As we discussed in section 1.2, such transitions are rare in molecules. In bilaklai systems, the platform on which most long-range studies were carried out, this requirement can be side-stepped. These molecules, which are associated from atoms using a fully coherent scheme, can be dissociated back into atoms via a reversal of the same process, which can then scatter photons very efficiently.

When it comes to studying the short-range chemistry, the quantum state specific nature of optical imaging renders it ineffective as a detection method, as the intermediate complex and the reaction products exist in a multitude of quantum states. To this end, ion spectrometry, which has seen widespread usage in traditional reaction dynamics studies, provides a universal and efficient way to detect all species involved in a reaction. Atoms or molecules involved in the reaction, regardless of their quantum states, can be ionized with photons of sufficiently high energy, and subsequently detected by time-of-flight (TOF) mass spectrometry. Ion imaging techniques[69], on the other hand, enable measurements of the kinetic energy distribution of the ions, from which valuable information on either the ionization process or the chemical reaction itself can be extracted. Ion detection also boasts high sensitivity and low background noise, making it ideal for detecting intermediates and products which are much less concentrated compared to the reactants. For example, it enabled the observation of a sample of ground state KRb molecules too dilute (10^6 cm^{-3}) to be optically imaged[1]. Finally, quantum state sensitivity, when desired, can be added into the detection using state-selective ionization methods such as resonance-enhanced multi-photon ionization (REMPI).

Thus, a comprehensive investigation of ultracold chemical reactions is best achieved by bring-

ing together techniques from ultracold physics and reaction dynamics. In this thesis (Ch. $3-4$),
we describe the construction of a new experimental apparatus that does just that.

1.5   Our platform: KRb + KRb

For our first venture into ultracold reaction dynamics, we decided to study the bimolecular exchange reaction between ground state potassium-rubidium molecules

$$^{40}\text{K}^{87}\text{Rb}(v=0, N=0) +^{40}\text{K}^{87}\text{Rb}(v=0, N=0) \rightarrow \text{K}_2 + \text{Rb}_2. \tag{1.5}$$
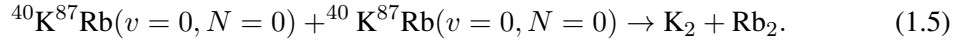
Here, v and N denote the rotational and vibrational quantum numbers, respectively. First identified Ospelkaus *et al.*[162], the reaction was proposed as a mechanism to explain two-body losses observed in an ultracold gas of KRb molecules. Based on spectroscopic data of KRb, K_2, and Rb_2, it was estimated that the reaction is exothermic, with an exothermicity of $\Delta E = -9.53(7)$ cm^{-1}, equivalent to ~ 14 K (see Appendix I for more details). The energetics of this reaction has been the subject of several of theoretical studies. Byrd *et al.*[37] calculated the potential energy of the reaction along its minimum energy path. Key aspects from their results are schematically illustrated in Fig. 1.4. Here, zero energy is defined as the zero-point-energy-adjusted binding energy of two non-interacting KRb molecules.

Three different reaction pathways were considered in Byrd's calculation, two of which are three-center pathways

$$\text{KRb} + \text{KRb} \rightarrow \{\text{KRb}_2 + \text{K}\}^* \rightarrow \text{K}_2 + \text{Rb}_2, \tag{1.6}$$

$$\text{and} \quad \text{KRb} + \text{KRb} \rightarrow \{\text{K}_2\text{Rb} + \text{Rb}\}^* \rightarrow \text{K}_2 + \text{Rb}_2, \tag{1.7}$$
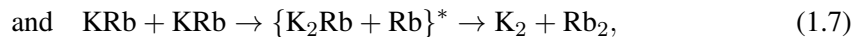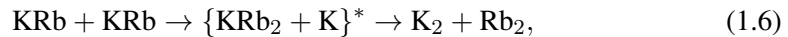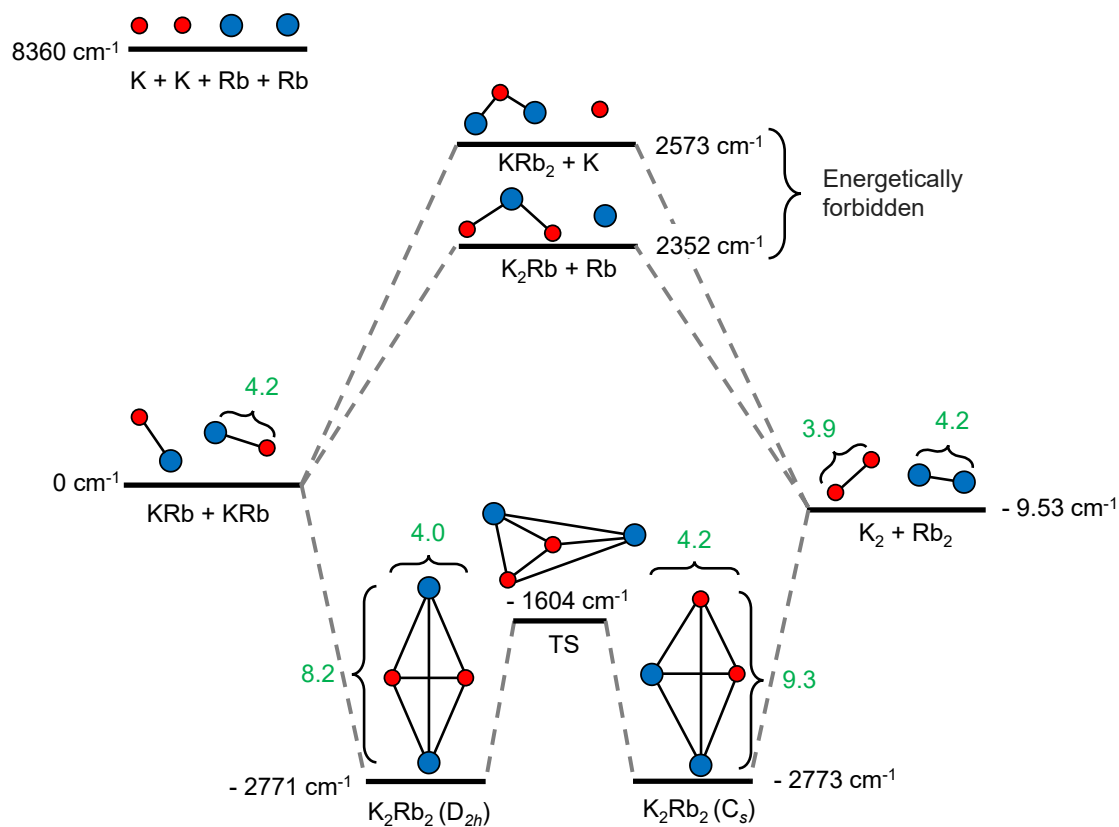
Figure 1.4: Energetics of the KRb + KRb reaction. Here, zero is defined as the energy of two ground-state KRb moelcules. Energy values and bond lengths are from Ref.[37]. TS: transition state.

and one is a four-center pathway

$$KRb + KRb \rightarrow K_2Rb_2^* \rightarrow K_2 + Rb_2. \tag{1.8}$$

Here, * denotes transient intermediate complex. In each of the three-center pathways, one of the KRb bonds is broken first to form a three-atom complex, which then breaks one of its bonds to form the products. In the four-center pathway, on the other hand, two pairs of bonds are broken and formed in a concerted fashion. In most chemical reactions of the type AB + AB $\rightarrow$ A$_2$ + B$_2$ (or the reverse reaction), four-center pathways possess forbiddingly high energy

barriers as a result of broken orbital symmetry. Thus the dominant reaction mechanism is almost always three-center in its nature. This phenomenon is known in the chemistry literature as the Woodward-Hoffmann (WH) rule[214]*. Remarkably, the theory shows quite the opposite in the case of KRb + KRb – three center pathways possess large barriers, while the four-center one feature a deep potential well. Thus at ultralow temperatures, the reaction, if occurring, must proceed via the four-center pathway. The intuitive reason for KRb + KRb to defy WH remains unclear. However, the strong metallic bonding that exists in alkali clusters is likely a contributing factor.

Along the minimum energy path, there exist two minina that are very similar in energy, corresponding respectively to deeply-bound K_2Rb_2 clusters belonging to the D_{2h} and C_s symmetry groups. Their structures, along with selected bond lengths, are shown in Fig. 1.4. The two minina are connected by a transition state (TS) that is ~ 1000 cm^{-1} higher in energy. A more recent calculation by Yang $et\ al.$[216] reproduced these structures to within a 50 cm^{-1} accuracy in energy. They also identified a new global minimum that is also of D_{2h} symmetry, but has the two Rb atoms closer and the two K atoms farther apart. In their calculation, this new minimum structure, which they call D_{2h}-II, is 163 cm^{-1} below the original one, which they call D_{2h}-I. As such, the overall well depth remained similar.

An important feature of the KRb + KRb enregy landscape is that the well depth exceeds the reaction exothermicity by more than two orders of magnitude. Intuitively, this means that the reactants, once proceeding into this well and form the complex $K_2Rb_2^*$, will need to explore a vast phase space while looking for a very small exit to dissociate, either into products or back as reactants. The size of this exit shrinks further as the initial energy of the reaction is lowered, and is minimized when the reactants are prepared in their quantum ground states at ultralow temper-

---

*An often cited example on this subject is the reaction $H_2 + I_2 \rightarrow HI + HI$, the mechanism for which were a subject of much debate, before it was eventually shown to proceed via a three-center pathway[106].

atures. Such a condition will lead to a long-lived complex that ergodically explores the entire available phase space, and the short-range dynamics can be adequately captured by statistical theory[129]. In Chapter 6, we discuss the subject of long-lived complexes in detail, and present relevant experimental results.

Based on the assumption of statistical behavior, Gonzalez *et al.*[85] calculated the quantum state distribution of the products. Experimentally, the low exothermicity, and therefore the few accessible product exit channels, makes the reaction amenable to full product quantum state mapping. In chapter 7, we present relevant results on this subject. Ultimately, measuring both the product state distribution and the complex lifetime will provide fundamental tests for the applicability of statistical theory to this reaction. Detecting departures from statistical behavior would in itself be interesting, and reasons for expecting such departures are suggested by Nesbitt[151], which will be discussed in detail in section 7.4.3.

1.6   This thesis

The content of this thesis is organized as follows. In chapter 2, we describe the design and construction of the "ultracold chemistry machine", a new experimental apparatus that bridges techniques from both the realms of ultracold physics and reaction dynamics to produce ultracold KRb molecules and probe their chemistry. Chapter 3 discusses the procedure of molecule production, the key steps to which include the laser and evaporative cooling of K and Rb atoms, followed by molecule association using the fully-coherent scheme introduced by Ni *et al.*[154]. Chapter 4 discusses probing ultracold reactions using ion-based detection methods, including time-of-flight and kinetic energy spectrometry. In Chapters 5–7 we present the main experimental results of this work. Chapter 5 describes our observation of the KRb + KRb reaction in its entirety, including direct detection of both reaction products and the intermediate complex. In

Chapter 6, we further explore the complex, including its photoexcitation properties and lifetime, and demonstrate steering of the reaction pathway via light. In Chapter 7, we probe the population distribution among different quantum states of the reaction products using state-selective ionization and detection. This allowed us to understand how nuclear spins behave throughout the reaction, and eventually exploit their behavior to control the reaction outcome on a quantum state level. We also discuss an ongoing effort to obtain a complete product state map of the KRb + KRb reaction, and how to extract information about the reaction dynamics from such a map. Finally, in Chapter 8, we summarize the thesis and discuss future directions.

Chapter 2

The ultracold chemistry machine

2.1   Overview of the apparatus

With the general goal of studying ultracold chemistry, and the immediate goal of investigating reactions between KRb molecules, we set out in early 2015 to construct a new experimental apparatus that we came to call "the ultracold chemistry machine" (shortened to simply "the machine" in later parts of this thesis). The result from that effort is shown in Fig. 2.1. The machine is built on two optical tables – a "laser table" that houses various laser systems used to generate light of different frequencies for cooling, trapping, molecule formation, etc., and a "machine table" that houses the vacuum system in which the atoms and molecules live as well as optics to direct lasers to different parts of the system. This chapter provides details on the construction and functions of various parts of the machine, including the vacuum system (Section 2.2), the laser and optical systems (Section 2.3), the magnetic field coils (Section 2.4), and the ion detection system (Section 2.5). Other hardware, including the RF and microwave systems, will be discussed in Chpater 4 where the relevant techniques are introduced.
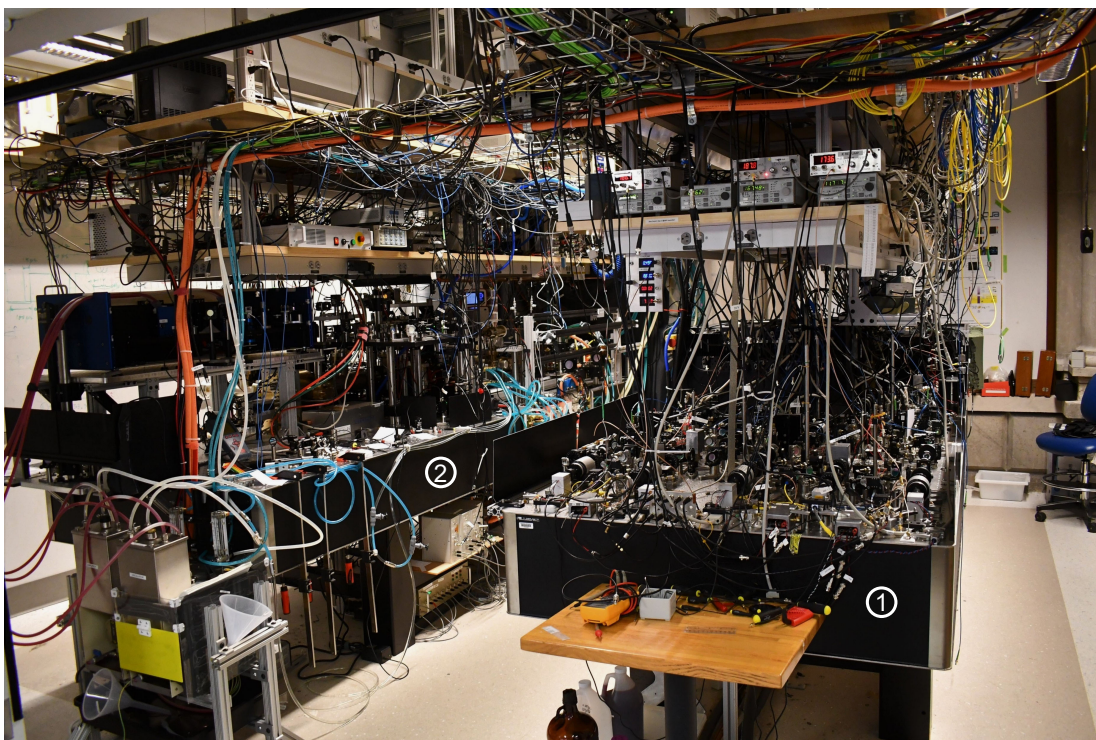
Figure 2.1: The ultracold chemistry machine. ① The laser table; ② the machine table.

Finally, making ultracold molecules requires various lasers and fields to be switched on and off at well-defined times. To this end, the timing for the entire experiment* is controlled via a FPGA-based computer control system, with instructions programmed by Matlab-based computer scripts. Details of this system will be provided in the thesis of Yichao Yu, who was instrumental its setup and maintenance.

2.2 The vacuum system

A vacuum system is an essential part to any ultracold experiment, isolating the atoms and molecules from the environment. A schematic of our vacuum system is shown in Fig. 2.2. The

---

*with the exception of the ionization and detection portion described in section2.5.4

26
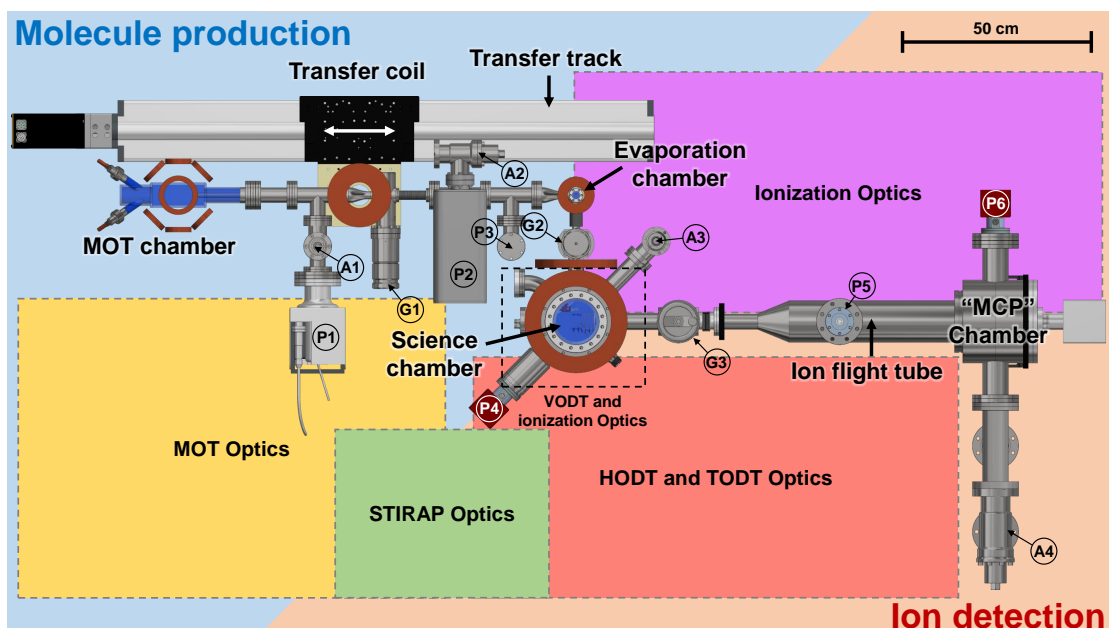
Figure 2.2: The ultracold chemistry machine. A bird's-eye view of the apparatus is shown, with key components highlighted and labeled. Supporting structures for the vacuum chambers and magnetic coils are hidden in the interest of clarity. G1-3: gate valves; A1-4: angled valves; P1-6: vacuum ion pumps; FC: Feshbach magnetic field coil pair. Dashed boxes mark the regions different optical setups occupy.

light blue shaded part can produce a mixture of ultracold, state-selected reactant atoms/molecules on-demand. As the reactions proceed, the ion spectrometer in light orange shaded part can detect the reactants, products, and the transient intermediates with mass and quantum state sensitivity.

Differences in ultracold physics and reaction dynamics techniques bring about many competing apparatus design requirements that needed to be resolved. Our strategy is to build interconnected vacuum chambers that each specializes in a set of mutually compatible tasks, and transfer the atoms and molecules in between them using electric, magnetic, and optical (laser) fields. These include the MOT chamber (2.2.2), the evaporation chamber (2.2.3), the science chamber (2.2.4), and the MCP chamber (2.2.5). The multi-chamber design allows the machine to be built and tested one section at a time. Each time a new section is built, it is shut off from the
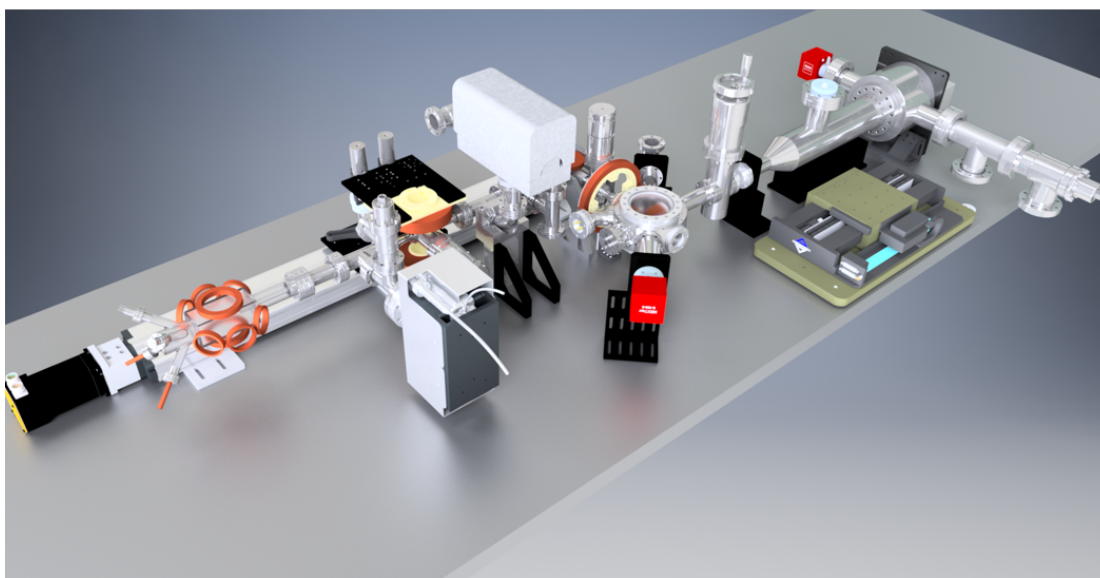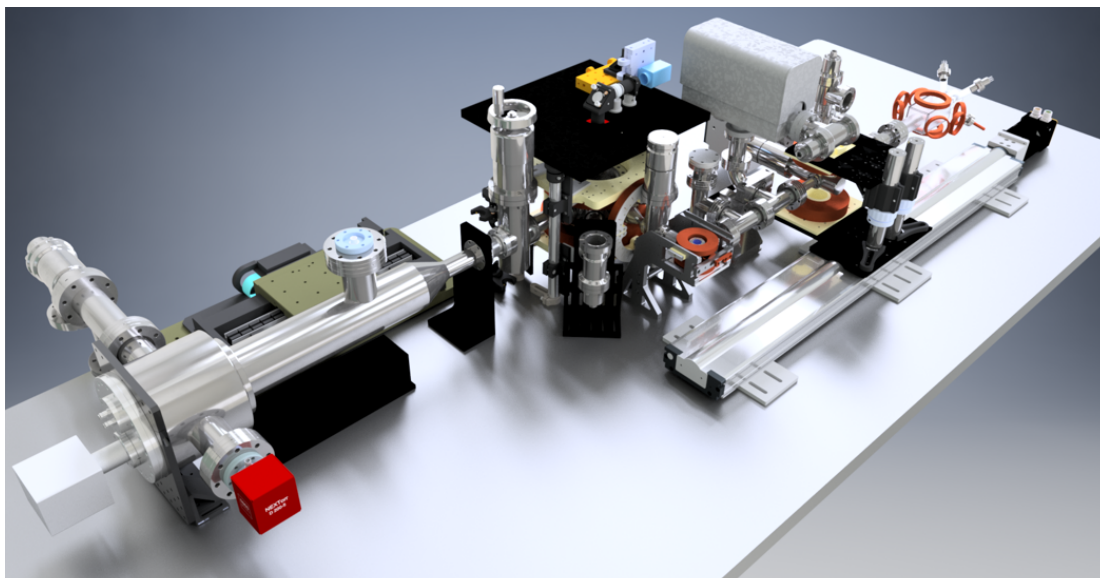
Figure 2.3: CAD renderings of the ultracold chemistry machine, viewed from two different angles.

outside environment with a gate valve (G1-3 in Fig. 2.2), via which another section can be connected later. In the event that a particular section is to be serviced or replaced, and air-exposure is required, the gate valves allow the negative impact on the vacuum to be localized.

This section describes the process of achieving and maintaining vacuum, and provides details on the construction of each chamber.

2.2.1 Achieving UHV: preparation, pump-down, and bake-out

Ultracold experiments typically demand a pressure below 10^{-10} mbar, a regime of vacuum characterized as ultra-high vacuum (UHV). The stringent requirement is due mainly to the long experimental cycle time (typically a few to a few tens of seconds) during which the collisions between the ultracold sample and background particles must be minimized. This is in contrast to molecular beam experiments, the traditional platform for studying chemical dynamics, where the short cycle time (order 100 ms) relaxes the vacuum requirement to 10^{-6} to 10^{-8} mbar.

The pressure inside a vacuum system is ultimately balanced by the rate at which gas loads are generated, and that at which they are evacuated. Therefore, achieving UHV requires both reducing the gas load inside the system, and providing sufficient pumping for what remains. Many different types of vacuum pumps are available to choose from, each with its own pros and cons. While mechanical pumps such as turbo pumps and scroll pumps offer substantial pumping capacity and are essential for bringing the pressure down from atmosphere, their mechanical vibrations are incompatible with the stability required by optics and optical techniques. Therefore, we followed the standard approach to achieving UHV in ultracold experiments – use mechanical pumps only for the initial pump-down of the system, and switch to non-mechanical ones afterwards to maintain the vacuum.

To reduce the gas load inside the vacuum system, the following pre-assembly practices were

exercised:

- Material selection. Naturally low out-gassing, UHV compatible materials were selected to construct or be placed into the vacuum system. These include 304 or 316 stainless steel (for chamber wall, and in-vacuum support structures), oxygen-free copper (for in-vacuum support structures), molybdenum (for electrical wiring), alumina ceramic (for in-vacuum support structures), and Kapton plastic (used in UHV-compatible SMA cables).

- Air-baking. All stainless steel components, with the exceptions of valves pumps, and viewports, are baked in air prior to assembly at a temperature of 400 °C, for a duration of at least 24 hours. The purpose is to reduce the material's out-gassing of hydrogen, the dominant gas load at UHV pressures[211]. This process results in a yellowish oxidization layer

- Sealing. Every joint in a vacuum system is a potential source for leakage and must be well-sealed from the atmosphere. Standard Conflat (CF) flanges are used throughout the system to join components. Before assembly, the knife edge of on every flange was inspected for chips, and cleaned of dirt and debris by wiping it off with first acetone and then ethanol. Sealing is achieved by tightening the bolts on the flange in a star pattern up to an appropriate torque (measured using a torque wrench), which depends on the size of the flange of the type of copper gaskets used (soft, annealed gaskets were used to attach viewports, which can warp or crack under high sealing force).

After a section of the vacuum system is assembled, we first pump it down using a mechanical pumping station (Agilent Varian TPS-Compact) that consists of turbomolecular pump and a fore-line scroll pump. After the vacuum level reaches 10^{-7} mbar, we perform the vacuum bake-out, the final and arguably most critical step in the reduction of vacuum out-gassing. In this process,
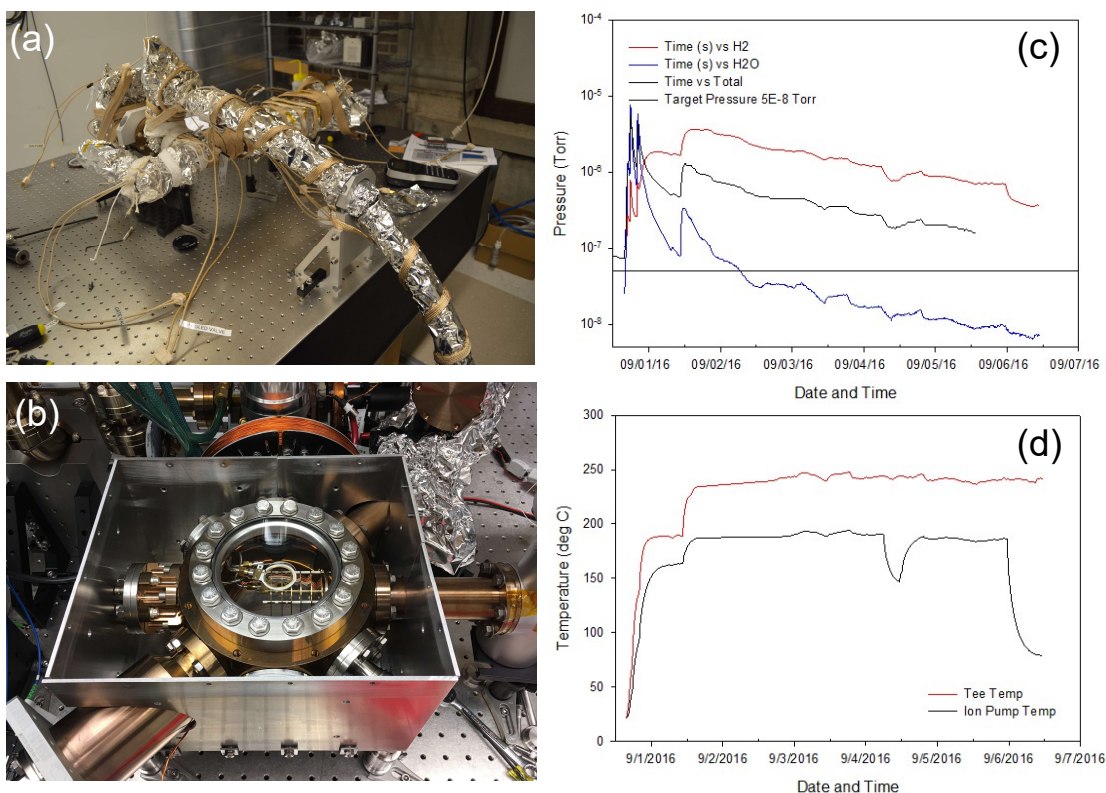
Figure 2.4: Baking out the vaccum system. (a) A typical bake-out setup. The entire vaccum setup is wrapped in layers of different materials. From inside out, the layers are alumimum foil, thermocouple temperature probes, fiberglass heating tape, fiber glass insulation tape, and finally aluminum foil again. The long bellows in the picture connects a turbo pumping station to the vacuum system via an angled valve to provide pumping during the bake-out. (b) Custom oven built around the science chamber to ensure temperature uniformity during the bake-out (2.2.4). (c) Evolution of the total pressure (black curve) and partial pressures of H_2O (blue) and H_2 (red) during the week-long bake-out of the evaporation chamber (2.2.3). Pressure changes are correlated with both time since the start of the bake-out and changes in chamber temperature. (d) Chamber temperature during the bake-out, shown for two probes placed at two different locations on the chamber body. After initial ramp ups, the temperatures are maintained to a constant value for the remainder of the bake-out ("ion pump temp" suffered drops due to failures of the Variac powering the heating tape responsible for that section of the chamber).

the system is heated up to a temperature greater than 100 °C such that water and other major

gas loads* absorbed onto in-vacuum surfaces can be driven out and pumped away. While higher

bake-out temperatures result in more efficient gas load reductions, they are ultimately limited by

---

*e.g. H_2, N_2, O_2, CO, Ar, and hydrocarbons

the temperature rating of various components. To apply appropriate heating to different parts of the system, individual heating tapes and thermocouple probes were applied. During bake-out, the system is thermally insulated from the environment using a combination of fiberglass tapes and aluminum foils. In some cases, specialized ovens are built around parts to ensure a high degree of homogeneity during the heating (see, for example, section 2.2.4).

Figure 2.4 shows the setup for the bake-out, as well as the evolution of pressure during the process. Partial pressure of various gas species in the system are monitored by a residual gas analyzer (SRS RGA 200) attached to the pumping station. As the system is heated up, the pressure rises up to $\sim 10^{-5}$ mbar due to the increased out-gassing of materials. The system is kept heated and pumped until the pressure reaches below $\sim 10^{-8}$ mbar, which typically takes one to two weeks. The system is then cooled back down to room temperature, and the pressure typically drops by another two to three orders of magnitude, reaching the target UHV level. The net gain in vacuum level, compared to the pre-baked system, is about three to four orders of magnitude. After bake-out, the mechanical pumps are separated from the system by shutting of the angled valves (A1-4 in Fig. 2.2) via which they are attached to. From this point on, the vacuum is maintained by ion, titanium-sublimiation (Ti-sub), and non-evaporative getter (NEG) pumps which work efficiently at UHV pressures.

Finally, leak checking is performed to ensure the system is free of vacuum leaks, which can limit the ultimate achievable pressure. This is performed by spraying small puffs of highly permeable He gas in a targeted fashion at various locations around the system. Leak points are identified by rises in the ion pump pressure reading as He is applied. We found that electrical feedthroughs are most prone to such leaks, likely resulting from the heating and cooling process during the bake-out. Fortunately, all leaks can be effectively sealed using VacSeal, a silicone based liquid resin. Once applied to the affected area, the liquid base quickly evaporates into the vacuum (and get pumped away), leaving behind a silicone residue that plugs the microscopic

gaps responsible for the leaks.

2.2.2 The MOT chamber

The MOT chamber and the vacuum parts attached to it are shown in Fig. 2.5. The body of the chamber is a rectangular, fused silica (Pyrex) glass cell, with a glass-to-metal transition fused on one end and a glass manifold housing the atom sources fused on the other end (Fig. 2.5(b)). Dimensions of the MOT chamber can be found in a CAD drawing in Appendix A. This chamber is where the laser cooling and trapping and K and Rb atoms takes place, and is therefore designed to be filled with atomic vapors. Since MOT loading requires relatively high vapor pressure ($\sim 10^{-9}$ mbar), which subsequent steps like magnetic transfer and evaporative cooling cannot tolerate, it is important to maintain a separation in pressure between the MOT chamber and the rest of the vacuum system. To this end, we reduce the conduction of gas out of the MOT chamber using a differential pumping tube, as shown in Fig. 2.5(a) and (c). Its long and thin construction limits the molecular flow conductance to 0.35 L/s *. The vacuum inside the region immediately after the tube is maintained by an ion pump (Agilent VacIon Plus 55) with a conductance-limited pumping rate of 35 L/s. This means a pressure differential of a factor of ~ 100, which is simply the ratio of the pumping rate and the conductance, can be maintained across the two ends of the tube.

To generate the atomic vapors inside the MOT chamber, K and Rb atom sources are attached to the four glass tubes at the end of the chamber. ^{40}K is a rare isotope, with a natural abundance of only 0.012%. Therefore, isotopically-enriched sources must be used to generate a substantial vapor for MOT loading †. To this end, we purchased two samples of enriched potassium in the form of KCl (potassium-chloride) salt, from Trace Science International and Oak Ridge National

---

*All conductance/pumping rate are specified for N_2 unless otherwise noted.
†Zwirlein group, Zeeman slower, non-enriched source.
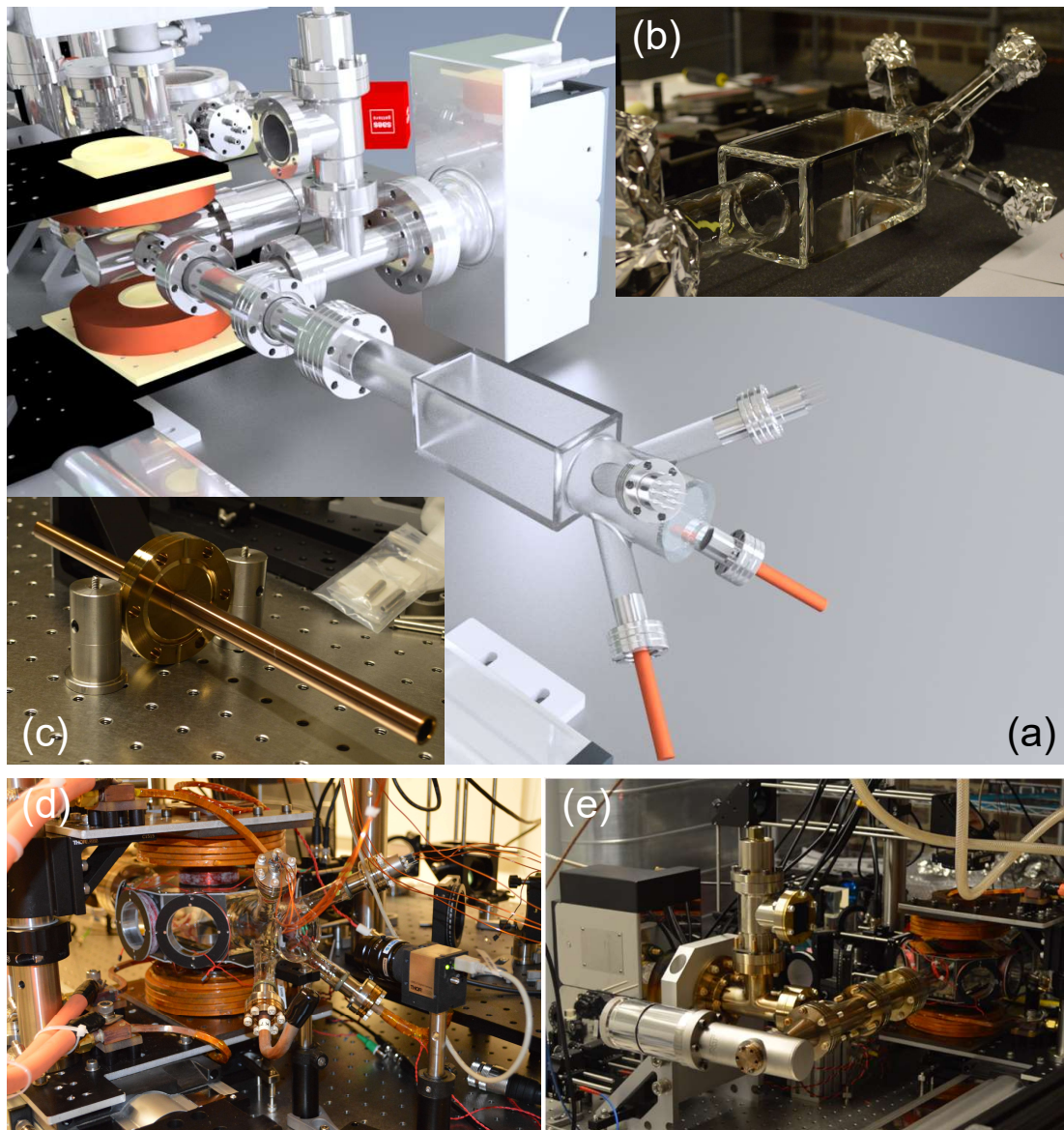
Figure 2.5: The MOT chamber. (a) CAD rendering of the MOT glass cell and associated vacuum parts. (b) Photo of the MOT glass cell pre-assembly. (c) Photo of the differential pumping tube mounted on a flange after air-bake but before vacuum assembly. Length of the tube is $12''$. (d) Photo of the MOT chamber with transfer coil pair (2.4.1) parked at the MOT position. A CCD camera (Thorlabs DCU223M) monitors the fluorescence of atoms within the MOT. (e) Photo of the MOT chamber region viewed from a different angle from (d).

Lab, respectively. The Trance Science sample has an potassium elemental weight of 25 mg and is enriched to a 7% ^{40}K abundance. The Oak Ridge sample has an potassium elemental weight of 50 mg and is enriched to a 3.15% ^{40}K abundance. These two samples are distilled by Precision Glass Blowing into pure potassium metal, and deposited respectively into two glass ampoules sealed under protective argon atmospheres (Fig. 2.6(b)). Each K ampoule is placed inside a soft, annealed copper tube with one end open and the other end pinched shut to form a UHV compatible seal. Each tube is bent into an L-shape, and attached to one of the two lower glass tubes on the chamber (Fig. 2.5(d) and Fig. 2.6(a)). Alkali metal can react chemically with glass at a temperature of 110 - 120 °C, rendering the source unusable. Therefore, care was taken during the vacuum bakeout to ensure that the source temperature never exceeded 100 °C. Once vacuum is established inside the MOT chamber, potassium vapor can be released into the chamber by cracking the glass ampoule open with externally-applied pressure *, using the setup depicted in Fig. 2.6(a). By the time of completion of this thesis work, only the 3.15% source has been cracked open, and the 7% source remains sealed. A foil heater wrapped around the copper tube is originally intended to be used to control the K vapor pressure. Over time, however, we found that due to the migration of the potassium deposit out of the tube and the Rb metal in, the K vapor pressure can no longer be independently controlled (see further discussion in 3.2).

For the Rb atom sources we use dispensers from SAES Getters shown in Fig. 2.6 (c) and (e). A total of six dispensers, in two groups of three, are spot-welded onto two electrical feedthroughs, which are then attached to the MOT chamber. The pinouts of the two feedthroughs are shown in Fig. 2.6 (d) and (f). A dispenser releases Rb vapor upon the passage of an electrical current that resistively heats up a mixture of an Rb-containing salt and an oxidizer, resulting in the chemical displacement of Rb out of the salt. During the vacuum pump-down and bakeout, the dispensers

---

*The release of the argon gas inside the glass ampoule resulted in a sudden pressure spike at the ion pump (P1), which resembles a vacuum leak. However, the pressure at the pump drops back down to UHV pressure as the gas load is pumped away.
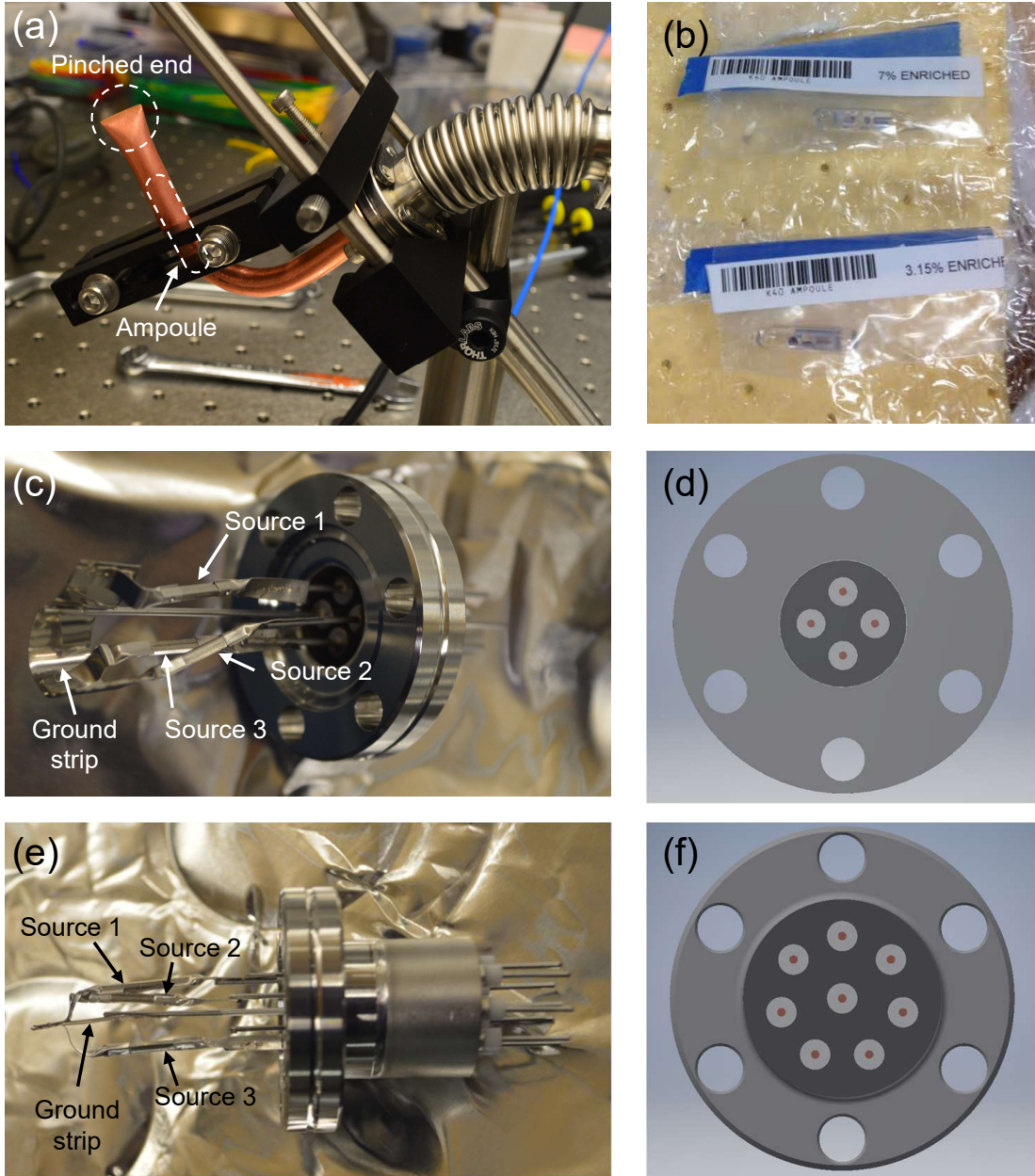
Figure 2.6: The atom sources. (a) Photo of a test setup used to crush the K ampoule, which also reflects the actual setup used in the experiment. A glass ampoule filled with enriched K metal is placed next to the bent section of a copper pinch-off tube. The pinched end makes a UHV seal, while the other end of the tube is attached to the MOT glass cell. K vapor is realeased into the cell by crushing open the ampoule via the mechanism shown in the picture. (b) Photo of the 3.15% and 7% ^{40}K enriched source sealed inside glass ampoules before they are loaded into the MOT cell. (c,e) Photos of the Rb dispensers. A total of six dispensers mounted in groups of three on two 1.33″ CF feedthroughs. (d,f) pinout diagrams for the dispenser feedthroughs.

36

are heated by running currents through them (2.0 A for 1 min, and 4.5 A for another 35 s) to allow absorbed gas loads to be released into the vacuum and pumped away (this process is commonly known as conditioning). After vacuum was first established inside the MOT chamber (in May of 2015), one of the dispensers is fired for $10 - 15$ min at a current of $4.0 - 4.5$ A each time before MOT loading experiments are performed. After no more than ten such firings, we observed that the amount of Rb atoms that can be loaded into the MOT reaches an equilibrium value of $\sim 10^9$, regardless of whether the dispenser is fired before MOT captures. The implications of this observation, and the ensuing changes in how we operate our MOT, are discussed in 3.2. Since the initial firings of one of the dispensers, none of the dispensers were fired again as of the completion of this thesis.

Electromagnetic coils, mounted on an aluminum support surrounding the MOT chamber, are used to control the magnetic field at the center of the chamber during the MOT, optical molasses, and optical pumping (OP) stages (Fig. 2.7). Three pairs of coils (x shim, y shim, and z shim) are aligned co-axially with the MOT beams, and a fourth pair (OP) is co-axial with the OP beam. The two coils within each pair are wired in series, and share the same current flow direction. The dimensions of the MOT coils and other relevant parameters are documented in Tab. 2.1 The currents through the coils are controlled by a servo with proportional and integral gain, with set points provided by DAC voltages such that the magnetic field can be dynamically changed during the experiment.

Finally, flexible resistive foil heaters (Thorlabs HT10K) are attached to various parts of the

Table 2.1: MOT coil parameters. Field strengths are specified at the center of the MOT cell, where the MOT resides. All coils are wound from 20 gauge magnet wires.

Coil pair	Number of turns	ID (cm)	D (cm)	Field (G/A)
Z shim	2×14	6.99	6.64	1.63
X shim, Y shim, and OP	13×5	5.72	16.5	1.00
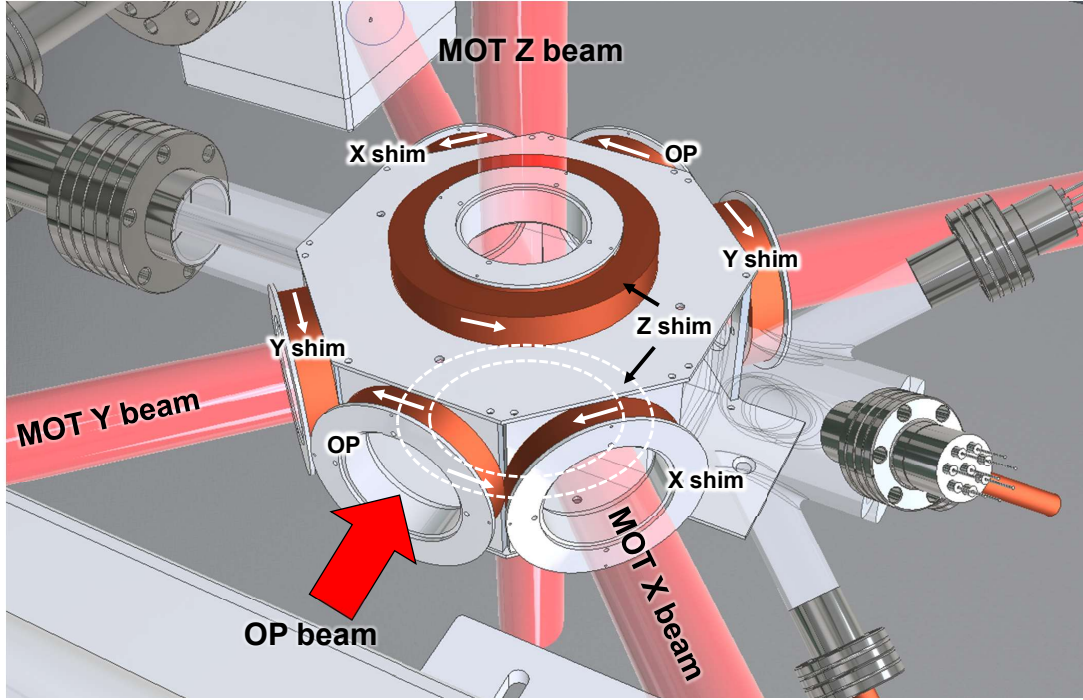
Figure 2.7: Geometries of the MOT shim coils and laser beams. Three pairs of beams propagate along the x, y, and z directions as indicated in the figure, and intersect at the center of the MOT glass cell to form a standard six-beam MOT configuration. An additional OP (optical pumping) beam is sent into the cell to overlap with the MOT region. With each beam, there is a pair of shim coils oriented coaxially to provide a shim magnetic field in the beam's direction. White arrows on the coils indicate the direction of current flow when a positive DAC voltage is applied. All coils are affixed to an aluminum mounting form.

glass cell and the coil support to control the temperature of the MOT chamber and adjust the alkali vapor pressure inside. Their placements are documented in Appendix A.

2.2.3 The evaporation chamber

The evaporation chamber and the vacuum parts attached to it are shown in Fig. 2.8. The chamber itself is a 1.33" CF spherical cube from Kimball Physics (MCF133-SphCube-A6), with three standard viewports and one re-entrant viewport (Fig. 2.8(c)) attached to it for optical access. The viewports feature UV fused silica windows, AR-coated on both sides over a wavelength range of
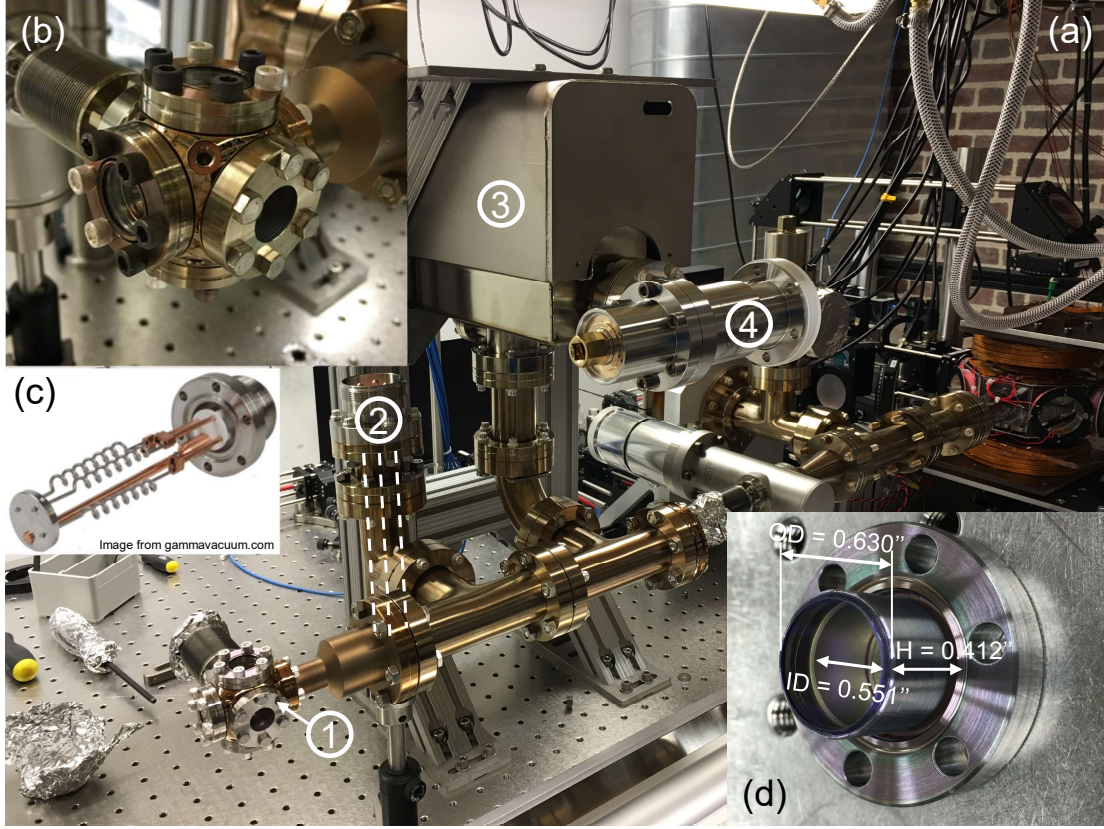
Figure 2.8: The evaporation chamber and its association vaccum setup. (a) photo of the evaporation chamber section after it is fully assembled but before joining to the MOT chamber section and bakeout. ① Evaporation chamber; ② TSP; ③ ion pump; ④ angled valve. (b) Close-up of the evaporation chamber, which is a 1.33″ CF cube with four standard viewports attached to it, as well as a re-entrant viewport that is shown in (d). (c) Photo of the TSP. During the bakeout, the TSP is degassed by Running through each filament, 21 A of current for a duration of 150 s, and then 42 A for another 150 s, with a 100 s break in between firings.

550 - 1100 nm, with an average reflectance $R_{avg} \leq 0.5\%$. This chamber, as its name suggests, is where the radio frequency (RF) evaporation of atoms take place. The small physical size of the chamber is limited by the QUIC magnetic trap[71] that surrounds it (section 2.4.2), which itself needs to stay clear of the path of the transfer coil (section 2.4.1). The re-entrant viewport allows the Ioffe coil of the QUIC trap to closely approach the atoms, which are confined near the center of the chamber during evaportaion.

39

Since the evaporation takes place on a long time scale of tens of seconds, it is critical to maintain good vacuum inside the chamber and minimize atom loss due to collision with background gas. To this end, we installed a standard ion pump (TiTan 75 L/s, Gamma Vacuum), as well as a Titanium sublimation (TSP, Gamma Vacuum) pump near the evaporation chamber. The working principle of a TSP is as follows: as high currents are passed through a titanium filament, titanium atoms sublimate off of it and subsequently deposit on nearby surfaces inside the vacuum system. This creates a thin layer of titanium atoms over a large surface area which background gas molecules can chemically bind to and be pumped out of the system. In our setup, the TSP is placed without direct line-of-sight to any of the viewports (to avoid significant metal coating on optical windows), pumps, or valves (to avoid interfering with their functions). During the vacuum pump down and bakeout, the TSP filaments are degased by running a pre-programed firing sequence with its current controller (see caption). After the bakeout and before the separation of the turbo pumping station from the system, one of the filaments is fired for two 60 s cycles at a current of 46 A to create the desired titanium pumping layer within the system.

2.2.4   Science chamber

The science chamber, shown in Fig. 2.9, can be regarded as the heart of our experiment. It is where molecule association and the ensuing chemical reactions take place. The chamber consists of a spherical octagon (Kimball Physics MCF600-SphOct-F2C8), with various components attached to its eight 2.75" CF ports and two 6.00" CF ports. Viewports with DUV fused silica windows provide optical access for various laser beams into the chamber. RF and microwave coils, mounted on a copper support structure, provide control over the hyperfine states of the K and Rb atoms (section **??**). The velocity-map imaging (VMI) electric field plate stack, a key component in our ion detection scheme (section 2.5), provide acceleration and velocity map-
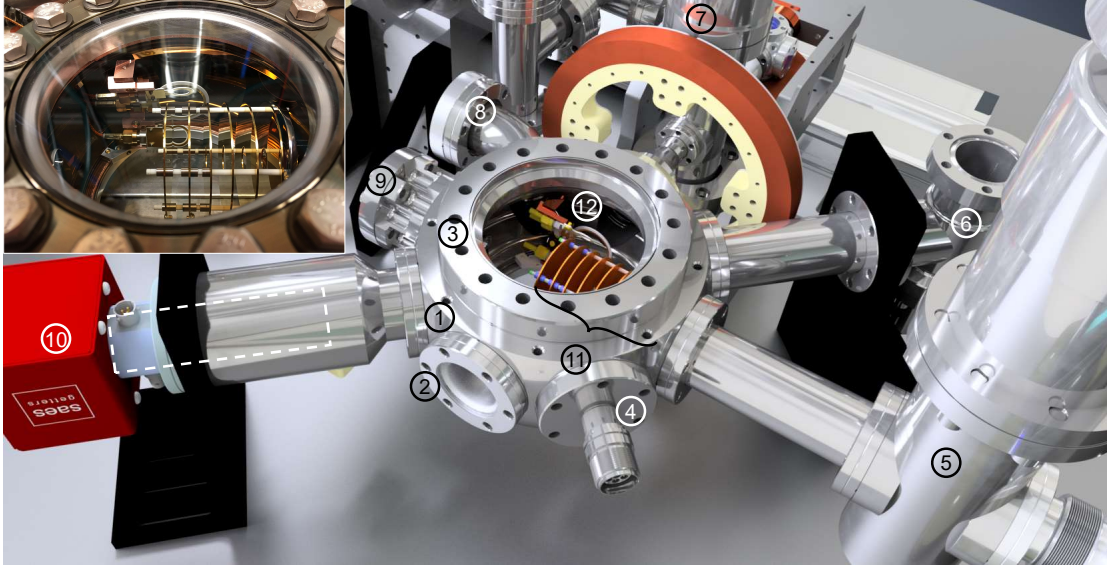
Figure 2.9: CAD rendering of the science chamber. ① Spherical octagon (Kimball Physics MCF600-SphOct-F2C8); ② 2.75" CF viewport with DUV fused silica window, AR-coated on both sides for 532 - 1100 nm ($R_\mathrm{avg} \leq 0.5\%$); ③ 6.00" CF viewport with DUV fused silica window, un-coated to accommodate high energy UV pulses that can potentially damage most AR-coatings; an identical viewport is mounted on the opposing side of the chamber; ④ 7-pin HV feedthrough for voltage supply to the VMI electric field plates; ⑤ Gate valve with (VAT 48132-CE01, ID = 1 1/2") separating the science chamber from the TOF tube; ⑥ Angled valve for the attachment of the turbo pumping station; ⑦ Gate valve with (VAT 48124-CE01, ID = 5/8") separating the science chamber from the evaporation chamber; ⑧ 4-port SMA feedthrough for connections to in-vacuum RF and microwave coils; ⑨ Channel electron multiplier (CEM) mounted on an SHV feedthrough; unfortunately the CEM became unfunctional after the vacuum baking; ⑩ ion-NEG combination pump (SAES getters, NextTorr D200-5) housed inside an over-sized 2.75" nipple; the white dashed frame indicates the location of the pumping element within the nipple; ⑪ VMI electric field plate stack; ⑫ in-vacuum RF and microwave antenna mounted on copper support structure, to be used for atom state manipulation inside the science chamber; unfortunately none of the antenna are currently functional, and have been replaced by out-of-vacuum antenna and horns. (Inset) Photo of the inside of the science chamber as viewed from the top viewport.

41

ping for photoionized species. Finally, a channel electron multiplier (CEM, 10RS-EDR) was installed as an ion/electron detector in addition and complimentary to the micro-channel plate (MCP) detector farther down stream. Further details on all the components and their purposes can be found in the caption of Fig. 2.9. Vacuum inside the science chamber and its surrounding parts is maintained by an ion-NEG* combination pump (SAES getters, NextTorr D200-5), which offers a particularly high pumping rate for H_2 molecules – the typical dominant gas load at UHV pressures.

Compared to the previous chambers, the science chamber houses many more in-vacuum components, all of which can outgas and contribute to the background gas load inside the chamber. Therefore, a thorough bakeout at high temperature is desired. However, many of the components (*e.g.* viewports, feedthroughs, in-vacuum cables, antenna, CEM) have stringent limits on temperature and/or temperature gradient. For this reason, we built a specialized oven around the chamber to provide uniform, controlled heating during the bakeout (see Fig. 2.4(b)). Despite the care taken, all three antenna as well as the CEM, which were tested to be in working order before the bakeout, became nonfunctional afterwards. The two microwave antenna, previously tuned to efficiently transmit at 6.8 and 8.5 GHz respectively to drive transitions between hyperfine manifolds in ^{87}Rb in the presence of low and high magnetic field, became strongly reflective at those frequencies. The RF antenna, designed to operate at $\sim$80 MHz to drive transitions between Zeeman sub-levels in ^{40}K, demonstrated poor coupling of RF power to the atoms. Fortunately, all failed in-vacuum antenna were replaced successfully by external ones, and we were spare from breaking vacuum. The CEM failed to produce any response to photoions hitting it, and all ion detections were perfomred by the MCP instead.

---

*Non-evaporative getter, in contrast to evaporative getters like the TSP. Here the getter material is localized within the pump itself.
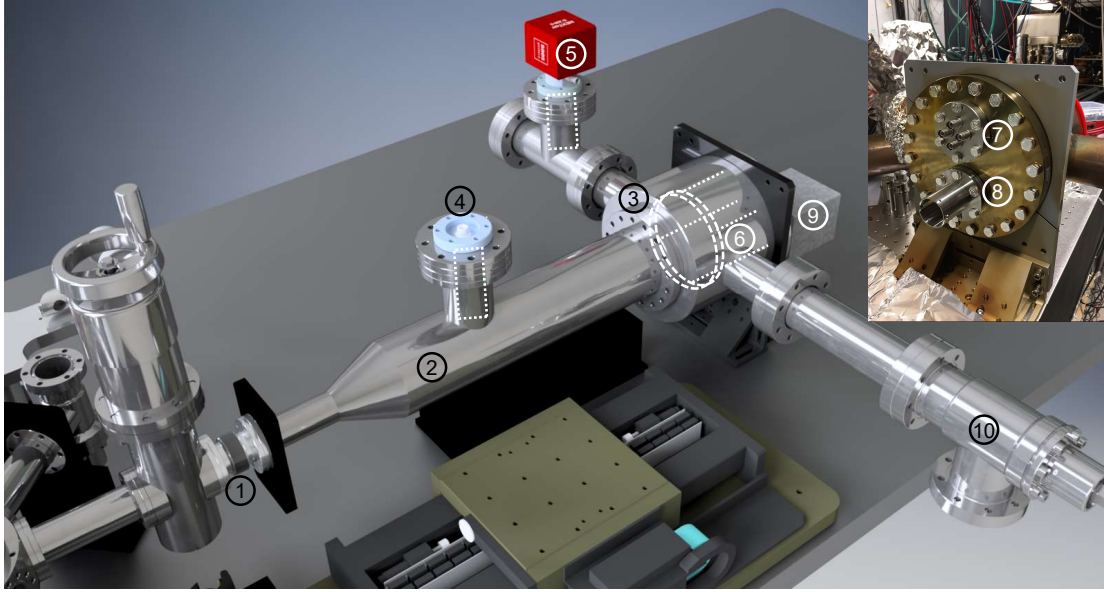
Figure 2.10: CAD rendereing of the TOF tube and the MCP chamber. ① bellows connection between science chamber and TOF tube; ② TOF tube; ③ MCP chamber; ④ NEG pump; ⑤ ion-NEG combination pump; ⑥ MCP assembly (section 2.5.3); ⑦ MCP HV feedthrough; ⑧ MCP signal feedthrough; ⑨ MCP signal decoupler; ⑩ angled valve.

2.2.5   TOF tube and MCP chamber

The final section of our vacuum system is the TOF (time-of-flight) tube and the MCP chamber, shown in Fig. 2.10. Photoions generated in the science chamber fly through the empty TOF tube, and are eventually detected by the MCP housed inside the MCP chamber (see Section 2.5.3). The vacuum inside the TOF tube and the MCP chamber are maintained by a NEG pump (SAES getters, CapaciTorr D200) and an ion-NEG combination pump (SAES getters, NextTorr D200-5), respectively. The choice of an NEG pump, as opposed to an ion or a combination pump, for the TOF tube is to prevent stray electric fields from ion pump elements from distorting the ion flight trajectory. The combination pump attached to the MCP chamber is placed out direct line-of-sight from the MCP to prevent stray ions generated by the pump from hitting the detector. High voltages and ion signals are coupled in and out of the MCP respectively via electrical

feedthroughs.

2.3 Laser and optical systems

In this section we describe the various laser systems used to generate the optical fields for the cooling and trapping of atoms (2.3.1), the optical dipole trapping of atoms and molecules (2.3.2), and the formation of ground state molecules from loosely-bound atom pairs (2.3.3).

2.3.1 Rb and K laser systems

The manipulation of Rb and K atoms, including cooling, optical pumping, and imaging, requires narrow-band, frequency-tunbale laser lights that directly target the strongest optical transitions (D_1 and D_2 lines) in these atoms. To this end, we constructed the laser systems as shown in Fig. 2.11 and 2.12. We use DBR (distributed Bragg reflector) lasers as the original sources of the lights, which are then frequency-stablized, split off into various branches, and in some cases further amplified, to generate all the necessary frequencies for the experiment.

The Rb laser system (Fig. 2.11) contains two DBRs – cooling and repump – whose frequencies are tuned to be close to the $|F = 2\rangle \rightarrow |F' = 3\rangle$ and the $|F = 1\rangle \rightarrow |F' = 2\rangle$ transitions of the D_2 line of ^{87}Rb around 780 nm, respectively. The repump DBR, which also functions as a master laser, is frequency referenced to the $|F = 1\rangle$ to $|F' = 1, 2\rangle$ crossover transition via saturated absorption spectroscopy performed on a Rb atomic vapor cell. Its frequency is then shifted by AOMs to generate lights required for repumping of the atoms. The cooling DBR's frequency, on the other hand, needs to be dynamically changed between different stages of the experiment. To this end, we reference its frequency to that of the repump DBR using an optical phase-locked loop (PLL)[191]. In short, lights from both DBRs are beat against each other on a fast photodiode
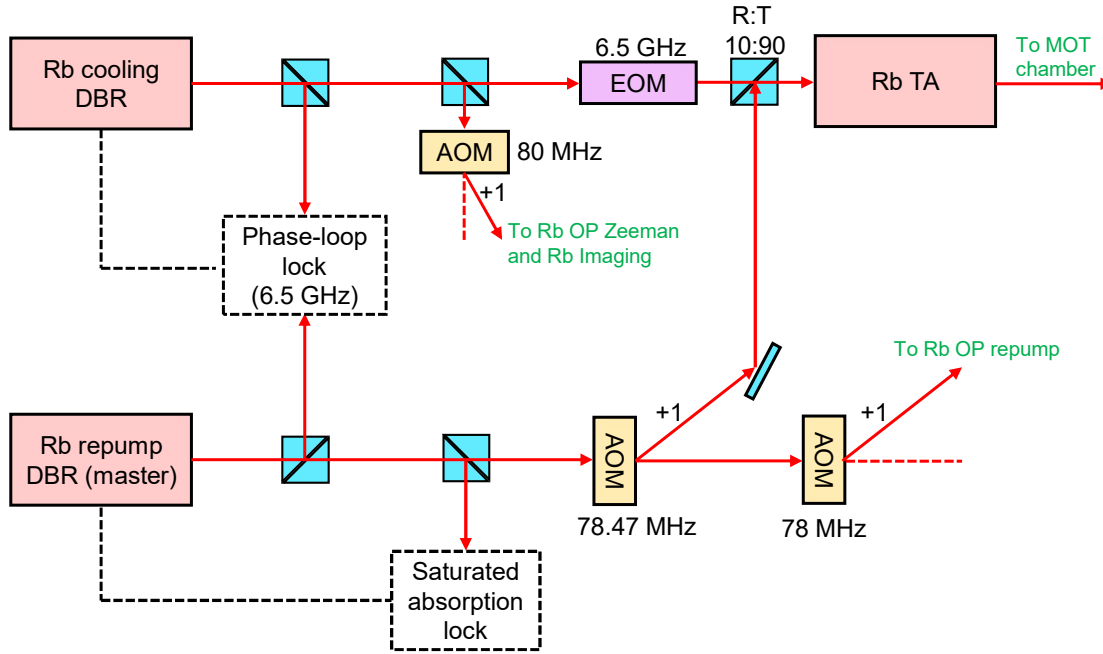
Figure 2.11: The Rb laser system. Cooling and repump lights are generated by two separate DBR lasers. The repump DBR is frequency-referenced to [87]Rb transitions via saturated absorption spectroscopy, and acts as the master laser of this system. The cooling DBR is referenced to the repump via an optical phase-locked loop (PLL). Both lights are combined on a NPBS and injected into a TA, where they are amplified in optical power before fiber-coupling to the MOT chamber. Alternatively, repump light can be generated as a sideband of the cooling light via the 6.5 GHz EOM. In addition to providing the lights required for laser cooling and trapping, this system also generates lights for optical pumping and imaging.

(EOT ET-4000). The resulting beatnote signal, together with a frequency-tunable reference RF signal, are fed into a phase frequency detector (PFD, ADF4159) and compared. Their difference is encoded in an error signal, which is then used to feedback the cooling DBR. As the reference RF frequency is changed, the DBR frequency is changed accordingly. The relative frequency stability between the two phase-locked DBRs is measured to be better than a few Hertz.

Two laser systems are constructed for K, targeting the D_2 and D_1 transitions of ^{40}K at 766.7 and 770.1 nm, respectively. The D_2 laser system for K is similar to that for Rb in many regards, except in this case three DBRs are used – a master DBR for the sole purpose of locking to

45

K atomic transition, and cooling and repump DBRs phase-locked to the master. This design allows both cooling and repump frequencies to be tuned during the experiment. Due to the low natural abundance of ^{40}K, the master DBR's frequency is referenced to a D_2 line transition in ^{39}K from $|F = 1, 2\rangle$ crossover to the unresolved excited state hyperfine manifold. The cooling and repump DBR's frequencies are tuned to be close to the $|F = 9/2\rangle \rightarrow |F' = 11/2\rangle$ and the $|F = 7/2\rangle \rightarrow |F' = 9/2\rangle$ transitions of ^{40}K, respectively, which are +500 and -650 MHz detuned from the master frequency. The D_1 system, dedicated to performing Λ-enhanced gray molasses cooling of K atoms (see Section 3.2), follows a simpler design. Here, a single DBR is frequency-referenced to a D_1 line transition in ^{39}K from $|F = 1, 2\rangle$ crossover to $|F' = 2\rangle$. Its output light is splitted into two branches which are respectively frequency-shifted by double-passed AOMs to generate the cooling and repump frequencies required for the molasses cooling.

Laser cooling demands a moderate amount of optical power – generally a few tens of milli-watts for each cooling beam given a typical beam diameter of $1 - 2$ cm. Therefore, in each laser system, the cooling and repump lights are combined and amplified by a tapered amplifier (TA) The amplified cooling plus repump light is then sent via optical fibers to the machine table, and directed into the MOT chamber as shown in Fig. 2.7. In each of the three spatial directions, a beam is sent through the MOT cell and retro-reflected onto itself, generating the six-beam configuration required for laser cooling. Each beam has a $1/e^2$ Gaussian width of 2.5 cm, and an optical power of ~ 50 mW in the case of the Rb and K D_2 lights, and ~ 35 mW in the case of the K D_1 light.

2.3.2 Optical-dipole trap laser system

Optical-dipole trapping[90] (ODT) is employed to confine the atoms and molecules during various stages of the experiment. In this technique, a laser, with frequency far-detuned from any elec-
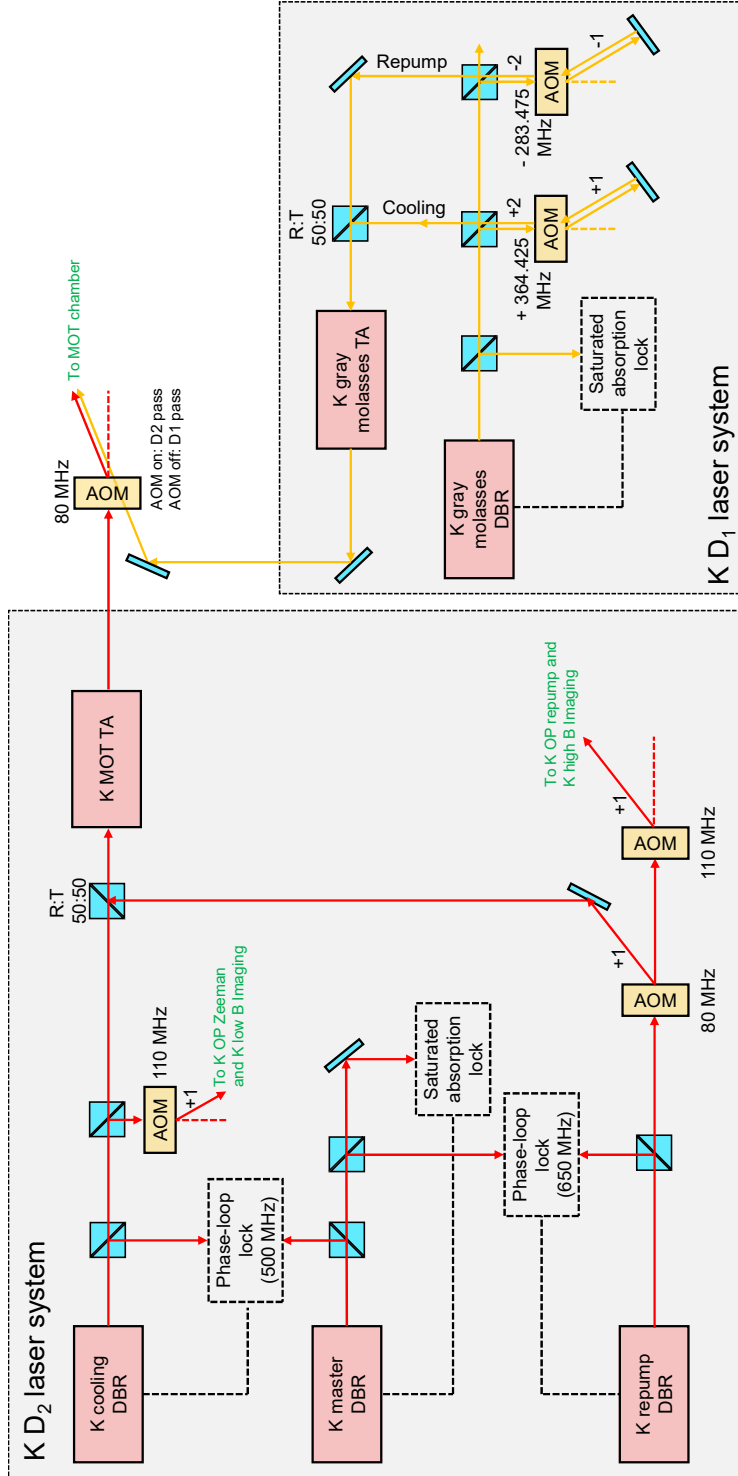
Figure 2.12: The K laser systems. (The D_2 system) Cooling and repump lights are generated by two separate 766.7 nm DBR lasers. A third DBR is frequency-referenced to ^{39}K D_2 transitions via saturated absorption spectroscopy, and acts as the master laser of this system. The cooling and repump DBRs are frequency-referenced to the master via a optical phase-locked loops (PLL). Both lights are combined on a NPBS and injected into a TA, which amplifies their optical power. In addition to providing the lights required for laser cooling and trapping, this system also generates lights for optical pumping and imaging. (The D_1 system) Light from a single 770.1 nm DBR is split into two paths and double-passed through AOMs to generate the cooling and repump frequencies used during Λ-enhanced gray molasses cooling. The DBR's frequency is referenced to ^{39}K D_1 transitions via saturated absorption spectroscopy. After the AOMs, the cooling and repump branches are again combined on a NPBS and injected into a TA, which amplifies their optical power. Finally, the amplified D_1 and D_2 lights are combined on a AOM before fiber-coupling to the MOT chamber. This AOM passes the D_2 light when its RF power is fully on, and the D_1 light when off. As such, the D_1 and D_2 lights can share the same optical fiber as well as subsequent optical paths around the MOT chamber.

47

tronic transitions in the confined particles, exerts an attractive force on the particles via electric dipole interaction, creating a confining potential around where the laser is focused. Three different ODT beams are used in the experiment – a "transfer" beam (TODT) for transporting atoms from the evaporation chamber to the science chamber after RF evaporation (section 3.3), and a "hortizontal" beam (HODT) and a "vertical" beam (VODT) for confining atoms and molecules inside the science chamber. All three beams are derived from a single 1064 nm MOPA* laser with an output power of 55 W and a spectral linewidth of 1 kHz (Coherent Mephisto 55W), according to the schematic diagram in Fig. 2.13(a). The TODT light is further amplified by a 20 W fiber amplifier system (ALS-IR-1064-20-A-SF). AOMs with 80 MHz resonant frequencies are used to control the intensities of the beams during the experiment. To avoid spatial interferences when pairs of ODT beams are turned on simultaenous during the exerpiment, we shift the frequency of the HODT beam away from that of the VODT and TODT by using the +1 AOM order for the prior and the -1 order for the latter two.

The HODT and VODT beams are fiber-coupled† to the machine table and launched into the science chamber as shown in Fig. 2.13(b)&(c). The HODT (VODT) beam, collimated to Gaussian intensity profiles, is focused by a single lens with a focal length of 25 cm (50 cm) to the geometric center of the chamber to a waist size of 35 μm (100 μm). The VODT is aligned slightly off from gravity to avoid the science chamber imaging optics (section 2.3.4), and intercepts the HODT at a 70° angle to form a crossed trap (XODT) towards the final stage of the sequence (section 3.6).

Optical transport is a commonly employed technique in AMO experiments, in which atoms are moved between two different locations within a vacuum system by translating the focus of the trapping beam. This focus tuning can be accomplished by either physically moving the focusing

---

*Master Oscillator Power Amplifier

†We used fiber couplers from Oz Optics (HPUC-23AF-1064-P-6.2AS-11) on laser table side which can handle high optical powers.
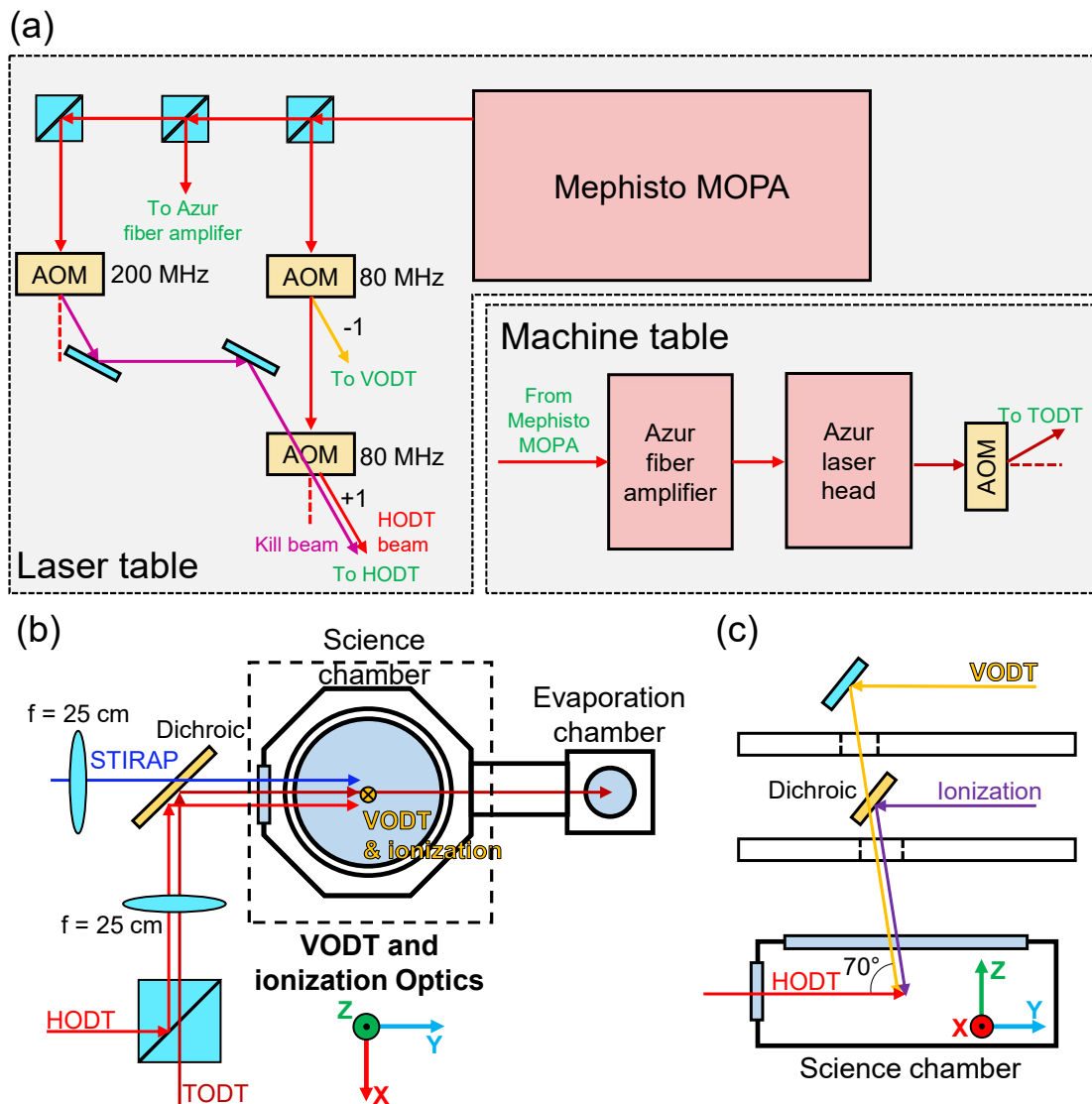
Figure 2.13: The ODT laser system. (a) Optical setup for generating the various ODT beams, including the HODT, VODT, and TODT, as well as the "kill" beam used for studies described in Chapter 6. All beams are derived from a single MOPA source, and, after appropriate frequency-shifting by AOMs, fiber-coupled to the machine table. In the case of the TODT, the light is further amplified by fiber amplifiers on the machine table. The HODT and "kill" beams are combined on a 80 MHz AOM as indicated, such that they are passed to the experiment when the RF power is off or on, respectively. This ensures that they share the same optical path on the machine table. (b,c) Optical setup around the science chamber for routing the various ODT beams as well the STIRAP and ionization beams to the center of the chamber, where molecules are formed. The black dashed frame in (b) indicates the locations of two breadboards placed above the science chamber, shown in (c) as viewed from the side.

49
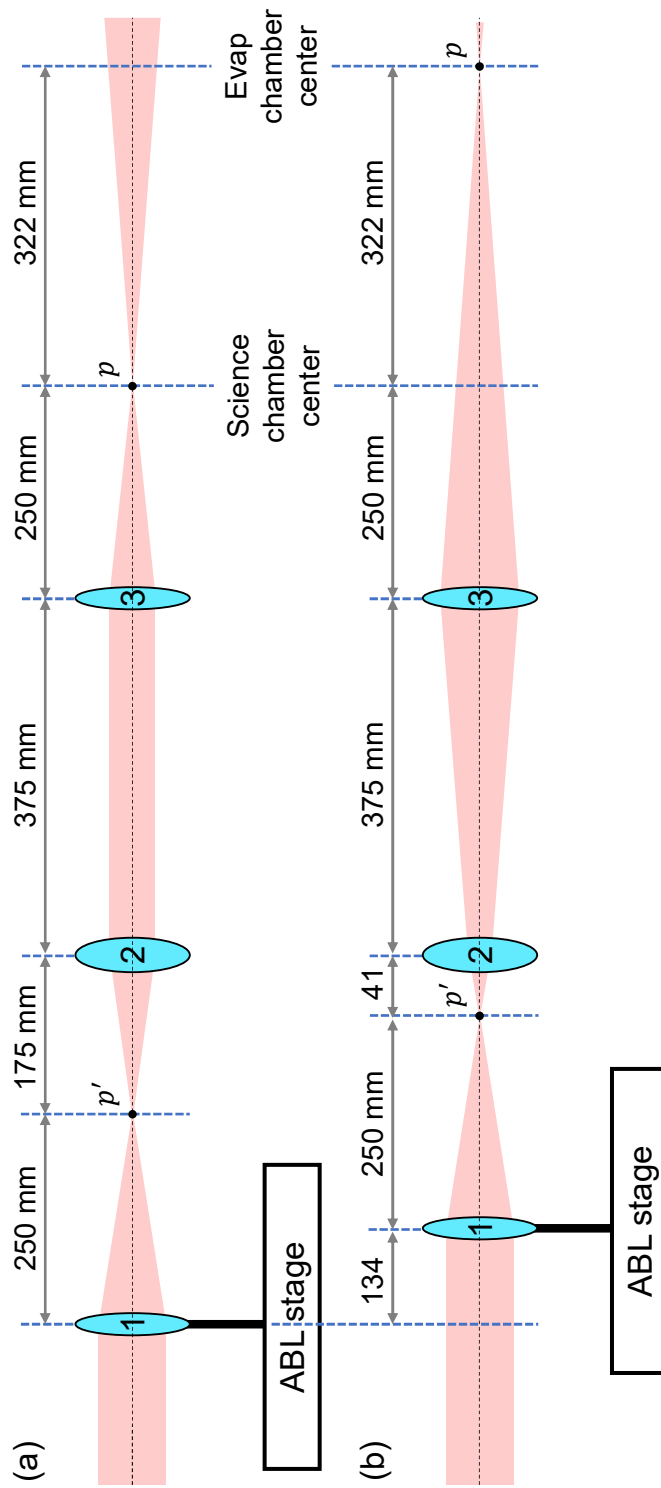
Figure 2.14: Schematic of the transfer ODT (TODT) optical setup. The setup consists of three biconvex lenses, with focal lengths of $f_1 = 250$ mm, $f_2 = 175$ mm, and $f_3 = 250$ mm, respectively. Lens 1 is placed on an air-bearing linear stage (ABL) with a 200 mm travel, and focuses down a collimated beam with an elliptical profile to point p'. Lens 2 and 3 together form a $4f$ imaging system which projects p' to point p within the vacuum system. Actuating the ABL allows the position of p to be translated, accomplishing atom transfer. (a) and (b) indicate the arrangements of the optics when the TODT is focused to the centers of the science and evaporation chambers, respectively.

lens for the beam, or by changing its focal power (e.g. through a focus-tunable lens). We took the prior approach for our TODT, and designed the optical transport setup schematically illustrated in Fig. 2.14. A collimated input beam is focused to p' by lens 1 ($f = 250$ mm), which is mounted on an air-bearing linear (ABL) translation stage (Aerotech, ABL15020) that has a 200 mm range of motion. p' is then projected by a $4f$ imaging system, composed of lens 2 ($f = 175$ mm) and lens 3 ($f = 250$ mm), to p inside the vacuum system. The position of p is tuned by actuating the ABL and moving the position of p'. Note that the $4f$ system magnifies the distance by which the focus is translated by a factor equal to the square of the ratio of the component lenses, which, in our design, is $(250/175)^2 \approx 2.04$. This is necessary since the separation between the centers of the science and evaporation chambers is 322 mm, longer than the range of the stage. In practice, we found this ratio to be 2.4. Fig. 2.14(a) and (b) show the optical paths when the TODT is focused to the centers of the science and the evaporation chambers, respectively.

During the transfer, atoms inside the TODT are subjected to forces from the acceleration and decceleration. If the confinement along the axial direction of the beam is too weak, these forces can result in large oscillations or even spillage of the atom cloud. The restoring force constant of an ODT along an axis is proportional to the square of its trapping frequency (ω) in that direction. To maximize the axial trapping frequency of the TODT while maintaining a reasonable radial cross sectional area*, we chose an elliptical beam profile, with waists of $w_z = 25$ μm and $w_x = 45$ μm in the directions along and perpendicular to gravity, respectively. Compared to a circular beam of same radial area ($w_z = w_x = 33.5$ μm), the axial trapping frequency of the elliptical beam, at the same optical power, is higher by a factor of 1.32, corresponding to a confining force 1.75 times stronger.

While the the waist size of the TODT at p is supposed to remain constant during the course of the transfer by design, we find in practice that the science chamber beam waist to be somewhat

_____

*Mode-matching

smaller compared to the evaporation chamber beam waist, manifested as differences in measured trapping frequencies at the two locations. See section 3.4 for more details.

Stabilization and control of the intensities of the ODT beams is accomplished by the feedback system shown in Fig. 2.15. In this design, light going to the experiment is generated from a diffraction order of an AOM driven by an RF signal. A portion of the light hits a photodetector (PD), and generates a photo-current that is converted into a voltage (PD voltage) by a sense resistor (R_{sense}). The PD voltage is then compared to a set point voltage using a PID (proportional, integral, differential) servo. Their difference results in a servo output (V_{servo}) that is then fed into a box housing RF components (RF box), where it is mixed with a local oscillator (LO) on a frequency mixer. In this case, the LO is a voltage-controlled oscillator (VCO) tuned close to the AOM's resonant frequency (80 MHz). The output voltage of the mixer (RF port) can be approximated as the product of the voltage from the VCO (LO port) and V_{servo} (IF port). The RF output is then amplified by an RF amplifier to up to 2 W and fed into the AOM, completing the feedback loop. An RF switch is placed between the mixer and the RF amp to shut off the RF signal when the ODT needs to be completely turned off. In the above configuration, the PD voltage (and correspondingly the ODT power) is stabilized to the DAC set point which can be dynamically changed during the experiment, for instance, during ODT evaporation (section 3.6). For the experiments described in Chapters 5, 6, and 7, square wave modulations of the ODT powers are required. This was initially accomplished by simply enabling and disabling the RF switch via a TTL signal, while the DAC voltage is held constant. This, however, resulted in a significant integration and build up of error during the off-phase of the ODT modulation, and an ensuing overshoot of the ODT power during the on on-phase, as shown in the scope trace of the ODT power in Fig 2.16(a). To resolve this issue, we used a new version of the servo where a relay is added to enable/disable the integral gain. By operating the relay in synchrony with the RF switch, error accumulation was prevented, resulting in the cleaner switching as shown in Fig
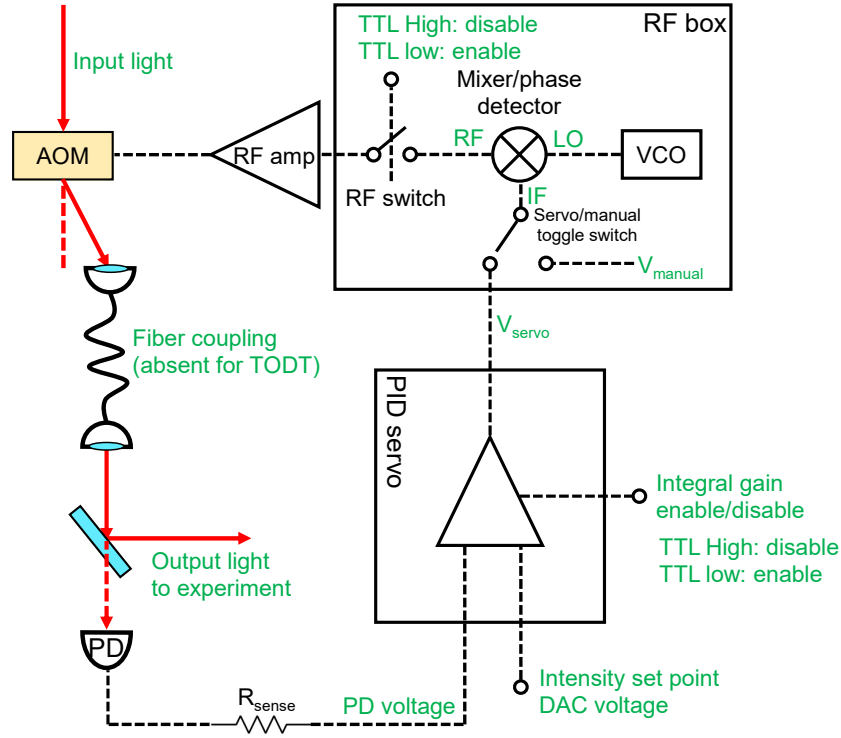
Figure 2.15: The ODT intensity servo schematic. A portion of the ODT light is directed onto a photodetector (PD), and generates a photo-current that is converted into a voltage (PD voltage) by a sense resistor (R_{sense}). The PD voltage is then compared to a set point voltage using a PID servo. Their difference results in a servo output (V_{servo}) that is then fed into a box housing RF components (RF box), where it is mixed with a local oscillator (LO) on a frequency mixer. In this case, the LO is a voltage-controlled oscillator (VCO) tuned close to the AOM's resonant frequency (80 MHz). The output voltage of the mixer (RF port) can be approximated as the product of the voltage from the VCO (LO port) and V_{servo} (IF port). The RF output is then amplified by an RF amplifier to up to 2 W and fed into the AOM, completing the feedback loop. An RF switch is placed between the mixer and the RF amp to shut off the RF signal when the ODT needs to be completely turned off. In this configuration, the PD voltage (and correspondingly the ODT power) is stabilized to the DAC set point which can be dynamically changed during the experiment.
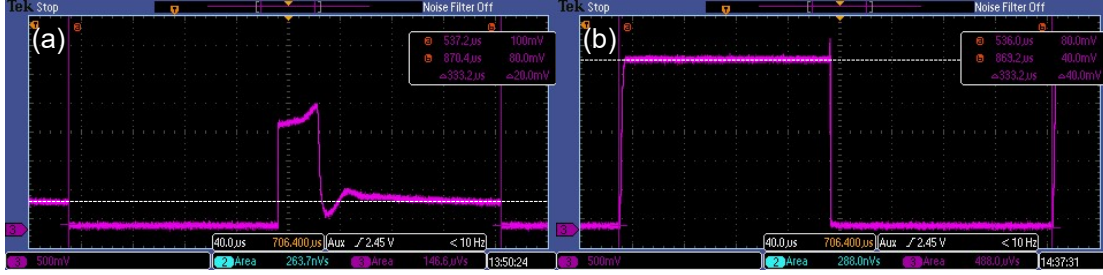
Figure 2.16: ODT intensity overshoot and correction. (a) Scope trace showing the ODT intensity during one period of a 3 kHz square wave modulation. In this case, the modulation is applied by enabling and disabling the RF switch gating the RF power to the AOM of the ODT. (Fig. 2.15). This resulted in significant overshoots in the ODT intensity at the beginning of each bright phase, due to errors accumulated during the preceding dark phase by the servo. This issue is fixed by disabling the integral gain of the servo during the dark phase of the modulation, resulting in the much improved following of the ODT intensity to the square wave modulation as shown in (b). The white dashed lines in both (a) and (b) represent the same actual optical power level.

2.16(b).

Finally, I wish to highlight issues we have experienced with regard to the pointing stability of the TODT beam and their resolutions. Note that while the HODT and VODT beams, after emerging from their respective AOMs on the laser table, are fiber-coupled to the machine table, the TODT beam is not. Instead, the TODT beam is launched directly on the machine table and diffracted to the experiment via an AOM. This, coupled with the long beam path of the TODT (~ 2 m), yielded two beam pointing instability issues both related to the AOM:

- Since the diffraction angle of the beam is directly proportional to the frequency of the AOM, any frequency noise in the RF signal driving the AOM translates to a beam pointing noise and therefore shaking of the trap, which can result in heating of the confined particles.

- Driving of the AOM requires substaintial RF power ($1 - 2$ W), which heats the AOM crystal and result in the thermal expansion/warping of the crystal that deflects the output beam. Thus when the TODT is switched on or off, the beam position drifts by an amount

54

corresponding to approximately a beam waist over a time scale of a few seconds, resulting in poor atom loading and transfer performances.

The first issue is solved by replacing the VCO providing the LO signal in the feedback loop (Fig. 2.15) with a DDS signal that has a much lower frequency noise *. Doing so resulted in a 4-fold reduction in the heating rate experienced by the atoms while inside the TODT. The second issue is solved using a setup similar to that described in Ref.[76]. Here, we use a "main" RF tone at 90 MHz to control the power of the TODT at the experiment, and use a second "auxiliary" RF tone at 60 MHz to keep the crystal heated while the main tone is off or at reduced power. The beam diffracted due to the auxiliary tone is terminated at a beam dump, and the 30 MHz frequency difference between the two tones maintains a clear angular separation between the useful and dumped beams. In hindsight, we note that both of the above issues can be resolved by coupling the ODT light after the AOM to the experiment through an optical fiber, in which case any beam pointing fluctuation would translate into an intensity fluctuation on the other side of the fiber, and be suppressed by the intensity feedback loop (Fig. 2.15).

2.3.3 STIRAP laser system

STIRAP (STImulated Raman Adiabatic Passage)[21] is used in our experiment to transfer the molecular population from a weakly-bound state, $|f\rangle$, into the rovibronic ground state, $|g\rangle$ (section 3.8). This technique employs a pair of (Raman) lasers whose photon energy difference equates the difference between the binding energies of $|f\rangle$ and $|g\rangle$, and couples these states via an excited intermediate state $|i\rangle$ (Fig. 2.17 inset). In our case, the frequencies for the up leg ($|f\rangle \rightarrow |i\rangle$) and down leg ($|i\rangle \rightarrow |g\rangle$) transitions correspond to laser wavelengths of around 970 and 690 nm, respectively. As a quantum-coherent process, the efficiency of the state transfer, η,

---

*We believe the instability of the VCO frequency is due to noise in its control voltage, which upon improvement could also have solved the problem
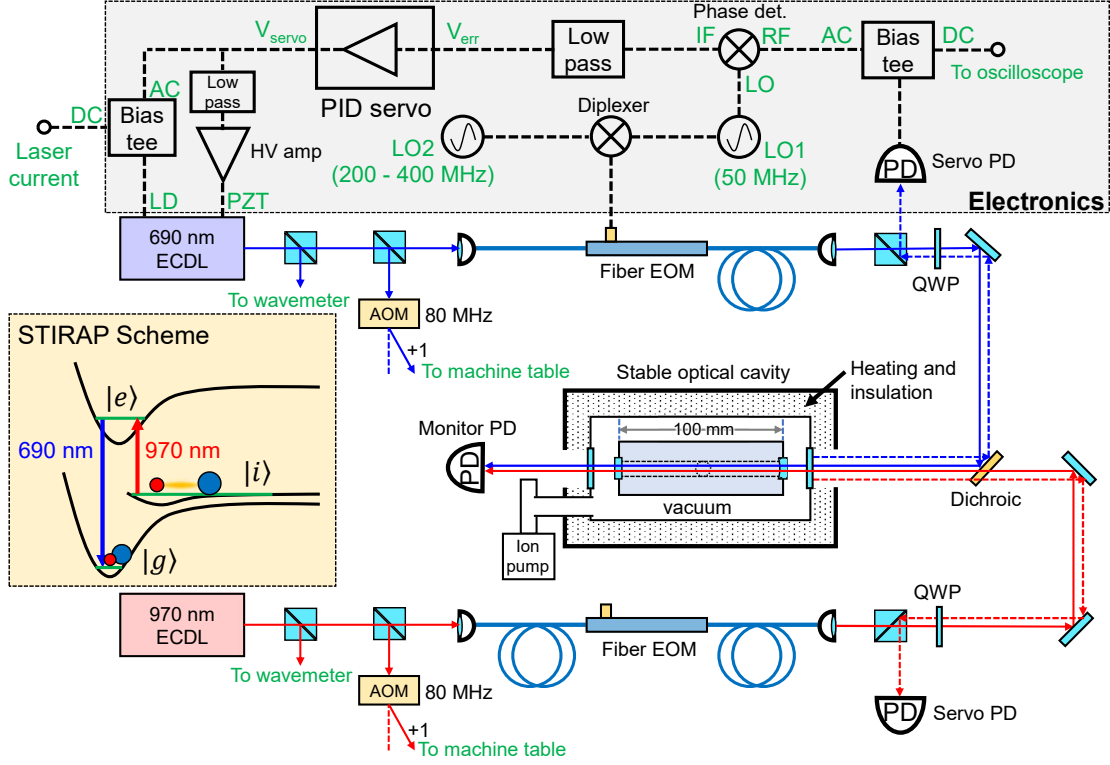
Figure 2.17: STIRAP laser system. Two ECDLs, operating at 970 nm and 690 nm respectively, generate the lights used for the up and down leg transitions used in the STIRAP scheme as shown in the inset. The frequencies of the two lasers are referenced to modes of a stable optical cavity, and offset to the molecular transition frequencies by locking to EOM-generated sidebands. The frequency locking follows a standard PDH scheme. The same set of locking electronics is used for both lasers, though shown here only for the 690 nm laser.

depends critically on the phase stabilities the two lasers during the transfer process. Given the relevant parameters for our molecular system (the expected Rabi frequencies of the two transitions and the excited state decay rate), in order for η to not be limited by phase noise, both lasers should be stablized to a linewidth of less than 1 kHz. To this end, we generate two narrow-line Raman beams using the optical setup depicted in Fig. 2.17, similar to the one used in the second generation KRb experiment at JILA [148]. In this setup, two external cavity diode lasers (ECDL) are frequency-referenced to cavity modes of a high-finesse, stable optical cavity (Stable Laser
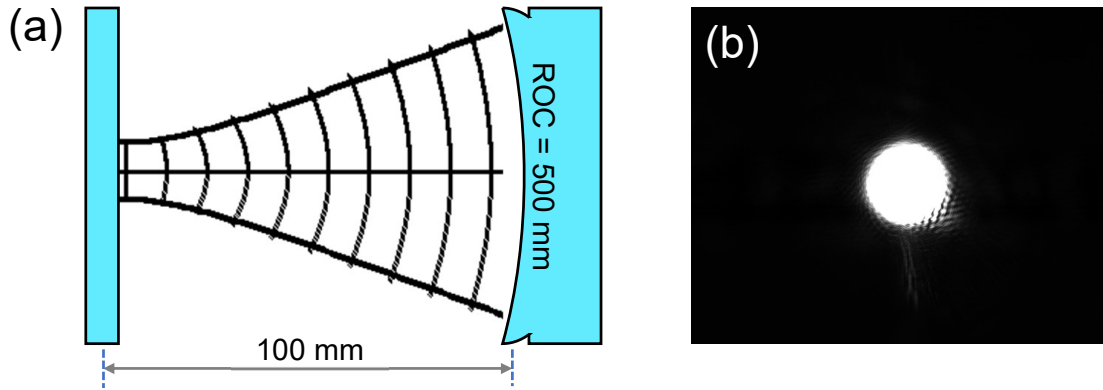
Figure 2.18: Gaussain $TEM_{0,0}$ mode inside the cavity. (a) Schematic showing the longitudinal profile of the mode as it is contained by the cavity. We employed a plano-concave cavity with a 100 mm length and a concave mirror with a 500 mm ROC. The beam is injected from the curved side. In order to be coupled into the cavity, the beam's wavefront must match the curvatures of the two end mirrors as shown. (b) Camera image showing the transverse profile of the beam right after it transmits through the plano mirror.

Systems) using the Pound-Drever-Hall (PDH) locking scheme[25].

The SLS reference cavity features a plano-concave design, with a cavity length of 10 cm (corresponding to a free spectral range (ν_{FSR}) of 1.5 GHz), and a radius-of-curvature (ROC) of 50 cm for the concave mirror. The sub-kilohertz target laser linewidth requires the width of the cavity mode we reference to to be of order 10 kHz, which is achieved in the SLS cavity through highly reflective mirrors and a highly mechanically-stable cavity design. Through cavity ring-down measurements, we determined the cavity linewidths (FWHM) to be 4.5 and 11 kHz for 690 and 970 nm, respectively, corresponding to finesse values of 3.36×10^5 and 1.32×10^5. In addition, the absolute frequency stability of the cavity modes matters for maintaining the Raman condition for the molecular transfer. Given the expected two-photon linewidth of 500 kHz, the relative shift in frequency between the two laser frequencies should be within 100 kHz on a day-to-day basis. To this end, the cavity is housed under vacuum inside an inner can (pressure below 10^{-7} mbar, maintained by an ion pump (Agilent VacIon 10 L/s)), which is in turn enclosed in a temperature-stabilized outer can (temperature stablized to better than 10 mK).

In a plano-concave cavity, there is a unique set of longitudinal modes associated with each transverse spatial mode*, and we choose the $\text{TEM}_{0,0}$ mode, a simple Gaussian mode, for frequency reference. The confinement of a $\text{TEM}_{0,0}$ beam inside our cavity is shown schematically in Fig. 2.18(a) (not to scale). A key feature is that the ROC of the beam's wavefront at either end of the cavity matches the ROC of the corresponding mirror. To best match this condition and obtain good coupling to the $\text{TEM}_{0,0}$ mode, the light sent into the cavity is shaped into a Gaussian beam with a waist of ~ 200 μm placed at the location of the flat mirror. Fig. 2.18(b) shows the profile of the light transmitted through the cavity once it is coupled to the $\text{TEM}_{0,0}$ mode. The profile is radially symmetric, in contrast to higher order modes ($\text{TEM}_{m,n}$, known as Laguerre-Gaussian modes) which display nodes and are therefore easily distinguished from the $\text{TEM}_{0,0}$ mode.

Frequency stabilization requires an error signal (V_{err}) which is proportional to the difference ($\Delta\nu$) between the laser frequency (ν_{L}) and the reference frequency (ν_{ref}) to provide feedback. In PDH locking, this error signal is generated in the following manner: a portion of the laser's output light is split off and phase-modulated by a fiber-based electro-optical modulator (EOM, from EOSpace) driven by a 50 MHz RF source (LO1) to generate a set of PDH peaks that include a carrier and a pair of first-order sidebands, in $\sim$ 2:1 amplitude ratio (Fig. 2.19(a)), as well as a pair of smaller second-order sidebands that are unimportant for locking; the modulated light is sent to the cavity, and the reflected light is detected by the servo PD; if one of the three frequencies comes near a cavity resonance it will (partially) transmit, resulting in an interference (amplitude modulation) in the reflected light that carries the laser's frequency noise, at a frequency around that of the EOM modulation (see Ref.[25] for a derivation); the servo PD signal is then demodulated using a phase detector and low-passed to reveal the underlying error signal. Fig. 2.19 shows the error signal (green), along with the cavity reflected (magneta) and

*Due to the Gouy phase.

58
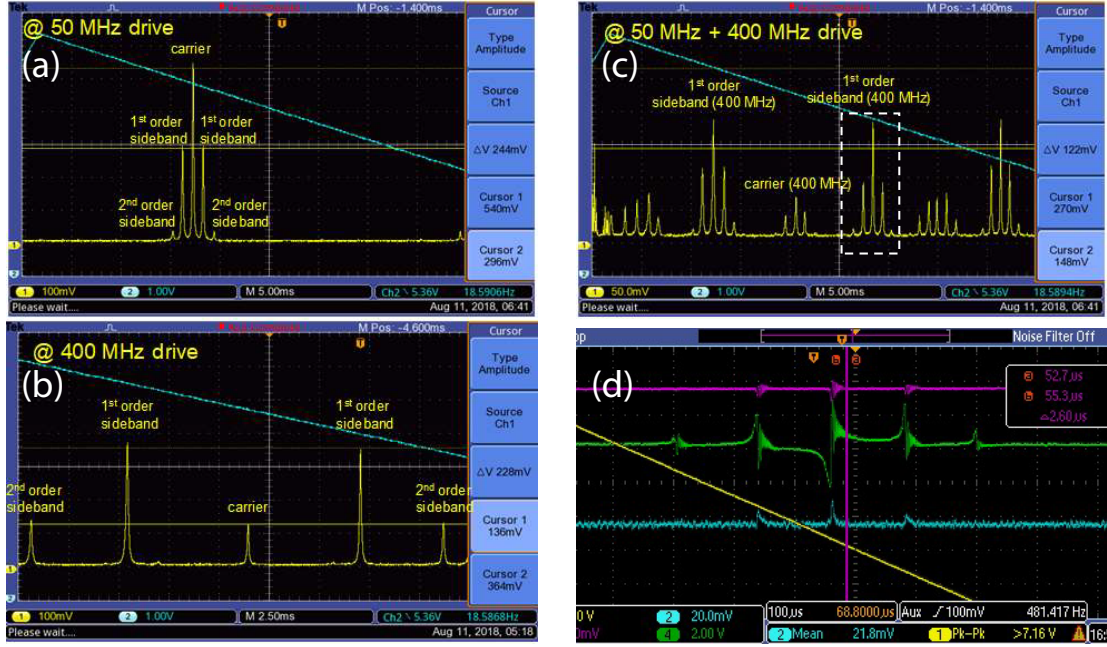
Figure 2.19: Frequency modulation of the 690 nm STIRAP laser via the EOM. (a) Spectrum of the laser after an 50 MHz modulation is applied. This generates the (1st order) sidebands required for PDH locking. We maintain a carrier-to-sideband ratio of 2:1 in order to maximize the strength of the resulting PDH error signal. (b) Spectrum of the laser after an 400 MHz modulation is applied. In this case, the modulation depth is chosen to maximize the 1st order sidebands, one of which is used for offset locking. The exact frequency of this modulation depends on the difference between the frequency of the molecular transition and that of the nearest cavity mode, and is in the 200 - 400 MHz range in our experiment. (c) To lock the laser frequency, both modulations are switched on to produced the spectrum as shown, which features sidebands on top of sidebands. (d) The cavity reflected light signal (magenta), the cavity transmitted light signal (cyan), and the demodulated PDH error signal (green) as the laser frequency undergoes a linear ramp (yellow). The resonances observed here correspond to the group of peaks in the white dashed box in (c). The laser frequency is locked to the zero-crossing of the central feature of the error signal. The fast oscillations associated with the reflected and error signals are due to cavity ring-down.

transmitted (cyan) signals, as the 690 nm laser's frequency is scanned linearly across a cavity resonance. The five visible features correspond to each of the frequency components in Fig. 2.19(a) coming into resonance with the cavity mode, and we use the central feature which results from the carrier resonance for locking. Specifically, the center slope of the feature, which is linearly proportional to $\Delta\nu$, provides the negative feedback to the laser frequency.

Quality of the error signal is critical for good locking performance. First, to maximize V_{err} (and therefore its S/N), the phase of the servo PD signal must be matched to that of the demodulation signal for constructive interference to occur at the phase detector. This is accomplished by applying a phase-delay to the demodulation signal using a long BNC cable. Secondly, residual amplitude modulation (RAM) noises[212], arising from the misalignment between the EOM crystal axis and the polarization of the input light, can result in a non-zero offset in the error signal. This offset is sensitive to the temperature and stress experienced by the crystal, and its fluctuation can lead to long term drifts of the locking point. To counter this effect, a Glan-Taylor polarizer (extinction ratio $> 10^5$) is placed before the EOM's fiber input to clean up the input light's polarization and orient it along the crystal axis. The polarizer is rotated until the offset in the error signal is zeroed.

The frequency of the cavity mode we reference to (ν_{ref}) is in general different from that of the molecular transition we target (ν_0), by an amount up to half the FSR. To put the laser on resonance with the molecule, we apply a second RF drive (via LO2) with frequency on the order of a few hundred MHz to the EOM (Fig. 2.19(b)). This drive, in combination with the 50 MHz drive, creates multiple sets of PDH peaks, and we use either the plus or minus first order set for locking (Fig. 2.19(c)). When the laser is locked, the various frequencies satisfy the relation

$$\nu_{\mathrm{L}} = \nu_{\mathrm{ref}} \pm \nu_{\mathrm{LO2}} - \nu_{\mathrm{AOM}}, \tag{2.1}$$

where $\nu_{\mathrm{AOM}} = 80$ MHz is the driving frequency for the AOMs used to control the intensity of the laser light during the experiment. Thus by tuning ν_{LO2}, the laser can be brought onto resonance, such that $\nu_{\mathrm{L}} = \nu_0$.

Finally, the error signal is fed into PID servo (Vescent Photonics, D2-125) to obtain an output $V_{\mathrm{servo}} = G(\nu)V_{\mathrm{err}}$, where $G(\nu)$ is the frequency-dependent gain that can be shaped by adjusting

the servo's PID gain parameters. The servo output is applied to both the laser diode (LD) current and (after low-pass filtering and amplification) the laser cavity PZT (piezo-electrical transducer) voltage for feedback on the high (> 1 kHz) and low (< 1 kHz) frequency portions of the laser's noise spectrum, respectively*. $G(\nu)$ is initially optimized, based on the frequency-responses of the various elements in the feedback loop, to maximize the servo bandwidth. For the 690 and 970 nm lasers, bandwidths of 2.0 and 1.5 MHz were respectively obtained. The linewidths[†] of both lasers were measured to be ~ 100 Hz.

Later when we used these lasers to drive the STIRAP transition, we found, counter-intuitively, that the transfer efficiency can be improved by lowering down the servo bandwidth and thus degrading the overall noise suppression of the feedback loop. Reducing the bandwidths to 500 and 200 kHz for the 690 and 970 nm lasers respectively, the (one-way) transfer efficiency was increased from 80% to 92%. We rationalize this improvement as follows: during the STIRAP process, the radiation fields create, in addition to the dark state, a pair of bright states which, if populated, lead to a decoherence of the system via spontaenous emission[21]. The energies of the bright states differ from that of the dark state by $\pm\hbar\sqrt{\Omega_1^2 + \Omega_2^2}$, where Ω_1 and Ω_2 are the Rabi frequencies for the up and down leg transitions, respectively; laser frequency noises at frequencies around $\sqrt{\Omega_1^2 + \Omega_2^2}$ can drive transitions to these lossy bright states and are therefore most detrimental to the transfer efficiency. In any feedback loop, the servo bump increases the noise at and around the servo bandwidth. Given the characteristic Rabi frequencies of 2 - 4 MHz for our system, it was therefore advantageous to place the servo bump at a few hundred kHz rather than a few MHz, and the gain of doing so seems to outweigh the loss in overall noise suppression.

Finally, frequency-stabilized STIRAP beams are sent via optical fibers to the machine table,

---

*The addition of the PZT feedback markedly improved the capture range and the system's robustness against acoustic noises.

†Defined as the frequency below which $\sim 90\%$ of the laser's noise power is contained.
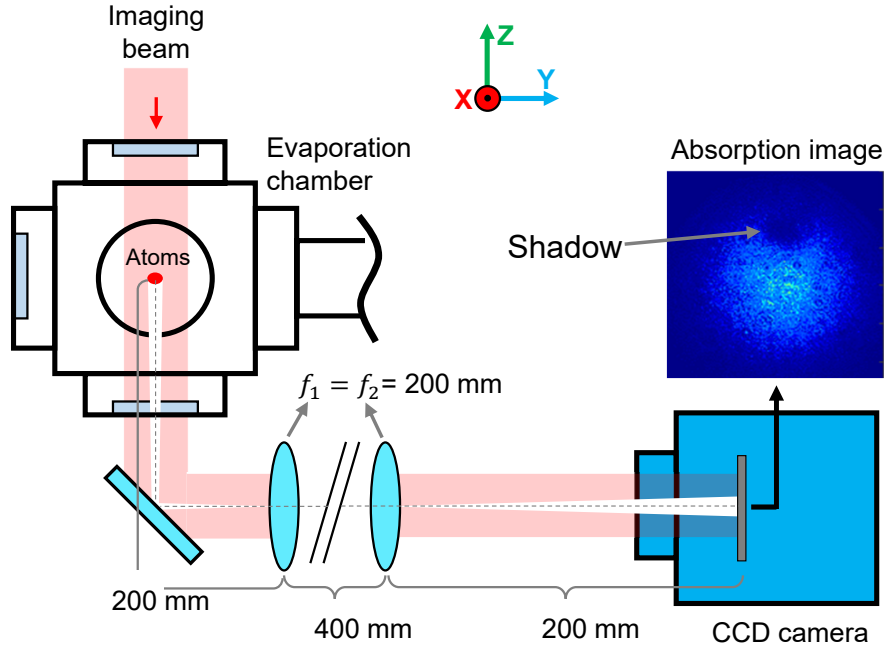
Figure 2.20: Evaporation chamber absorption imaging setup. The atom cloud, located at the center of the evaporation chamber, is situated at the object plane of a $4f$ imaging system, consisting of a pair of achromatic lenses ($f_1 = f_2 = 250$ mm) as well as a CCD camera placed at the image plane. As the collimated imaging light passes through the cloud, the shadow cast by the cloud is imaged on the camera, resulting in the absorption image shown in the inset.

combined with the HODT beam on a dichroic mirror, and focused to the center of the science chamber (Fig. 2.13(b)). At the molecule location, the 690 (970) nm laser has a beam waist of 40 (35) μm, and a maximum optical power of 8.5 (27) mW. The optical power of each beams during the molecule transfer is controlled by mixing the 80 MHz RF signals driving the AOMs with signal from an arbitrary waveform generator (BK Precision 4054B) programmed to the desired power ramp profile (Fig. 3.12).
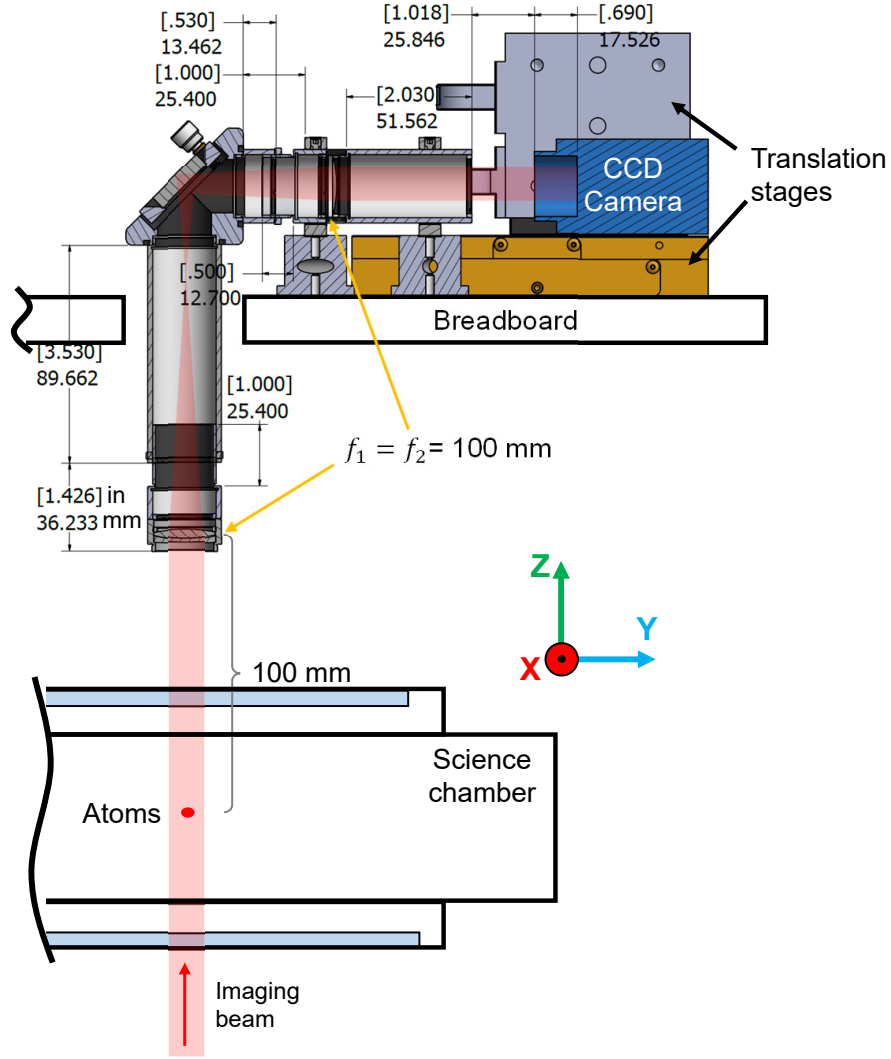
Figure 2.21: Science chamber absorption imaging setup. The atom cloud, located at the center of the science chamber, is situated at the object plane of a $4f$ imaging system, consisting of a pair of achromatic lenses ($f_1 = f_2 = 100$ mm) as well as a CCD camera placed at the image plane. The entire imaging setup sits on a breadboard directly above the science chamber.

2.3.4 Imaging systems

Absorption imaging is a workhorse technique in AMO experiments for characterizing the conditions of ensembles of atoms. In our experiment, this is realized through the imaging setups depicted in Fig. 2.20 and 2.21, which provide imaging for atoms in the evaporation and science chambers, respectively. In each setup, a cloud of atoms is situated at the object plane of a $4f$ imaging system, consisting of a pair of lenses with equal focal power, as well as a CCD camera (PCO Pixelfly) placed at the image plane. When taking an image, a laser beam tuned to be resonant in frequency with a quasi-cycling transition of the atom is passed through the cloud, which absorbs light from the beam and casts a shadow in it. This shadow is then projected onto the camera, resulting in the absorption image as shown in the inset of Fig. 2.20. This image carries information about the density distribution of the cloud, from which information such as temperature and atom number can be extracted. The procedure for doing so is discussed in section 3.1.

2.4 Electromagnetic coils

Electromagnetic coils are widely used in AOM experiments, including ours, to generate controllable magnetic fields for trapping, quantization, level shifting, etc. While various coils are described throughout the thesis, this section focuses on three more specialized coil sets – the transfer coils, the QUIC trap coils, and the Feshbach coils – as well as their current control circuitry.

2.4.1 Transfer coils

The transfer coil pair (Fig. 2.22) is used to capture the laser cooled atoms in the MOT chamber, transfer them through the vacuum system into the evaporation chamber, and hand them off to the QUIC trap. It consists of a pair of identical coils wired for opposite directions of current flow (anti-Helmholtz configuration) to generate a quadrupole magnetic field, which has a linear field gradient along each of the three spatial directions, to confine the atoms. The gradient required for trapping and transfer are determined by two factors

- Along the gravity direction (or axial direction of the coil), the gradient needs to be strong enough to support the atoms against gravity. For Rb and K prepared in their respective stretched hyperfine states ($|2, 2\rangle$ and $|9/2, 9/2\rangle$), this gradient is 30 G/cm.

- When transferring the atoms down the differential pumping tube (Fig. 2.5(c), the characteristic size of the cloud inside the quadurpole trap should stay safely below the ID of the tube, which is 3/8" (9.5 mm). Given an expected cloud temperature of $T = 500~\mu$K inside the trap, a field gradient of 100 G/cm corresponds to a $2k_BT$ cloud diameter of 6 mm, which is sufficient.

Given the relatively high field gradient required, as well as geometric constraints on how close the coil can be from the atoms, we designed and constructed the coils as shown in Fig. 2.22. Each coil consists of 30 windings (5 axial x 6 radial turns) of square, Kapton-coated magnet wires whose profile is shown in the inset of the figure (the setup used for the winding is shown in Appendix B). The windings are glued to each other using a room temperature cure epoxy (Araldite 2000 PLUS). Each coil is wound on a Ultem support, structurally reinforced by an aluminum platform. Current and water flow in and out of the coils via the connection adapters highlighted by white dashed boxes. With a hollow center core that allows cooling water to

65
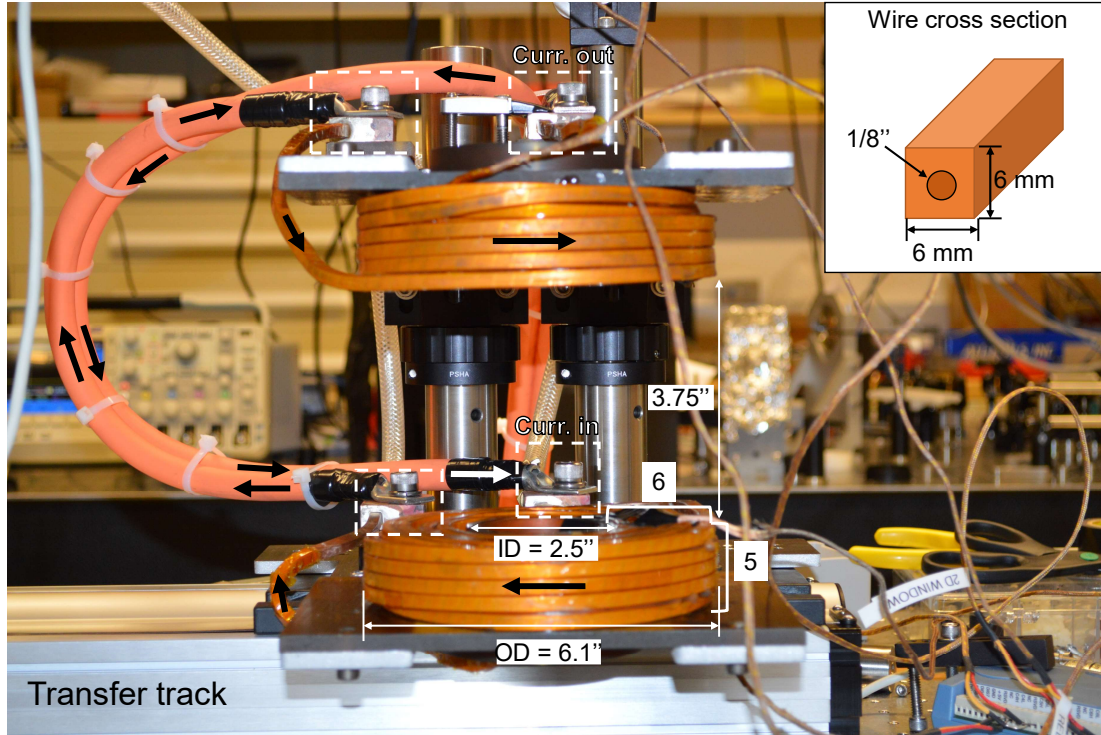
Figure 2.22: Photo of the transfer coil pair. Each coil is wound from the square copper wires shown in the inset, which has an 1/8″ hollow-core that allows cooling water to be flowed through the coil. Electrical currents are passed in and out of the coil pair through the orange cables, which interface with the coil wires through the copper lugs indicated by white dashed boxes. Black arrows indicate the direction of nominal current flow as the trap operates in the anti-Helmholtz configuration during the experiment. The coil pair is shown mounted on the carriage of the transfer track.

directly through the wires and a low total resistance (7 mΩ per coil), this construction allows currents of up to 400 A to flow through (for up to several seconds at a time) to generate the requisite gradients. The designed field gradient per unit current, with the wires approximated as infinitesimal in thickness, is 0.48 G/cm along the axial direction and 0.24 G/cm along the radial directions. The corresponding measured values for the real setup are 0.43 G/cm an 0.22 G/cm, respectively*.

The transfer coil setup is mounted on the carriage of a meter-long linear mechanical track

*Calibrated by both Hall probe and measuring the current at which atoms are spilled out of the trap

66
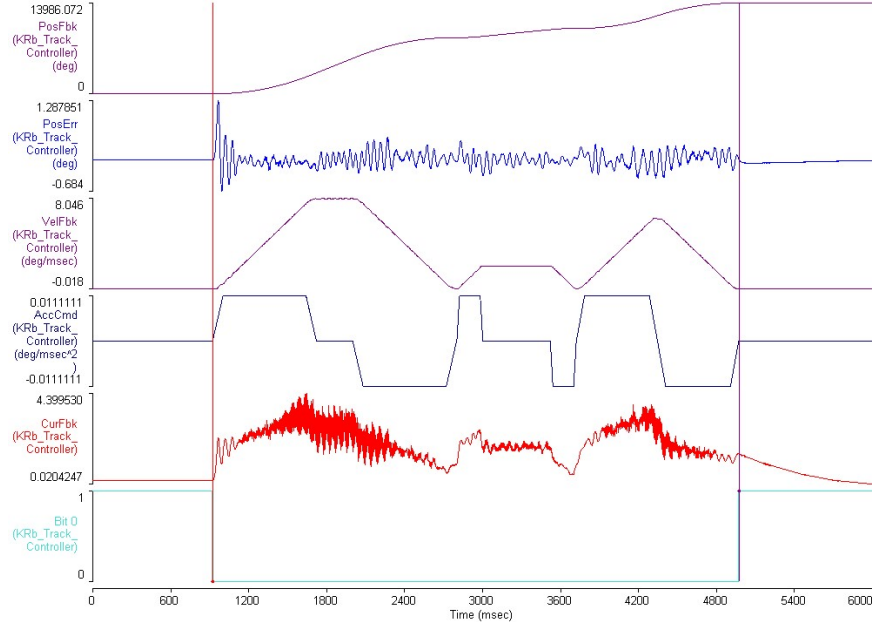
Figure 2.23: Motion of the transfer coil during atom transfer. The distance unit used by the mechanical track's controller is degrees, which quantifies the rotation of its lead screw that has a pitch of 25 mm/revolution. Thus each degree in rotation corresponds to 0.0694 mm travel distance along the track. The horizontal axis marks time (in milliseconds). The top four curves show the position, position error (difference between command and actual position), velocity, and acceleration of the transfer coil during the trip from the MOT chamber to the evaporation chamber, which are separated by 960 mm in distance. The bottom two curves show the track motor current and state of the trigger bit during the transfer. The transfer is slowed down in the middle to avoid a "speed bump" likely created by magnetic field gradients.

(Parker 406XR) actuated by a servo motor (BE342KL-NPSN). The actual distance of transfer between the centers of the MOT and evaporation chambers is 960 mm. Position feedback and control is achieved via a commercial PID servo (Aerotech Soloist Hle 20-40-A ES16521-5) and the transfer trajectory is programmed via its associated software (Soloist Motion Composer).

67

After experimenting with different trajectories, we determined the optimum position, velocity, and acceleration profiles as shown in Fig. 2.23. The total transfer time is 4 s. Various motional parameters are scanned to maximize the fraction of Rb atoms* that remain in the trap after they are subjected to a round-trip of transfer (with mirrored forward and reverse trajectories). We found the following two factors that most strongly impacted the transfer efficiency.

- Most of the atom loss during the transfer process occurs while the atoms are within the MOT chamber, through background collisions with the trapped atoms. We therefore minimized time spent inside the MOT chamber (as well as the beginning section of the differential pumping tube) by accelerating as quickly as possible out of it, and retain $\sim 24\%$ of the atoms after the differential pumping tube.

- There is a "speed bump" to the transfer at $600 - 700$ mm away from the MOT chamber – by reducing the transfer velocity (to $\sim 1/4$ of its peak value) while traversing over this region, we saw a factor of two gain in the round-trip recaptured fraction. The bump is most likely due to strong magnetic field gradient from nearby magnetized components. After the speed bump, we increase the speed back up for the final stretch of the transfer.

With the above trajectory, we achieve a round-trip transfer efficiency of 4.9%. Assuming equal fractional loss in forward and return trips, this corresponds to 24% of the atoms captured in the MOT chamber eventually transferred to the evaporation chamber. After the forward trip in an experimental cycle, the transfer coil slowly returns (over 8 s) to the MOT chamber to wait for the next loading.

---

*Atom number in the MOT chamber is characterized by MOT recapture. We assume the optimization also applies to the K atoms, which are too few in number to be measured by MOT recapture.

2.4.2 QUIC trap coils

The QUIC (Quadruple-in-Ioffe configuration) trap surrounds the evaporation chamber (section 2.2.3) and provides magnetic confinement for the atoms during the RF evaporation (section 3.3). A simple quadrupole field is unsuitable for atom trapping during evaporation, since the B field zero at its center leads to Majorana spin flip losses as the atoms get colder and denser towards the final stretch of the evaporation[29]. This zero point can be eliminated using a variety of techniques, including optically plugging the center[150], creating an optical dimple trap offset from the center[49], using a time-averaged orbiting potential[98], and using additional coils to create a quadratic trapping potential (*i.e.* harmonic traps). While each technique has its pros and cons, we chose the last which is most involved in fabrication but highly robust once set up. Among the most popular harmonic trap configurations – the Ioffe-Pritchard (IP) trap[70], the cloverleaf trap[143], and the QUIC trap[71] – we chose the last because it involves the least amount of coils (3, compared to 6 - 8 in IP trap and 12 in the cloverleaf trap) and therefore the simplest in construction.

Our QUIC trap consists of a pair of quadrupole coils (QC1 and QC2) plus a smaller Ioffe coil (IC), arranged in the geometry shown as a half section view in Fig. 2.24. Photographs of the constructed trap are shown in Fig. 2.25. The QUIC coils need to be compact in order to stay clear of the transfer coil, and be able to generate large field curvatures to provide strong confinement for the atoms during the evaporation and keep the collision rate high. To fulfill these requirements, we adopted the coil style from the Rb experiment in the Greiner lab[81], and fabricated the coils using thin, Kapton-laminated copper tapes (Bridgeport magnetics, Laminax). The tape has a 5 mil-thick* copper layer, laminated on one side with a 1 mil-thick Kapton layer to provide electrical insulation between windings. The QC (IC) coil consists of 131 (19) turns

---

*1 mil = 0.001"
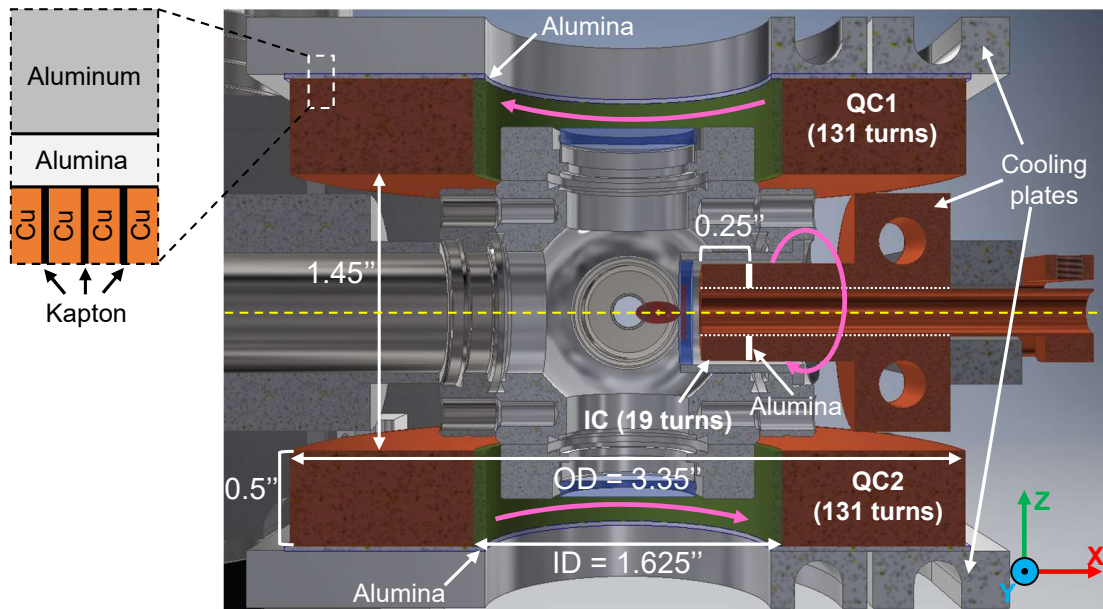
Figure 2.24: CAD rendering of the QUIC trap coils. The trap consists of two quadrupole coils (QC1, QC2) and a Ioffe coil (IC). Each coil is wound as a single-layered pancake using thin Kapton-laminated copper tapes (see inset). Each coil is expoxied to a homemade water-cooling plate, with a thin layer of alumina ceramic in between the plate and coil to provide electrical insulation. Magneta arrows indicate the direction of nominal current flow when the trap operates in the QUIC configuration during the experiment. In this design, heat generated during the operation is conducted efficiently along the transverse direction of the copper tape to the cooling plate.

of 0.5"-wide tapes wound on an FR-4 (copper) core and epoxied (Epo-Tek, 301-2) into a single pancake. Two major advantages of the tape-design are:

- Its small thickness allows many turns to be packed along the radial direction into limited space;

- Heat generated during the operation of the trap* conducts efficiently along the wide direction of the tape to one of its faces, which can then be carried away.

Home-made water cooling plates, designed specifically to the coils' dimensions, are used to keep the coils from overheating during operation. For the cooling to be efficient, good thermal

---

*150 W for each QC and 20 W for IC, for a duration of 20 - 30 s of evaporation time.
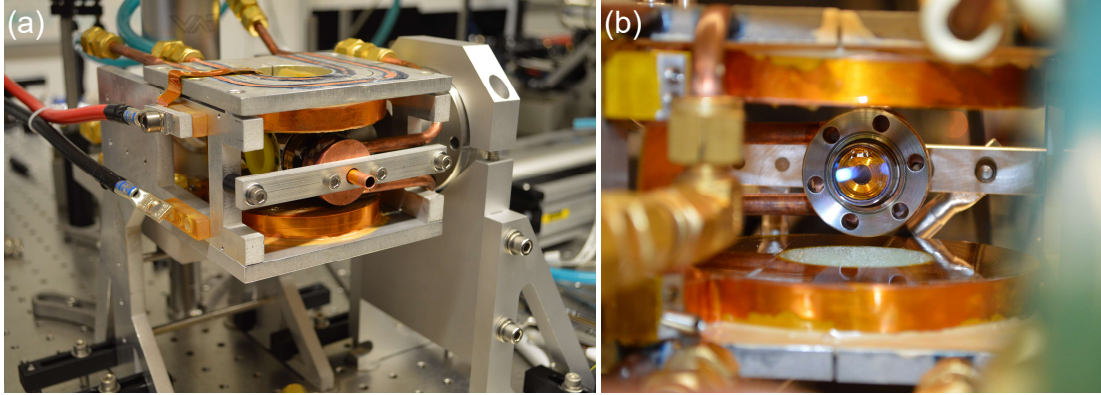
Figure 2.25: Photos of the QUIC trap. (a) Overview of the trap after it is fully assembled around a test evaporation chamber setup. (b) A closeup of the Ioffe coil fitted into the re-entrant viewport, viewed without the evaporation chamber, from the side opposite to that in (a).

contact between the coil and its cooling plate must be established. To this end, one side of each coil is faced-off on a lathe and hand-polished to provide a highly flat surface, which eliminates large gaps during contact. On the other hand, the cooling plates are made out of metal (aluminum for the QC plates and copper for the IC plate) and need to be electrically insulated from the coils. This is achieved in Ref.[81]'s design by mixing glass microspheres (25 μm in radius, from Cospheric) in the thermal epoxy used to glue the coil to the cooling plate. These glass spheres act as spacers between the coil and the plate, preventing them from physically contacting while keeping the epoxy layer between them thin. However, following the same technique in constructing our first set of coils, we found it difficult to keep shorts from developing between the coil and the plate. In our second iteration, we instead used a thin (25 mil) sheet of alumina (Al_2O_3) ceramic as the spacer. Alumina is electrically insulating (Volume resistivity $\sim 10^{14} \Omega$-cm) but has a high thermal conductivity of 20 - 30 W/m-K, second only to common metals (Al: 205 W/m-K; Cu: 401 W/m-K) and much higher compared to other common insulators like plastic (typically < 0.5 W/m-K). The alumina sheet is sandwiched between the coil and the cooling plate, with a thin layer of thermally conductive epoxy (Epo-Tek, 930-4) applied to

71

the interfaces. This construction yielded adequate cooling performance, with the average temperature of the QC (IC) rising up to 25°C (18°C) during the evaporation. Further details on the fabrication of the coils and the cooling plates can be found in Appendix B.

The fact that the QUIC coils require constant and efficient cooling became painfully clear when the cooling water was accidentally left off during a few experimental cycles in the Spring of 2018. Heat generated by the quadrupole coils softened the epoxy, and the mutual attraction between the quadrupole coils during operation resulted in their irreversible deformations. The Ioffe coil, generating relatively little power, survived the lack of cooling. Since the accident, we replaced the QC's with identical ones, and installed a Raspberry Pi-based interlock system, conditioning the current flow to all the high power coils on their temperatures as well as the flow rate of the cooling water.

During the evaporation, the QUIC trap undergoes two modes of operation – the quadrupole configuration, and the QUIC configuration. Fig. 2.26 shows the simulated evolution of the B field (dashed lines) along the x-axis of the trap (yellow dotted line in Fig. 2.24) as the system transforms from the prior to the latter configuration. As shown (in solid lines) is the absolute value of the B field, which is proportional to the trapping potential experienced by the atoms. In the quadrupole configuration, QC1 and QC2 are switched on to the nominal operating current of 20 A to produce field gradients of 216 and 108 G/cm along the axial (z) and radial (x,y) directions, respectively, at the geometric center of the evaporation chamber. Halfway through the evaporation and before the atoms get too cold, the IC current is ramped also to 20 A, superimposing a field on the existing quadrupole field to yield an overall field that is approximately quadratic at its minimum and has a positive bias of $B_0 = 2.5$ G. During trap transformation, the atom cloud tracks the potential minimum, and moves a total of 4 mm towards IC. After assembling the QUIC trap, we measured the B field along the x-axis under both quadrupole and QUIC configurations using a Hall probe. The results, shown in Fig. 2.27, match well to our design.
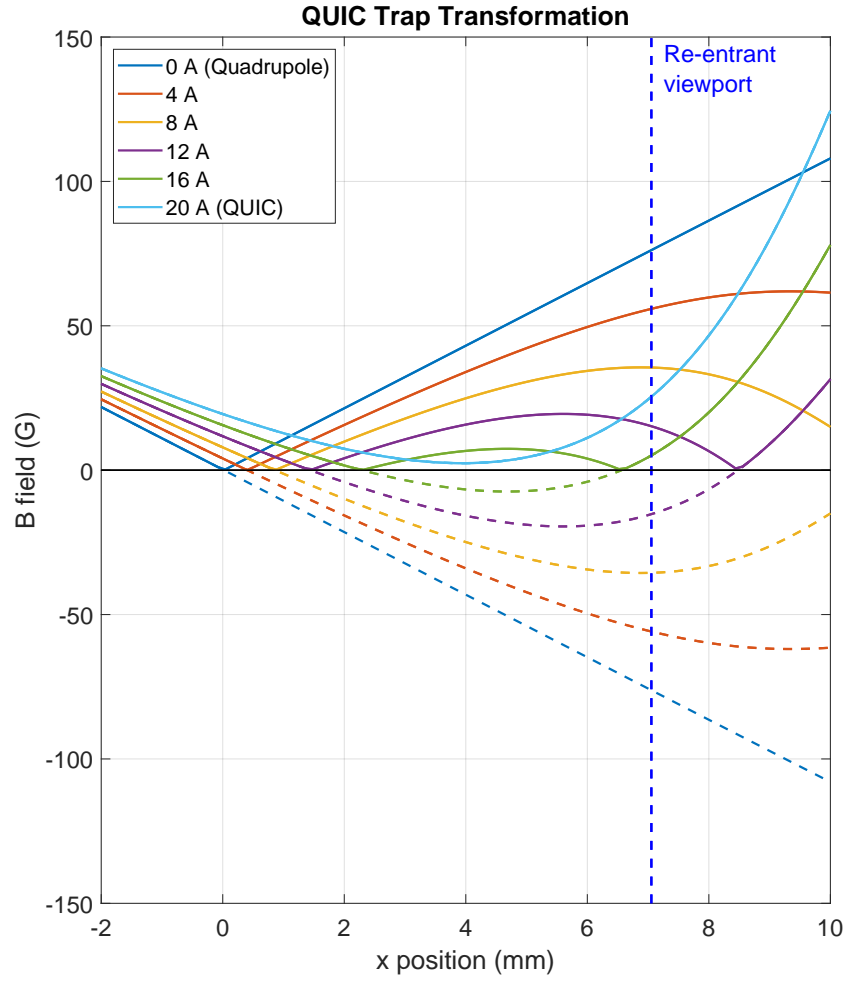
Figure 2.26: The QUIC trap transformation. Different curves indicate the calculated B field (dashed) as well as their absolute values (solid) along the central axis of the Ioffe coil (yellow dashed line in Fig. 2.24) as the current of the Ioffe coil gradually increases. The quadrupole coils are kept at 20 A in all cases. The center of the evaporation chamber is at $x = 0$ mm, while the inner surface of the re-entrant viewport is at 7.2 mm, as indicated by the dashed blue line. As the current of the Ioffe coil ramps from 0 A to 20 A, the trap transforms from a quadrupole configuration to the QUIC configuration. During this process, the atom cloud tracks the location of the trap minimum, which is the zero-crossing of the B field until it is eliminated at sufficiently high Ioffe current and turned into a harmonic bottom. In the QUIC configuration, the bottom of the trap is offset from zero by 2.5 G.

Under the Ioffe configuration, the simulated B field curvatures* are $B_x'' = 3.37$ G/cm^2,

---

*Defined as the second position derivative of the magnetic field along each principal axes at the trap minimum.
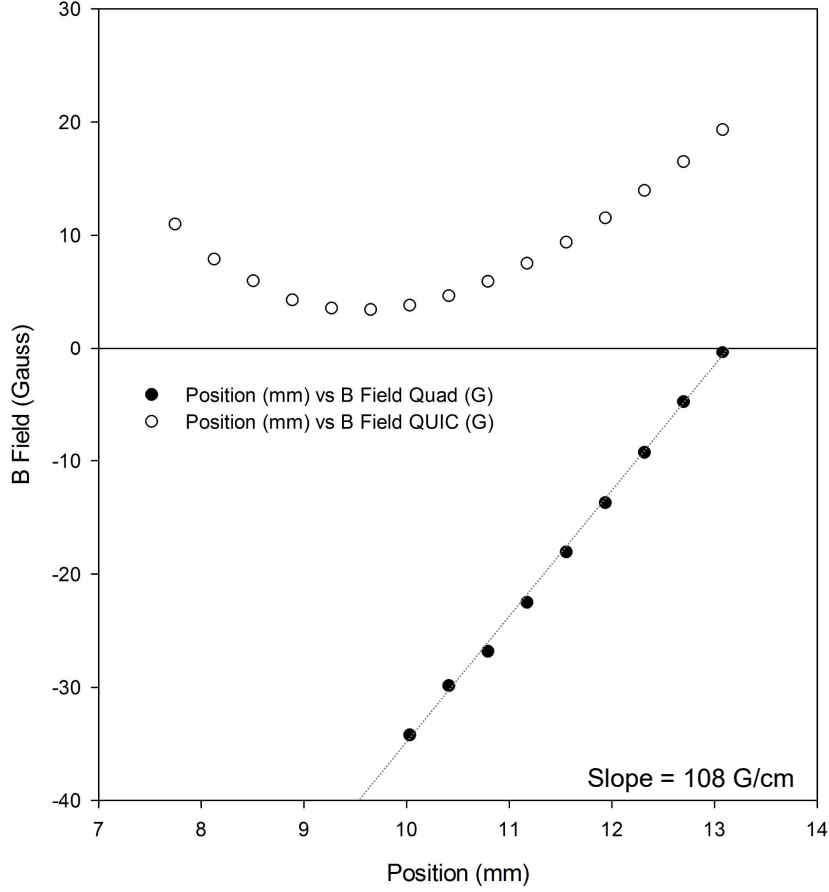
Figure 2.27: Measured field of the QUIC trap. Strengths of the magnetic field along the central axis of the Ioffe coil when the QUIC trap operates in the quadrupole (bottom panel) or QUIC configuration (top panel), measured by a Hall effect probe. The zero for the x-axis is arbitrarily defined. The measured results match well to our design as shown in Fig. 2.26.

$B_y'' = 111$ G/cm^2, and $B_z'' = 105$ G/cm^2. These curvatures correspond to Rb trap frequencies* of $\{\omega_x, \omega_y, \omega_z\} = 2\pi\{23.4, 134, 131\}$ Hz, comparable to those found in similar experiments[144,226]. Experimentally, we measured the trap frequencies using parametric heating to be $2\pi\{21.7, 116, 116\}$ Hz, matching well to the simulation. B_y'' and B_z'' depend inversely on

---

*$\omega = \sqrt{\frac{\mu_B g_F B''}{m}}$, where μ_B is the Bohr magneton, g_F is the g-factor of the trapped atoms' hyperfine state $|2, 2\rangle$, and $m = 87$ amu is the mass of the atom. Trap frequencies for K can be scaled from those of Rb by multiplying the factor $\sqrt{m_{Rb}/m_K}$.
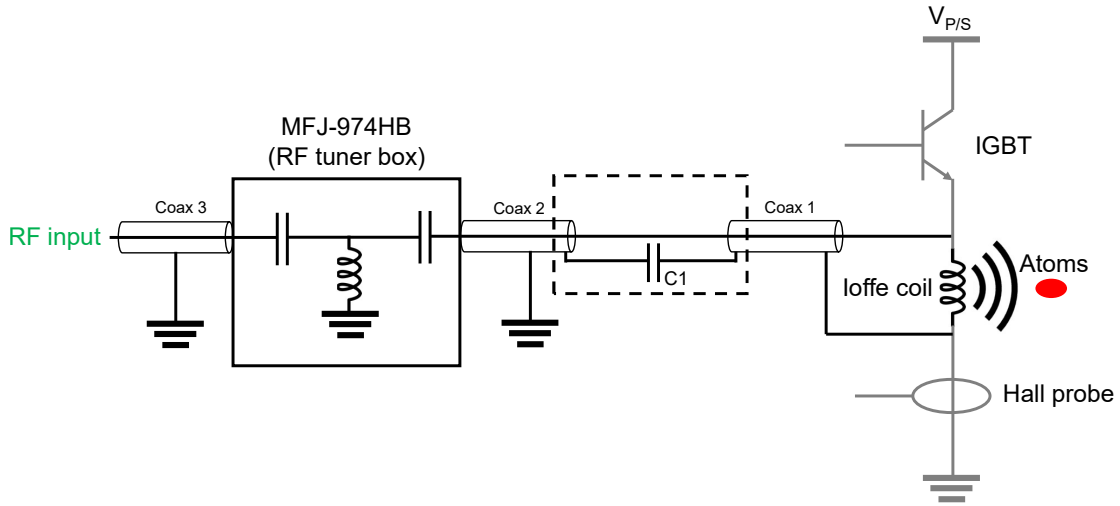
Figure 2.28: Coupling RF signal to the atoms through the Ioffe coil. RF signal for evaporative cooling is capacitively coupled to the Ioffe coil, which is also part of a DC circuit. An RF tuner box provides impedance matching for the signal. The close proximity of the Ioffe coil to cloud location allows efficient coupling of the RF signal to the atoms.

the bias field B_0 [144] and therefore can be tuned by changing the IC current relative to that of the QC's. While a lower bias will increase ω_y and ω_z and potentially make for a more efficient evaporation*, it will also make the trap more susceptible to magnetic field noises, which threaten to bring the overall field across zero, leading to spin flip losses. Empirically, we found B_0 in the range of 1.5 to 3.0 G to be optimal, and eventually settled to $B_0 = 2.5$ G.

Lastly, the Ioffe coil also functions as an RF antenna during evaporative cooling. RF signal (2 - 40 MHz) is capacitively-coupled to the Ioffe coil using the setup schematically illustrated in Fig. 2.28. Optimization of the coupling is achieved through a balance line tuner (MFJ-974HB). At first glance, the Ioffe coil, which has 19 windings and therefore a relatively large inductance, may not efficiently couple signals in the few to tens of megahertz frequency range. Despite this, we found that the Ioffe coil provides much improved coupling of RF signals to the atoms

---

*The figure of merit for evaporation (in the absence of 3-body loss) is $\omega_x\omega_y\omega_z$, which is proportional to the density of the gas.

compared to other antennae used in the past, due mainly to its close proximity (3 - 7 mm) to the atoms.

2.4.3   Feshbach and fast B coils

The Feshbach and fast B coil pairs surround the science chamber (section 2.2.4) to provide the magnetic fields required to associate K and Rb atoms into weakly-bound KRb molecules (section 3.7). Their geometries are shown in Fig. 2.29.

The Feshbach coil pair is designed to generate a spatially uniform magnetic field along the z-axis (yellow dotted line) to access a ^{40}K–^{87}Rb inter-species Feshbach resonance centered at 546.62 G. To produce this relatively large field while limited by the physical size of the science chamber in how close the coils can approach the atoms, we chose to fabricate the Feshbach coils in the high-current, low-winding style similar to the transfer coil (2.4.1). Each coil consists of 36 windings (6 axial $\times$ 6 radial) of hollow-core magnet wire epoxied to an Ultem plastic support. By design, the coil produces a magnetic field of 2.898 G/A at the center of the science chamber, which corresponds to a 546 G field at 188 A. Various geometric parameters of the coil pair are scanned during simulation to minimize the spatial curvatures of the magnetic field to 0.80 G/cm^2 and - 0.40 G/cm^2 in the axial (z) and radial (x and y) directions, respectively. These values correspond to a B field variation of 0.1 ppm across a distance of 200 μm, the upper-bound on the spatial extend of the KRb cloud. Once the Feshbach coils are placed into the experimental setup, we calibrated its current-to-field coefficient by measuring, as a function of coil current, the Rb $|2, 2\rangle \rightarrow |1, 1\rangle$ microwave transition, which has a well-known dependence on the B field. The resulting coefficients are 2.6820 G/A at around 30 G (the field we use to provided quantization during Rb imaging), and 2.7796 G/A at around 546 G (the Feshbach field).*

---

*The difference between the low and high field coefficients is not understood but does not impact the experiment.
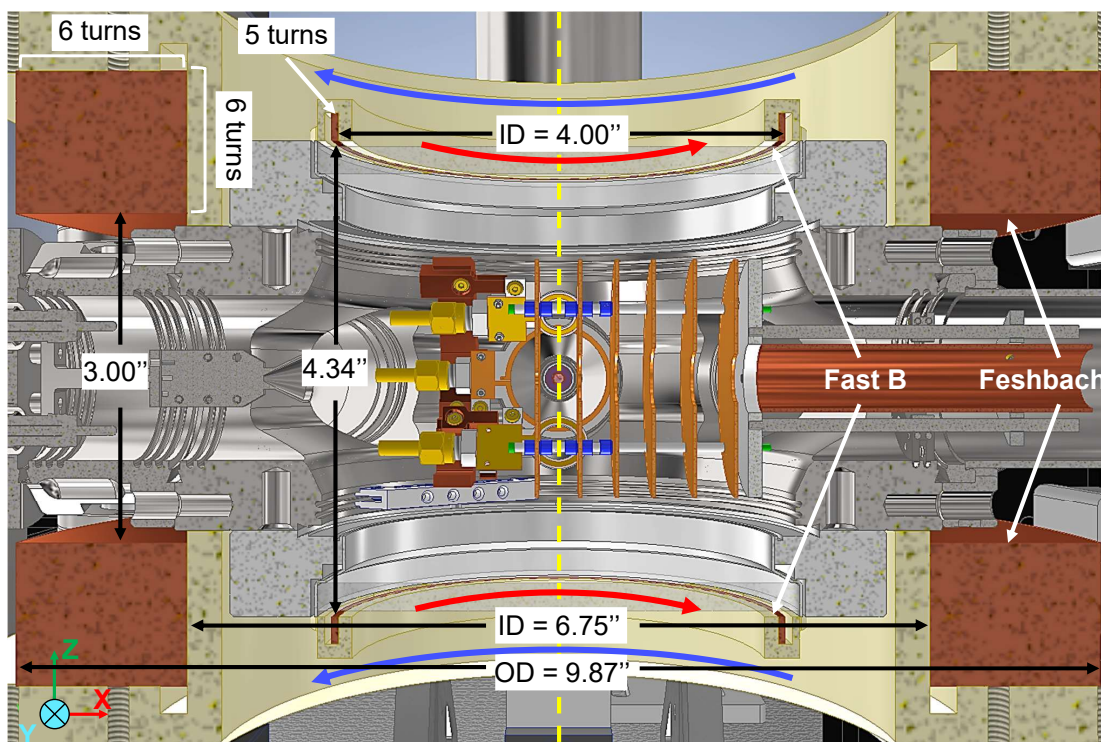
Figure 2.29: Feshabch and fast B coils. The Feshbach coils are wound from hollow-cored copper wires, same as what was used for the transfer coil (2.22). The Ioffe coils are wound from copper tapes, same as what was used for the QUIC trap coils (2.24). These coils provide both static and dynamic fields during the magneto-association of K and Rb atoms. Red and blue arrows respectively indicate the directions of current flow through the fast B and Feshbach coils during the association process.

For the association of molecules from atoms and their dissociation back into atoms for imaging, the magnetic field is needs to be ramped rapidly (ideally 4 G/ms forward and > 20 G/ms back) across the Feshbach resonance to avoid three-body losses (section 3.7). Initially, these ramps were carried out by the Feshbach coil. However, since the response of the Feshbach coils is relatively slow due to its inductance, we had to settle for slower ramp rates (0.3 G/ms forward and 5 G/ms back) which limited the conversion efficiencies. Additionally, the slow response led to large field oscillations following the ramps, which are undesirable to the subsequent state transfer steps. To counter this problem, we added a fast B coil pair coaxial with the Feshbach

coil pair. With only 5 windings per coil and smaller diameters, the fast B coils have a much smaller inductance and therefore better suited for the fast field ramps. Each coil is wound out of 0.125"-wide copper tapes identical to those used in the Ioffe coil (2.4.2). The fast B coil pair is wired to have current flow directions opposite to those of the Feshbach coil pair, such that the B field is reduced when the fast B coils are on. This arrangement also leads to a cancellation of the curvatures of the fields produced by the two coils, resulting in a net field curvature of < 0.2 G/cm. Under this new configuration, the Feshbach coil pair generates a constant field of 550 G during the association/dissocation, and the fast B coil pair is switched on and off to produce the desired field ramps. By design, the fast B coil produces a field of 0.3673 G/A, corresponding to the required 5.5 G ramp at a current of 15.0 A. The current-to-field coefficient is calibrated, again using Rb microwave transition, to be 0.3241 G/A. By measuring the current responses of the fast B coils during the field ramps, we found that target ramp rates can be achieved with minimal oscillations.

2.4.4   Coil current feedback system

For all the coil systems described in this section, magnetic field control and stabilization are accomplished by performing feedback on coil current using the system shown schematically in Fig. 2.30. The current loop consists of a power supply as a current source, the coil (or coil pair), an IGBT (insulated gate bipolar transistor) switch for current control, and a Hall probe for current measurement. In this setup, the power supply operates in CV mode and provides a preset voltage drop that is shared between the coil(s), the IGBT, and the connecting cables in between. The IGBT controls the loop current I_{loop} by modifying its effective resistance as the V_{GE} applied to its gate changes. The servo Hall probe measures I_{loop}, and converts it proportionally into a much smaller current I_{sense}, which is in turn converted by R_{sense} to V_{sense}. Inside the coil servo
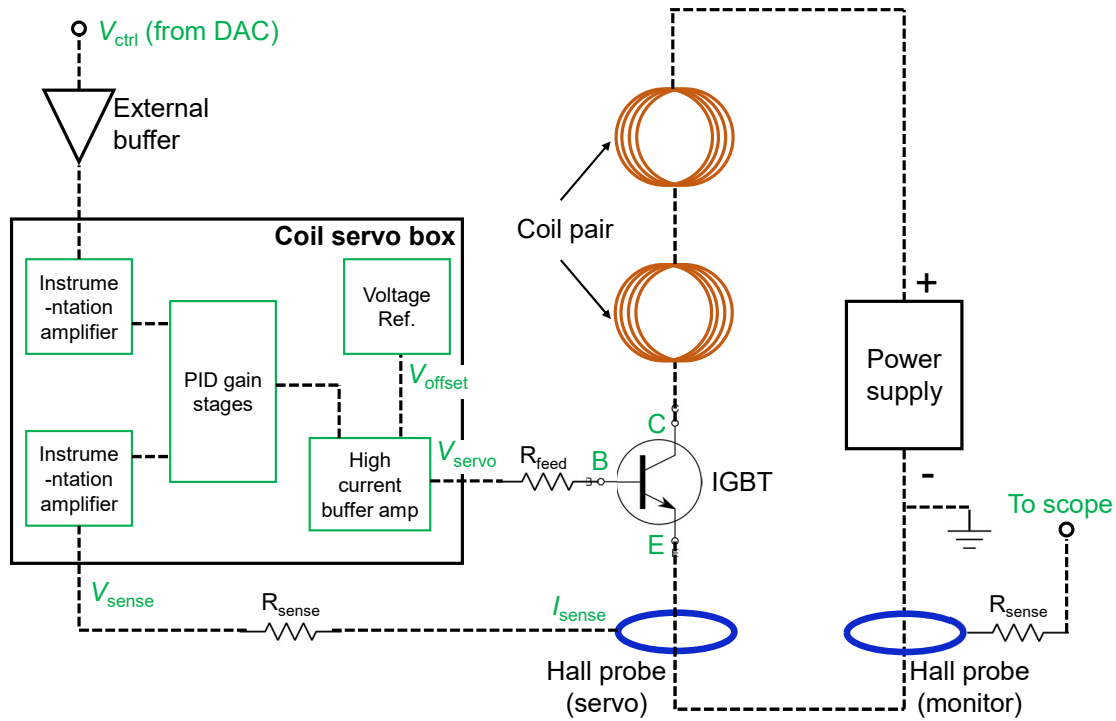
Figure 2.30: Coil current feedback system. The servo loop consists of the coil (or coil pair), an IGBT switch, a Hall probe sensor, a high current power supply, and a servo box that contains the PID control circuitry. This circuit stablizes the coil current to a DAC control voltage (V_{ctrl}), which can be dynamically changed during an experimental sequence to adjust the magnetic field experience by the atoms and molecules. A second, out-of-loop Hall probe is used to monitor the current flow through the loop. Such a system is used to control the transfer, QUIC, Feshbach, and fast B coil systems.

box, V_{sense} is compared to the set point V_{ctrl} provided by the computer-controlled DAC to generate a feedback voltage V_{GE} (gate-emitter), which is then fed via R_{feed} to the gate of the IGBT. V_{GE} adjusts I_{loop} such that V_{sense} and V_{ctrl}, after their respective instrumentation amplification stages, are equal to each other. Thus we obtain a I_{loop}, and therefore a magnetic field, that is proportional to V_{ctrl}. The proportionality constant, I_{loop}/V_{ctrl}, is 40 A/V for the transfer coils, 4 A/V for the QUIC coils, 20 A/V for the Feshbach coils, and 5 A/V for the fast B coils. PID parameters of the coil servo are adjusted following the procedure described in Ch. 3 of Ref. [164], which provides an excellent discussion of current stabilization for our type of system. We characterized the current

stability while the feedback is active by measuring I_{loop} using a monitor Hall probe that is out of the feedback loop. The current fluctuation essentially mirrors the fluctuation of the DAC voltage, which is $\sim 10^{-5}$. These measurements are made using a high precision multimeter (Keithley 2000), which is sensitive to noises below 1 kHz.

While the above discussion covers the basic operation of the coil current feedback system, I will highlight a few additional design choices that improved the operation.

Biasing the IGBT gate. Like most transistors, the IGBT has an $I - V$ response that starts out flat but rises sharply once V_{GE} exceeds a certain threshold. The threshold value depends on the specific IGBT model, as well as the collector-emittor voltage (V_{CE}), and is found to be 5.0 - 5.5 V in our setups. Such an $I - V$ characteristic leads to significant delays and distortions in the current response of the system during turn on, if V_{GE} is swept all the way from zero to its final value. To counter this effect, a constant DC bias V_{offset}, typically 4.0 - 4.5 V, is added to V_{servo} to produce V_{GE}. This results in a one-to-one following of the loop current to the DAC control voltage, so long as the bandwidth of the system is not exceeded. The values for V_{offset} is chosen to be as close to the threshold as possible without introducing leakage currents in the loop.

Adding a varistor to each IGBT. When fully energized, the coils can store a large amount of energy that results in a back-EMF voltage as large as 1 kV if the coil is suddenly switched off. This can cause discharges between isolated coil windings and result in irreversible shorts. To prevent this from happening, a varistor with appropriate ratings is added in parallel to each IGBT to clamp any voltage spikes down below a safe value. We use varistors with 500 V clamping voltages for the transfer and Feshbach coil systems, and those with 50 V clamping voltages for the QUIC and fast B coil systems.

Designing the coil servo circuit against RF rectification. During the RF evaporation stage (sec-

tion 3.3), a large mount of RF radiation, in the frequency range of 1 - 40 MHz, is broadcast over the experiment. The RF signal can be picked up and rectified by op-amps in various circuits, causing disruptions in their output voltages. While most electronics, *e.g.* laser frequency and intensity servos, do not require stable operation during the RF evaporation stage, the QUIC trap coil servos are exceptions. To protect against RF rectification, the inputs into the coil servo are aggressively filtered using a combination of bypass capacitors, ferrite beads, and low-pass RC filters.

2.5   Ionization and ion detection systems

In this section we describe the hardware used for universal detection of chemical species involved in ultracold reactions. In our experiment, neutral species from the reaction are first photoionized by a laser pulse (section 2.5.1), then accelerated by VMI ion optics (section 2.5.2), and finally detected by a micro-channel plate (MCP) detector (section 2.5.3. The MCP records the TOFs and hit locations of the ions, from which mass and kinetic energy information can be respectively extracted. In the subsections below, we discuss the design of key components of the spectrometer.

2.5.1   Photoionization lasers

UV ionization laser system

Photoionization is used to covert neutral particles involved in the chemical reactions we probe into detectable ions. Two general types of ionization schemes are used in studies to be described in Chapters 5, 6, and 7 – non-resonant ionization, in which a single ultraviolet (UV) photon results in the direct or dissociative ionization of the neutral; and resonant ionization, or

more specifically resonantly-enhanced multiphoton ionization (REMPI), in which a first photon resonantly excites the neutral to an intermediate, excited molecular state, and a second photon ionizes it (Fig. 4.1). These two methods will be referred to hereon as UV ionization and REMPI, respectively.

We first discuss the UV ionization laser system and the considerations that went into its selection.

Frequency tunability The ultracold reactions we probe involve a variety of chemical species with distinct photoionization characteristics (Fig. 4.3). To efficiently ionize each species, a frequency tunable source is desired.

Pulsed vs. CW TOF mass spectrometry (section 4.3) requires a well-defined time-zero, which demands a pulsed source.

Repetition rate and pulse energy The requirement for a pulsed source is somewhat at odds with the continuous nature of our reactions. As the reaction progresses, both the intermediate complex and the products are continuously produced and then quickly "lost" by either dissociation or escaping from the detection region. Since the cycle time of our experiment is long and the particle number low, it is important to maximize the total number of products/intermediates that can be ionized in each experimental cycle in order to achieve a reasonable data collection rate. This number scales linearly as both the pulse energy and the repetition rate, i.e. the time-averaged power, of the ionization source. Very high pulse energies can result in undesirable effects such as the saturation of ionization probability, space-charge effects, and two-photon processes. Therefore, an ionization source with a high repetition rate and a moderate pulse energy is desired.

To fulfill the above requirements, we chose, as our ionization source, a frequency-doubled, broadly tunable dye laser (LIOP-TEC/LiopStar-HQ) pumped by a pulsed, frequency-doubled
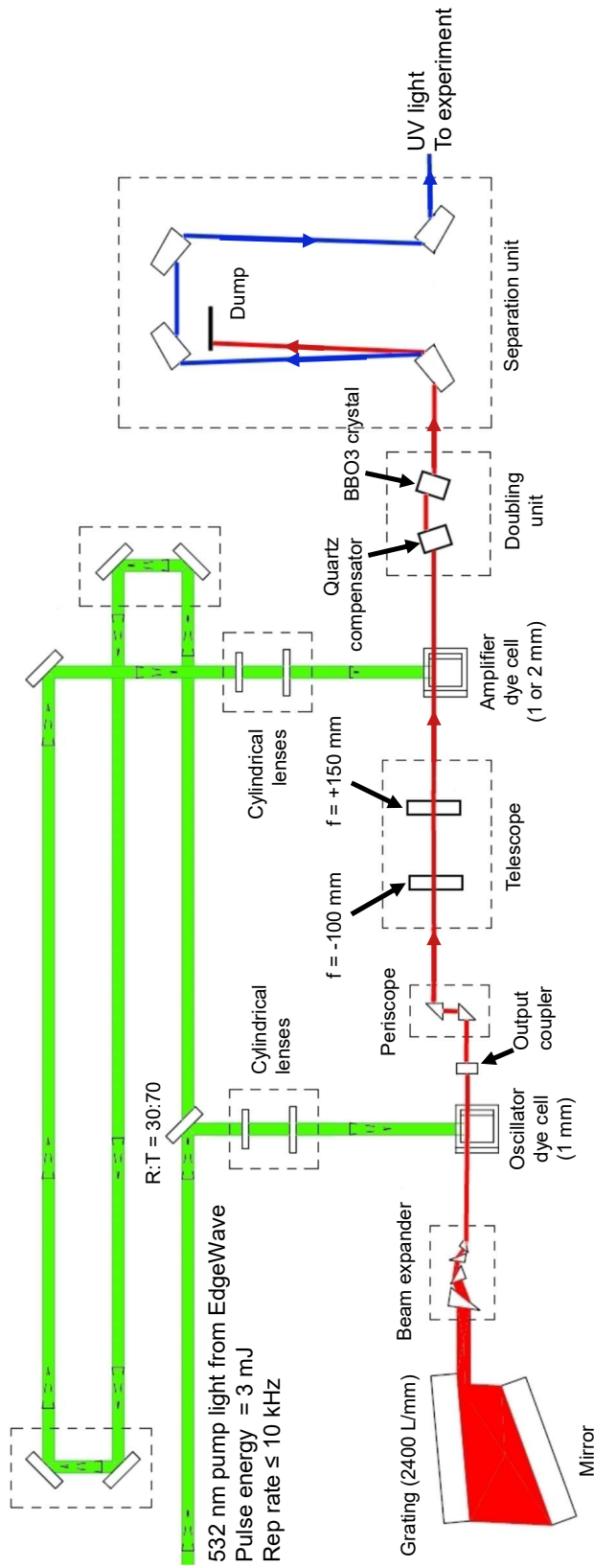
Figure 2.31: The frequency-doubled dye laser system for pulsed UV generation (adapted from the LiopStar-HQ user manual). The laser consists of an oscillator stage, an amplification stage, and a frequency-doubling stage. Laser dye, circulated at a high flow rate (5 - 10 L/min) through the oscillator and amplifier dye cells, act as the gain medium for lasing and amplification. The pump light is split off inside the dye laser in 30:70 intensity ratios, shaped by two sets of cylindrical lenses into line-shaped profiles, and focused into the oscillator and amplifier dye cells transverse to the direction of the dye laser beam path. The grating inside the oscillator cavity allows the laser's fundamental wavelength to be tuned from 532 nm (the pump light wavelength) to 800 nm, depending on the type of dye used. The oscillator's output is then amplified by a factor of 4 - 6, and frequency-doubled via second-harmonic generation (SHG) into the UV by a BBO3 crystal. The UV light is spatially separated from the fundamental light inside a separation unit, and sent to the experiment. When the dye laser cavity alignment is optimal, ∼ 9 - 13 % of the pump light's energy is converted into fundamental output, of which ∼ 20 - 25 % is converted into UV, yielding a UV pulse energy of 50 - 100 μJ.

83

Nd:YAG laser (EdgeWave BX80) (Fig. 2.31). The 532 nm pump light from the EdgeWave output has a pulse duration of 7 ns, an adjustable repetition rate of up to 10 kHz *, and a maximum pulse energy of 3.0 mJ (independent of the repitition rate). The dye laser consists of an oscillator stage, an amplification stage, and a frequency-doubling stage. Laser dye, circulated at a high flow rate (5 - 10 L/min) through the oscillator and amplifier dye cells, act as the gain medium for lasing and amplification. The pump light is split off inside the dye laser in 30:70 intensity ratios, shaped by two sets of cylindrical lenses into line-shaped profiles, and focused into the oscillator and amplifier dye cells transverse to the direction of the dye laser beam path. The grating inside the oscillator cavity allows the laser's fundamental wavelength to be tuned from 532 nm (the pump light wavelength) to 800 nm, depending on the type of dye used. The oscillator's output is then amplified by a factor of 4 - 6, and frequency-doubled via second-harmonic generation (SHG) into the UV by a BBO3 crystal. The UV light is spatially separated from the fundamental light inside a separation unit, and sent to the experiment. When the dye laser cavity alignment is optimal, $\sim$ 9 - 13 % of the pump light's energy is converted into fundamental output, of which $\sim$ 20 - 25 % is converted into UV, yielding a UV pulse energy of 50 - 100 μJ.

A few different laser dyes were used to generate the UV wavelengths required in different experiments. Details about their concentrations, tuning ranges, output performances, etc. are summarized in Table 2.2. All dye recipes are obtained from the huge body of existing dye laser literature, with tweaks applied to optimize performance for our higher repetition rate system[†]. We note here that though the maximum rep rate of pump laser is 10 kHz, we never operate it above 7 kHz. This is due to the observation of reduced time-averaged fundamental power at a

---

[*]An 100 kHz EdgeWave, with a 0.4 mJ pulse energy, was first used as a pump. Its higher repetition rate would have allowed for a more uniform sampling of reaction products (K_2 and Rb_2) of different velocities. However, the reduced pulse energy made it difficult for the dye laser to lase and for the SHG to be efficient, and we exchanged to a 10 kHz unit instead.

[†]Dye recipes from literature are most commonly reported for 10 or 20 Hz pump rep. rates, which are most commonly used for pulsed dye lasers.

Table 2.2: Laser dye information

Dye	Solvent	Conc.‡§ (g/L)	Peak§ (nm)	Tuning range§¶ (nm)	Rep. Rate (Hz)	Fund. pulse energy‖ (μJ)	UV pulse energy‖ (μJ)	Used for
R590*	EtOH	0.09/0.09	566	565 – 600	10		2600	Single-photon ionization of K, Rb, K$_2$, and Rb$_2$ @ 285 nm; Dissociative ionization of K$_2$Rb$_2^*$ @ 285 nm
R610†	EtOH	0.20/0.20			10		2000	dissociative ionization of K$_2$Rb$_2^*$ at 296 nm and 300 nm
DCM	DMSO	0.3/0.3	660	626 – 685	10		2500	dissociative ionization of K$_2$Rb$_2^*$ @ 330 nm
R590*	EtOH	0.23/0.18	566	565 – 600	1000	800	200	Single-photon ionization of K, Rb, K$_2$, and Rb$_2$ @ 285 nm;
R610†	EtOH	0.20/0.20	590	585 - 602	7000	107	14	Two photon ionization of K and Rb at 298 nm
R610† + R640	EtOH	0.17+0.04 / 0.085+0.02	602	596 – 616	3000	580	120	Single-photon ionization of K$_2$, and Rb$_2$ @ 305 nm; dissociative ionization of K$_2$Rb$_2^*$ at 296 nm and 300 nm
LDS698	EtOH	0.25/0.25	690	675 – 705	7000	320	72	photodissociation of KRb @ 330 – 358 nm; dissociative and single photon ionization of K$_2$Rb$_2^*$ @ 335 – 356 nm
LDS698	DMSO	0.25/0.25	710	690 – 732	7000	225	62	single photon ionization of K$_2$Rb$_2^*$ @ 355 nm

* Rhodamine 590 (also known as Rhodamine 6G).
† Rhodamine 610 (also known as Rhodamine B).
‡ Specified as "oscillator/amplifier" dye concentration.
§ Values are based on our experimentation and may be different from the commonly known literature values; this is especially true for the 10 kHz rep. rate system, for which literature values are not available.
¶ Wavelengths at which the UV pulse energy drops to a quarter of its peak value.
‖ At the peak wavelength.

rep rate above 7 kHz, which most likely results from the dye inside the cells not being able to refresh fast enough to keep up with higher rep rates. In the cases of dyes that emit on the bluer side of the spectrum (R590, R610, and R640), we found further limitations to the rep rate from thermal effects in the doubling crystal resulting from high time-averaged power. This results in significant change in power as well as steering of the UV beam over the timescale of our ionization sequence (~ 1 s), forcing us to limit the rep rates to appropriate values below 7 kHz.

For experiments aimed at ionizing the reaction products, the required UV photon energies exceed the ionization threshold of KRb and can therefore lead to its ionization and depletion. To circumvent this issue, we shape the UV beam into a hollow-bottle beam with a ring profile around the reactant cloud (Fig. 2.32(b)). The products will have enough kinetic energy to escape the shallow trapping potential ($\sim 10\mu$K) of the ODT and reach the ionization beam. Reactants, on the other hand, are left mostly in the dark. The optical setup we use to create the hollow-bottle beam [124] is shown in Fig. 2.32. The combination of two lenses and an axicon (L1, L2, and AX in Fig.2.32) transforms the input Gaussian beam first into a Bessel beam, and finally into a hollow-bottle beam. The beam is combined with the VODT beam on a dichroic mirror, and sent into the science chamber. The focal plane of the bottle beam, where the ring becomes the sharpest (0.45 mm diameter, 5.4 μm Gaussian ring width), intercepts the reactant KRb cloud (Fig. 2.32(b)). The bottle closes up at 6.4 mm and 16.5 mm away from either side of its focus. We measure a 500:1 contrast ratio between the intensities at (the peak of) the ring and the center of the beam. At the UV pulse energy and repetition rate we typically use to ionize the products, we observe an acceptable amount of depletion ($\sim 30\%$) of the reactants over the course of its lifetime. For experiments aimed at velocity map imaging (VMI) of the products, it is desirable for most product ionization to occur inside the VMI volume (section 4.4.3). To this end, half of the UV power is diverted to generate a second, identical beam that crosses the first one at a 40° angle around the KRb cloud (Fig. 2.32(a)).
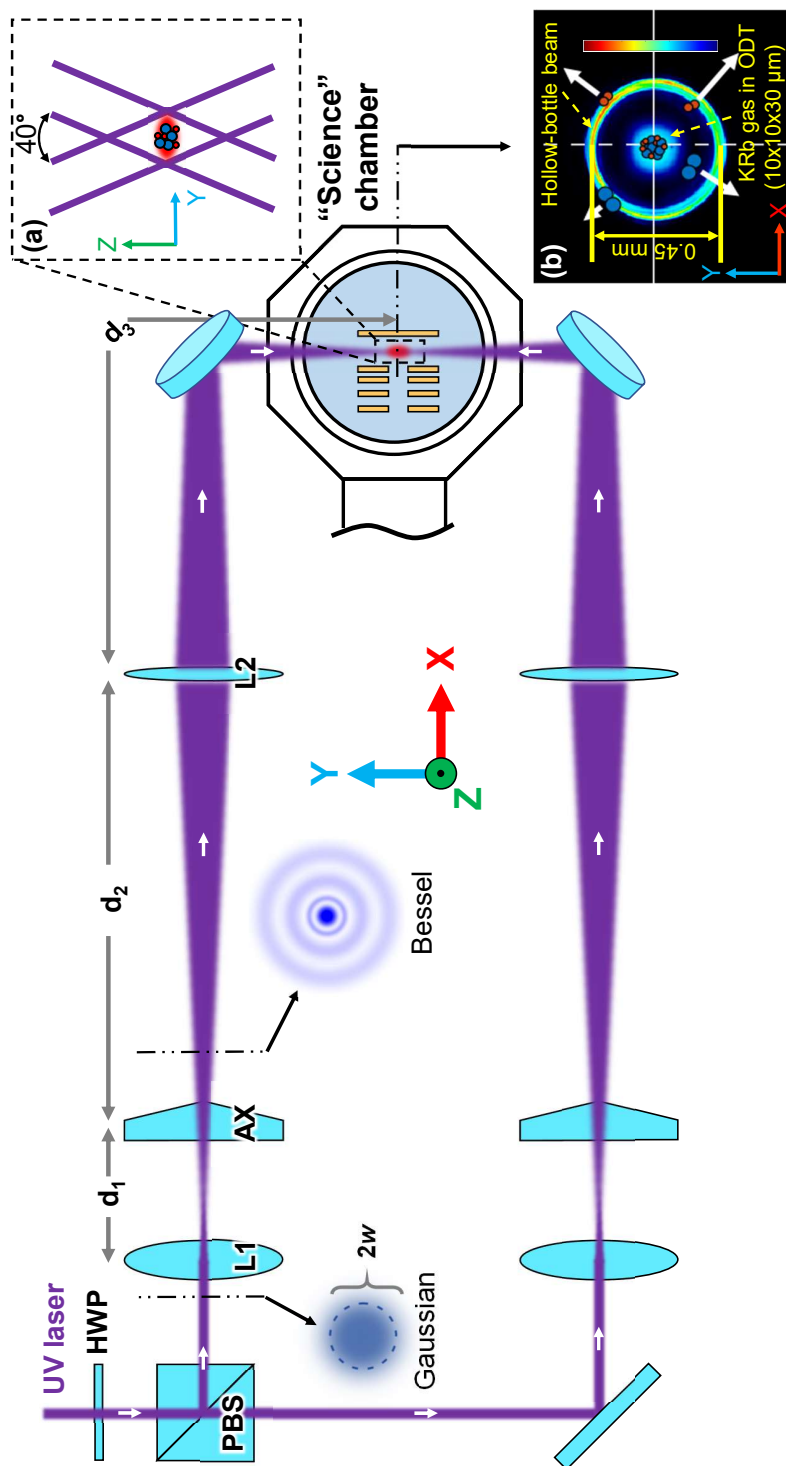
Figure 2.32: Crossed hollow-bottle beam optical setup. HWP: half-wave plate; PBS: polarizing beam-splitter; L1: bi-convex lens (effective focal length 283 mm). AX: axicon (physical angle 1°); L2: bi-convex lens (effective focal length 46.2 mm); $d_1 = 80$ mm ; $d_2 = 670$ mm; $d_3 = 472$ mm. (a) Schematic cross-sectional view in the yz plane showing the relative placement of the pair of crossed hollow beams with respect to the reactant cloud. (b) Schematic cross-sectional view in the xy plane with the intensity profiles of the hollow-bottle beams and the VODT beam superimposed; the reactant cloud is located at the center of the VODT. A fraction of the products flying away from the reactants are intercepted and ionized by the hollow-bottle beams.

Finally, we note that before the 10 kHz repetition ionization laser system was purchased, we used a 10 Hz system loaned to us by the Doyle group here at Harvard. This system consists of a Quanta-Ray Lab 130 as the pump, and a frequency-doubled Cobra-Stretch dye laser as the UV source. Despite the low repitition rate, this system was instrumental in the early days of data-taking.

REMPI laser system

We now turn our attention to the REMPI laser system (Fig. 2.33). The REMPI scheme shown in Fig. 2.33(a) is used in experiments described in Chapter 7 to ionize K_2 and Rb_2 product molecules with quantum state selectivity via rovibrational transitions from the $X^1\Sigma_g$ to the $B^1\Pi_u$ electronic state. The resonant lights, at around 648 and 674 nm respectively for K_2 and Rb_2, are provided by two nearly identical ECDL-based laser systems shown schematically in Fig. 2.33(b). The stabilization of each frequency is achieved by a feedback loop that involves: 1. measuring the frequency of the laser using a wavemeter (Bristol 771A); 2. comparing the measured frequency to the desired set point using a Matlab-based PC program; 3. converting the frequency difference to analog voltages via a programmable power supply (Keithley G2230G-30-3); and 4. feeding the analog voltages to the laser didoe current and PZT voltage to provide frequency feedback. From the 648 (674) nm system, we obtain ~ 10 (15) mW of optical power at the experiment. The ionizing light at 532 nm is provided by the EdgeWave laser, and we use ~ 350 mW at the experiment. At the above optical powers and with ~ 0.8 mm $1/e^2$ beam diameters, the resonant (ionization) leg of the REMPI transition is completely (nearly) saturated, resulting in near unity ionization probability for each particular rotational state of the product. The REMPI beams are combined with the VODT beam on a dichroic mirror and sent into the science chamber as shown in Fig. 2.13(c).

The REMPI lights, for both the resonant and the ionizing transitions, can potentially excite
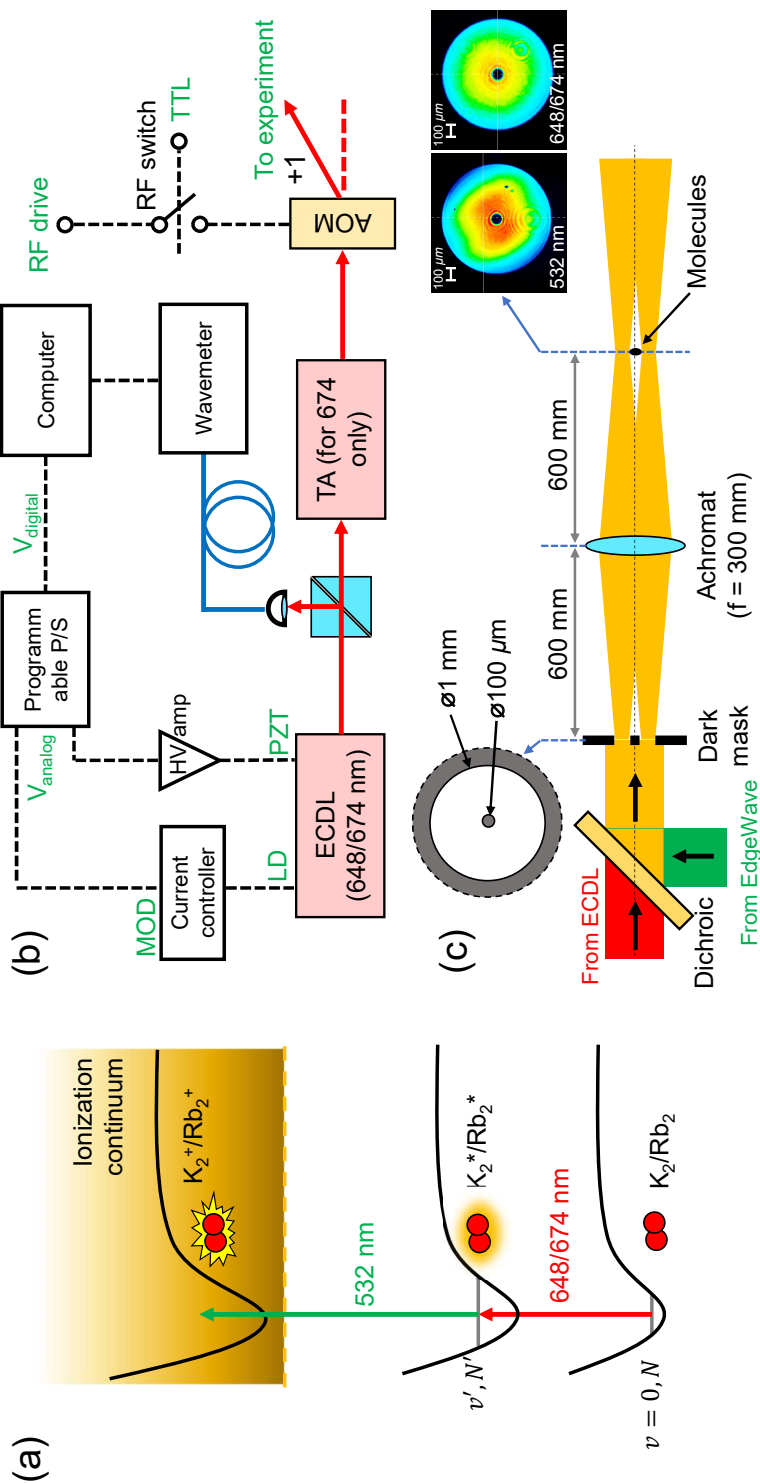
Figure 2.33: Resonance-enhanced multi-photon spectroscopy and associated laser systems. (a) Two-photon REMPI scheme for the state-selective ionization of reaction products. K_2 and Rb_2 emerging from chemical reactions are first optically excited from their ground electric state to an excited rovibronic state via a resonant transition, the lights for which are provided by CW ECDLs operating at around 648 and 674 nm, respectively. A 532 nm photon from the pulsed Edge-Wave laser then ionizes the excited molecule, resulting in detectable K_2^+ and Rb_2^+ ions. (b) Schematic of the REMPI laser system, including a wavemeter-based frequency feedback loop. (c) Generating a dark-mask beam around the KRb molecules. The 648/674 nm and 532 nm lasers are combined on a dichroic mirror, and are then sent through a dark mask (Thorlabs R1DF100) and an achromatic lens ($f = 300$ mm). The resulting beam profiles in the image plane (insets) have a 1 mm outer diameter and a 100 μm inner diameter.

89

the reactant KRb molecules. To eliminate these undesirable effects, we generate dark spots at the centers of the REMPI beams using the optical setup illustrated in Fig. 2.33(c). After combining on a dichroic mirror, the resonant and ionizing beams are sent through a dark mask (Thorlabs R1DF100), which has a 100 μm diameter center dark spot and a 1 mm clear aperture. The mask is placed at the object plane of a achromatic imaging lens (f = 300 mm), and is then projected onto the image plane coinciding with the molecular cloud location, resulting in the beam profiles shown in the insets. The dark spot size is chosen based on the size of the KRb cloud, which is up to 80 μm (4σ) in its longest direction. The length of the dark region along the direction of propagation is approximately 7 mm on either side of the image plane (defined as the brightness of the dark spot increases to half the peak intensity). Compared to the hollow-bottle beam, the dark mask beam samples a much greater volume of products around the KRb cloud. Combined with the near unity ionization efficiency, this results, to our initial surprise, in a higher signal rate compared to what we could achieve using UV ionization, despite detecting only a single product quantum state at a time.

2.5.2   VMI ion optics

In ion detection schemes, electric field plates are commonly employed to apply the acceleration E-field to the ions. While a simple two-plate design could provide mapping between an ion's velocity and position on the detector, it also inevitably maps its initial location in the ionization volume onto the position on the detector. The kinetic energy resolution of such a design is ultimately limited by the initial spatial extent of the ion distribution. This issue can be circumvented by employing VMI ion optics, which consists of multiple field plates with carefully designed geometries and voltages. Such a configuration creates an E-field in which a one-to-one mapping between the velocity of the ions and their position on the detector is achieved.
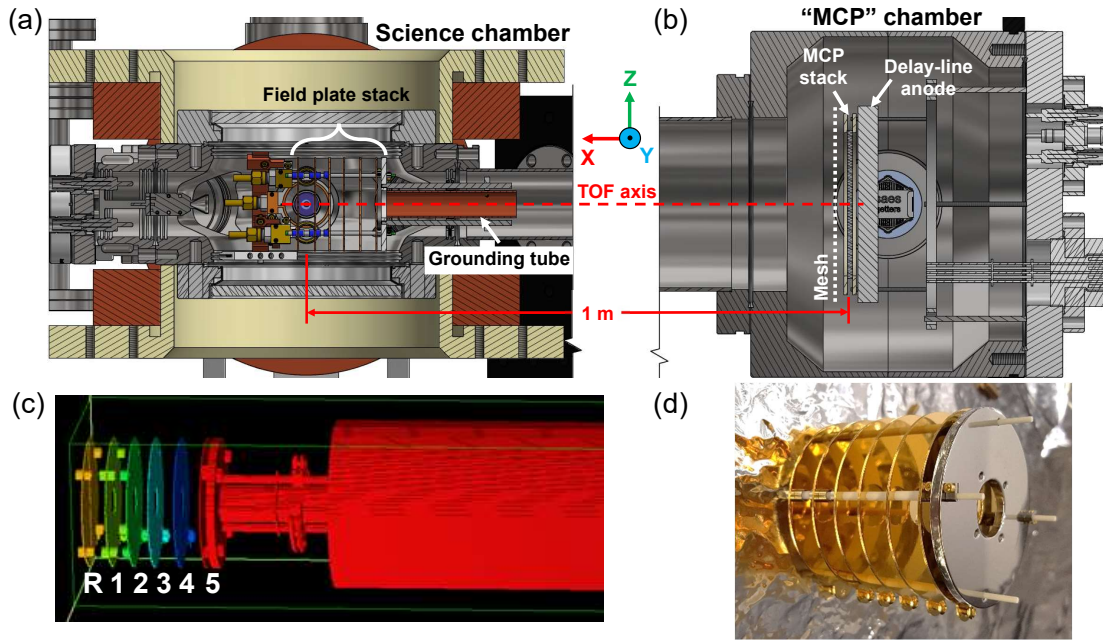
Figure 2.34: **The ion spectrometer.** (a)(b) CAD drawing showing VMI ion optics and MCP detector situated inside the "science" and "MCP" chambers, respectively. (c) A realistic 3D model of the ion optics is imported into SIMION for geometry optimization. The six electric field plates are labeled R, 1, 2, 3, 4, and 5. The final design parameters are summarized in Tab. 2.3. (d) Photo of the electric field plate stack before it was placed into the science chamber.

Our VMI setup design is guided by Ref.[69] and[127]. The CAD drawing of the VMI ion optics is shown in Fig 2.34(a). The electric field plate stack consists of five gold-plated copper plates (labeled from left to right as R, 1,2,3,4,and 5) supported by four alumina rods and spaced from

Table 2.3: Dimensions of the electric field plates consisting the VMI ion optics. All plates have an outer diameter of 35 mm and are 0.81 mm thick.

Electrodes	Aperture diameter (mm)	Relative voltage (%)	Dist. to previous electrode (mm)
R	3.0	100.0	-
1	11.0	82.0	9.19
2	12.5	58.5	7.70
3	14.0	35.0	7.70
4	12.5	17.5	8.71
5	11.0	0.0	8.71

91

each other by alumina spacers (Fig. 2.34(d)). The reactant cloud is placed at the center between the repeller (R) and extractor (1) plates. To determine the optimal geometries and voltages of the five plates, we used SIMION to simulate VMI performance. The optimization parameters include the aperture size of each plate, the distances between neighboring plates, and the voltages of the electrodes. We imported our 3D mechanical model into SIMION (v8.1) to perform an accurate simulation (Fig. 2.34(c)). The final design parameters are summarized in Tab. 2.3. The voltage applied to each plate is reported as a percentage of the repeller voltage V_R. An appropriate V_R must be chosen for each chemical reaction we study to achieve a balance between kinetic energy resolution and detection range, given the finite size of the MCP and the apertures along the TOF axis (see further discussions in 4.4).

2.5.3   Micro-channel plate ion detector

For detecting the ions we used a commercial setup from Roentdek, depicted schematically in Fig. 2.35. The main components are a delay-line MCP detector (DLD80), front-end electronics for analog signal processing, and digital readout electronics for data acquisition. The detector parts were shipped to us as a kit and assembled in-house (Fig. 2.36). We chose this detector mainly for its ability to record, with high resolution, the location *and* time of every ion hit. This provided several advantages over the more traditional phosphor screen MCPs*, including the abilities to time-slice ion images (section 4.4), post-select on ions associated with certain ionization laser pulses, and, in the future, perform coincidence detection. The detector has an active diameter of 80 mm, a spatial resolution of 0.08 mm, and a temporal resolution of 1 ns. Further details of its design and performance can be found in Ref.[114]. Here, we highlight the key components in

---

*Timing resolution in these devices are limited by the readout device, which is typically a CCD camera. However, we learned from Ed Narevicius that timing resolution similar to that of a DLD ($\sim$ 1 ns) can be added to a phosphor detector. This is achieved by correlating the amplitudes of voltage pulses resulting from ion hits with the fluorescence intensities of ion spots on the screen.
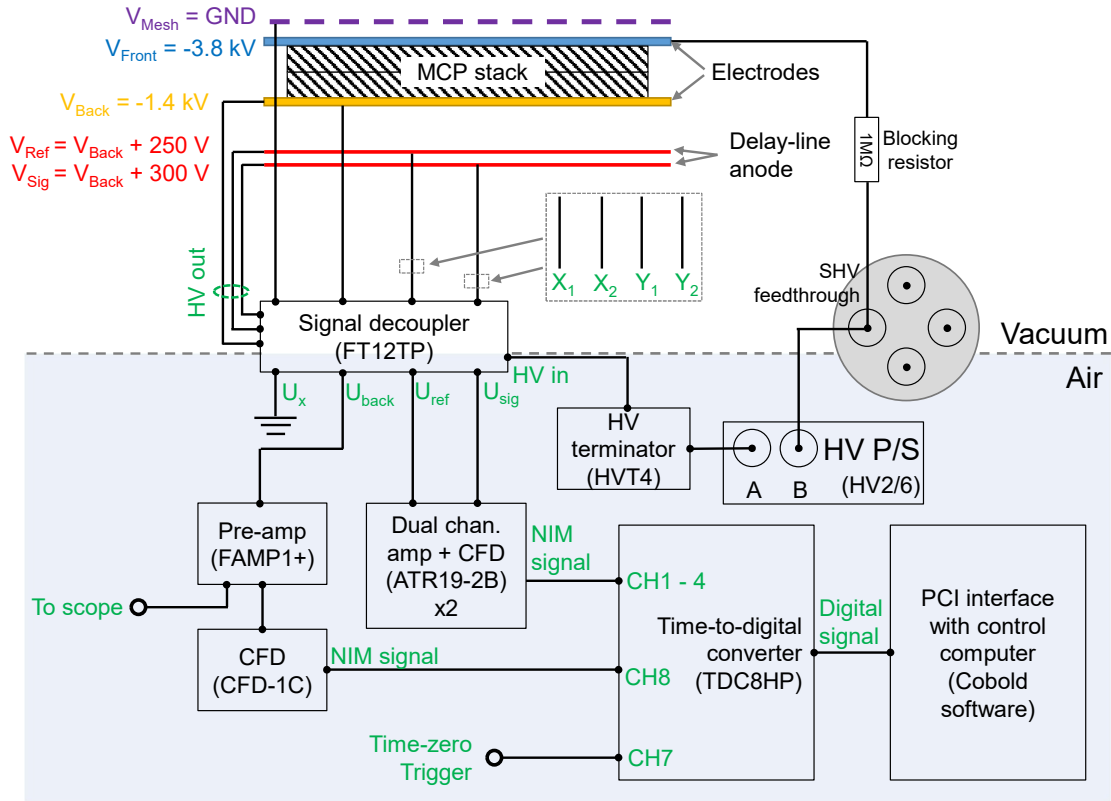
Figure 2.35: MCP schematics and wiring diagram. See main text for descriptions of the various components and their connectivity.

the setup and describe the role each plays in the detection.

The MCP assembly consists of a stainless-steel mesh, a stack of two chevron micro-channel plates sandwiched between a pair of metalized ceramic ring electrodes ("Front" and "Back"), and a delay-line anode. The mesh is composed of square cells, with a wire thickness of 0.02 mm and a center-to-center distance of 0.16 mm between cells. It is electrically grounded and placed 3.2 mm in front of the "Front" ring (or 5.0 mm away from the front surface of the MCP stack), which is held at -3.8 kV. This creates an extra stage of acceleration for all positive ions before they hit the stack, boosting their kinetic energy and result in better ion detection efficiency. Given the mesh transmission (75%),

the MCP open-area-ratio (60%), and the mass-dependent intrinsic MCP efficiency (calculated based on an empirical formula developed in [123]), is 0.394 (0.282) for the lightest (heaviest) ion, K^+ ($K_2Rb_2^+$), in our experiment. Once the accelerated ion strikes a pore on the MCP stack, an electron avalanche is initiated, generating a charge cloud that eventually hits a location on delay-line anode. The anode consists of two layers (X and Y) of crossly-arranged wires, with a "Sig" and a "Ref" wire comprising each set. Within each layer, the signal wire is biased to be slightly more positive such that the charge cloud preferentially hits it. This generates a voltage differential between the "Sig" and "Ref" wires, which then propagates after some time to two corners of the layer ($\{X_1, X_2\}$, $\{Y_1, Y_2\}$). The delay between the times at which the voltage pulse hits X_1 and X_2 (Y_1 and Y_2) provide the necessary information to calculate the hit location of the ion in the X (Y) direction.

The signal decoupler sends the high voltages from the HV power supply to the various components of the MCP assembly (except for V_{Front}, which is provided through an SHV feedthrough), and capacitively decouples the voltage pulses from the MCP "Back" electrode (U_{Back}) and the four corners of the anode ($U_{\text{Sig}}^{X_1, X_2, Y_1, Y_2}$ and $U_{\text{Ref}}^{X_1, X_2, Y_1, Y_2}$).

The Front-end electronics first amplify the analog voltage pulses, and then convert them into NIM logic timing pulses via constant-fraction discriminators (CFDs). A NIM pulse, a negative-going square pulse, provides a time-stamp for its analog counterpart in a pulse-height-independent fashion. In the end, we obtain a NIM signal corresponding to U_{Back}, which provides a zero-of-time for the ion hit, and four NIM signals each corresponding to the hit time of a corner of the anode.

The digital readout device, a time-to-digital converter (TDC), takes the NIM pulses in and convert them to digital timing signals which can then be recorded by a PC. The TDC

also admits a TTL trigger, which we use to provide a time-zero for the ion time-of-flight (section 4.3). Time stamps of all relevant pulses are recorded by Roentdek's data acquisition software (Cobold-PC), which then yields the time and XY coordinate of the ion hit. This data, recorded in Cobold's native listmode file format, is then converted into ASCII format and written into a .dat file by a Matlab program we wrote.

2.5.4   Ionization and detection synchronization

During an experiment, ionization and ion detection must be synchronized to each other, to other processes during the detection (e.g. ODT intensity modulation, see Chapter 6), and to the rest of the experimental cycle. To accomplish this, we trigger a function generator (BK Precision 4054B), using a TTL channel from the computer control (TTL 18), to produce a train of pulses that function as the master clock during the ionization sequence. One channel of the function generator is used to trigger the Edge-Wave laser for ionization pulse*, while the other is fed into a delay generator (Highland Technology P400), from which four time-delayed pulses, each with a user-defined pulse width, are derived. Three of the channels are respectively used to trigger the MCP (time-zero for TOF), and modulate the H and VODT intensities. A fourth channel is dedicated to a specialized task, such as controlling the "kill" beam intensity in the complex lifetime study (Chapter 6), or controlling the in intensity of the resonant light in REMPI (Chapter 7). For all experiments described in this thesis, the VMI electric field plates are switch on at the beginning of and held at some constant value during the ionization sequence.

---

*A great advantage of the Edge-Wave, compared to most traditional pulsed YAG lasers, is its ability to be triggered at any duty-cycle and thus generate on-demand pulses, with little to no thermal effects from doing so.

C — 1.6mm — PEEK screw and nuts

D — Mesh, Holder, MCP front, MCP back, 4-pin SHV feedthrough

E

No. 5	x_1-reference
No. 6	x_2-signal
No. 7	x_2-reference
No. 8	x_1-signal
No. 9	y_1-reference
No. 10	y_1-signal
No. 11	y_2-reference
No. 12	y_2-signal

B — MCP front connection, 1MΩ blocking resistor

Center panel labels: X_2, C, B, A, D, F, E, Y_2, Y_1, X_1, MCP pore tilt direction

A — MCP back connection

F — Anode signal and ref connections

Figure 2.36: The MCP assembly. Center frame: overview of the assembly, including the MCP stack, the supporting structures, signal and HV wiring, and the mounting flange. Red circles labeled (A) – (E) highlight essential features of the assembly, which are shown as zoomed views in the surrounding frames. X_1, X_2, Y_1, and Y_1 label the four corners of the MCP, through which the delay-line anode signals are coupled out. They also define the coordinate system of the MCP: lines defined by $\{X_1, X_2\}$ and $\{Y_1, Y_2\}$ represent the x and y directions of all ion images presented in this thesis. (A) HV connection to the "back" electrode of the MCP stack. (B) HV connection to the "front" electrode of the MCP stack; a 1 MΩ blocking resistor is included to limit the current in the event of a breakdown discharge. (C) PEEK plastic nuts are used to set the distance between the mesh and the front plate of the MCP. (D) HV connection feedthrough viewed from the vacuum side. (E) Signal connection feedthrough viewed from the vacuum side. See table within the figure for pin assignments.

Chapter 3

Preparing ultracold reactants: atom cooling and molecule association

In this chapter we describe key experimental steps in the production of ultracold KRb molecules, as summarized in Fig. 3.1. Our goal is to produce a sample of sub-microkelvin KRb molecules in their absolute rovibronic ground-state, with which we can investigate chemistry in the ultracold regime. To this end, our experiment benefits tremendously from the clear roadmap towards ground-state KRb provided by the first generation JILA KRb experiment – first cool the precursor atoms to ultracold temperatures, then magneto-associate them into pairs of loosely-bound molecules, and finally Raman transfer the molecules into the ground-state.

In all of our studies, the data collection rate scales linearly as the number of reactions that occur in the sample. Given the relatively long experimental cycle time (52 s), it is important to maximize the number of KRb molecules and thereby the number of their reactions. This requires both the production of a large number of precursor atoms, and an assembly of a reasonable fraction of them into molecules. The efficiency of the molecular assembly is mostly limited

Figure 3.1: Experimental steps in the production of ultracold KRb molecules and their durations.

by that of the magneto-association (3.7), and the figure-of-merit is the precursor atoms' phase-space-density (PSD). For each atomic species, PSD is defined as

$$PSD = n\lambda^3, \tag{3.1}$$

where n is the peak number density of the atoms, and $\lambda = \frac{h}{\sqrt{2\pi m k_B T}}$ is the thermal de Broglie wavelength for particles of mass m at temperature T. Magneto-association becomes significant as the PSD of the precursor atoms reach order unity, and a conversion efficiency of $10 - 40\%$ have been achieved in the ^{40}K-^{87}Rb system[155,57].

In our experiment, PSDs of the K and Rb atoms are increased through the well-established laser cooling (3.2) and evaporative cooling (3.3,3.6) techniques. To keep track of the PSD during this process, it is useful to explicity express the atom density in Eq. 3.1 in terms of experimentally-measurable quantities. For thermal atoms confined in a 3D harmonic trap, n is given by

$$n = \frac{N}{(2\pi)^{3/2}\sigma_x\sigma_y\sigma_z}, \tag{3.2}$$

where $\sigma_{x,y,z}$ is the 1σ Gaussian cloud width along each principal axis of the trap, and is related to the trap frequency as

$$\sigma_{x,y,z} = \frac{1}{\omega_{x,y,z}}\sqrt{\frac{k_B T}{m}}. \tag{3.3}$$

Thus we obtain

$$PSD = N\frac{\omega_x\omega_y\omega_z}{(2\pi)^{3/2}(k_B T/m)^{3/2}} \times \left(\frac{h}{\sqrt{2\pi m k_B T}}\right)^3 = N\left(\frac{\hbar\omega_x}{k_B T}\right)\left(\frac{\hbar\omega_y}{k_B T}\right)\left(\frac{\hbar\omega_z}{k_B T}\right) \tag{3.4}$$

Note that in the thermal limit where $k_B T \gg \hbar\omega_i$, the quantity $(k_B T)/(\hbar\omega_i)$ roughly represents the number of energetically accessible harmonic oscillator modes in the i direction. As such,

Eq. 3.4 makes explicit the physical interpretation of PSD as approximately the average number of particles occupying each 3D harmonic oscillator mode, and we see that the PSD of a gas characterizes the degree to which it is quantum degenerate.

The content of this chapter is organized as follows. Section 3.1 discusses the imaging techniques used to characterize the conditions of the atoms during various stages of the experiment. The subsequent sections describe the key steps towards ground state KRb molecules in chronological order during an experimental sequence, including laser cooling in the MOT chamber followed by magnetic transfer to the evaporation chamber (section 3.2), further cooling by RF evaporation inside the QUIC trap (section 3.3), optical transport of the atoms to the science chamber (section 3.4), quantum state preparation of the atoms (section 3.5), magneto-association of pairs of atoms into weakly-bound KRb molecules (section 3.7), and, finally, Raman transfer of the weakly-bound molecules into the rovibrational ground state (section 3.8).

3.1 Imaging the atoms

As we have discussed in the introduction (section 4) optical imaging is the mostly widely used detection technique in ultracold experiments. In our experiment, both fluorescence and absorption imaging are employed to probe the condition of the atoms during various stages of the sequence, serving as critical diagnostics tools.

Fluorescence imaging is used to monitor the locations and distributions of atoms in the MOT (section 3.2). Photons scattered by the laser-cooled atoms are imaged onto a CCD camera (Thorlabs DCU223M) via a standard camera objective (Fig. 2.5(d)). Fig. 3.2 shows typical fluorescence images of Rb and K MOTs during steady-state operation, containing $\sim 10^9$ and $\sim 10^7$ atoms, respectively. The number of atoms within each MOT is deduced based on the strength of their fluorescence, according to a well-known formula that can be found, for example, in Ref. [190].
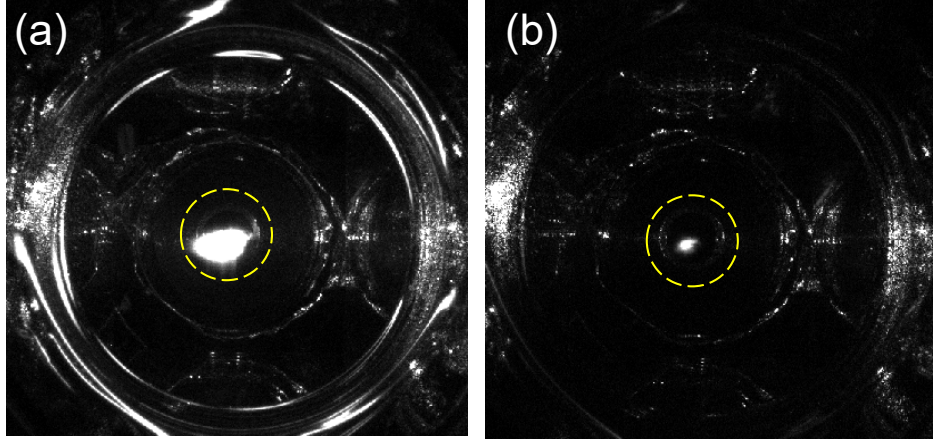
Figure 3.2: Fluorescence images of Rb (a) and K (b) MOTs, containing $\sim 10^9$ and $\sim 10^7$ atoms, respectively.

After laser cooling, the atoms undergo several additional stages of cooling, with transfers between different traps or quantum states in between these stages. To monitor the number of atoms at various stages as well as their temperature, we use time-of-flight (TOF) absorption imaging, with the hardware described in section 2.3.4. As a standard technique in the ultracold gas community, details about TOF imaging can be found in many references, *e.g.* Ref.[117]. Here, we describe in brief the scheme used in our experiment. Atoms originally confined in traps are released by abruptly shutting the trap off. The atoms then expands ballistically at a rate determined by their temperature T and their mass m. At this point, the frequency of the light used to image each atomic species is tuned to the resonant with a quasi-cycling transition of that species. For imaging ^{87}Rb, we use the $|F = 2, m_F = 2\rangle \to |F' = 3, m'_F = 3\rangle$ transition. For ^{40}K, we use either the $|F = 9/2, m_F = 9/2\rangle \to |F' = 11/2, m'_F = 9/2\rangle$ or the $|F = 9/2, -m_F = 9/2\rangle \to |F' = 11/2, m'_F = -11/2\rangle$ transitions, depending on the initial hyperfine state of the atoms. After a certain duration of expansion, three frames are acquired in succession, using the setup discussed in section 2.3.4, and following to the timing diagram in Fig. 3.3. Each frame consists of a pair of images – one for K and the other for Rb. The

101

camera has a interline-transfer design, such that the delay between the acquisitions of images within a given pair is limited only by the minimum camera exposure time, which is 500 μs. The minimum time between frames, however, is limited by the image readout time to be 400 ms.

During the "shadow frame", the imaging light for K and Rb are pulsed on at times TOF_K and TOF_Rb after the trap off, respectively, each for a duration of 100 μs. The atom clouds partially absorb the lights that pass through them, casting shadows in the beams. The resulting intensity patterns are then recorded by two exposures of the CCD camera, each lasting for 500 μs. After a 400 ms readout, the camera then records the "light frame", which represents the intensity patterns of the imaging lights in the absence of atoms. After another 400 ms, the camera records the "background frame" in the absence of any imaging light. This is used to characterize background intensity pattern on the camera, which includes contributions from dark counts as well as stray lights from the environment.

The intensity pattern in each frame is represented by the brightness of pixels, $I_\text{frame}(x, y)$, where (x, y) is one of the 1040×1392 pixels on the camera chip. The absorption image for each atom cloud is given by its spatial-dependent optical depth, $\text{OD}(x, y)$, which can be calculated from the recorded intensity patterns as

$$\text{OD}(x, y) = -\log\left(\frac{I_\text{shadow}(x, y) - I_\text{bkgd}(x, y)}{I_\text{light}(x, y) - I_\text{bkgd}(x, y)}\right). \tag{3.5}$$

Fig. 3.4 shows the OD images of K and Rb atoms released from the QUIC trap at the end of the RF evaporation (section 3.3), calculated from the three frames shown in Fig. 3.3. Each OD image is then fitted with a two-dimensional Gaussian function to extract the peak optical depth, pkOD, as well as the Gaussian widths along the x and y directions, σ_x and σ_y. From these parameters as well as the TOF, we can calculate both the atom number and temperature of each
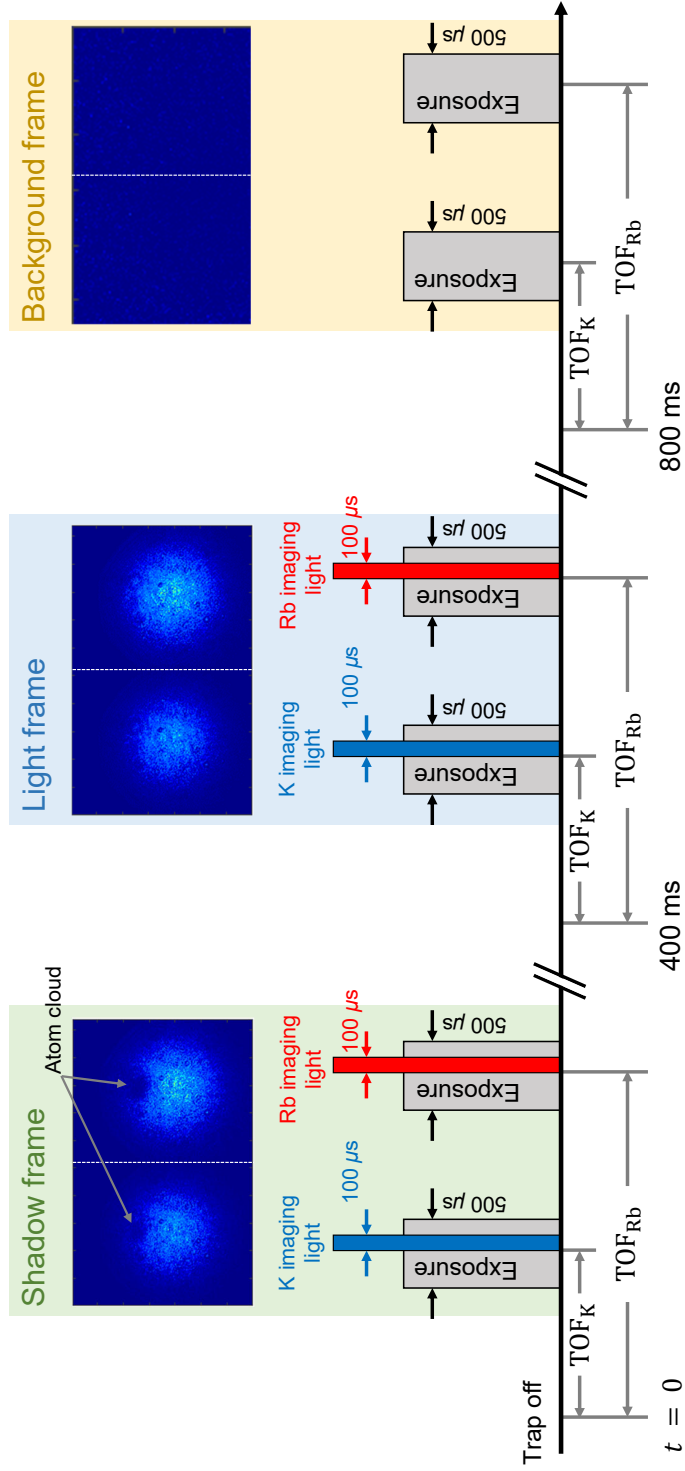
Figure 3.3: Absorption imaging. After the trap confining the atoms is switched off at $t = 0$, three frames of images are acquired in succession. The shadow frame is taken as the imaging lights passes through the atom clouds, which shadows cast in the beam profiles; the light frame is taken in the presence of the imaging lights but absence of the atoms; and the background frame is taken in the absence of any imaging light. There is a 400 ms image readout delay between each frame. Each camera exposure lasts for 500 μs, which is also the minimum exposure time for the camera.

103
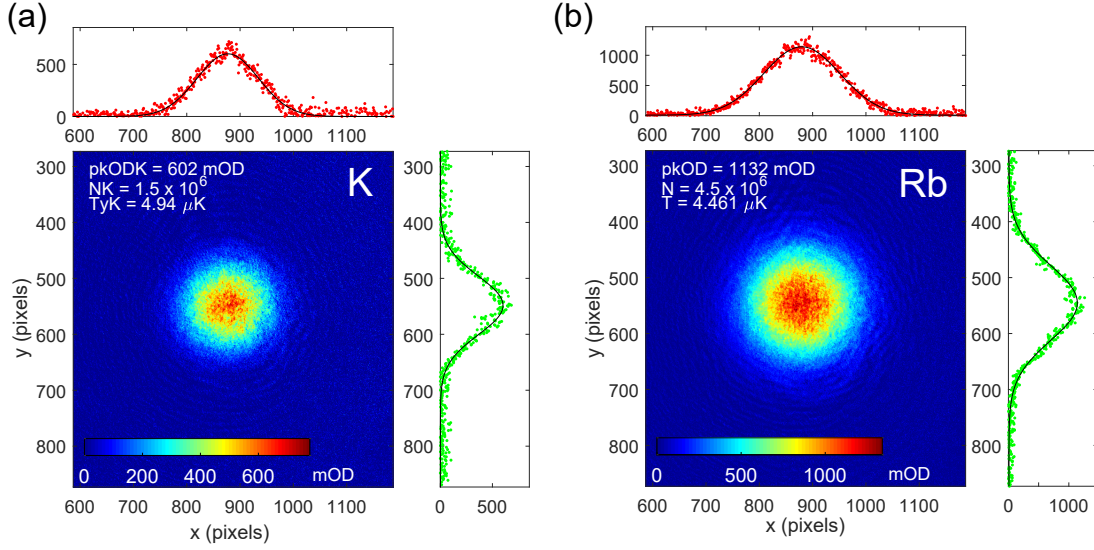
Figure 3.4: OD images of K (a) and Rb (b) after RF evaporation. The K and Rb atoms are released from the QUIC trap and imaged after TOFs of 7 and 10 ms, respectively. These images represent the distributions of the atoms in space, and is calculated from the three camera frames in Fig. 3.3, according to Eq. 3.5. The color scale is in units of milli-optical depth (mOD). The x and y scales are given in units of camera pixels, which relates to distance as 6.45 μm/pixel. 2D Gaussian fits are applied to extract the peak optical depth (pkOD) and Gaussian widths ($\sigma_{x,y}$) of the clouds. Using these parameters and the TOFs, the atom numbers (N) and temperatures (T) of the two clouds are calculated per Eq. 3.6 and 3.7. The 1D profiles associated with each image is obtained by summing the images as well as their 2D fits along rows or columns of pixels.

cloud, as*

$$N = \frac{2\pi}{\sigma_0} \text{pkOD} \sigma_x \sigma_y \left(1 + 4\frac{\Delta^2}{\Gamma^2} \right), \tag{3.6}$$

and

$$T = \frac{m}{k_B} \frac{\omega_{x,y}^2 \sigma_{x,y}^2}{\left(1 + \omega_{x,y}^2 \text{TOF}^2 \right)^2}, \tag{3.7}$$

respectively. Here, σ_0 is the resonant scattering cross section of the atom associated with the imaging transition (see Ref. [190] and [198]), Δ is the detuning of the imaging light with respect to the transition, Γ is the natural linewidth of the transition (see Ref. [190] and [198]), m is the mass of

---

*For a derivation of these expressions, see Ref. [117].

the atom, and $\omega_{x,y}$ is the trapping frequency along the x or y direction.

Finally, we discuss the procedures for focusing the camera and calibrating the imaging magnification. To focus the camera, we produce a small atom cloud of size no more than a 50 μm after the expansion, and acquire its absorption images at different camera positions along the imaging axis. The camera comes into focus when the size of the cloud on the OD image is minimized. At this point we calibrate magnification of the imaging system, such that the sizes of atom clouds measured from the OD images can be correctly related to their real space sizes. To this end, we move the atom clouds in the object plane by known distances, and measure the distances of those movements on the camera image. In the evaporation and science chambers, these movements are generated using the transfer track and the air-bearing linear stage, respectively. The ratio of the image plane distance to the object plane distance provides the imaging system's magnification, which is measured to be 1.05 and 1.00 for the evaporation and science chamber systems, respectively.

3.2   Laser cooling and magnetic transfer

In this section, we describe the steps towards the laser cooling of Rb and K, as well as their magnetic transfer inside a quadrupole trap. All relevant optical transitions are labeled in the energy level diagrams in Fig. 3.5 and Fig. 3.6. The optimization of most parameters in this section are achieved by maximizing the atom numbers inside the evaporation chamber at the end of the RF evaporation (section 3.3), as characterized by the absorption imaging technique discussed in the preceding section.

Each experimental cycle begins with the loading of a dual-species magneto-optical trap (MOT) from the background atomic vapor that floods the MOT chamber (section 2.2.2). The MOT beams are switched on, and their frequencies are set to target cooling and repump transitions

105
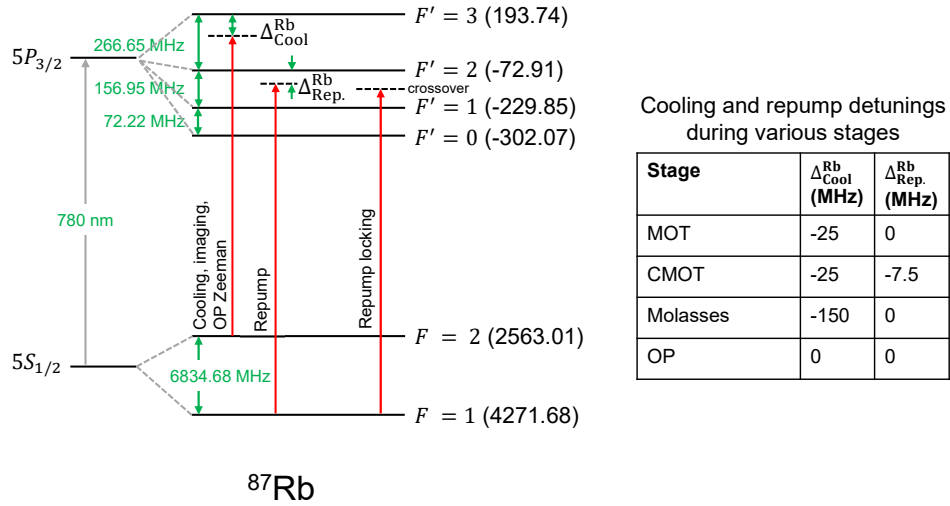
Figure 3.5: Electronic transitions in ^{87}Rb relevant for laser cooling and state-manipulation. F and F' specify the hyperfine state of the ground and excited state atoms, respectively. All frequency values are specified in units of MHz. The inset table summarizes the detunings of the cooling and repump lights with respect to their associated transitions during various stages within the MOT chamber.

in ^{87}Rb and ^{40}K, respectively. For ^{87}Rb, the cooling light is -25 MHz* detuned from the $|F = 2\rangle \to |F' = 3\rangle$ transition, and the repump light is resonant with the $|F = 1\rangle \to |F' = 2\rangle$ transition. For ^{40}K, the cooling light is -19 MHz detuned from the $|F = 9/2\rangle \to |F' = 11/2\rangle$ transition, and the repump light is resonant with the $|F = 7/2\rangle \to |F' = 9/2\rangle$ transition. The transfer coil pair (2.4.1), which at this stage centers around the MOT chamber, is turned on with 20 A of current to provide a quadrupole magnetic field with a gradient of ~ 10 G/cm along the z direction.

Loading a dual-species MOT is a balancing act, as the vapor pressure of one species that contributes the its loading also acts as a background pressure for the other species that leads to its loss. For example, too high of a Rb vapor pressure can greatly suppress the number of loaded ^{40}K atoms, which has a small (3.15%) abundance despite isotopic enrichment. To this

---

*Throughout this thesis, detuning is defined as $\Delta = \nu_0 - \nu_L$, where ν_0 is the resonant transition frequency and ν_L is the laser frequency.
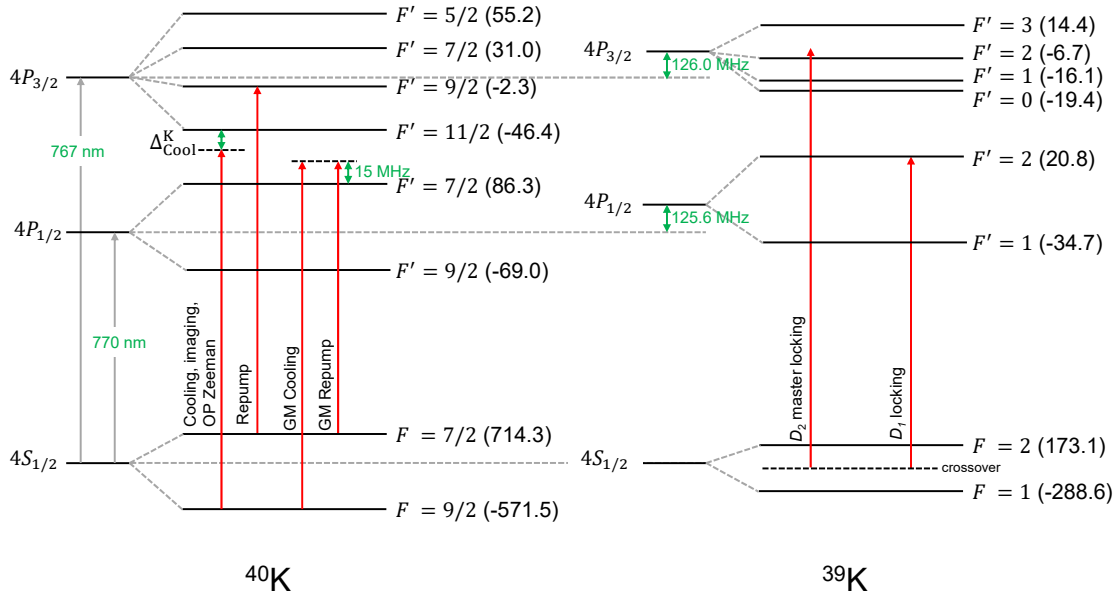
Figure 3.6: Left: electronic transitions in ^{40}K relevant for laser cooling and state-manipulation. Right: electronic transitions in ^{39}K relevant for laser frequency locking. F and F' specify the hyperfine state of the ground and excited state atoms, respectively.

end, we originally intended to use the Rb dispensers and the K ampoules to provide some degree of independent control over their individual vapor pressures. However, over time, we found that the steady-state atom number in either MOT no longer depends on firing the Rb dispenser or heating up the K ampoule. For the Rb MOT, this indicates that its operation has entered a regime where its own vapor pressure greatly exceeds the background pressure[83]. As such, the Rb MOT number becomes independent of its vapor pressure. For the K MOT, on the other hand, this indicates either that the K atoms have migrated significantly out of the ampoule and into other parts of the cell, or that there is significant deposition of Rb inside the ampoule. In either case, the K MOT number becomes limited by the background pressure. Ultimately, we capture as many as 1×10^9 ^{87}Rb atoms and 7×10^6 ^{40}K atoms* in the MOT, as measured by monitoring

---

*Besides low atomic abundance, another factor that contributes to the reduction of the ^{40}K MOT number is light-assisted collisions with the co-trapped ^{87}Rb atoms.[82] When loading a ^{40}K MOT in the absence of a ^{87}Rb MOT, the atom number is 1.4×10^7 K^{40}.

their fluorescence intensities.

We note that increasing the atomic vapor pressures, while not affecting the MOT atom numbers, does change the MOT loading rate, or inversely the characteristic time it takes for the MOT to fill to a steady-state. The impact of this on the atom's lifetime inside the quadrupole trap is discussed towards the end of this section. We also note that while it is natural to expect the low ^{40}K number making it the limiting reagent in molecule formation (section 3.7), we oftentimes have to deliberately reduce the K atom number to maximize molecule production. This is because RF and ODT evaporations (section 3.3 and 3.6) are performed primarily at the expense of Rb atom number, not K, and the current Rb MOT number is barely enough to support the K atoms during evaporation.

After the MOT stage, we apply MOT compression (CMOT) to the Rb atoms, for a duration of 20 ms, by detuning the repump light 7.5 MHz to the red of the $|F = 1\rangle \rightarrow |F' = 2\rangle$ transition. This causes some of the Rb atoms to fall out of the cycling transition, reducing the radiation pressure inside and MOT so that its size can shrink. The purpose of this step is to reduce the heating experienced by the atoms as they are loaded into the quadrupole magnetic trap*. For the intrinsically smaller K MOT, compression is not necessary.

Following the Rb CMOT, we perform 10 ms of molasses coolings on both K and Rb to further reduce the atom temperature. To this end, the MOT B field gradient is switched off, and the shim coils are switched on to null the field at the center of the MOT cell. For K, we use a gray molasses (GM) scheme via the D_1 transition as described in Ref[74]. In the scheme, the cooling and repump lights are blue-detuned by 15 MHz (2.5 natural linewidths) from the $|F = 9/2\rangle \rightarrow |F' = 7/2\rangle$ and the $|F = 7/2\rangle \rightarrow |F' = 7/2\rangle$ transitions, respectively. Compared to without GM cooling, we gain a factor of 2 more K atoms at the end of the RF evaporation. For Rb, we perform regular

---

*A larger atom cloud, on average, experiences a more substantial slosh inside the quadrupole trapping potential as it is turned on.

optical molasses via the D_2 transition by increasing the detuning of cooling light to -150 MHz.

We also attempted GM cooling on the Rb atoms[175], following the recommendation from the 2nd generation JILA KRb experiment, where such a scheme resulted in a factor of 2 gain in the post-evaporation Rb number and a similar gain in the final molecule number. In our case, however, the gain is only $\sim 10\%$. The reason of this sub-optimal performance is unclear, although we have ruled out, as factors, the transition frequencies of the cooling and repump lights, as well as their relative coherence. In the future, a more thorough characterization of the GM performance in the MOT chamber, including a measurements of the atom temperature and phase space density, may help rationalize and improve upon the sub-optimal performance.

Following the molasses stage, K and Rb atoms are optically pumped (OP), over a duration of 6 ms, into their respective stretched hyperfine states ($|2, 2\rangle$ for Rb and $|9/2, 9/2\rangle$ for K) in preparation for loading into the quadrupole magnetic trap. During this stage, all shim coils are switched off, and the OP coil pair is switched on to produce a 1.8 G magnetic field along the propagation directions of the OP beams (see Fig. 2.7). For Rb OP, $\sigma+$ polarized lights resonantly target the $|F = 2\rangle \rightarrow |F' = 3\rangle$ ("Zeeman") and $|F = 1\rangle \rightarrow |F' = 2\rangle$ ("repump") transitions, respectively. For K, the corresponding transitions are $|F = 9/2\rangle \rightarrow |F' = 11/2\rangle$ and $|F = 7/2\rangle \rightarrow |F' = 9/2\rangle$, respectively.

As the final step inside the MOT chamber, the optically pumped atoms are loaded into a quadrupole magnetic trap produced by the transfer coil, and transferred out of the MOT cell. During the transfer, significant background gas load present inside the MOT chamber, including the differential pumping tube, causes the loss of trapped atoms. This was particularly significant in the earlier stages of the experiment, when the vapor pressure inside the MOT chamber was quite high. By measuring the round trip transfer efficiency as a function of transfer distance, we found that 60% of the atoms are lost before even reaching the tip of the transfer tube, and 90% is lost by the time the atoms clear the tube (no additional losses are measured for the rest

of the trip). To ameliorate this issue, we reduced the background pressure inside the chamber by first heating up the MOT cell to 70 - 80 °C for several days in an attempt to drive out some of the alkali atoms absorbed onto chamber walls, and then reduced the cell temperature to 35 - 40°C. Doing so resulted in the increase of the MOT loading $1/e$ time constant from 150 ms to 1.5 s (indicating a similar factor of reduction in the chamber pressure), and improved the overall transfer efficiency to 24%.

The reduced chamber pressure allowed us to further improve the MOT atom number by incorporating light-induced atom desorption (LIAD) into the MOT loading[12]. In this scheme, a portion of the MOT cell is exposed to UV light* with a wavelength of 365 nm during the MOT loading (1.5 s). This results in the desorption of K and Rb atoms, and a transient increase of the chamber pressure, resulting in a factor of 3 more atoms loaded into the MOTs. We then hold the MOT for 5.0 s while the chamber pressure decreases back to a level before the UV exposure to reduce loss during the magnetic transfer. While the MOT diminishes in number during this time, an overall gain of a factor 1.5 is seen in the final transferred atom number.

After arriving at the center of the evaporation chamber (2.2.3), the atoms are handed over from the quadrupole field of the transfer coil to that of the QUIC coil, by ramping down the transfer coil current to zero while ramping up the QUIC quadrupole coil (2.4.2) current to 20 A.

3.3 RF evaporation

Once in the evaporation chamber, RF-induced evaporative cooling[102] is applied to the Rb atoms to further reduce the sample's temperature, while the K atoms are sympathetically-cooled via collisions with Rb. The RF signal, generated by a DDS channel of the computer control, is amplified (Mini Circuits, LZY-22+) and coupled to the atoms via the Ioffe coil (section 2.4.2).

---

*400 mW optical power, produced by a Thorlabs M365L2 UV LED.

The RF drives "hot" Rb atoms at the outer edge of the trap from their initial low-field-seeking $|F, m_F\rangle = |2, 2\rangle$ sate to the high-field-seeking $|2, -1\rangle$ and $|2, -2\rangle$ states via cascaded m_F transitions, after which they are ejected from the trap. While the atoms are confined in the quadrupole trap, we sweep the RF frequency from 30 MHz to 15 MHz over the course of 7 s. This frequency range corresponds to an atom temperature change from 300 to 150 μK. At this point, we ramp on the Ioffe coil to 20 A to form a QUIC trap, and perform the rest of the evaporation by sweeping the RF from 15 MHz to around 2 MHz over 17 s. As the cloud temperature lowers we gradually reduce the RF power, from 2 W at 30 MHz to 100 mW at 2 MHz, in order to avoid power-broadening the spin-flip transition, which will result in less sharply-defined cloud temperature. The trajectories of the RF frequency and power during the evaporation are shown in Fig. 3.10.

During evaporation, the temperature lowers as a function of the number of atoms according to

$$T = AN^{\gamma}, \tag{3.8}$$

where A is a proportionality constant, and γ is the evaporation efficiency parameter that is commonly used in experiments to characterize the performance of evaporation[83]. In a harmonic trap, runaway evaporation, in which the rate of thermalizing elastic collisions increases rapidly as the temperature decreases, occurs for $\gamma \geq 1$. To evaluate the evaporation performance inside the QUIC trap, we first measured, in the absence of K atoms, the number (N_{Rb}) and temperature (T) of Rb atoms at various points during evaporation, as shown in Fig. 3.8. In Fig. 3.8(c), T is plotted versus N_{Rb}, and the data is fitted using Eq. 3.8. Two separate fits are applied to points with T greater or smaller than 50 μK, and we obtain $\gamma = 0.91$ and $\gamma = 1.37$, respectively. As is common with evaporation in magnetic traps, the evaporation efficiency improves as the phase space density (PSD) of the cloud increases.
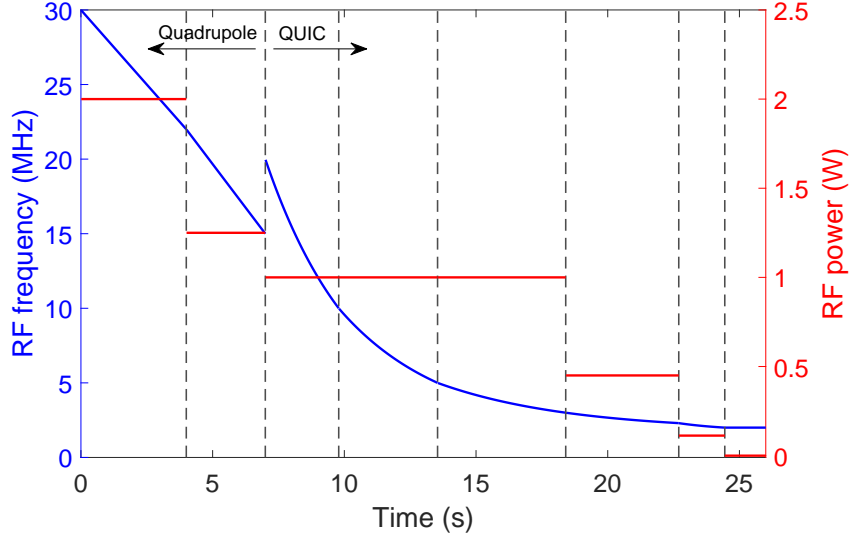
Figure 3.7: RF evaporation trajectory. The evaporation is divded into several stages, marked by gray dashed lines. The first two stages occur while the magnetic trap operates in the quadrupole configuration (Fig. 2.26). The frequency of the RF signal (blue curve) decrease via two linear ramps over the course of 7 s, from 30 to 15 MHz. The rest of the evaporation, consisting of 5 stages, are carried out after the trap is transformed into the QUIC configuration. The frequency follows an exponential decay over each stage, and the time constants for the 5 stages are 3.5, 4, 5, 5, and 2 s. Overall, the frequency decreases from 20 to $\sim$ 2 MHz over 17 s. Different final atom temperature can be obtained by tuning the final cutoff frequency. During the evaporation, the RF power is gradually reduced to prevent power-broadening the spin-flip transition, which will result in less sharply-defined cloud temperature.

When K atoms are included in the evaporation, they thermalize through collisions with the Rb atoms, and therefore act as a heat load. This results in a factor of 2 reduction in the number of Rb atoms at the end of the evaporation, compared to the case where K atoms are absent. Since the evaporation is performed on Rb atoms only, the number of K atoms inside the trap essentially remains constant throughout the process. In a typical experimental sequence, we end the RF signal at 2.1 MHz, at which point we obtain 5.0×10^6 Rb atoms and 2.4×10^6 K atoms at a temperature 3.5 μK. The exact atom number and temperature of the sample can be tuned, albeit in an anti-correlated fashion, by changing the final RF cutoff. Given the heating that will be experienced by the atoms during the optical transfer step (section 3.4), we found that the above

112
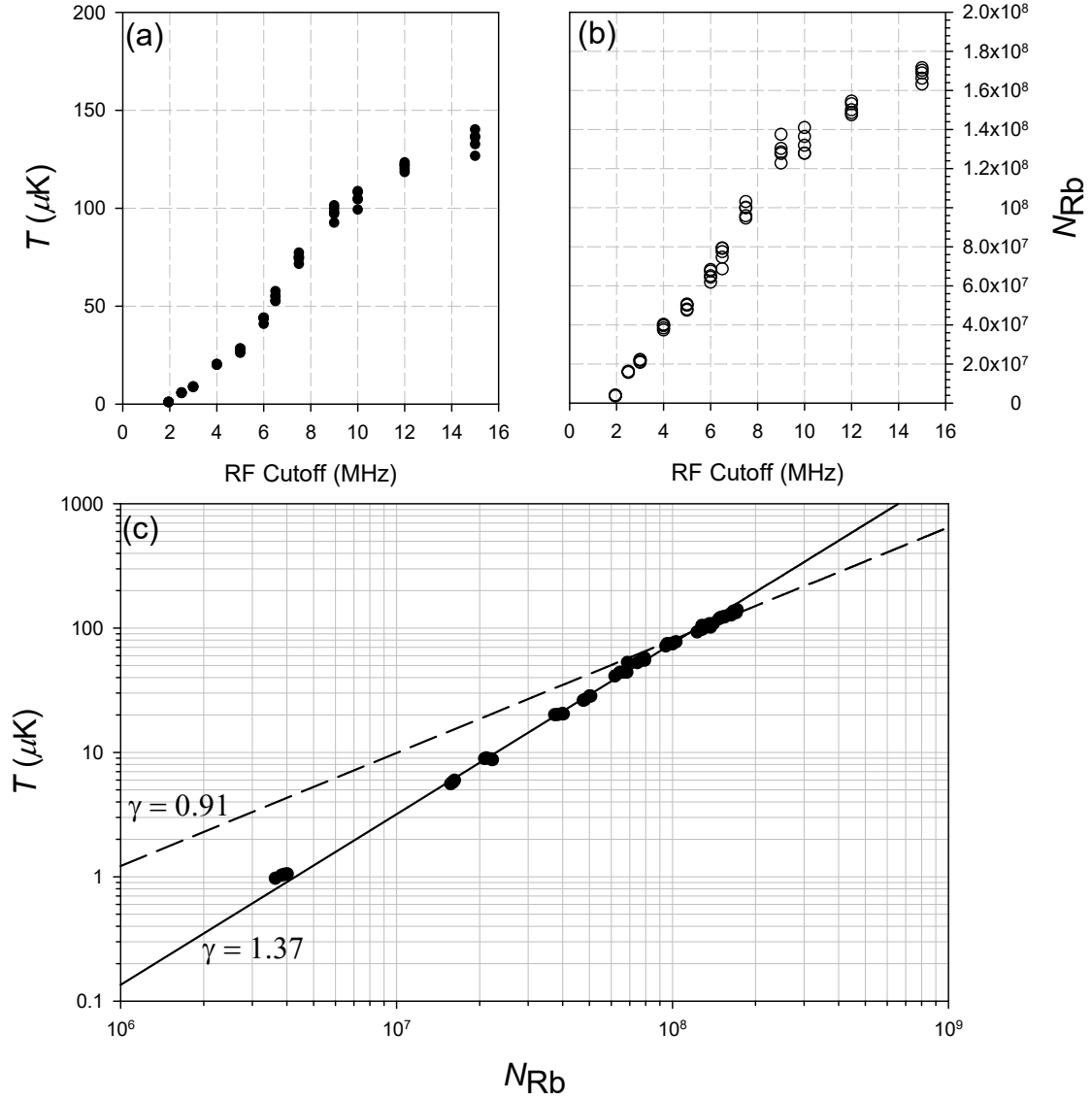
Figure 3.8: RF evaporation of Rb atoms in QUIC trap. (a,b) Temperature (T) and number (N) of the atoms as functions of the RF cutoff frequency at various points of the evaporation. (c) T vs. N during the evaporation, shown on a log-log scale. The dashed and solid lines represent fits to the data points at $N > 10^8$ and $N < 10^8$, respectively, using Eq. 3.8. We observe an increase in the evaporation efficiency parameter, γ, as the temperature of the cloud is lowered, indicating good evaporation performance.

atom condition leads to the highest molecule yield.

Heating effects can interfere with the efficiency of the evaporation and limit the atom number and temperature at the end. Low heating rates, on the order of a few to a few tens of nanokelvins per second, are routinely achieved in magnetic traps, so long as their mechanical and current stabilities are good. In the early days of operating the QUIC trap, we measured a heating rate of ~ 40 nK/s for atoms evaporated down to a few microkelvins. Some time after early 2018, however, we noticed the heating rate has increased to ~ 250 nK/s. This essentially prevents us from evaporating below 2μK, which we were previous able to do. The origin of this anomalous heating remains unclear, but we rule out current and mechanical stabilities as factors. While the heating does not significantly impact our current operation given the target temperature of 3.5 μK, future studies that aim at colder atoms will require the heating source to be identified and eliminated.

3.4 Optical transport

After RF evaporation, the atoms are loaded into the transfer optical-dipole trap (TODT, 2.3.2) by ramping down the QUIC coil currents while ramping up the TODT power to 2.4 W*, over a duration of 500 ms. At this power, the trap frequencies for the TODT are measured via parametric heating to be $\{\omega_x, \omega_y, \omega_z\} = 2\pi \times \{11.8, 965, 1790\}$ Hz for Rb atoms. Due to adiabatic compression resulting from the increased confinement as well as heating, the temperature of the atoms increase to 18 μK†. We transfer $\sim 60\%$ of the atoms from the QUIC trap, resulting in 4.0×10^6 Rb atoms and 1.4×10^6 inside the TODT. A factor of 3.5 in PSD is lost as a result

---

*All ODT powers quoted in this chapter are measured right before the viewport via which they enter enter the Science chamber, and should therefore represent the power as seen by the atoms/molecules.

†If the transformation is purely adiabatic, then based on the change in trap frequencies going from the QUIC trap to the TODT, we should expect a cloud temperature increase to 13 μK.

of this transfer process (Table 3.1), coming from both the lost of atom number and temperature increased beyond that accounted for by adiabatic compression. The reason for this loss is yet to be identified, but we found that prolonging the transfer ramp, in an effort to make the change more adiabatic, turns out to be counter-productive.

To maintain the magnetic spin of the atoms during the optical transport, we installed the quantization coil (Fig. 2.2), situated between the Science and evaporation chambers, to produce a magnetic field along the transport axis. In practice, however, we found that such field does not improve the transfer efficiency, likely indicating that the spins are maintained by background fields. In fact, any amount of quantization field applied leads to strictly worse transfer efficiency and higher heating, possibly due to the high spatial inhomogeneity of this field.

The atoms are then trasported, over the course of 1 s, from the evaporation chamber to the center of the science chamber, which are separated by a distance of 322 mm. The transport uses s-curve velocity profiles for acceleration and deceleration in order to minimize the jerks exerted on the atoms. At the end of the trasport, we retain 3.1×10^6 Rb atoms and 1.4×10^6 K atoms inside the TODT at a temperature of 30 μK. The increased atom temperature is due both to heating experienced by the atoms during the trasport, and a slight change in the TODT beam

Table 3.1: Conditions of the atoms at various steps after the RF evaporation. PSD: phase-space density

Stage	T (μK)	N_{Rb}	PSD (Rb)	N_{K}	PSD (K)
QUIC trap (15 MHz)	140	1.6×10^8	4.7×10^{-5}	−	−
QUIC trap (2.1 MHz)	3.5	5.0×10^6	8.4×10^{-2}	2.4×10^6	1.2×10^{-1}
TODT pre-transport	18	4.0×10^6	2.4×10^{-2}	1.4×10^6	2.7×10^{-2}
TODT post-transport	30	3.1×10^6	6.6×10^{-3}	1.4×10^6	9.6×10^{-3}
HODT	13	3.0×10^6	1.9×10^{-2}	1.4×10^6	2.9×10^{-2}
XODT post-evaporation ($P_{\mathrm{VODT}} = 790$ mW)	0.5	7.0×10^4	$\mathcal{O}(1)$	5.0×10^4	$\mathcal{O}(1)$
XODT post-evaporation ($P_{\mathrm{VODT}} = 386$ mW)	0.5	1.6×10^5	$\mathcal{O}(1)$	1.7×10^4	$\mathcal{O}(1)$

shape during the trip which increases the confinement to the atoms*. At the science chamber, the TODT trap frequencies increase to $2\pi \times \{14.4, 1120, 2055\}$ Hz, corresponding to a factor of 1.63 decrease of the trap volume compared to when the TODT is in the evaporation chamber. Over the optical transport, we lose another factor of 3.5 in the PSD of the atoms.

Heating during the transport has plagued our experiment for more than half a year. Before arriving at the current, optimized transport efficiency, many solutions were attempted,including several different transfer optics designs. These often improve upon over certain aspects of the transport while worsen others, and the transfer efficiency stayed at $\sim 5-20\%$. Amount the many attempts, we found that the following lead to definite improvements over the transfer efficiency.

- In previous TODT designs, the translation of the beam focus is accomplishing using a pair of mirrors mounted on the ABL carriage. We believe the kinetic mounts in which the mirrors are mounted caused excessive shaking of the beam during the transport, resulting in heating of the atoms. Later designs in which these mirrors are replaced by a single lens on the carriage lead to significant improvements in the transfer efficiency.

- The ABL stage floats the carriage on a thin layer of N_2 gas, and the portion of the TODT beampath directly over the ABL can be exposed to the gas flow, causing fluctuations in the beam pointing. To eliminate this source of heating, we shielded the beampath using a thin, flexible tarp that covers up the upper surface of the ABL, leaving only a slit for the lens to move through.

While the exact source(s) of heating in the current TODT configuration is yet to be pinpointed, we are tempted to attribute it generally to the trap shaking caused by the motion of the ABL during transport. To this end, focus-tunable lenses[128] are an attractive alternative to the ABL

---

*The increase in temperature due to compression is just 3 μK.

and is considered in future upgrades. With no mechanical moving parts, it offering a potentially smoother ride for the atoms, and many groups have reported positive experiences with them.

From the end of RF evaporation to the atoms arriving at the science chamber, a factor of 11 is lost in the PSD of both species. While the current atoms condition is acceptable for studies of ultracold chemistry, future experiments aimed at quantum degenerate molecules[155] must identify and eliminate sources of loss. On the other hand, we note that optical transport was an issue that also plagued the JILA Gen II KRb experiment. Their solution was to get rid of this step all together, and magnetically transfer (3.2) the atoms straight to their final destination. This is one of the critical improvements in the atom condition that resulted in the first quantum-degenerate dipolar molecular gas[60]. While the geometry of our chamber (Fig. 2.2) prevents us from eliminating the optical transport step, it is possible to build another, smaller science chamber inline with the magnetic transfer direction, enabling a one-step transfer.

3.5 Atom state preparation

After arriving at the Science chamber, the atoms are handed over from the TODT to the HODT by simultaenously ramping their intensities over 250 ms. With a power of 2 W, the HODT has measured trap frequencies of $2\pi \times \{8.5, 970, 970\}$ Hz. This transfer is nearly 100% efficient, and we end up with 3.0×10^6 Rb atoms and 1.4×10^6 K atoms at 13 μK. At this point, the goal is to prepare the atoms in the appropriate magnetic hyperfine states, *i.e.* science states, for which there is an interspecies Feshbach resonance favorable for molecule association[226]. For ^{87}Rb and ^{40}K, the science states are $|F, m_F\rangle = |1, 1\rangle$ and $|9/2, -9/2\rangle$, respectively. The hyperfine levels relevant for the transfer are shown in Fig. 3.9. The inset of the figure shows the hardware involved. A pair of coils is switched on to produce a 25.8 G field along the $-y$ direction to maintain spin quantization during the state transfer. Note that the degeneracy between m_F
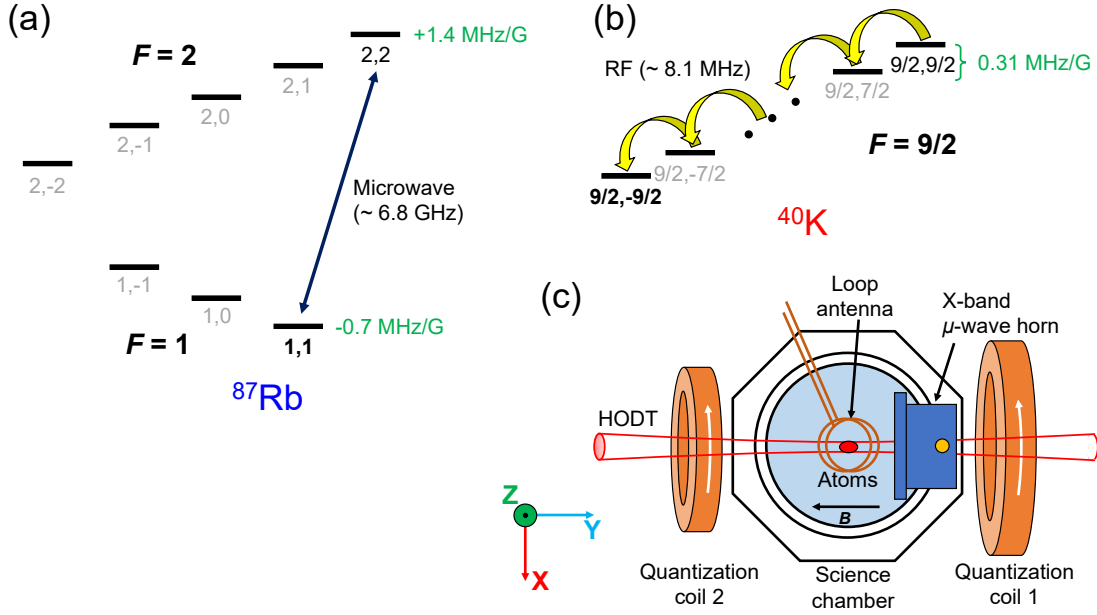
Figure 3.9: Atom state transfer. (a) ^{87}Rb atoms originally in the state $|F, m_F\rangle = |2, 2\rangle$ are transferred to $|1, 1\rangle$ – the science state – via a microwave ARP at around 6.8 GHz (dark blue arrow). (b) ^{40}K atoms in the state $(|9/2, 9/2\rangle)$ are transferred to the science state $|9/2, -9/2\rangle$ via a cascaded RF ARP at around 8.1 MHz. (c) Hardware around the science chamber used for the atom state transfer, including a loop antenna for driving the K RF ARP, an X-band microwave horn for driving the Rb ARP, and a pair of magnetic coils to provide a quantization field during the transfer. The atoms are confined inside the HODT during these processes. White arrows indicate the direction of current flow through the coils when they are energized.

levels within each F manifold is lifted in Fig. 3.9 due to the presence of this field.

State-transfer for both species are performed via adiabatic rapid passage (ARP), driven by oscillating magnetic fields. The basic idea of this scheme is to first initiate a driving field with frequency ω_D that is detuned from the resonant frequency of the transition between target states ν_0, and then sweep the drive frequency by Δ_{dev} across ν_0 to the other side of the resonance. This creates a dressed, superposition of the pair of target states which fully resembles the initial state at the beginning of the sweep and the final state at the end, resulting in a coherent transfer of the population.

For ^{87}Rb, the initial $(|2, 2\rangle)$ and final $(|1, 1\rangle)$ hyperfine states of the transfer are separated, in

the presence of the 25.8 G quantization field, by a frequency of $\nu_0 = [E(|2,2\rangle) - E(|1,1\rangle)]/h = 6.889$ GHz. We generate the microwave around this frequency by mixing a tunable-frequency DDS channel from the computer control with a fixed-frequency local oscillator at 7.067 GHz. The difference frequency signal is then amplified and sent via an X-band microwave horn to the atoms (see Fig. 3.9(c)). During the state transfer, we switch the microwave on to several Watts, and sweep its frequency by 2 MHz across ν_0 at a rate of 0.5 MHz/ms. After the transfer, we push any ^{87}Rb atoms that remained in the $F = 2$ manifold out of the ODT by shining light resonant with the $|F = 2\rangle \rightarrow |F = 3\rangle$ transitions at the atoms for 5 ms.

For ^{40}K, the initial ($|9/2, 9/2\rangle$) and final ($|9/2, -9/2\rangle$) states sit at the two ends of the $F = 9/2$ manifold, and direct transition between them via magnetic-dipole transition is forbidden by the $\Delta m_F = 0, \pm 1$ selection rule. However, note that going from the initial to the final state, the splitting between adjacent sates, in the presence of the 25.8 G field, decreases monotonically from 8.46 to 7.65 MHz. Taking advantage of this trend, we perform the state transfer using a cascaded ARP driven by an RF signal centered around 8.1 MHz as illustrated in Fig. 3.9. The RF signal is derived from a computer control DDS channel and amplified to 2 W. The signal is coupled to the atoms via a two-turn loop antenna situated directly above the atoms right outside of the top viewport of the science chamber. During the experiment, we sweep the RF frequency from 9.5 to 6.7 MHz, and transfer the atoms via the sequence $|9/2, 9/2\rangle \rightarrow |9/2, 7/2\rangle \rightarrow ... \rightarrow |9/2, -7/2\rangle \rightarrow |9/2, -9/2\rangle$, at a rate of 0.4 MHz/ms. The clean-up of non-science-state K atoms is performed after ground-state molecule formation (3.8).

The efficiency of the state transfer is 100% in terms of the atom number to within our detection accuracy. However, we do observe a $\sim$2.5 μK heating, and attribute it to a trap slosh induced by the magnetic field gradient produced by the quantization coil pair*.

---

*Due to geometric constraints, the two quantization coils cannot be made identical to cancel gradients at the atom location inside the Science chamber.

3.6   ODT evaporation

As a final step before the atom are associated into molecules, we further increased their PSD by forced evaporation inside the optical dipole trap. This can be performed by lowering the HODT power, and correspondingly its trap depth, over the course of a few seconds, until the desired temperature or PSD is reached. As we discussed in 3.3, frequent re-thermalizing collisions between atoms are required for good evaporation. In this regard, one draw back of evaporating inside an ODT compared to a magnetic trap is that as the trap depth of the ODT is lowered, so does its confinement. This effect, combined with the naturally low axial trapping frequency of an ODT, leads to a less efficient evaporation. To improve confinement during evaporation, we add a second beam (VODT) to the HODT beam to form a crossed ODT (XODT), as shown in Fig. 2.13. This leads to a significant increase of the ODT's axial trapping frequency, from 8.5 Hz to 60 Hz.

We found another improvement to the ODT evaporation by performing it in a magnetic field near the Fesbach resonance. Evaporating in the presence of a 550 G field, which is 3.3 G above the resonance, we found a factor of 1.5 gain in the final Rb atom number compared to if the evaporation occurs far away from the resonance, e.g. at 30 G. We attribute the improved efficiency to the increase in the negative K-Rb scattering length, from its background value of $-185a_0$ to around $-400a_0$ at 550 G. This leads to an increase in the cross section, and therefore rate, of inter-species elastic collisions. We note that the choice of evaporating at high field was made when only the HODT was in use. With the addition of the VODT, the density of the gas is increased, and enhanced three-body losses near a Feshbach resonance can be come significant at lower temperatures. The optimum magnetic field for evaporating inside the XODT should be investigated in the future.

Here, we present the evaporation scheme used in the majority of the experiments described in

this thesis. After transferring the atoms into their science states, we ramp down the quantization magnetic field to zero while ramping up the current in the Fesbach coil to produce a 30 G field. we switch on the VODT to a power of 790 mW, and perform evaporation by lowering the power of the HODT only from 2 W to 104 mW over the course of 4.5 s, following a two-stage exponential trajectory as shown in Fig. 3.10. At the end of the evaporation, we are left with 7×10^4 Rb and 5×10^4 K atoms inside the XODT at a temperature of 500 nK. When the experiment operates normally, the atom numbers fluctuate on a day-to-day basis by up to $\pm 20\%$, and typically in an anti-correlated fashion – if we gain 10% in K, we loose about 10% in Rb, and vice versa. This can be traced to K number fluctuations at the MOT stage, which creates either more or less thermal load on the Rb atoms during RF evaporation. If atoms numbers drift significantly out of the typical range, a small tweak in either the K MOT beam power or the cutoff frequency for RF evaporation will usually restore the balance. We found the final molecule number to be insensitive to fluctuations within 20%. Using parametric heating, we measure the trap frequencies at this stage to be $2\pi \times \{60, 265, 265\}$ Hz for Rb atoms.

In late Febuary of 2020, we accidentally found that the atom number can be improved by lowering the power of the VODT during evaporation. For example, using a VODT power of 386 mW instead of 790 mW, we obtain 1.6×10^5 Rb and 1.7×10^5 K inside the XODT at the same temperature (500 nK), gaining a factor of $2 - 3$ in atom number, and a factor of 2 in the final KRb number. This resulted in a welcoming boost to our data collection rate. In fact, there is a monotonic trend in the final molecule number as the VODT power is lowered, which is possibly attributed to the aforementioned enhanced three-body loss. Too low of a VODT power, on the other hand, results in a significant elogation of the molecular cloud along the axial direction, which becomes detrimental for velocity-map imaging (section 4.4) and makes it difficult to keep the KRb atoms from exposure to the ionization beam (see Fig. 2.33(c)). To this end, we found 386 mW to be a reasonable compromise.
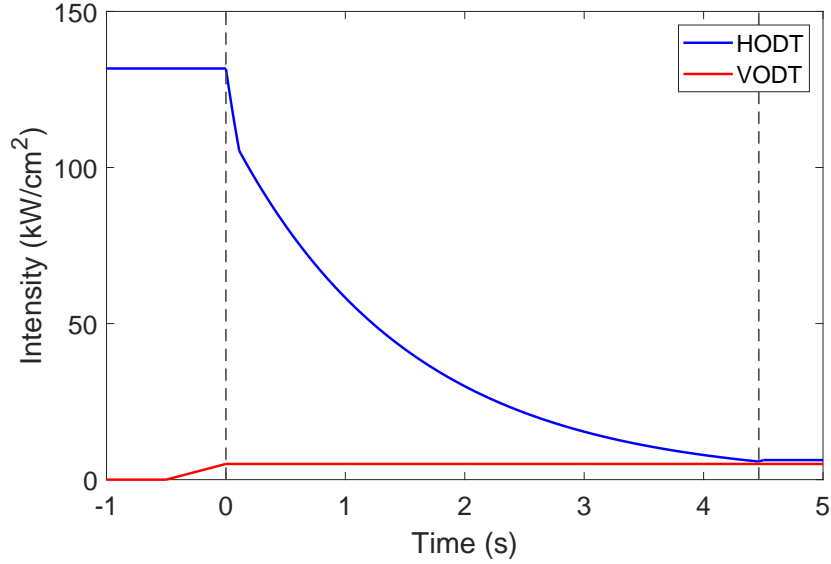
Figure 3.10: The ODT evaporation trajectory. The VODT (red curve) is ramped on over a duration of 500 ms prior to the start of the evaporation, to an intensity of 5.03 kW/cm^2 at the atom cloud location. During the evaporation, the HODT (blue curve) intensity is lowered in two stages following standard exponential trajectories to 5.77 kW/cm^2, over the course of 4.5 s. The beginning and the end of the evaporation are marked by gray dashed lines. The VODT intensity is kept constant during this period. Finally, the HODT is ramped back slightly to 6.27 kW/cm^2, forming, together with the VODT, the XODT configuration.

3.7 Magneto-association

Once the desired PSD is reached by the atoms, the goal is to assemble them into ground-state (GS) KRb molecules. To this end, we employ the fully-coherent scheme discussed in the introduction (section 1.2), in which pairs of free Rb and K atoms are first magneto-associated into weakly-bond Feshbach (FB) molecules, then transferred into the rovibronic ground state via STIRAP (2.3.3).

Magneto-association is performed by ramping the magnetic field from 550 G to 544.1 G across the inter-species Feshbach resonance at $B_0 = 546.7$ G at a rate of 4 G/ms (Fig. 3.11). This adiabatically transforms the quantum state of the atom pair from an "open" channel via
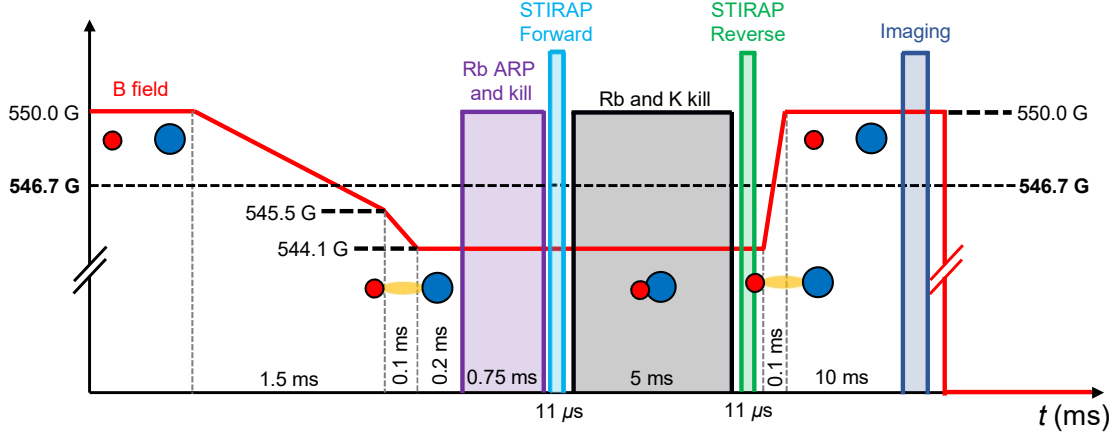
Figure 3.11: The coherent association and dissociation of ground state KRb molecules. During the association process, free K and Rb atom pairs are first formed into weakly-bound Feshbach (FB) molecules by ramping the B field (red curve) across an interspecies Feshbach resonance at 546.7 G. At this point, most of the Rb atoms that failed to bound with a K are pushed out of the ODT. The FB molecules are then transferred to the ground state (GS) via STIRAP (Fig. 3.12), and all the unpaired K and Rb atoms are removed from the ODT. To characterize the GS molecules, the STIRAP and B field ramps are reversed to coherently dissociate GS KRb back into free atoms, which can be efficiently imaged and serve as proxies for the molecules.

which they freely collide to a "closed" channel in which they bind. In our case, the open channel is the Rb $|1, 1\rangle$ + K $|9/2, -9/2\rangle$ hyperfine state, whereas the closed channel is the Rb $|1, 0\rangle$ + K $|7/2, -7/2\rangle$ hyperfine state of the second least-bound ($v = -2$) vibrational level in the $a^3\Sigma^+$ potential. At 544.1 G, the state of the FB molecule is predominately ($\sim 90\%$) closed channel in character, with a binding energy of ~ 4 MHz, and a size of ~ 50 a_0[226]. For initial Rb and K atom numbers of 7.0×10^4 and 5.0×10^4 (see Tab. 3.1), we estimate that 6×10^3 Feshbach molecules are formed by the magneto-association, corresponding to an atom-to-molecule conversion efficiency of $\sim 10\%$.

The lifetime of the Feshbach molecule is limited by its collisions with the unpaired atoms inside the trap, especially with Rb since the Rb - FB collision is fully allowed by Bose statistics*.

---

*Such collisions cause vibrational relaxation of the FM, resulting in a release of the vibrational energy as translational energy that ejects both the FM and the atom out of the trap[226].

To this end, we remove Rb atoms shortly after the magneto-association by first driving them from the $|1, 1\rangle$ state back to the $|2, 2\rangle$ state via microwave ARP, and then pushing them out of the trap by exposing them to light resonant with the quasi-cycling $|2, 2\rangle \rightarrow |3, 3\rangle$ transition. In the interest of minimizing the time between the formation of FM and its transfer to the GM which is more stable against collisions, we keep the duration of the ARP and push-out to be a relatively short 0.75 ms. This results in an incomplete removal, with $\sim 15\%$ of the unpaired Rb atoms remaining in the trap after the push-out. Nevertheless, the collision load on the FM is significantly reduced, and a further removal of Rb is reserved for after the formation of GM.

3.8 Raman transfer (STIRAP)

The next and final step in our reactant preparation is to transfer the molecular population from the FB molecule state $|i\rangle$, into the rovibronic ground-state $|g\rangle = |X^1\Sigma^+, v = 0, N = 0\rangle$ via STIRAP, with an electronically excited state $|e\rangle$ acting as an intermediate (see Fig. 3.12 (a)). While many excited rovibronic states can potentially serve as the intermediate state for the transfer, previous work on KRb has identified the $|2^3\Sigma^+, v' = 23\rangle$ state is identified to be particularly favorable due to its good wavefunction overlap with both $|i\rangle$ and $|g\rangle$, as well as its mixed singlet-triplet electronic character[153].

Besides rovibronic states, the STIRAP transfer also target specific hyperfine states of the molecule. The hyperfine structure of GS KRb is discussed in more detail in Appendix K. Since the electrons of the GS KRb is in a singlet configuration, the hyperfine structure of the molecule is determined by the spin-spin coupling between the K and Rb nuclei ($\vec{I}_\text{K} \cdot \vec{I}_\text{Rb}$), as well as their individual Zeeman couplings to an external magnetic field ($\vec{I}_\text{K} \cdot \vec{B}$, $\vec{I}_\text{Rb} \cdot \vec{B}$). In the high field limit ($B \gtrsim 20$ G), where the latter dominates over the former, the nuclear spin projections m_I^K and m_I^Rb are good quantum numbers, and the hyperfine eigenstates can be labeled as $|m_I^\text{K}, m_I^\text{Rb}\rangle$.

For all studies carried out in this thesis, we prepare GMs in the $|m_I^K, m_I^{Rb}\rangle = |-4, 1/2\rangle$ state. The hyperfine state purity is ensured by targeting, in the upleg ($|i\rangle \to |e\rangle$) transition, a particular (unassigned) hyperfine state of $|e\rangle$, which is only coupled, in the downleg ($|e\rangle \to |g\rangle$) transition, to the $|-4, 1/2\rangle$ state.

The frequencies, transition dipole moments, and polarizations for the STIRAP transitions are summarized in Table 3.2. In Ref. [154] the absolute frequency for these transitions are measured to megahertz percision by comparing and locking the frequencies of STIRAP lasers to a frequency comb. In our experiment, the frequency of all lasers are measured by a wavemeter (Bristol 771A), which has a systematic uncertainty of ~ 100 MHz. Therefore some spectroscopy work was required to put our STIRAP lasers on resonance with the molecules. To search for the upleg transition, we scan the 970 nm laser frequency and look for depletion of the Feshbach molecule signal. Once it is found, we park the 970 nm laser on resonance, and scan the 690 nm laser frequency to look for the downleg transition. A so-called "dark resonance" condition is satisfied when both lasers are resonant, at which point the upleg transition is suppressed, resulting in reduced depletion of the Feshbach molecules. For details on depletion spectroscopy as well as dark resonance spectroscopy in KRb, we refer the reader to Ref. [156].

Coherent transfer of the molecular population is carried out by ramping the intensities of the STIRAP lasers according to the "forward" part of the timing diagram in Fig. 3.12(d). The 690 nm laser is switched on first, and as its intensity is linearly ramped down, the 970 nm laser

Table 3.2: STIRAP transition parameters. Here, $|f\rangle = |a^3\Sigma^+, v = -2\rangle|F^{Rb} = 1, m_F^{Rb} = 0; F^K = 7/2, m_F^K = -7/2\rangle$, $|i\rangle = |2^3\Sigma^+, v' = 23\rangle$, and $|g\rangle = |X^1\Sigma^+, v = 0, N = 0\rangle$.

Transition	Frequency (GHz)*	Polarization*	Transition dipole (ea_0)*	Rabi rate (MHz)†
$|f\rangle \to |i\rangle$	309602.752	σ^+	0.005(2)	4.27
$|i\rangle \to |g\rangle$	434922.454	-	0.012(3)	5.53

* From Ref. [153];
† Extrated from the fitted spectral widths of the FB molecule depletion spectrum as well as the dark resoance spectrum. For details on this method see Ref. [156].
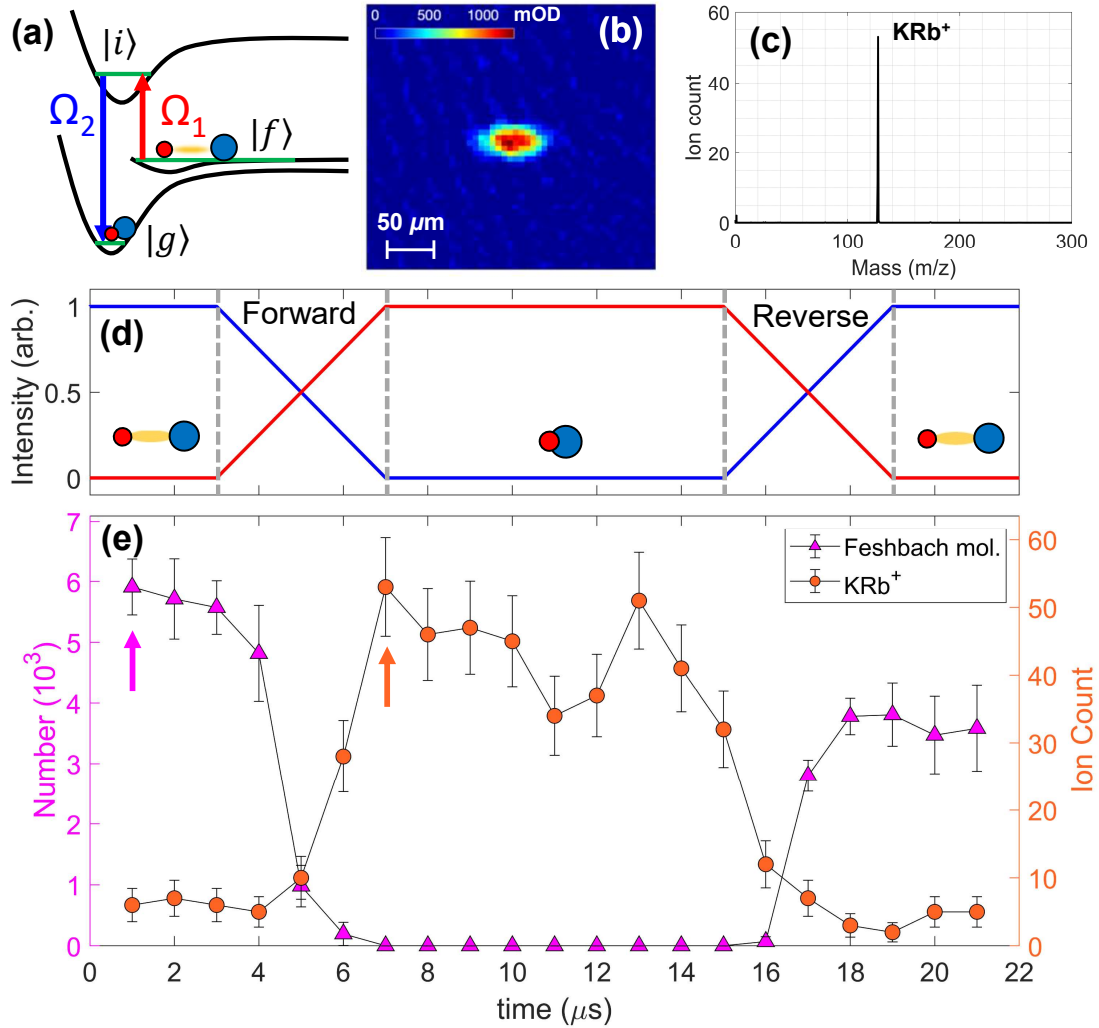
Figure 3.12: **Ground state molecule creation via STIRAP.** (a) Schematic diagram of STIRAP in KRb, showing how the 970 nm (red) and 690 nm (blue) lasers connect the $|f\rangle$, $|i\rangle$ and $|g\rangle$ molecular states. the Rabi rates for the $|f\rangle \rightarrow |i\rangle$ and $|i\rangle \rightarrow |g\rangle$ transitions are $\Omega_1 = 4.3$MHz and $\Omega_1 = 5.5$MHz, respectively. (b) An absorption image of ~ 6000 GS KRb molecules taken after the reverse STIRAP. The colorscale is in units of mOD (milli-optical-depth). (c) TOF mass spectrum showing the KRb$^+$ peak at $m/z = 127$. (d) The timing diagram of the (normalized) intensities of the 970 nm (red) and 690 nm (blue) lasers during a forward plus reverse STIRAP sequence. (e) The number of Feshbach molecules (magenta triangles) and KRb$^+$ ions (orange circles) at various times during the sequence in (d), showing the conversion of Feshbach molecules into ground state molecules and back. The data point indicated by the magenta (orange) arrow corresponds to the absorption image (mass spectrum) in (b)((c)).

126

intensity is linearly ramped up. During this process, the molecule exists in a dark state that evolves according to [207]

$$|\psi_{\text{KRb}}(t)\rangle = \cos\theta(t)|f\rangle - \sin\theta(t)|g\rangle, \tag{3.9}$$

with

$$\tan\theta(t) = \Omega_1(t)/\Omega_2(t), \tag{3.10}$$

where Ω_1 and Ω_2 are the Rabi frequencies for the up and downleg transitions, respectively. Therefore, by the end of the ramp, the molecules are transferred into the ground state. The trap frequencies of the KRb molecules inside the XODT are $2\pi \times \{68, 300, 300\}$ Hz, estimated based on the measured trap frequencies for Rb and the known AC polarizabilities of Rb and KRb at 1064 nm.

For the purpose of studying the KRb + KRb reaction, we clean out the remaining K and Rb atoms in the trap in 5 ms (Fig. 3.11). For Rb, we simply repeat the push-out sequence described in 3.7, but now with a longer duration. To push out K, we shine in the imaging light for K in the $|F, m_F\rangle = |9/2, -9/2\rangle$ state, which is resonant with the quasi-cycling $|9/2, -9/2\rangle \rightarrow |11/2, -11/2\rangle$ transition. We note that the resonant light push-out method works effectively only for atoms in the photon-cycling states. Atoms in other hyperfine states, *e.g.* originating from imperfections in the state transfer, will likely survive the removal and remain in trap. Residual atoms is a common problem in bulk ultracold gas experiments but often escape detection because they are dark to optical imaging detection. In our experiment, the ion spectrometry capability allows us to ionize and detect atoms with high efficiency regardless of their quantum state. Using such a technique, we place an upper-bound of on the number of residual atoms after the push-out to be 200 for each species. This is a small fraction of our molecule number ($6 \sim 13 \times 10^3$), and therefore does not impact the reactions we study.

To characterize the number and temperature of the ground-state KRb sample, the STIRAP ramps and Feshbach ramps are reversed, and the resulting Rb atoms are imaged (Fig. 3.11 and Fig. 3.12(d)). An example absorption image of the back-converted Rb atoms is shown in Fig. 3.12(b), which corresponds to a sample of 6000 ground-state molecules at a temperature of 500 nK and a peak density of 10^{12}cm^{-3}. The reversibility of the STIRAP process is demonstrated in Fig. 3.12(e), which shows the number of Feshbach molecules at various times during the STIRAP ramp sequence in Fig. 3.12(d). Additionally, we can directly probe the ground-state molecules using ion spectrometry (see TOF mass spectrum in Fig. 3.12(c)). The evolution of the KRb$^+$ counts, which is proportional to the number of ground state molecules, shows a pattern complimentary to that obtained from imaging Feshbach molecules, as one would expect. We note that the measurement in Fig. 3.12(e) was made with a 80% one-way STIRAP efficiency, which we later optimized to 92% (see 2.3.3).

Chapter 4

Probing ultracold reactions: ion mass and kinetic energy spectrometry

As we have discussed in the introduction of this thesis (section 1.4), probing the short-range behaviors of chemical reactions require sensitive, multi-species detection. Towards this goal, we have integrated ionization and ion spectrometry capabilities into our setup. Such capabilities set our experiment apart from most ultracold chemistry experiments to date[162,156,61,220,95], which have relied on detecting the loss of reactants, via optical imaging (section 3.1), to investigate the long-range portion of the reaction PES (section 1.3.1). In this chapter, we describe the operation and characterization of the ionization and ion detection hardware described in section 2.5 to perform photoionization (section 4.1), ion time-of-flight mass spectrometry (section 4.3), and ion kinetic energy spectrometry (section 4.4). We will also discuss considerations for the ionization sampling of different species involved in the reactions (section 4.2), as well as effects of magnetic fields on ion spectrometry (section 4.5).
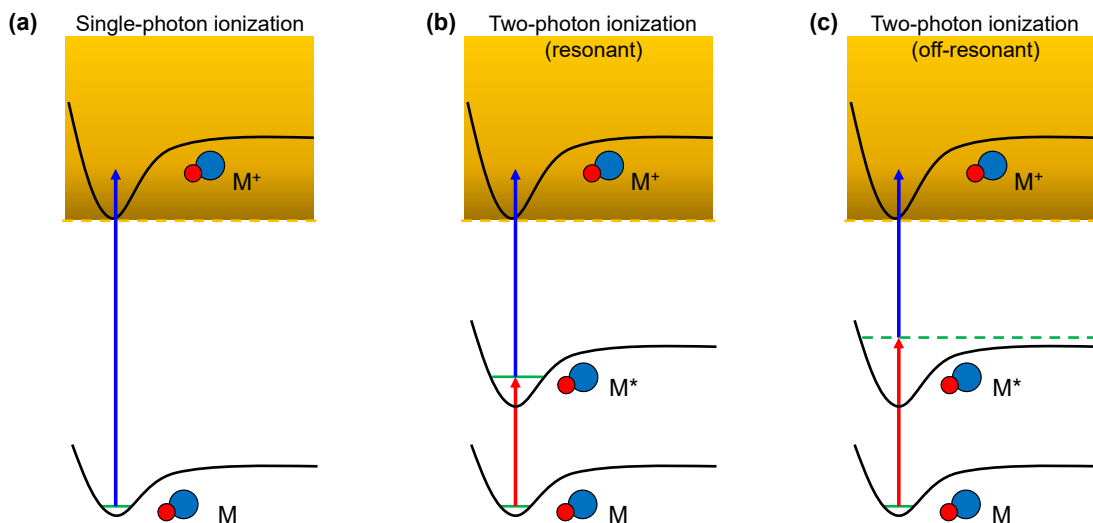
Figure 4.1: Various photoionization processes encountered in our experiments. Yellow shaded region in each sub-figure represents the ionization continuum. M, M^*, and M^+ represent neutral, excited, and singly ionized molecules, respectively. (a) Single-photon ionization. Here, a single photon, typically in the UV frequency range, converts M into M^+. (b) Resonance-enhanced two-photon ionization. Here, M is resonantly excited to M^*, followed by ionization via a second photon. (c) Off-resonant two-photon ionization. Here, M^* is a virtual state that contributes oscillator strength to a one-step, two-photon process. (d) Single-photon dissociative ionization. Here, the photon energy exceeds the sum of the ionization potential (IP) of M and the binding energy of M^+, resulting in dissociation into an ionic fragment M_1^+ and a neutral fragment M_2. Note that processes all three processes produce ions that are close in translational energy to their parent neutrals.

4.1 Photoionization

Photoionization is a process in which a valence electron of an atomic or molecular species (M) is ejected from the system by light, resulting in a positively-charged ion (M^+) and a negatively-charged free electron (e^-). The resulting M^+ largely retains the mass and kinetic energy of M, but is now amenable to electric field manipulation and ion detection. For many of the studies carried out in this thesis, we use single-photon ionization, as schematically illustrated in Fig. 4.1(a), to probe the various species involved in ultracold reactions in a quantum-state-independent manner. Such a transition is characterized by its ionization potential (IP), which is the difference

(a) Single-photon dissociative ionization

$M_1^+ + M_2$

M

(b) Two-photon ionization followed by dissociation

$M_1^+ + M_2$

M^+

M

(c) Two-photon dissociation followed by ionization

M_1^+

$M_1^* + M_2$

M
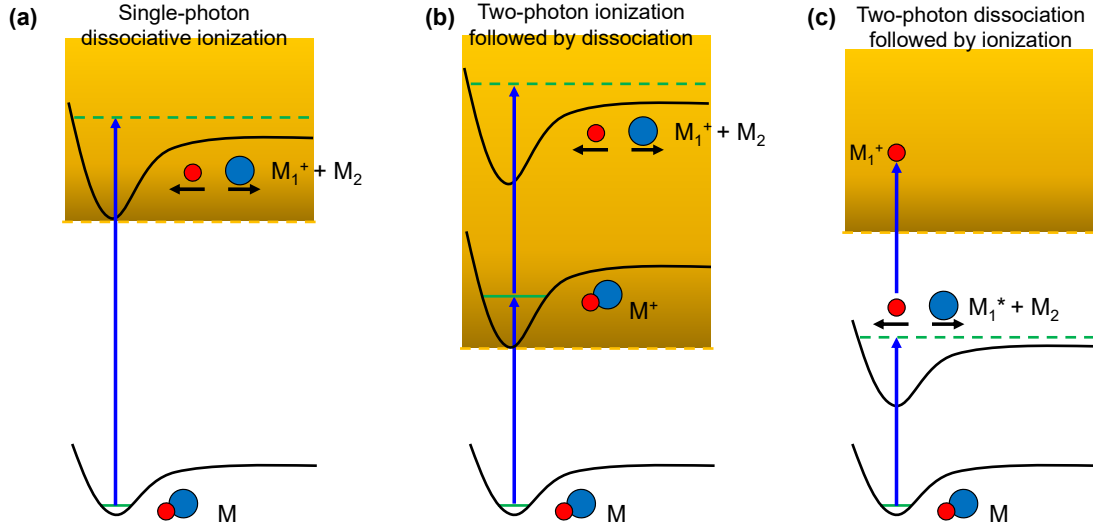
Figure 4.2: Various processes encountered in our experiments that involve both photonionization and photodissociation. (a) Two-photon ionization followed by dissociation. This is a two-step process in which a photon first ionizes M into M^+, and another photon of the same color photodissociates M^+ into M_1^+ and M_2. (b) Two-photon dissociation followed by ionization. This is a reversal of the previous process – M is first photodissociated into neutral fragments M_1 and M_2. At the range of photon energies used in our experiment, one of the fragment will be eletronically excited, while the other remains in the ground state. The excited fragment, M_1^*, is then ionized to produce M_1^+. These processes produce ions that carry significant translational energy from photodissociation, which can be detected using kinetic energy spectrometry (section 4.4).

between the ground-state energies of M and M^+, and its cross section ($\sigma(\lambda)$), which represents the likelihood for ionization and is a function of the photon wavelength (λ). For a light field with photon energy ($E_{\text{ph}} = h\nu = hc/\lambda$) exceeding IP, the rate of the induced photoionization transition is given by

$$W = \frac{I\sigma(\lambda)}{h\nu},\tag{4.1}$$

where I is the light intensity. In the case of pulsed ionization light, such as what is used in our setup (section 2.5.1), the more relevant quantity is the probability to ionize M with each pulse,

P_{ion}, related to W as

$$P_{\text{ion}} = 1 - \exp\left[-\int W(t)\mathrm{d}t\right] = 1 - \exp\left[-\frac{\sigma(\lambda)}{h\nu}\int I(t)\mathrm{d}t\right] = 1 - \exp\left[-\frac{F\sigma(\lambda)}{h\nu}\right], \quad (4.2)$$

where $F = \int I(t)\mathrm{d}t$ is the fluence of the laser sampled by M, and is also given by the pulse energy divided by the cross-sectional area of the beam. In the case where $F\sigma(\lambda)/h\nu \ll 1$, we have $P_{\text{ion}} \sim F\sigma(\lambda)/h\nu$, meaning that the ionization probability depends approximately linearly on the laser fluence.

To add quantum state sensitivity to the ionization process (see Chapter 7), we use the resonantly-enhanced multi-photon ionization (REMPI) scheme as illustrated in 4.1(b). Here, M is first promoted to M^* via a bound-to-bound rovibronic transition driven resonantly by light with photon energy $h\nu_1$, and then ionized via a bound-to-continuum transition induced by light with photon energy $h\nu_2$. In this case, the condition for ionization becomes $h\nu_1 + h\nu_2 > E_{\text{th}}$. As the bound-to-bound transition is easily saturated due to its resonant nature, the probability of a REMPI transition is mostly determined by the cross section of bound-to-continuum transition. In the case of K_2 and Rb_2 REMPI, both transitions are saturated, resulting in order unity ionization efficiency for products in any given rotational states.

The ground-state energies for all neutral and ion species relevant to the studies described herein are given in Fig. 4.3, and the values of E_{th} for transitions between them are summarized in Table 4.1, along with σ for single-photon ionization at selected wavelengths. An important point to note is that photoionization convert the population of M proportionally into M^+, *i.e.* $N_{M^+} = P_{\text{ion}}N_M$. This proportionality relation allows us to infer relative changes in the population of a given species in the sample by monitoring that of its ion count.

Besides the originally intended ionization pathways, other ones, as shown in Fig. 4.1(c) and Fig. 4.2(a)–(c), were also identified. These pathways manifest as unexpected ion signals during
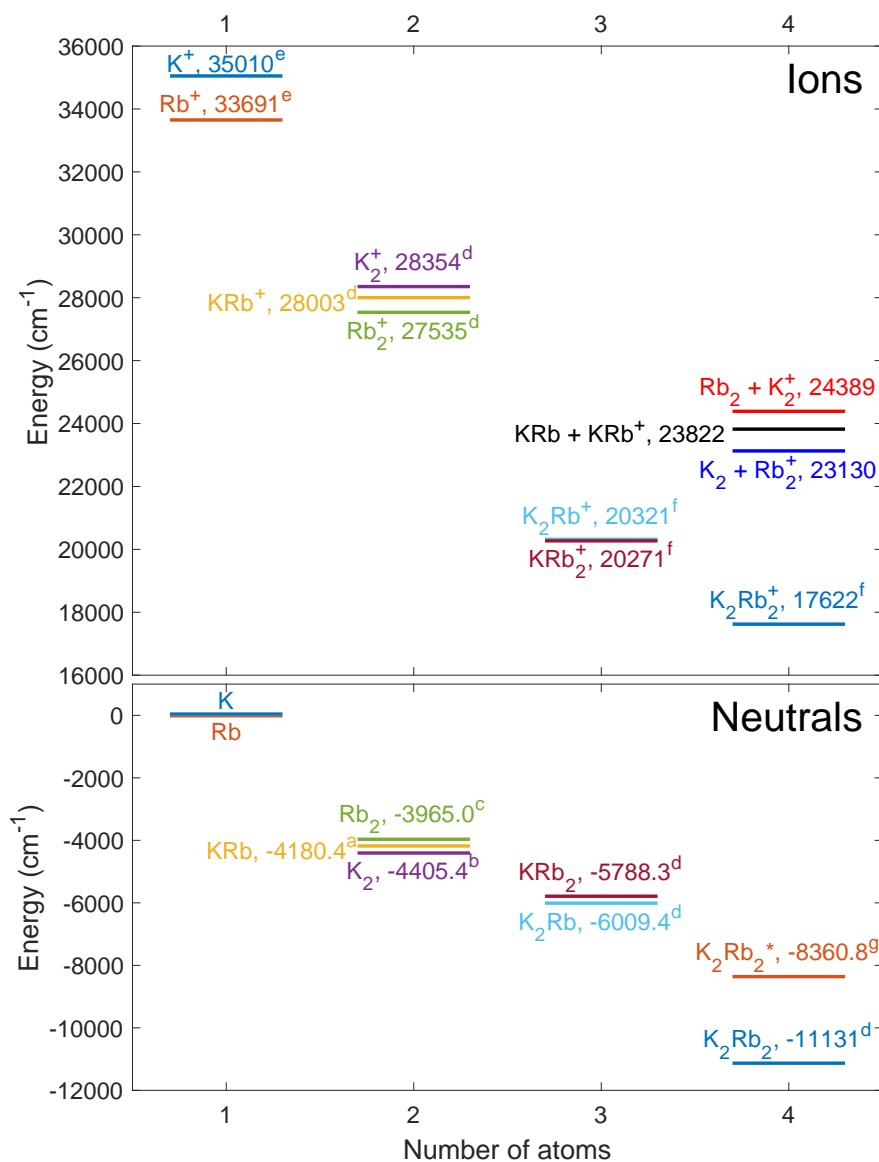
Figure 4.3: Ground state energies of neutral (lower panel) and ionic (upper panel) species relevant to the ultracold reactions between KRb molecules. The species are sorted horizontally by the number of constituent atoms.

[a] spectroscopic data, Ref. [154].
[b] spectroscopic data, Ref. [72].
[c] spectroscopic data, Ref. [185].
[d] *ab initio* calculation, Ref. [37].
[e] spectroscopic data, Ref. [177 178].
[f] *ab initio* calculation, Ref. [107].
[g] The energy of the $K_2Rb_2^*$ complex is equal to that of two separate ground-state KRb molecules.

133

various experiments, and some turn out to be quite useful once we understood them. In particular, the single-photon dissociative ionization pathway (4.2(a)) was responsible for the mysterious K_2Rb^+ and KRb_2^+ triatomic ions signals observed in our mass spectra, and an investigation of this pathway led to the direct identification of the long-lived intermediate complex $K_2Rb_2^*$ (Chapter 5); the two-photon dissociation plus ionization pathways (4.2(c,d)) resulted in the generation of ions (M_1^+ or M_2^+) with well-defined and tunable kinetic energies from the parent M, which

Table 4.1: Ionization information for all relevant species in the experiment. We define the ionization potential (IP) here as the energy required to excite from the ground ro-vibronic state of the neutral to the ground ro-vibronic state of the ion. The photoionization cross section is shown for excitation at 285 nm.

Species	IP (nm)	cross section σ (Mb[*])	MCP detector efficiency[†]
K	285.6 (Ref.[112])	0.01 (Ref.[112])	0.394
Rb	296.8 (Ref.[195])	0.049 (Ref.[195])	0.355
K_2	305.1[‡] (Ref.[32])	0.50 ± 0.25 (Ref.[53])	0.360
Rb_2	317[‡] (Ref.[195])	0.58 ± 0.26 (Ref.[53,195])	0.310
KRb	$310.0 - 320.3$[‡] (Ref.[115])		0.331
K_2Rb	374.9[§] (this work)		0.313
KRb_2	377.6[§] (this work)		0.295
K_2Rb_2	347.65[¶] (this work)		0.282

[*] 1 Mb = 10^{-18} cm^2.

[†] Values are calculated using the empirical formula developed in Ref.[123] based on the ion's mass and translational energy. We take into account both the intrinsic efficiency of the channel plates (60% open-area-ratio) of our MCP and the 75% optical transmission of a mesh in front of the plates. The maximum detection efficiency, in the limit of light mass and high translational energy, is $0.60 \times 0.75 = 0.45$.

[‡] It is calculated to be 305.2 nm for K_2, 317.5 nm for Rb_2, and 310.72 nm for KRb in this work.

[§] These values are calculated for the equilibrium geometries of the ionic complexes KRb_2^+ (C_{2v}): $R = 7.15$ a.u., $r_{Rb_2} = 8.88$ a.u., $\theta = 90°$ and RbK_2^+ (C_{2v}): $R = 7.51$ a.u., $r_{K_2} = 8.08$ a.u., $\theta = 90°$. Here we use Jacobi coordinates: r is distance of the homonuclear pair and R is distance from the third partner to the center of the homonuclear pair. The threshold for $K_2Rb_2^* + h\nu \rightarrow K_2Rb^+ + Rb(5S) + e^-$ is 345.4 nm and the threshold for $K_2Rb_2^* + h\nu \rightarrow KRb_2^+ + K(4S) + e^-$ is 346.0 nm.

[¶] This value is calculated for the equilibrium geometry of the ionic complexes $K_2Rb_2^+$ (T-shaped): $R = 11.8$ a.u., $r_{K_2} = r_{Rb_2} = 8.5$ a.u.. Here R is distance between K_2 center and Rb_2 center. The threshold for $K_2Rb_2^* + h\nu \rightarrow K_2Rb_2^+ + e^-$ is 384.9 nm.

allowed us to calibrate the VMI setup used for ion kinetic energy spectrometry (4.4).

4.2 Ionization sampling

Ultracold experiments such as ours work with much smaller molecular samples and have much longer experimental cycle times compared to traditional physical chemistry experiments. In the interest of achieving a reasonable data collection rate, it is important to efficiently sample the species of interest from reactions. To this end, a unique challenge is posed by the fact products and complexes form continuously by the reactions but only last transiently. As such, our pulsed ionization and detection in general only sample a portion of them, while the rest escape or dissociate in between dections*. In this section, we develop models for understanding the sampling of reaction products and complexes by photoionization. Such models should be generalizable to experiments aimed at studying the ultracold chemistry of trapped neutral particles.

4.2.1 Sampling of products by single-photon ionization

We first discuss the sampling of reaction products by single (UV) photon ionization. As reactions occur inside the XODT, products are generated with substantial velocity (up to 20.3 m/s for Rb_2 and 44.2 m/s for K_2) and fly away from the reactant cloud and into the vacuum. Our region-of-interest (ROI) for the ionization is limited to a sphere with a 0.75 mm radius around the cloud, a volume within which ions are properly imaged (section 4.4.3). In steady-state†, the number of products within the ROI is balanced by their generation and their escape, resulting in a velocity-

---

*This is in contrast to molecular beam experiments, where the ionization laser pulses are usually synchronized to the pulsing of the molecule beams.

†The timescale for the products to establish a steady-state within the ROI is discussed in Appendix F.

dependent steady-state density distribution given, for either species, by

$$\rho(r,v) = \frac{1}{4\pi}\frac{1}{r^2}\frac{\Gamma}{v}.$$ (4.3)

Here, r is the radius away from the KRb cloud*, v is the product velocity, and Γ is the rate at which products are generated. The ionization beam is placed to overlap with the ROI, and each pulse converts a portion of the products exposed to it into detectable ions. The number of ions generated by the m-th pulse is given by

$$N_m^{\text{ion}}(v) = \int_{\text{ROI}} \rho(r,v) P_{\text{ion}}(\vec{r})\mathrm{d}^3\vec{r} = \frac{1}{4\pi}\frac{\Gamma(mT)}{v}\int_{\text{ROI}}\frac{P(\vec{r})}{r^2}\mathrm{d}^3\vec{r},$$ (4.4)

where $\vec{r} = \{x, y, z\}$ is the spatial coordinate, T is ionization pulse period, and P_{ion} is the probability of ionization, which is proportional to the fluence of the ionization laser, $F(\vec{r})$, in the linear regime of ionization (see Eq. 4.2). Eq. 4.4 provides three pieces of important information about the ionization sampling.

- The $1/v$ velocity factor indicates that the slow products are preferentially sampled over the fast ones. This is due to the fact that faster products escape the ROI faster and therefore has a lower steady-state density. This factor is used to normalize measured product ion velocity distributions.

- The $1/r^2$ factor in the product density distribution indicates that products are much more concentrated around the reactant cloud and rapidly thins out away from it. Given the hollow-bottle profile we use for the UV ionization beam 2.5.1, this means that a beam with a smaller radius will result in higher ion counts. Practically, however, we are limited by the fact that the intensity at the "dark" center of the beam increases as its radius is reduced,

---

*here approximated to be an infinitesimal dot

resulting in more losses of the KRb reactants during ionization. As a compromise, we chose the 0.45 mm diamter beam shown in Fig. 2.32 for our experiments.

- For the linear regime of ionization in which we operate, the ion number is proportional to the total pulse energy ($E = \int F \mathrm{d}A$) contained in the beam, and is independent of small changes in its area. This is because the gain in the volume of products sampled by a beam with increased area exactly cancels out the loss in the ionization probability due to decreased fluence. If there is enough UV fluence to saturate P_{ion}, however, then increasing the exposure area will result in more ions.

In each experimental cycle, we typically expose the ROI to several thousand UV pulses over the course of 1 s to probe for products. The total ion number per cycle can be found by integrating Eq. 4.4 over the velocity distribution of products $P_v(v)^*$, and summing over a total of M pulses, *i.e.*

$$N^{\text{ion}} = \sum_{m=1}^{M} \int P_v(v) N_m^{\text{ion}}(v) \mathrm{d}v. \tag{4.5}$$

Using the experimental parameters for the product detection experiments described in Chapter 4, we find the number of K_2^+ and Rb_2^+ ions generated per cycle to be ~ 2 and ~ 4, respectively, which represent 0.2 and 0.4% of the total number products generate by the reactions. The factor of 2 difference between the numbers of K_2^+ and Rb_2^+ arises from the ~ 2 difference in their average velocities. These estimated ion numbers more or less agrees with what we measure experimentally.

Improvements in the above efficiencies are hindered by both the technical challenges in obtaining higher UV power[†], as well as the depletion of KRb reactants by the UV light. A potential way around this conundrum is to use probe products with UV photons with energy close to but

---

[*] $\int P_v(v) \mathrm{d}v = 1$

[†] Generating more than several hundred milliwatts of time-averaged UV laser power, such as what we have, becomes difficult with table-top lasers.

below that of the IP of KRb. This will drastically reduce the ionization depletion effect on KRb, thus allowing the beam to sample closer to the reactants, where the products are more concentrated. However, since $IP_{K_2} > IP_{KRb} > IP_{Rb_2}$ (see Tab. 4.1), only Rb_2 will be ionized.

4.2.2 Sampling of products by REMPI

We now turn our attention to the quantum-state-selective sampling of reaction products using resonance-enhanced multi-photon ionization (REMPI). In this case, products emerging in specific rotational states, N_{K_2} and N_{Rb_2}, are converted to ions via a bound-to-bound electronic excitation followed by a bound-to-continuum ionization. Despite ionizing products one quantum state at a time, we actually detect ions at a much higher rate compared to when using the non-state-selective ionization discussed in the previous section – typically obtaining 10 - 20 K_2^+ or Rb_2^+ ions per experimental cycle at peaks of resonances. As it turns out, the loss in ion counts from the state-specific nature of REMPI is more than made up by its high efficiency. As we have discussed in section 2.5.1, both legs of the REMPI transition become saturated at quite reasonable optical intensities, resulting in a $\sim 100\%$ ionization for those products that are illuminated by the beams. The low intensity requirement also enables us to increase the area of the beams with respect to that of the hollow-bottle UV beam (see Fig. 2.33), allowing a much larger portion of the ROI to be exposed by each pulse. However, due to the finite repetition rate of the REMPI light sources, the sampling of REMPI is still non-uniform for products of different velocities. Compared to the single-photon ionization case, where the velocity dependence of the sampling is given simply by $1/v$, the dependence here is more complicated due to the large spatial extend of the REMPI beams and the high ionization efficiency.

To model such a dependence, we developed a numerical simulation that generates and samples reaction products according to the beam geometry and timing diagram shown in the insets of
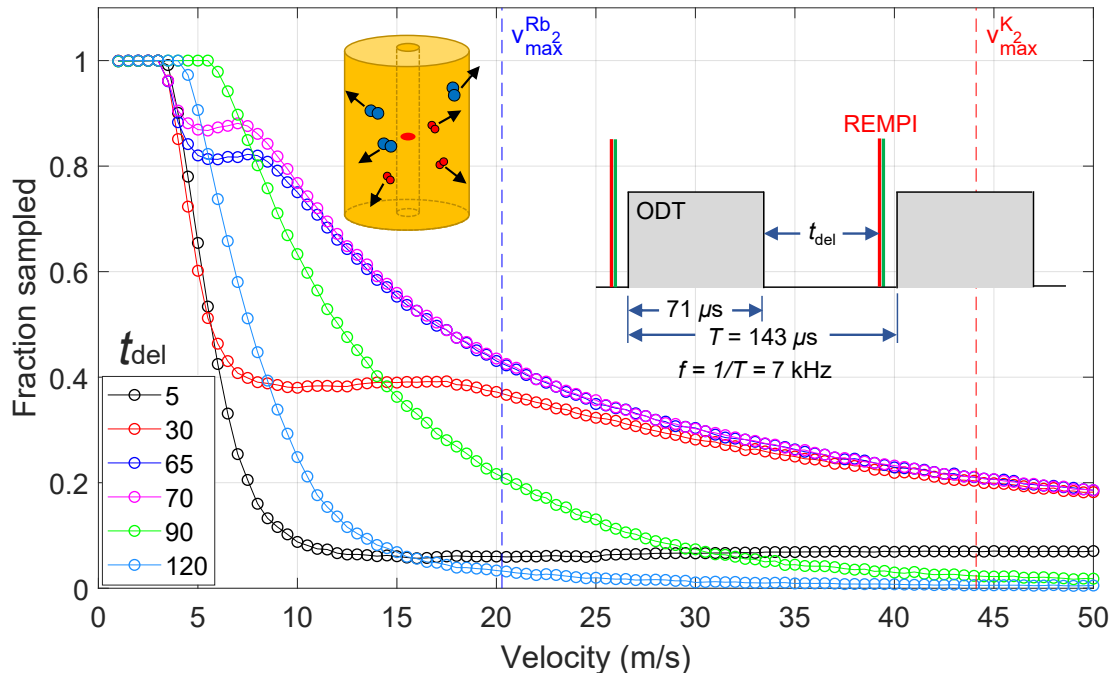
Figure 4.4: Sampling products using REMPI and effects of the ionization timing delay t_{del} on the sampling efficiency (simulation). Here, we have factored out the intrinsic ionization efficiency, *i.e.* products at zero velocity are sampled with unity efficiency. Left inset: products emerging from the reactant cloud are periodically exposed to cylindrical-shaped REMPI beams with a hollow center, the profile for which is shown in Fig. 2.33(c). Right inset: timing scheme used for REMPI sampling. The ODT undergoes a 50% duty-cycle square-wave modulation at a frequency of $f = 7$ kHz. The REMPI beams, overlapping in time, sample the products during the dark phase of the modulation, and are pulsed on at time t_{del} after the turn off of the ODT in each cycle. Main figure: the fraction of products sampled as a function of their velocities. Different colored curves correspond to different values of t_{del} listed in the legends (in units of microseconds). Blue and red dashed lines mark the maximum allowed velocities of the Rb_2 and K_2 products given the 9.53(7) cm^{-1} reaction exothermicity. The highest overall sampling efficiency is found for $t_{del} \sim T/2$, where $T = 1/f$ is the repetition period.

Fig. 4.4. As we will discuss in Chapter 6, the ODT strongly suppresses the formation the reaction products via photo-excitation of the intermediate complexes, and must therefore be time-modulated to create "dark" phases during which products can be monitored without its interference. The simulation takes the velocity of the products and other parameters from the experiment (*i.e.* repitition rate f and details of the timing) as inputs, and reports the fraction

of products sampled. In brief, each cycle of the REMPI detection begins with the turn off of the ODT confining the KRb molecules, at which point products begin to emerge from reactions at a rate* Γ with velocity v and propagate outward; after a time t_{del}, the REMPI beams are pulsed on to convert all products under its exposure into ions; this cycle is repeated several hundred times to collect statistics. In the end, the number of ions is divided by the total number of products generated to obtain the sampled fraction. Using this simulation, we calculated the velocity-dependence of REMPI sampling for different relative timings and repetition rates, and the results are displayed in Fig. 4.4 and 4.5.

Fig. 4.4 shows the simulated fraction of products sampled by REMPI as a function of their velocities, for different delays t_{del} between ODT off and REMPI, at a fixed repitition rate of $f = 7$ kHz. Vertical dotted lines mark the maximum velocities of K_2 and Rb_2 given the reaction exothermicity of $9.53(7)$ cm^{-1}. We analyze the behaviors of these plots using the one with $t_{del} = 65$ μs (blue), the value we used for all REMPI experiments carried out at $f = 7$ kHz. We highlight the following features of the plot

- For products with $v < 3.3$ m/s, the sampling is 100% efficient. These products are always sampled, if not by the REMPI pulse associated with the cycle in which they are generated, then by the next ones.

- For products with $5.0 < v < 7.7$ m/s, the sampling is $\sim 80\%$. The velocities of these products are low enough such that they are fully contained within the outer boundary of the REMPI beams by the time the pulses are fired. Those that are generated after the REMPI pulses and before the ODT switches back on, however, will escape before the next pulse comes.

- For products with $v > 7.7$ m/s, the sampled fraction decays approximately as $1/v$, similar

---

*Since it is the sampled fraction that we are interested in here, the exact value of Γ does not matter.

140
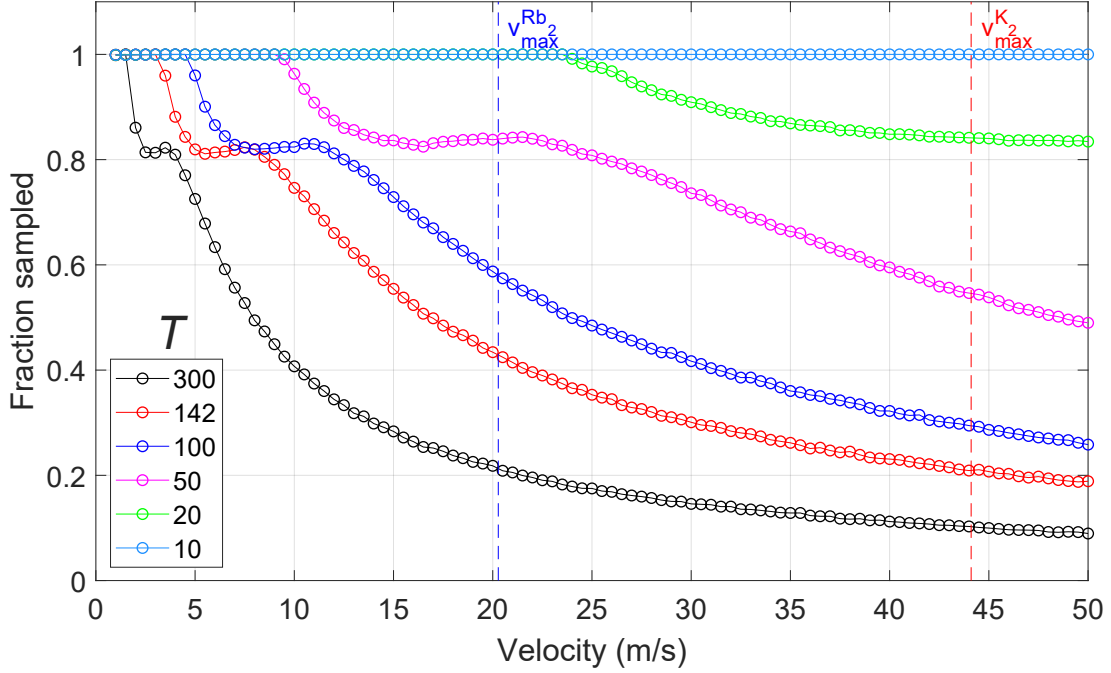
Figure 4.5: Effects of the repetition rate f (or inversely period T) on the REMPI sampling efficiency (simulation). Different colored curves correspond to different values of T listed in the legends (in units of microseconds). In each case, the delay between the ionization and the ODT turn off, t_{del}, is set to be a constant fraction (0.46) of the period. A higher repitition rate leads to a higher fraction of products sampled for all velocity classes. At $f = 100$ kHz, all product velocity classes are sampled with unity efficiency. See Fig. 4.4 inset for the timing scheme.

to the velocity-dependence of the UV ionization sampling. These products can expand beyond the outer boundary of the REMPI beams before the pulses are fired, and are therefore only partially sampled, with an efficiency that decreases for increasing velocities.

Overall, the sampling efficiency is maximized for $t_{\text{del}} \approx T/2$, which allows the maximum amount of time for product generation within each detection cycle. In practice, we use $t_{\text{del}} = 65$ μs for $T/2 = 71$ μs to avoid any overlaps in time between the 1064 nm ODT light and the REMPI lights, which can potentially lead to undesirable multi-photon effects.

Fig 4.5 shows the velocity dependence of the REMPI sampling for different repitition rate of

the REMPI lasers. The timing scheme here follows that illustrated in the inset of Fig. 4.4, and we fix t_{del} to be a constant fraction (0.46) of T as f is varied. We see that the overall sampling efficiency is improved as f is increased, reaching 100% at $f = 100\,\text{kHz}$ for all velocities relevant for the products from the KRb + KRb reaction. Future upgrades to higher repitition rate REMPI will allow us to uniformly sample reaction products regardless of their velocities, such that the ion signals associated with products from different rotational states directly reflect the population therein, and normalization using the simulated velocity-dependence of REMPI sampling is no longer required.

The velocity dependence of REMPI sampling obtained from the above simulations provide the necessary information to normalize the ion counts of products of different quantum states (and therefore different velocity classes, v_c). In particular, the inverse of the sampled fraction, which we shall refer to as the "velocity factor", $F_1(v_c)$, can be multiplied to product counts associated with v_c in order to normalize the counts into the underlying population. We discuss the subject of normalization further in Chapter 7.

In addition to the finite ionization repitition rate, another mechanism leading to velocity-dependent sampling is the Doppler effect – for products with velocity components v_z along or against the direction of REMPI beam propagation, the frequency of the bound-to-bound transition, nu_0, experiences a Doppler shift, $\Delta(v_z) = \frac{v_z}{c}\nu_0$. This introduces another velocity factor, $F_2(v_c)$, that need to be accounted for when considering the sampling efficiency. Fortunately, since we operate the bound-to-bound transition in the deeply-saturated regime for most of our studies, the Doppler effect has a relatively small effect on the sampling efficiency – for the fastest traveling products (~ 44 m/s), we expect a $\sim 20\%$ undersampling due to the Doppler effect, or $F_2 \sim 1.2$. The exact modeling of $F_2(v_c)$ is reserved for future studies that require highly accurate normalizations. Throughout the thesis, we will approximate F_2 to be 1 for all product velocity classes.

4.2.3 Sampling of intermediate complex

Intermediate complexes, $K_2Rb_2^*$, are formed by the collisions of pairs of ultracold reactants, and therefore bare very low center-of-mass velocities. Since the complexes only live for several hundred nanoseconds (Chapter 6) before dissociating into products, they essentially occupy the same spatial region as the KRb cloud. This means that the light used to ionize $K_2Rb_2^*$ needs to overlap the optical trap and inevitably expose the KRb molecules within. Fortunately, the wavelengths that are found to efficiently ionize $K_2Rb_2^*$, 335 - 356 nm, are not short enough to single-photon-ionize KRb, which has an IP corresponding to 310 nm. This allows us to simply use an UV beam with a Gaussian beam profile co-propagating with the VODT to probe for the complex. However, two-photon UV ionization of KRb is allowed, and the process becomes greatly enhanced when the first photon is resonant with a vibronic transition of KRb.

To avoid these resonances, we performed a spectroscopic survey of KRb prior to the complex ionization and detection experiments (Chapter 6), in a 1 nm-wide wavelength window centered around 354.75 nm*. A newly-prepared KRb cloud with a pkOD of 1400 mOD is exposed to UV pulses with energy of 30 μJ (peak fluence of 0.13 J/cm^2), at a repitition rate of 7 kHz, for a duration of 100 ms. In the absence of the UV the KRb cloud decays to a peak OD of 1200 mOD after 100 ms, and any additional decay is attributed to two-photon ionization by the UV light. Fig. 4.6(a) shows the measured peak OD of KRb as a function of the UV wavelength, which is varied in 0.01 nm (0.8 cm^{-1}) steps. We observe many resonances for KRb depletion, corresponding to rovibronic transitions in KRb that we do not attempt to assign. In between the dips, there exist windows of very mild depletion. The window between 354.8 and 354.9 nm

---

*We were interested in this particular wavelength because it can be generated by sum-frequency generation of the output of an YAG laser (1064.25 nm) and its second harmonic (532.13 nm). Such a setup can potentially provide more robust and higher power UV light for examining the intermediate complex compared to the frequency-doubled dye laser setup.
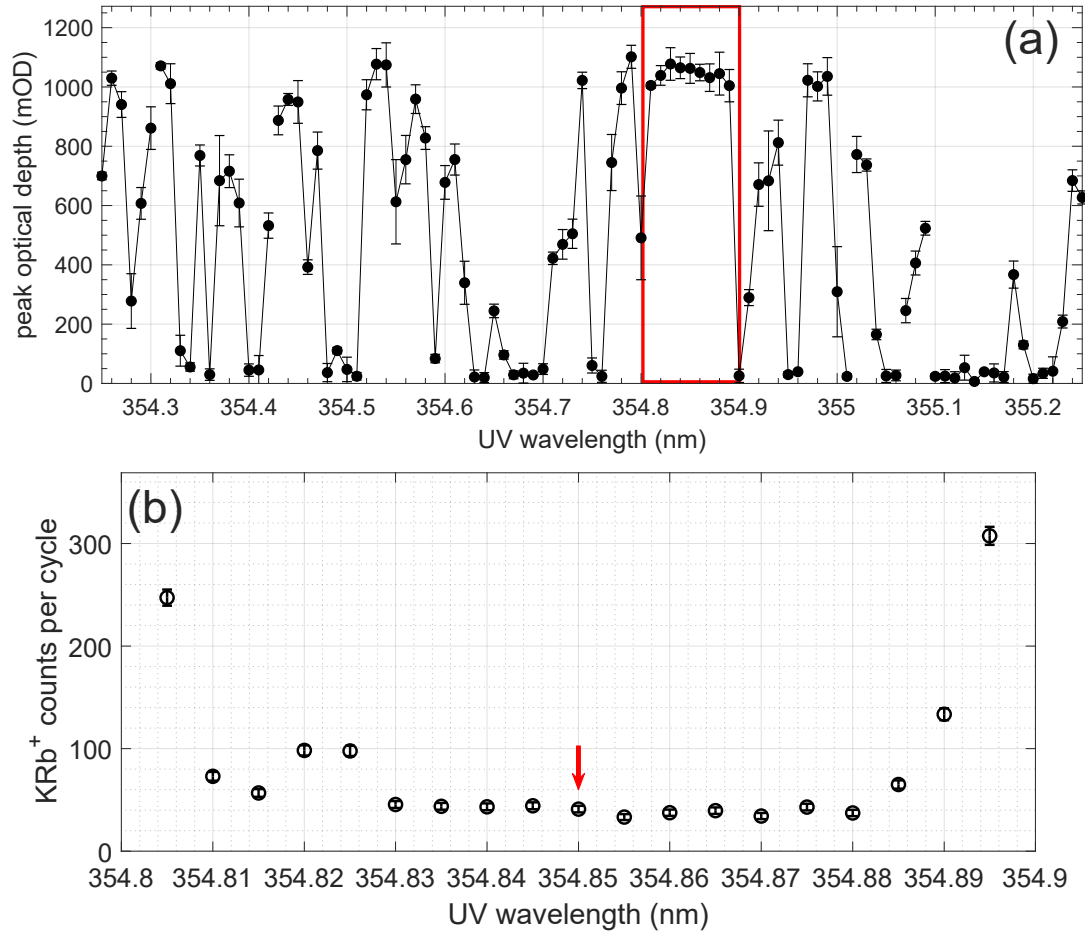
Figure 4.6: Two-photon ionization depletion of KRb. (a) Depletion of the KRb cloud when it is exposed to UV light in the wavelengh range 354.25 – 355.25 nm, measured through absorption imaging. For each data point, the cloud is exposed to UV pulses at a 7 kHz repetition rate, with a peak fluence of 0.13 J/cm^2, for a duration of 100 ms. The resulting depletion spectrum show many resonant dips that likely correspond to rovibronic transitions in KRb, which we do not attempt to assign. (b) KRb$^+$ ion counts (per experimental cycle) as a function of UV wavelength in the range 354.8 – 354.9 nm, corresponding to the red boxed portion of (a). This shows a pattern complementary to that observed in (a), and identifies 354.85 nm as the optimal wavelength for ionization sampling of the intermediate complex.

(red rectangle) is particularly wide, and therefore provides a suitable range of wavelengths for ionizing $K_2Rb_2^*$ without significantly depleting KRb.

As an additional check, we monitored the KRb^+ ion counts at UV wavelengths within the 354.8 – 354.9 nm window. Here, we increased the UV exposure time to 1 s. The result, plotted in Fig. 4.6(b), shows a pattern complementary to that of the depletion, as one would expect. From this plot, we also identify a background KRb^+ count of ~ 40 per experimental cycle, which we attribute to off-resonant two-photon ionization. Given these measurements, we chose 354.85 nm (red arrow) to be the final wavelength for complex ionization. At this wavelength, we observe a 10% overall depletion of the KRb molecules due to the UV.

4.3 Time-of-flight mass spectrometry

Time-of-flight (TOF) mass spectrometry is a technique in which ions of different masses are accelerated and distinguished based on the differing amount of times they take to fly over a fixed distance. In our ion spectrometer design (Section 2.5.2, Fig. 2.34), photo-ions with charge* e and mass m originate from midway between the repeller (R) and extractor (1) electric field plates and are accelerated by the VMI stack, with a voltage V_R applied to R and the final plate (5) held at ground. Note that the actual voltage drop experienced by the ions over the acceleration stage, V_0, is slightly less than V_R due to the fact that ions are born to the right of R. Given the geometry of the VMI stack and the relative voltages of the plates (see Table 2.3), we have $V_0 = 0.91V_R$. By the end of the acceleration, the electric potential energy is fully converted into the ion's kinetic energy, and we have

$$eV_0 = \frac{1}{2}mv_{\text{acc}}^2, \tag{4.6}$$

---

*Only singly-ionized species are generated in our experiment.

145

and the accelerated velocities of the ions are given by

$$v_{\text{acc}} = \sqrt{\frac{2eV_0}{m}}.$$ (4.7)

The time spent by the ions during acceleration is given approximately by

$$t_1 = s_0 \sqrt{\frac{2m}{eV_0}},$$ (4.8)

where s_0 is the distance between the origin and plate 5. With the accelerated velocity, the ions undergo free-flight in the TOF tube over a distance $L_0 \sim 1$ m and hit the MCP after a time

$$t_2 = \frac{L_0}{v_{\text{acc}}} = L_0 \sqrt{\frac{m}{2eV_0}}.$$ (4.9)

The ion TOF is therefore given by

$$\text{TOF}(m, V_0) = t_1 + t_2 = \left(\sqrt{2}s_0 + \frac{1}{\sqrt{2}}L_0 \right) \sqrt{\frac{m}{eV_0}}.$$ (4.10)

Note that since $t_1/t_2 = 2s_0/L_0 \sim 0.09$, the TOF is mostly determined by the free-flight time. To identify different ion species from an experiment, we sort ion counts accordingly to their TOF and display them as a TOF spectrum, an example of which is shown in Fig. 4.7. Here, we identify three prominent peaks, which can be assigned based on their centroid TOFs to K^+ ($m = 40$), Rb^+ ($m = 87$), and KRb^+ ($m = 127$), respectively. In many cases throughout the thesis, we also display the ion data as a mass spectrum where the TOF axis is converted into a mass axis using Eq. 4.10. The (1σ) width of a given TOF peak, which characterizes the spread of the ion's TOF, is found to be dTOF $= 5$ ns at the minimum, as measured for ultracold KRb molecules confined in the XODT (see Fig. 4.7 inset). We take this to be the fundamental timing

146
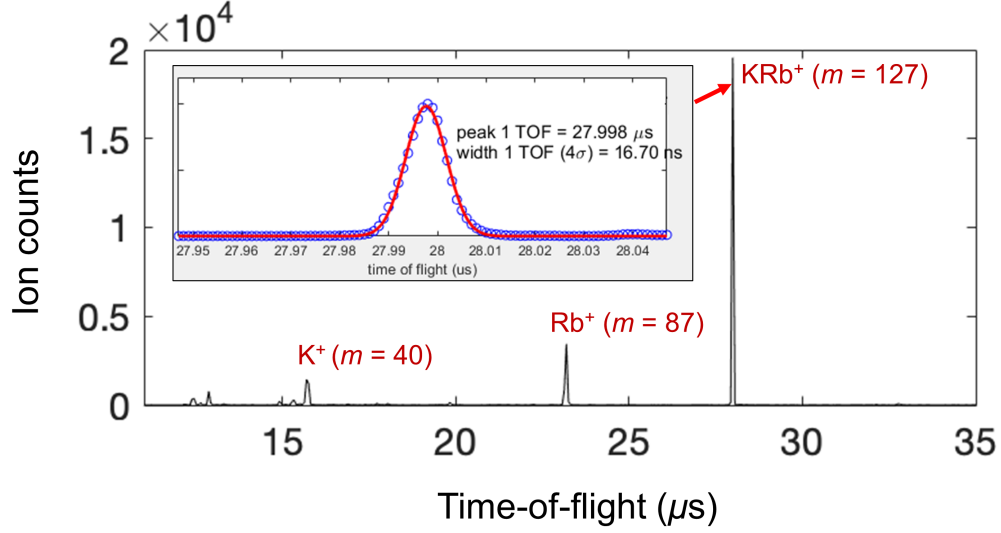
Figure 4.7: TOF mass spectrum acquired as KRb molecules confined in the XODT are ionized by UV light at 285 nm. The spectrum shows three prominent peaks, which can be assigned based on their centroid TOFs to K^+ ($m = 40$), Rb^+ ($m = 87$), and KRb^+ ($m = 127$), respectively. Inset: a zoomed in view of the KRb^+ TOF distribution. Gaussian fit (red curve) applied to the distribution shows a 1σ width of ~ 5 ns, which we take to be the fundamental timing resolution of our system.

resolution of our ion detection, which corresponds to a minimum-resolvable mass difference of

$$\mathrm{d}m = \frac{2m}{\mathrm{TOF}}\mathrm{dTOF} = \frac{2\sqrt{m}}{A}\mathrm{dTOF}, \tag{4.11}$$

where the constant $A = \left(\sqrt{2}s_0 + \frac{1}{\sqrt{2}}L_0\right)\sqrt{\frac{1}{eV_0}}$. Note that the resolution decreases for increasing ion mass. At the commonly used repeller voltage $V_R = 992$ V, we find $\mathrm{d}m = 0.025$ amu (0.064 amu) for the lightest (heaviest) species, K_2^+ ($K_2Rb_2^+$) observed in the experiment, which is more than sufficient to distinguish all relevant ions from each other. In practice, the width of the TOF distribution is typically dominated by other broadening mechanisms, which we discuss next.

So far, our discussion for TOF has been limited to the simple case where ions are born exactly in between plates R and 1 with no initial velocity. In practice, ions can have a range of starting

positions and velocities, giving rise to a distribution in TOF for each species. To understand the extent of such effects, consider first an ion of mass m that starts at a displacement of dx away from the origin, where a positive value means closer to plate R. In this case, the acceleration voltage drop experienced by the ion becomes $V = (1 + \mathrm{d}x/s_0)V_0$. A positive (negative) $\mathrm{d}x$ results in more (less) acceleration experienced by the ion, and therefore a higher (lower) v_{acc} and a correspondingly shorter (longer) TOF. Given the relation between TOF and V_0 in Eq. 4.10, the change in TOF as a result of the position shift is given by

$$\mathrm{dTOF} = -\frac{1}{2}\mathrm{TOF}\frac{\mathrm{d}x}{s_0}. \tag{4.12}$$

This result is perhaps a bit counter-intuitive, as ions born further away from the MCP actually arrive earlier. Eq. 4.13 allows us to estimate the broadening of a TOF distribution introduced by the finite initial position spread of the ion along the TOF axis. For ultracold KRb molecules ionized inside the XODT and accelerated using $V_R = 992V$, the spread in the initial KRb$^+$ position is characterized by the 2σ cloud width along the TOF axis, which is 6 μm. This corresponds to a TOF broadening of dTOF $\sim$ 2 ns, which is less compared to the fundamental limit. On the other hand, for $K_2(Rb_2)$ molecules ionized by the hollow-bottle beam, which has a ring diameter of 0.45 mm, the difference in TOF between ions can be as large as dTOF = 105 ns (154 ns). This broadening effect is modeled more precisely in Chapter 5.

Similarly, we can consider an ion born with initial velocity v_0 along the TOF axis, where a positive value means flying towards the repeller. The main effect of this is a modification of the velocity of the ion during the TOF by an amount v_0. Experimentally, we always operate in the regime where $v_0 \ll v_{\mathrm{acc}}$, in which case the change in TOF caused by v_0 is approximately given by

$$\mathrm{dTOF} = \frac{v_0}{v_{\mathrm{acc}}}\mathrm{TOF}. \tag{4.13}$$

148

For the K_2 (Rb_2) reaction product, which has a maximum velocity of 44 m/s (21 m/s), the maximum TOF broadening due to velocity is 3 ns, which is below the fundamental limit. On the other hand, for ions generated from photodissociation (Fig. 4.2(b,c)), where the kinetic energy release (KER) can be up to 10^4 cm^{-1}, the TOF broadening can be as large as 100 ns.

While the broadening of the TOF distribution is generally undesirable in mass spectrometry due to the limitation it places on the mass resolution, we find it to be a useful feature in our experiments. In particular, the broadening due to the spread in initial positions of the ions helped us confirm that the K_2^+ and Rb_2^+ ions we detected originated from the hollow-bottle UV beam, consistent with our expectation for products generated by chemical reactions (Chapter 5).

4.4   Kinetic energy spectrometry

4.4.1   Basic concepts and data analysis

Kinetic energy spectrometry is achieved through ion imaging, a workhorse technique behind many studies of gas-phase chemical dynamics[15]. In an experiment, ions of a given kinetic energy KE and corresponding velocity $v = \sqrt{2KE/m}$ are distributed on a Newton sphere. This sphere expands as the ion packet, accelerated by an electric field, flies towards the detector along the TOF axis. By the time the sphere reaches the detector, it will have expanded to a radius R that is related to KE according to

$$R = A\sqrt{\frac{KE}{V_R}}, \tag{4.14}$$

where V_R is the voltage of the repeller plate (Fig. 2.34), A is a proportionality constant that depends on the distance of flight, the mass of the ion, and details of the acceleration electric field pattern. The value of A is 16.44mm/$\sqrt{\text{cm}^{-1}/\text{V}}$ from simulation. Its experimental calibration is discussed in section 4.4.2. The Newton is projected onto the detector to form a 2D image,
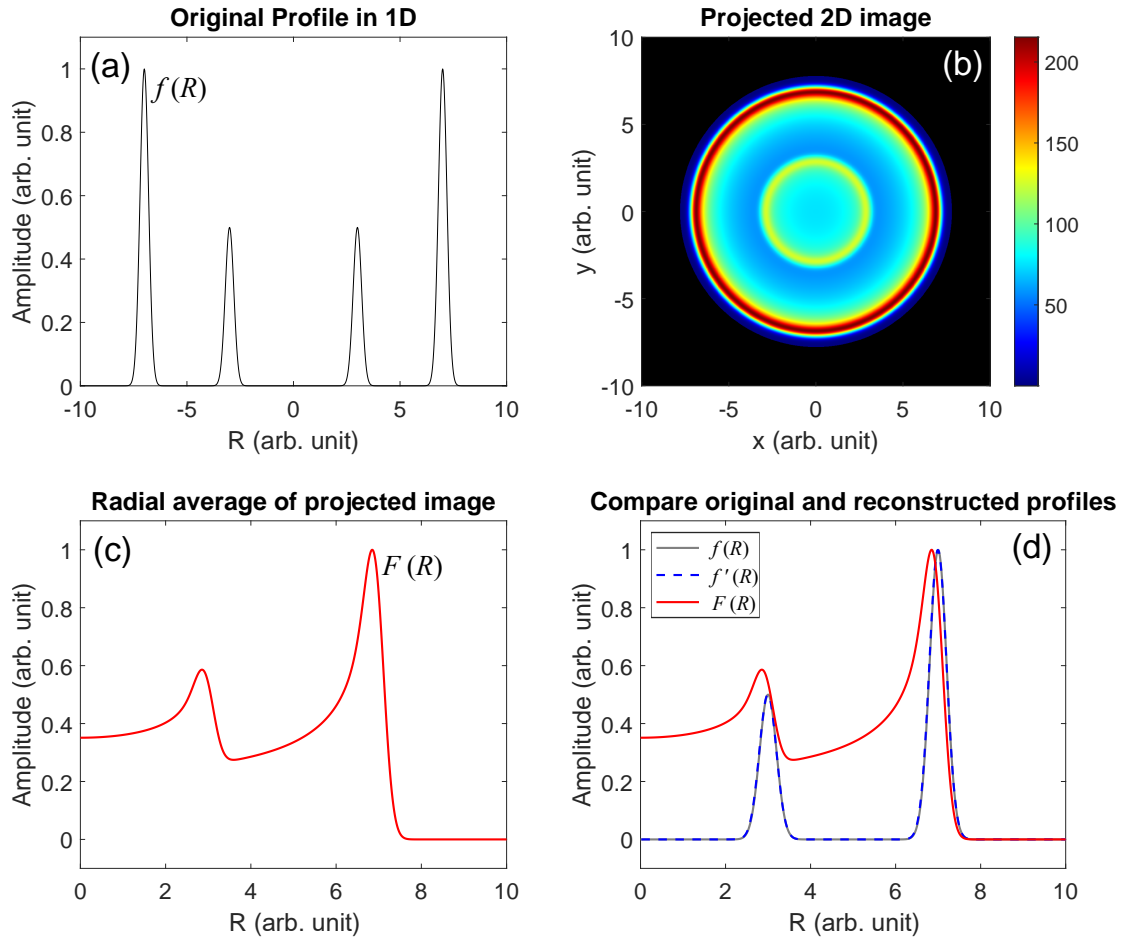
Figure 4.8: 1D Inverse Abel transform (IAT). (a) The 1D profile of two concatenated Newton spheres with radii 3 and 7 (arbitrary units), respectively. A Gaussian width (1σ) of 0.2 is assigned to each Newton sphere to simulate broadening effects from the imperfection of VM imaging. (b) The Newton spheres are integrated along the TOF axis (z), resulting in a 2D image that represents the ion image as observed on the MCP detector. (c) Radially averaged profile of the 2D image in (b). (d) 1D IAT is applied to the radially averaged profile (red solid), resulting in the reconstructed profile (blue dashed) that recovers the original profile (gray solid).

from which its radius R can be extracted and the corresponding KE of the ions inferred. In general, ions of many different velocities can co-exist to form concatenated Newton spheres, and the information about their KE is contained in the radial ion density distribution.

The key to extracting the $R-$distribution, $f(R)$, from a given ion image is to reconstruct the

3D Newton sphere from the 2D image. To this end, we use one of two established methods –
inverse Abel transformation (IAT) or time-slicing [15]. Fig. 4.8 illustrates the procedures involved
in IAT using a test example. Here, ions with two velocity components give rise to two concate-
nated Newton spheres with radii 3 and 7 (arbitrary units), respectively. A Gaussian width (1σ)
of 0.2 is assigned to each Newton sphere to simulate broadening effects from the imperfection
of VM imaging. The radial distribution profile of the ions, $f'(R)$, are shown in Fig. 4.8 (a). The
2D image resulting from the projection of ions onto the detector is shown in Fig. 4.8 (d), which
displays two distinct ring structures that we refer to as "VMI rings". To extract $f(R)$, we first ra-
dially average the image to obtain $F(R)$, as shown in Fig. 4.8 (c). This is achieved by averaging
the ion counts within pixels that belong to a constant radius R. Note that while in this idealized
example $F(R)$ is simply a slice of the 2D image, in practice the process of radial-averaging is
critical for noise reduction. $F(R)$ is then transformed into $f(R)$ using a Fourier-analysis based
Abel inversion algorithm, which has been shown to yield robust transformations despite high
noise levels in the ion image [171]. Comparing the reconstructed distribution $f(R)$ to the original
distribution in $f'(R)$, we find that the two closely resemble each other.

We note that the procedure for IAT described above is one-dimensional and therefore only
applies to ion images that are azimuthally isotropic. These correspond to processes that generate
isotropically distributed particles, such as the K_2 and Rb_2 products from KRb + KRb reactions.
For more general cases, where the ion distribution is not necessarily isotropic, there exist a
variety of two-dimensional reconstruction methods [105].

In cases where the ions possess significant KE that result in a wide TOF distribution, time-
slicing can be used to extract the radial distribution in a transformation-free manner. Here, a
narrow time slice in the middle of the Newton sphere, typically $\sim 10\%$ of the total ion packet
duration, is selected and then radially averaged to obtain $f(R)$. In our experiment, this is enabled
by the MCP's ability to record the time and location of every ion hit. This method is used to

151

analyze the ion images of K and Rb fragments resulting from KRb photodissociation, which are used towards the calibration of the spectrometer (4.4.2).

Our experiments deal with ions in a wide range of kinetic energies, from below 1 cm^{-1} to 10^4 cm^{-1}. To properly study their KE distributions, appropriate acceleration voltages, which controls the degree to which the ion images are magnified (Eq. 4.14), must be chosen to achieve a balance between the dynamic range and resolution. To this end, two primary settings are used in experiments carried out in this thesis. In the "low energy" setting, the repeller voltage V_R is set to be 100.2 V, which optimizes detection for ions within the energy range $\sim 0 - 150$ cm^{-1}, and is appropriate for studying the product kinetic energy distribution of the KRb + KRb reaction (7). In the "high energy" setting, $V_R = 992$ V, and the detection range is increased to $\sim 0 - 5000$ cm^{-1}. This setting was used to image fragments resulting from photodissociative events (Fig. 4.2(a–c)). Imperfections in the real experimental setup limits the energy resolution of VMI (the ability to distinguish adjacent VMI rings). For "low energy" setting, we find the minimum resolvable energy difference to be 0.1 cm^{-1} around 0 cm^{-1}, 2 cm^{-1} around 10 cm^{-1}, and 6 cm^{-1} around 100 cm^{-1}. The resolution for the "high energy" setting is overall ~ 3.3 times lower. The exact mechanisms that limit the VMI resolution is not well-understood, but a likely candidate is stray electric field gradients present along the ion flight path, which is difficult to characterize.

An additional effect that impacts the VMI resolution is the recoil experienced by the ion during the ionization process. In photoionization that generate a photoion (M^+) and an electron (e^-) (Fig. 4.1(a–c)), the excess photon energy, $E_{\text{ex}} = h\nu - IP$*, is deposited into the kinetic energies of the two particles as they recoil from each other. In order to satisfy both energy and momentum conservation in this process, the kinetic energies of the ion and electron are given

---

*This expression for the excess energy is exact in the case of atomic ionization. For molecular ionization, some energy of excess energy can also be deposited into the vibrations of the resulting molecular ion. As such, this expression only represents an upper-bound on the excess energy.
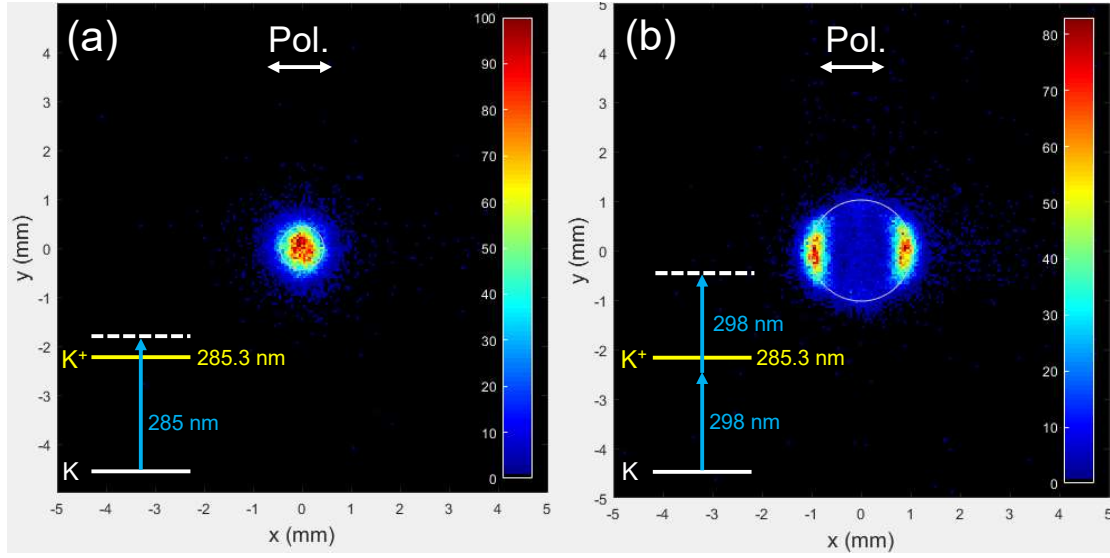
Figure 4.9: Photoionization recoil of K. (a) Ionization of K using a single photon at 285 nm. In this case, the ion recoil energy is only 0.001 cm^{-1}, and therefore results in a detector resolution limited ion distribution. (b) Ionization of K using a two 298 nm photons. In this case, the ion recoil energy is 0.44 cm^{-1}, resulting in a resolvable VMI ring structure peaked along the ionization polarization direction.

by

$$KE_{M^+} = E_{\text{ex}} \frac{\mu(M^+, e^-)}{m_{M^+}}, \tag{4.15}$$

and

$$KE_{e^-} = E_{\text{ex}} \frac{\mu(M^+, e^-)}{m_{e^-}}, \tag{4.16}$$

where $\mu(M^+, e^-) = m_{M^+} m_{e^-}/(m_{M^+} + m_{e^-})$ is the reduced mass of the ion-electron system. Due to the large mass difference between M^+ and e^-, the majority of the excess energy is carried away by the electron, leaving M^+ with a small remaining fraction that nonetheless can broaden ion images. The effect of recoil broadening is illustrated in Fig. 4.9. Here, we compare the images of K$^+$ ions resulting from single-photon ionization of ultracold K atoms at 285 nm (a) and non-resonant two-photon ionization at 298 nm (b), which have expected excess energies of 73.7 and 3.21×10^4 cm^{-1}, respectively, corresponding to ion recoil energies of 0.001 and 0.44

153

cm^{-1}. Note that in Fig. 4.9(b), the K$^+$ ions preferentially recoil along the polarization direction of the UV ionization laser, as one would expect.

4.4.2   Calibration of VMI

Calibrating the kinetic energy spectrometer amounts to experimentally determining the value of the proportionality constant A in Eq. 4.14, which quantifies the relationship between the radii of ion Newton spheres and their associated kinetic energies. This requires the generation of ions with sufficient and well-known kinetic energies, which is a challenge for ultracold systems where particles move with negligible kinetic energies. Photodissociation (PD) of diatomic molecules, which imparts a well-defined amount of kinetic energy into the recoiling photofragments, provides a suitable solution to this problem.[69] We used the one-color, two-photon dissociation plus ionization process shown schematically in Fig. 4.10 (a) and Fig. 4.11 (a). The first photon dissociates the ground state KRb molecules into K and Rb photofragments, and the second photon ionizes the optically excited fragment. Ion images were acquired at different photon energies. For each ion image, $\sim$ 5000 KRb molecules in their rovibrational ground state were exposed to 5000 UV laser pulses over 1 s for 500 - 1500 experimental cycles. The use of ultracold precursors in a single quantum level for PD ensures the production of photofragments with sharply-defined kinetic energies, a feature especially beneficial to calibration at low kinetic energies. The average number of ions generated per UV pulse is kept much less than one to ensure the resulting ion images not broadened by space-charge. Separate calibrations are carried out for the "low energy" and "high energy" repeller voltage (V_R) settings.

For "low energy" calibration, V_R is set to 100.2 V. We photodissociated KRb into K (5P) and Rb (5S) and ionized K (5P) to produce K$^+$ ions with kinetic energy (KE) in the 0 - 140 cm^{-1} range (Fig. 4.10 (a)) by varying the UV laser wavelength (photon energy) between 346 nm

Figure 4.10: One-color, two-photon dissociation plus ionization of ultracold KRb for ion kinetic energy spectrometry calibration at $V_R = 100.2$ V. (a) Schematic. The first photon dissociates KRb into photofragments with well-defined kinetic energies, and the second photon ionizes the excited K (5P) fragment (marked in bold). The values for D_0 and IP can be found in Tab. 4.2. (b) Ion image (projected) obtained by monitoring K^+ from KRb PD plus ionization with $V_R = 100.2$ V, $\lambda_{UV} = 345.8103$ nm, and vertical laser polarization. The inner and outer rings correspond to the K ($5^2P_{3/2}$) + Rb ($5^2S_{1/2}$) and K ($5^2P_{1/2}$) + Rb ($5^2S_{1/2}$) PD channels, respectively. The rings are broadened due to photoionization recoil (0.253 cm^{-1}). (c) Image of a 4 ns time-slice of the entire 40 ns ion packet. (d) The radial intensity distribution of the time-slice. Gaussian fits are applied to extract the radii (R) of the two Newton spheres, which are 5.18 ± 0.03 mm and 7.50 ± 0.05 mm, respectively. (e) The angular intensity distributions of the inner (red) and outer (magenta) rings in the time-slice. The distributions are fitted to the function $A(1 + \beta P_2(\cos\theta))$. The resulting anisotropy parameter β is 1.89 ± 0.05 for the inner ring, and 1.00 ± 0.08 for the outer ring, indicating a mix of "parallel" and "perpendicular" characters.

155

Figure 4.11: One-color, two-photon dissociation plus ionization of ultracold KRb for ion kinetic energy spectrometry calibration at $V_R = 992$ V. (a) Schematic. The first photon dissociates KRb into photofragments with well-defined kinetic energies, and the second photon ionizes the excited Rb (6P) fragment (marked in bold). (b) Ion image (projected) obtained by monitoring Rb^+ from KRb PD plus ionization, $\lambda_{UV} = 346.0789$ nm, and vertical laser polarization. The ring corresponds to the K ($4^2S_{1/2}$) + Rb ($6^2P_{1/2}$) PD channel, and is broadened due to photoionization recoil (0.125 cm^{-1}). (c) Image of a 3 ns time-slice of the entire 30 ns ion packet. (d) The radial and (e) angular distributions of the time-slice. $R = 8.73 \pm 0.01$ mm and $\beta = 1.91 \pm 0.07$.

156

(29802 cm^{-1}) and 344 nm (29070 cm^{-1}). A 5 Gauss magnetic quantization field is maintained for the molecules *. An example K$^+$ ion image acquired at a UV wavelength of 345.7325 nm is shown in Fig. 4.10 (b). From the image we identify two anisotropic ring patterns, and assign the inner and outer rings to ions dissociated from the K (5^2P$_{3/2}$) + Rb (5^2S$_{1/2}$) and the K (5^2P$_{1/2}$) + Rb (5^2S$_{1/2}$) channels, respectively. We note that the rings are broadened due to a 0.253 cm^{-1} of recoil energy imparted to the K$^+$ ions by the ionizing UV photon. To determine the radii of the two underlying Newton spheres, we select ions from the central 4 ns time-slice of a 40 ns-wide TOF distribution (Fig. 4.10 (c)). The time-slice is then angle-integrated to obtain the radial intensity distribution (Fig. 4.10 (d)). Gaussian fits are applied to the radial distribution to extract the radii R, which are 5.18 ± 0.03 mm and 7.50 ± 0.05 mm for the inner and outer Newton spheres respectively. The anistoropy of each Newton sphere is analyzed by examining the angular intensity distribution (Fig. 4.10 (e)) of the corresponding ring in the time-slice. The distributions are fitted to the function† $b(1 + \beta P_2(\cos\theta))$. The resulting anisotropy parameter β is 1.89 ± 0.05 (≈ 2) for the inner ring, indicating that the PD transition dipole moment is mostly parallel to the molecular axis. For the outer ring, $\beta = 1.00 \pm 0.08$, indicating a mix of parallel of perpendicular characters in the PD transition. Detailed understanding of the observed photofragment anisotropy in Fig. 4.10 is a subject for future study.

The kinetic energy of ions associated with each Newton sphere is given by

$$KE = \frac{m_{\text{Rb}}}{m_{\text{Rb}} + m_{\text{K}}} \left(E_\gamma - E_{\text{th}} + D_0 \right), \tag{4.17}$$

---

*As demonstrated in Ref. [162], maintaining the quantization to the fermionic KRb molecules is essential to keeping them in a single quantum state, such that they undergo p-wave collision and the sample enjoys a relatively long lifetime. A longer-lived sample allows us to collect more ions towards the calibration per experimental cycle.

†This formula results from a quasiclassical model describing the angular distribution of fragments produced by the photodissociation of molecules prepared in spherically symmetric states [222], *e.g.* KRb prepared in the rovibrational ground state. Here b is a constant, β is the anisotropy parameter that varies from +2 ("parallel" transition) to -1 ("perpendicular" transition), θ is the angle in the plane of the image, and P_2 is the second order Legendre polynomial.
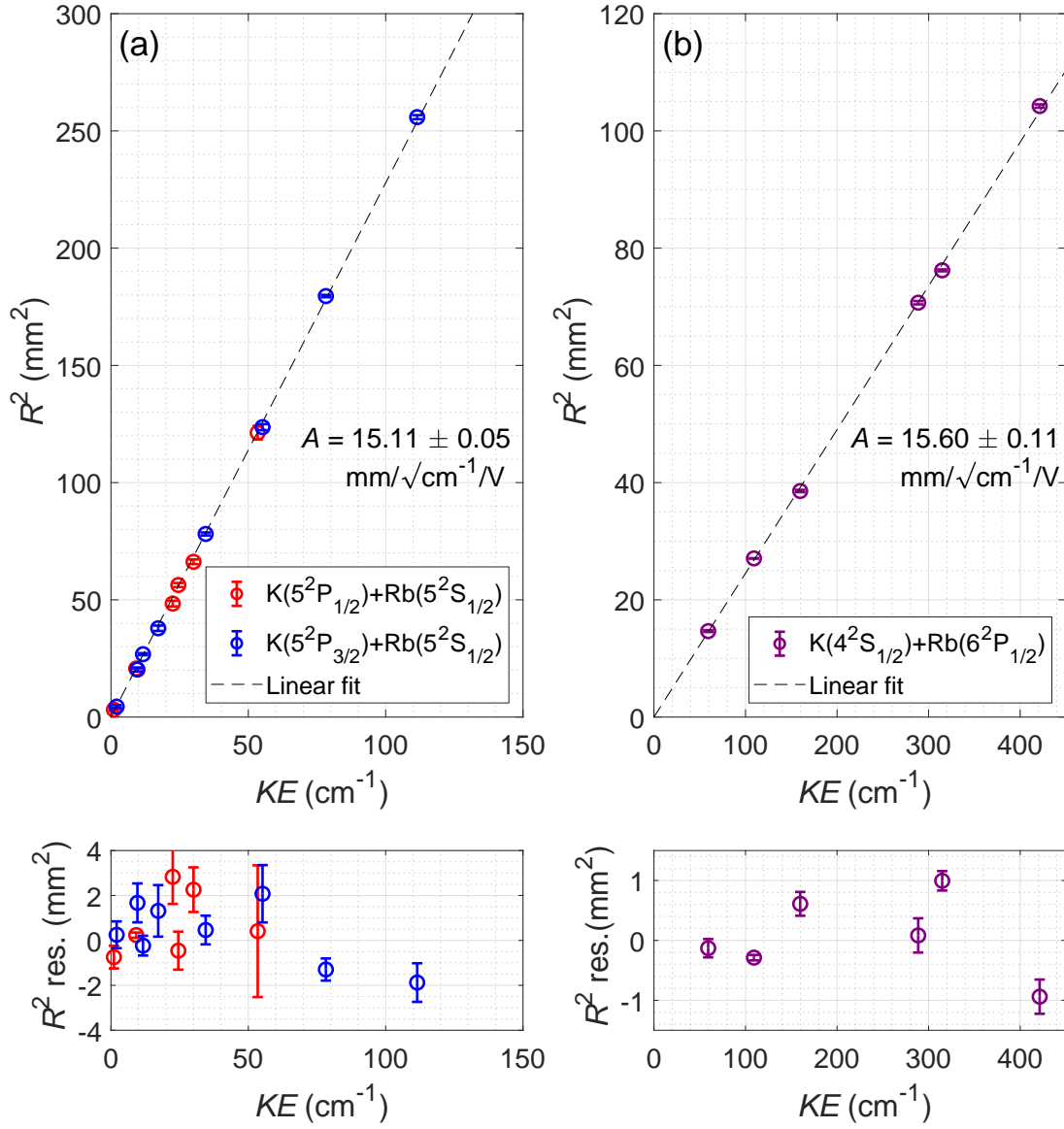
Figure 4.12: **Calibrating the kinetic energy spectrometer** (a) Top panel: calibration data and fit to $R^2 = A^2 KE / V_R$ for the "low energy" setting. Contributions from the K $(5^2\mathrm{P}_{3/2})$ + Rb $(5^2\mathrm{S}_{1/2})$ and K $(5^2\mathrm{P}_{1/2})$ + Rb $(5^2\mathrm{S}_{1/2})$ channels are colored blue and red, respectively. Bottom panel: residual of the fit. (b) calibration data and fit for the "high energy" setting. Bottom panel: residual of the fit. The values of the calibration constant A obtained from the fits are close to the designed value of $16.44 \mathrm{mm}/\sqrt{\mathrm{cm}^{-1}/\mathrm{V}}$.

where E_γ is the photon energy of the laser (calibrated to within 0.02 cm^{-1}), E_{th} is the atomic threshold energy of the corresponding PD channel, and D_0 is the dissociation energy of the rovibronic ground state KRb molecule (see Tab 4.2). The proportionality constant accounts for the fraction of the total PD kinetic energy release partitioned into the K photofragment. In the case of Fig. 4.10 (b), the KE of ions belonging to the inner and outer Newton spheres are calculated to be 11.67 and 24.52 cm^{-1}, respectively.

Fig. 4.12(a) shows a summary of R and KE obtained at different wavelengths. Contributions from the two different PD channels are color-coded. Time-slice analysis was used to extract R for all data points except for the two with the lowest KE, where the ion TOF distribution are not sufficiently broad to time-slice. In these two cases, inverse Abel analysis[63] using the PyAbel software package[104] was employed. The data set is fitted to the function $R^2 = A^2 KE/V_R$ to determine the calibration constant A.

For "high energy" calibration, V_R is set to 992 V. We photodissociated KRb into K 4S + Rb 6P and ionized Rb 6P to produce Rb$^+$ ions with KE in the 0 - 450 cm^{-1} range (Fig. 4.11 (a)) by varying the UV laser wavelength (photon energy) between 358 nm (27933 cm^{-1}) and 340 nm (29412 cm^{-1}). The magnetic field is 30G at the KRb cloud location. The ion image acquired at 346 nm and its time-slice are shown in Fig. 4.11 (f) and (g). R is determined

Table 4.2: Summary of relevant energies for KRb photodissociation and ionization. All values are relative to the ^{40}K ^{2}4S$_{1/2}$ + ^{87}Rb ^{2}5S$_{1/2}$ asymptote at zero energy. D_0: dissociation energy; E_{th}: atomic threshold energy; IP: ionization potential.

Quantity	Energy (cm^{-1})	Reference
D_0 (^{40}K^{87}Rb)	-4180.42	[162]
E_{th} (^{40}K 5^2P$_{1/2}$ + ^{87}Rb 5^2S$_{1/2}$)	24701.38	[142]
E_{th} (^{40}K 5^2P$_{3/2}$ + ^{87}Rb 5^2S$_{1/2}$)	24720.13	[142]
E_{th} (^{40}K 4^2S$_{1/2}$ + ^{87}Rb 6^2P$_{1/2}$)	23715.08	[177]
E_{th} (^{40}K 4^2S$_{1/2}$ + ^{87}Rb 6^2P$_{3/2}$)	23792.59	[177]
IP(^{40}K)	35009.81	[178]
IP(^{87}Rb)	33690.81	[177]

through inverse Abel analysis for the lowest KE data point and through time-slice analysis for all others. The data analysis follows the same procedures as for the "low energy" case and the results are shown in Fig. 4.12 (b). All identified Newton spheres are assigned to the K ($4S_{1/2}$) + Rb ($6P_{1/2}$) PD channel. Contributions from the K ($4S_{1/2}$) + Rb ($6P_{3/2}$) channel, which is 77.51 cm^{-1} higher in energy (see Tab. 4.2), were not identified from any of the ion images. The calibration constants for both the "low energy" (15.11 ± 0.05 mm/$\sqrt{\text{cm}^{-1}/\text{V}}$) and "high energy" ($15.60 \pm 0.11$ mm/$\sqrt{\text{cm}^{-1}/\text{V}}$) settings obtained from fits are reasonably close to the design value of (16.44 mm/$\sqrt{\text{cm}^{-1}/\text{V}}$).

4.4.3 Optimization of VMI

An important feature of velocity-map imaging , as its name suggests, is that the final ion image should directly reflect the velocities of the ions, independent of the spatial positions at which they are born. In physical implementations of VMI, however, such mapping only holds true for ions born within a finite spatial extent around the origin, which is typically defined as the point halfway in between the repeller and extractor plates lying along the TOF axis. This defines the region-of-interest (ROI) for our photoionization.

To explore the extend of the ROI in our VMI setup, we simulated the hit location ($\{y', z'\}$) of ions with zero initial velocity on the MCP detector for different initial ion born locations ($\{x, y, z\}$). The simulations are performed with the repeller voltage set to $V_R = 100$ V, and under a magnetic field of $B = 30$ G. The coordinate system is defined according to the schematic illustration in Fig. 4.13(a). Since the problem possesses cylindrical symmetry about the x-axis, we scanned the ion born location within the xy-plane. Fig. 4.13(b) shows the y' as a function of y for $y \in [-3, 3]$ mm, along the axes defined by $x = -1, 0$ and 1 mm, respectively. From the blue trace, which corresponds to $x = 0$ mm, we observe minimal dependence of the ion hit
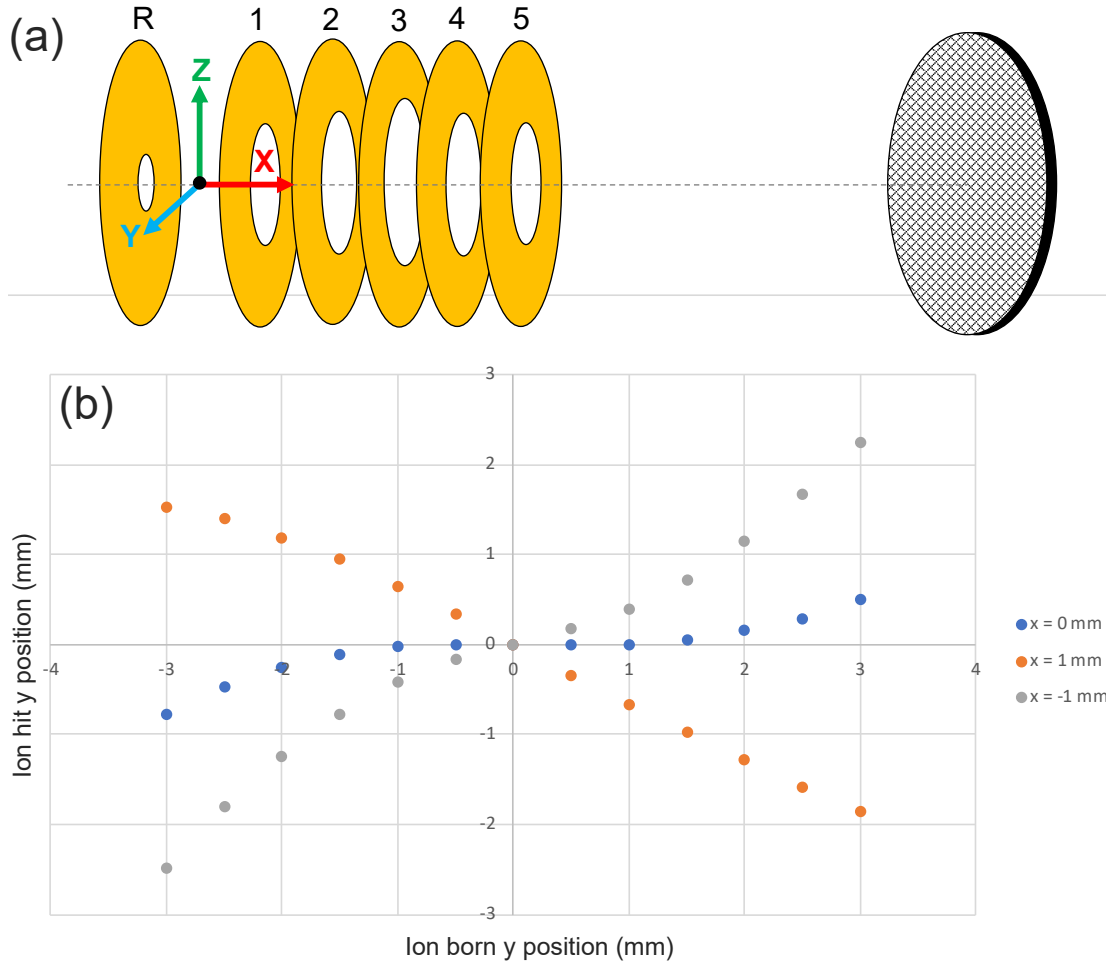
Figure 4.13: Optimization of the VMI (simulation). (a) Schematic of the VMI setup. (b) The y coordinate of the ion hit position on the detection as a function of the y coordinate of the ion born position, obtained from SimIon simulation of ion trajectories. The different colored series represent different x coordinates of the ion born location, as specified by the legends.

location on its born location for deviations of less than 1 mm from the origin in either directions along the y axis. The tolerance for deviation along the x-axis is smaller, around ± 0.75 mm. Note that the symmetry for deviations in positive and negative y-directions is broken by the magnetic field. From these results, we find the ROI for our ionization to be a sphere with a radius of 0.75 mm, centered around the origin.

Experimentally, we place the reactant cloud at the origin of the VMI setup using the following scheme (see inset of Fig. 4.14(a)). We prepare a cloud of Rb atoms at a temperature of 30μK trapped inside the HODT, which propagates along the y direction. The cigar-shaped Rb cloud has an overall length of ~ 10 mm. We then use a 296 nm UV beam with a small waist ($\sim 50\mu$m) to generate Rb^+ ions at different locations along the cloud, and record their (centroid) hit locations on the detector. This allows us to generate a plot as shown in Fig. 4.14(a), similar to the simulated one in Fig. 4.13. In this case, the origins are defined as the ion born and hit locations for an arbitrary rough alignment of the beams. By scanning the positions of both the HODT and the UV beams, we varied the born location of the Rb^+ ion packet in the xz-plane and along the y-axis respectively. From the measured hit location dependence, we identified a region of ion born locations within which this dependence is minimal*, matching up with the simulation. The center of this region, $\{x = -0.8, y = 1, z = 0\}$ mm, corresponds to the true origin of our VMI system. The VODT is then aligned to be co-propagating with the UV beam, such that the XODT trapping the KRb cloud is formed at the true origin.

Finally, we compare the spatial images associated with ions born within and outside the ROI for ionization, respectively. Since the Rb^+ ions bare almost no initial momentum, we expect their ion image to be a resolution-limited small dot. Fig. 4.13(b) shows the image for ions born at $\{x = 0, y = -3, z = 0\}$ mm, which is significantly outside of the ROI; and (c) shows that for ions born at $\{x = -0.8, y = 1, z = 0\}$ mm, the center of the ROI. While (c) displays a

---

*a separate scan, not shown here, is carried out for the z direction

162
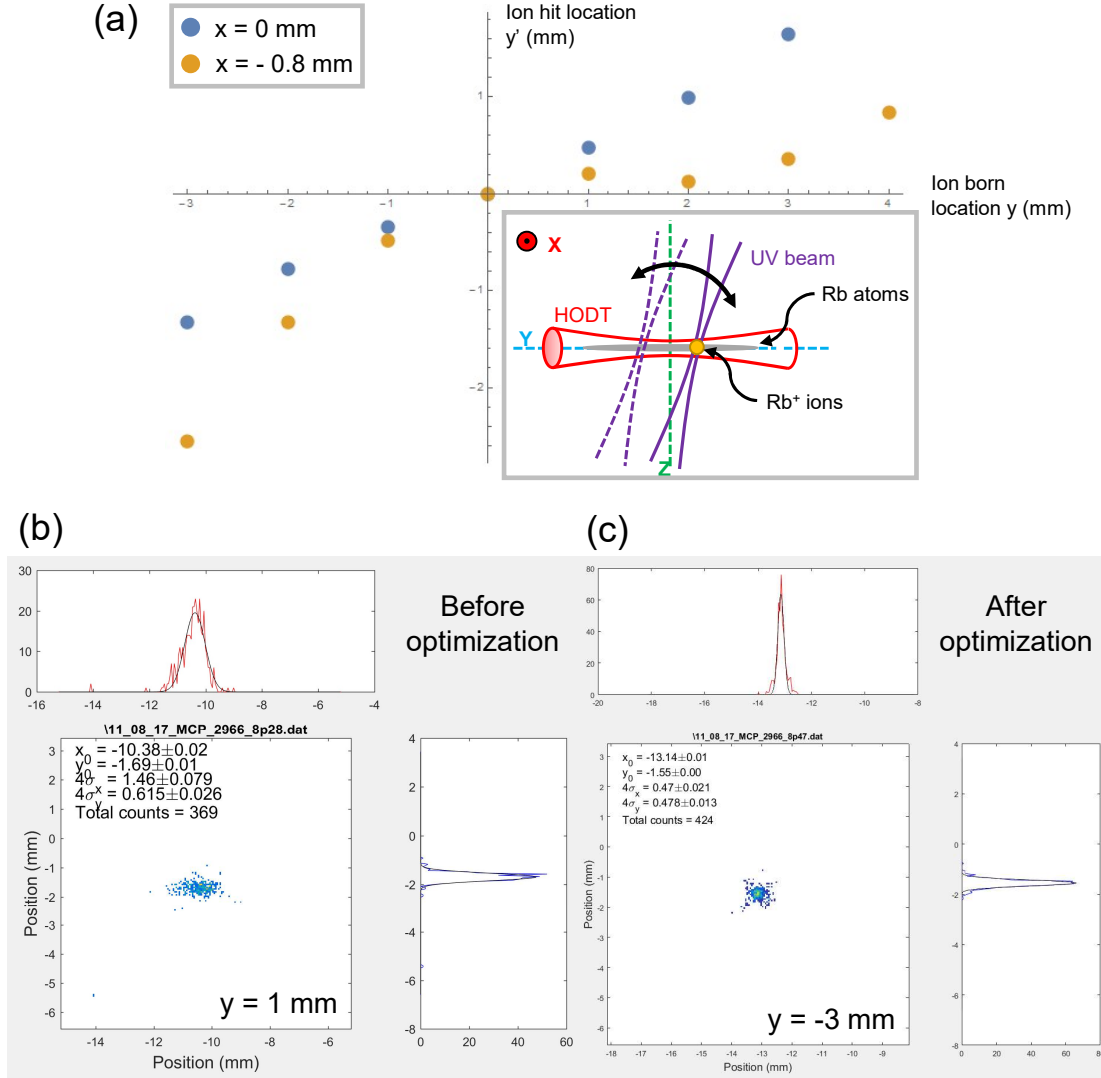
Figure 4.14: Optimization of the VMI (experimental). (a) Measured dependence of the y coordinate of the ion hit location on that of the ion born location. Blue and yellow series represent two trials in which ions are born with different x-coordinates, as specified by the legends. The origin of the coordinate system here is arbitrarily defined. Inset: schematic of the experimental setup for this measurement. A narrowly focused UV beam intercepts a portion an elongated cloud of Rb atoms trapped inside the HODT. The beam lies within the yz-plane and is scanned in this plane to produce Rb^+ ions at different positions along the y axis. (b) Distributions of the Rb^+ ions at $\{x = 0, y = -3, z = 0\}$ mm, which is significantly outside of the ROI for the VMI. (c) istributions of the Rb^+ ions at $\{x = -0.8, y = 1, z = 0\}$ mm, which is around the center of the ROI for the VMI.

163

circular spot with sizes consistent with the resolution limit, (b) shows an spot that is elliptical and significantly broadened. This example illustrates the importance of searching for the ROI for ionization, and provides a convenient way to check the alignment of the reactant KRb cloud with respect to the VMI setup.

4.5 Ion spectrometry in the presence of magnetic fields

We close out this chapter by discussing the effects of magnetic fields on ion spectrometry. In all of our experiments, an external magnetic field is required to maintain spin quantization of the KRb molecules, such that they collide via the p-wave channel. This presents unique challenges to performing ion spectrometry, as the Lorentz force experience by ions moving through the field results in deviations of their flight path. Prior works on KRb were performed at close to the Feshbach field (546 G)[154,162]. In our experiment, field of such a strength would cause the ions to completely miss the MCP detector. Further more, stray magnetic field can deform ion Newton spheres as they expand, resulting in distorted ion images that yield sub-optimal KE resolution[80]. While magnetic fields can be shielded away in most ion imaging experiments, this is not an option for us.

In order to minimize the magnetic field during VMI while maintaining KRb quantization, we investigated the loss of KRb molecules in the presence of varying magnetic field strengths. After the ground-state molecules are associated via STIRAP at 544.1 G, we ramp down the field produced by the Feshbach coil to a value B_{FB} over 5 ms, while keeping the field from the fast B coil at a constant value of -5.9 G. This produces an overall field of $B_{\text{hold}} = B_{\text{FB}} - 5.9$ G. Molecules are held at B_{hold} for 100 ms, during which their population decays via two-body collision. After the hold, the field is ramped back up to 550 G over 40 ms, and the molecules are dissociated into atoms for imaging. If B_{hold} dips below the minimum field required to maintain

164
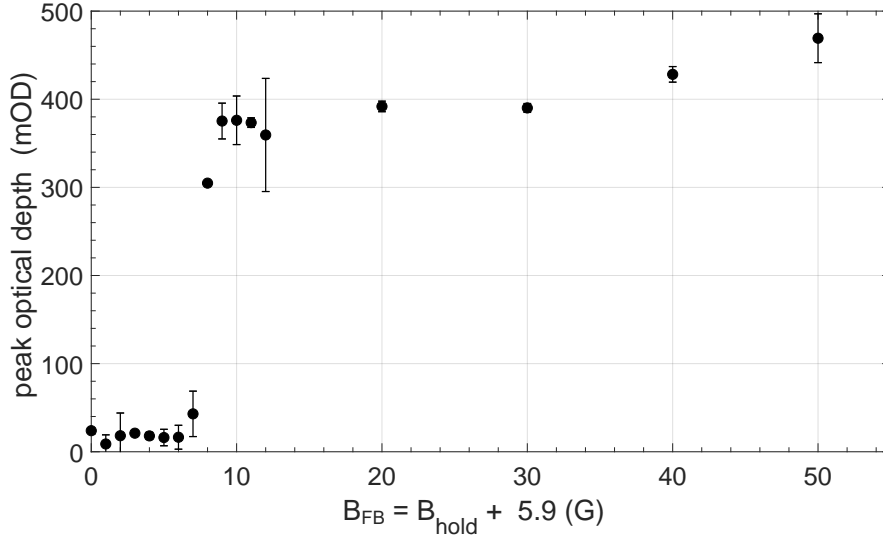
Figure 4.15: Maintaining the spin quantization of KRb. The pkOD of an intially spin-polarized cloud of KRb molecules is measured after it is held inside the XODT, for a duration of 100 ms, under different values of quantization magnetic field, B_{hold}. Note that x axis represents the magnetic field produced by the Feshbach coil, B_{FB} during the measurement, which can be converted to B_{hold} by subtracting a 5.9 G field produced by the fast B coil during the measurement. We observe a loss of KRb spin quantization for $B_{\text{hold}} \lesssim 2$ G.

quantization, KRb molecules in the sample will proceed into statistically mixed spin states and therefore loose their indisinguishability, allowing collisions to occur via the s-wave. At 500 nK, s-wave collisions occur ~ 40 times faster than p-wave[162], leading to much higher losses during the hold. The result is shown in Fig. 4.15, where the pkOD of the back-converted Rb molecules is plotted against B_{FB}. We find the minimum field required to maintain p-wave collision to be 2 G. Note that the slight decrease in the peak OD going from 50 G to 10 G is due not to increased loss rate, but instead to a reduction in the back-conversion efficiency as a result of oscillations in the field after it is ramped quickly across 500 G.

To characterize the distortion of ion images by the magnetic field, we monitored the VM images of K^+ ions resulting from the 298 + 298 nm two-photon ionization recoil (4.4) at four
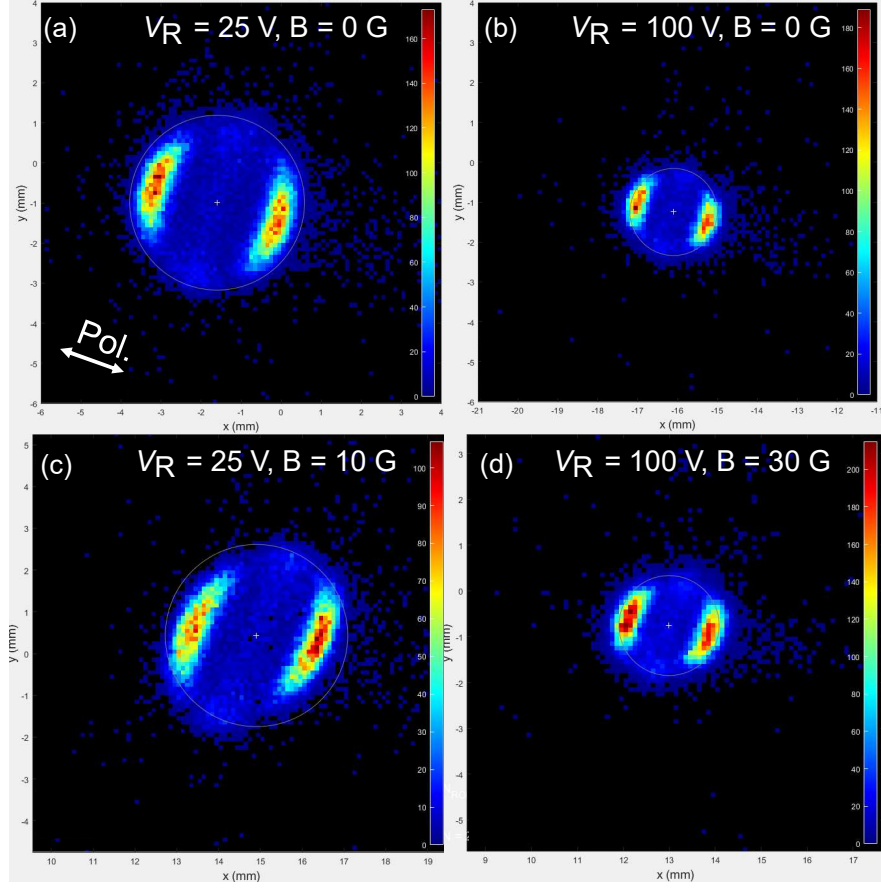
Figure 4.16: Distortion in ion recoil patterns observed at different electric and magnetic fields. White double arrow indicates the direction of the ionization laser polarization, which is the same in all plots.

different repeller voltage (V_R) - magnetic field (B) combinations*. The results are shown in Fig. 4.16. In the absence of magnetic fields (a,b), the ion image are highly circular, and are symmetric about the axes along and perpendicular to the polarization of the ionization laser. In the presence of magnetic fields (c,d), the images are sheared out of symmetry. In general, we find the distortion to be stronger for lower V_R and ions with larger KE. While a lower V_R magnifies the VMI images and help reveal detailed structures, this effect limits us to $V_R > 50V$. In many

---

*Here and throughout the thesis, we specify the magnetic field during VMI by its value at the center of the science chamber. In reality, the field varies along the TOF path and the overall pattern is quite complicated.

ion imaging experiments, image distortions can be attributed to the presence of stray electric and/or magnetic fields. We have attempted to reproduce the observed distortion in simulation, by adding stray electric or magnetic fields around the ion born location in addition to the intended fields during VMI. We could not, however, find a stray field configuration that led to the type of distortions observed. As such, the exact mechanism giving rise such a mode of distortion remains unclear. Fortunately we were able to largely avoid these effects – for most experiments in which the quality of the ion image is important, we use $B = 5 - 30$ G and $V_R = 100.2$ V.

Chapter 5

Direct observation of bimolecular reactions of ultracold KRb molecules

Equipped with the ability to prepare ultracold KRb molecules and the universal ionization detection technique, we set out to investigate the bimolecular reaction

$$KRb + KRb \rightarrow K_2 + Rb_2. \tag{5.1}$$

This reaction was first proposed in Ospelkaus *et al.* [162] as the mechanism underlying the two-body loss in a trapped gas of ultracold KRb molecules observed therein. At the time of its discovery the result came as a surprise, as it suggests that counter to common intuitions, chemistry is not halted at near-absolute-zero temperature, but rather remains quite active. The validity of this assumption, however, is supported by the following facts: 1. since all KRb molecules in the sample are prepared in the absolute rovibronic and hyperfine ground state, state-changing (inelastic) collisions – a common loss mechanism in ultracold gases – are not possible; 2. the reaction is exothermic by $\sim 10\,\text{cm}^{-1}$ according to spectroscopic data on the binding energies of

the reactants and products; 3. theoretical calculations by Byrd *et al.*[37] shows that the reaction lacks a chemical barrier at the short-range, but rather proceed through a ~ 3000 cm^{-1} deep potential well that corresponds to the four-atom complex K_2Rb_2 (Fig. 1.4). Taken together, the latter two points makes the reaction allowed even at ultracold temperatures.

The losses observed above challenged the suitability of KRb as a platform for the many applications it promises, including the creation of strongly-interacting dipolar quantum gases, and the realization of novel quantum phases[179,33,130]. Since chemical reactions were assumed to be the culprit for the loss, the race to create dipolar molecular samples that are stable against reactions was on. These are represented by molecules AB, for which the bimolecular reaction AB + AB is endothermic and therefore frobidden and ultralow temperatures. For bi-alkali molecules, which represented the most promising candidates to realized molecular quantum gases, these include NaK, NaRb, NaCs, KCs, and RbCs[227]. Over the past decade, ultracold gases of most of these species have been realized in labs around the world[196,220,88,165], via schemes similar to that used to create KRb (section 1.2). However, rapid two-body losses were still observed in gases of these molecules, with rate constants similar to that observed for KRb + KRb. Furthermore, experiments performed with NaRb molecules in either the ground vibrational state ($v = 0$) and the first excited one ($v = 1$), for which the reaction NaRb + NaRb $\rightarrow$ Na$_2$ + Rb$_2$ is either endothermic or exothermic, demonstrated no significant differences in the loss rate constants. These observations call into question whether the previously observed loss of KRb was indeed due to reactions, and more broadly the exact loss mechanism(s) in bi-alkali molecular gases. To answer these questions, we first search for direct evidences, or lack thereof, for the KRb + KRb reaction.

5.1 Detection of reaction products

We begin our investigation with a search for the reaction products K_2 and Rb_2. We prepared a gas of 5000 KRb molecules confined inside the XODT, at a temperature of 500 nK and a peak density of 10^{12} cm^{-3}. All molecules are formed in the $|m_K = -4, m_{Rb} = 1/2\rangle$ hyperfine state of the $X^1\Sigma^+(v = 0, N_{KRb} = 0)$ rovibronic ground state under a 30 G quantization magnetic field. After the sample is prepared, we measured the optical depth (OD) of the cloud as a function of time (Fig. 5.1), and observed the same two-body decay as found in Ref.[162], described by the equation

$$n(t) = \frac{n(t = 0)}{1 + t/t_{1/2}}. \tag{5.2}$$

Here, n denotes the peak density of the gas and is proportional to the peak OD obtained from absorption images of the cloud. By fitting the data in Fig. 5.1(a) to Eq. 5.2, we extract a decay halflife of $t_{1/2} = 258 \pm 25$ ms. We also measured the temperature of the cloud over the course of the decay, and find it to be essentially constant (Fig. 5.1(b)).

To probe for the reaction products, we tuned the UV wavelength to 285 nm, and shaped it into the crossed hollow-bottle beams as shown in Fig. 2.32. This wavelength corresponds to a photon energy that is above the IP of all species that are potentially found in our system4.1. To observe the reaction without the possible influence of the ODT light, we shut off the ODT for 170 μs prior to each ionization pulse, thereby precluding any role of the ODT in the formation of all but those products with translational energy less than 0.0127 cm^{-1}*. In each experimental cycle, the ROI for ionization is exposed to UV pulses with 100 μJ of energy (summed power of the two beams), at a repetition rate of 1 kHz, for a duration of 500 ms (Fig. 5.2 inset). Ions generated by each pulse are then accelerated onto the MCP detector, with the electric field plate

---

*170 μs is the time it would take for a Rb$_2$ molecule with translational energy of 0.0127 cm^{-1} to travel from the center of the KRb cloud to the ionization ring with a diameter of 0.45 mm
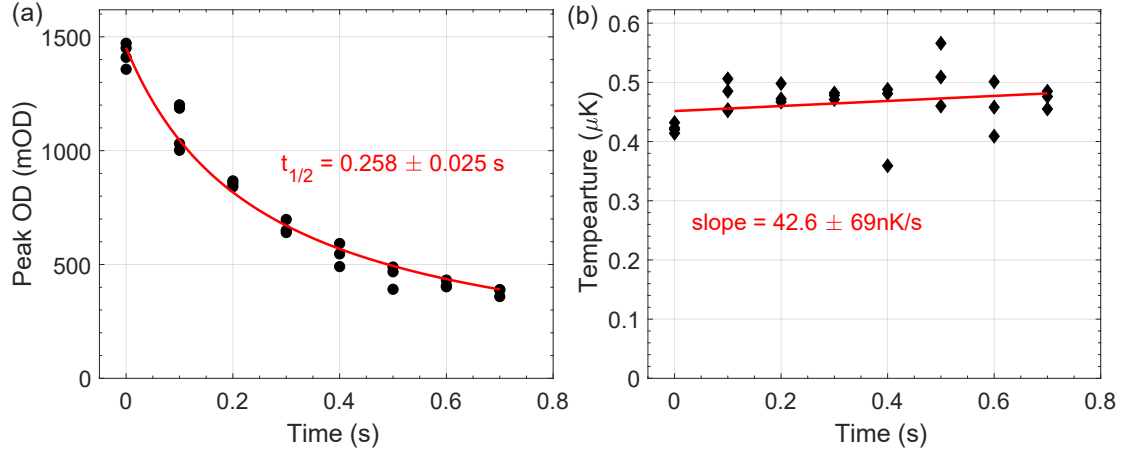
Figure 5.1: Decay and heating of the ultracold KRb gas measured by absorption imaging (section 3.1). (a) Decay of the peak optical depth (in units of milli-optial-depth) of a gas of KRb molecules over time. Here, time zero is defined as right after the ground-state molecules are first created by STIRAP. The peak OD of the gas is proportional to its peak number density, which are not directly reported here due to some uncertainties in the density calibration. The decay is consistent with a two-body loss described by Eq. 5.2, with a half-life of 256 ± 25 ms. (b) The temperature of the gas over time, showing a heating rate that is consistent with zero.

stack operating in VMI condition and the repeller voltage set to $V_R = 992$ V. A side effect of the UV light in our experiment is the generation of background ions from surfaces within the science chamber. This effect is discussed in more detail in Appendix D. In order to distinguish these from the ions of interest, we record a "background" dataset in additional to the "signal" dataset in each cycle. After the signal is recorded, the ODT is switched off for 400 ms to dump any species still remaining iniside, and the background is then recorded using the same timing sequence, but in the absence of any species of interest.

After data accumulation for over 1000 experimental cycles, we obtain the mass spectrum as shown in Fig. 5.2(a). The most dominant signal peaks, highlighted by bold black traces, correspond to K^+ ($m = 40$), Rb^+ ($m = 87$), and KRb^+ ($m = 127$). To understand the origins of these signal, we examined their associated ion images, as shown in Fig. 5.3(d) for KRb^+ and Fig. 5.4 (a,b) for K^+ and Rb^+. The KRb^+ image displays a small spot that is resolution-limited
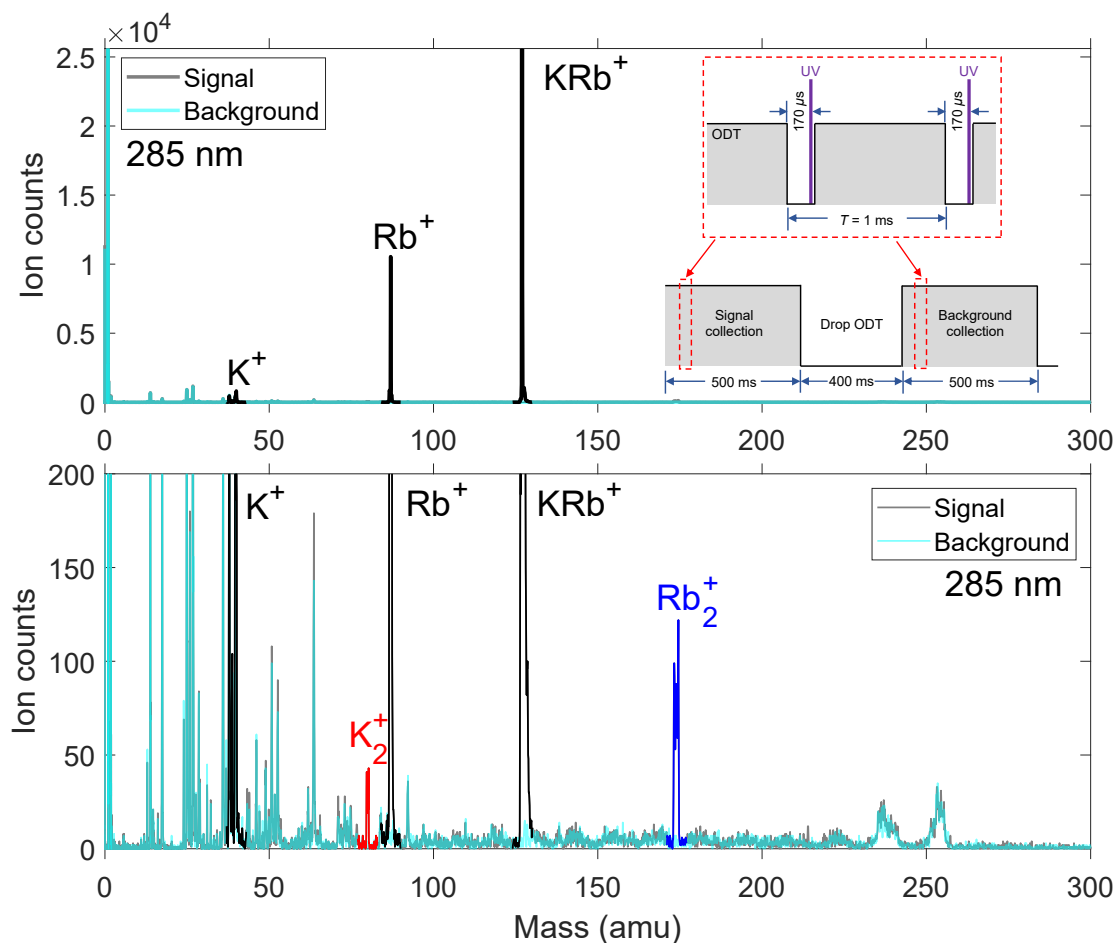
Figure 5.2: The TOF mass spectrum of the reaction products ionized by 285 nm UV laser pulses. Black and cyan traces the signal and background spectra, recorded respectively in the presence of absence of reactant molecules. Upper panel shows the spectra in their full scale, while the lower panel zooms in closer towards the noise floor to show product signals (highlighted as red and blue). Noise ions that show up in both the signal and the background spectra have no significant effect on the ion signals of interest (see Appendix D). Inset: timing scheme of the ODT and pulsed UV lasers used for this measurement.

in size, indicating that they originate from the single-photon ionization of the ultracold KRb molecules within the XODT. This is attributed to a small but finite amount of UV power present at the center of the hollow-bottle beams. The images for K^+ and Rb^+ both display two distinct components: an isotropic central peak and an anisotropic ring. The ions forming the central peak

172
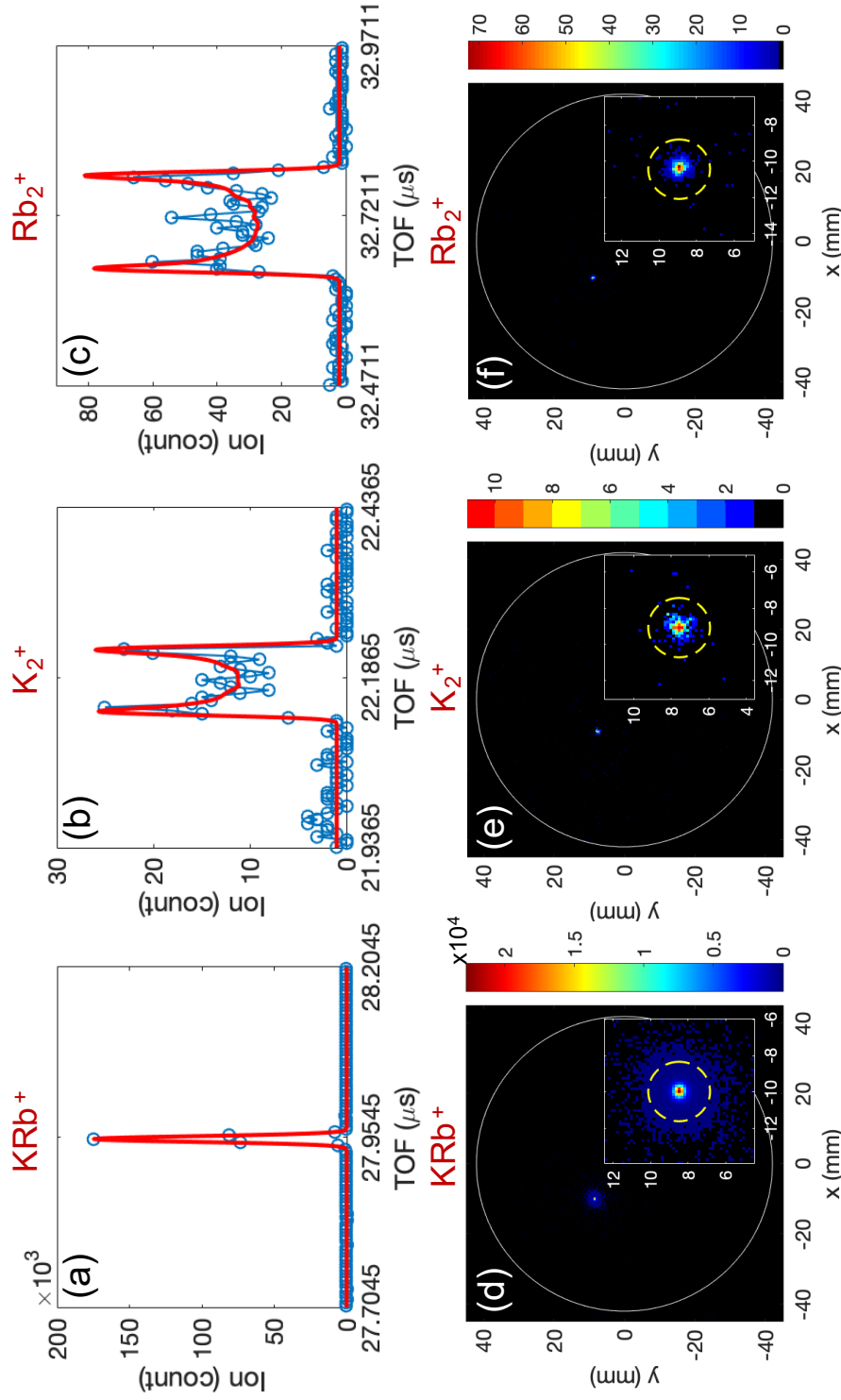
Figure 5.3: (a - c) The TOF distribution for KRb$^+$, K$_2^+$, and Rb$_2^+$ ions, respectively. The red curve in (a) is a time resolution limited Gaussian to describe TOF lineshape for the ions generated in the center, while those in (b) and (c) are simulated TOF lineshapes for the ions generated by the hollow-bottle beams (Fig. 2.32). For the simulation, we use physical parameters of our system such as the diameter of the beams, 0.45 mm, their, 40°, and the VMI electric field (section 2.5.2). The only fitting parameter in this model is the overall amplitude of the signal. (d - f) The ion images of the KRb$^+$, K$_2^+$, and Rb$_2^+$ ions, respectively. The white solid circles represent the active area of the detector. The yellow dashed circles represent 9.53 cm^{-1}, which is the exothermicity limit.

173
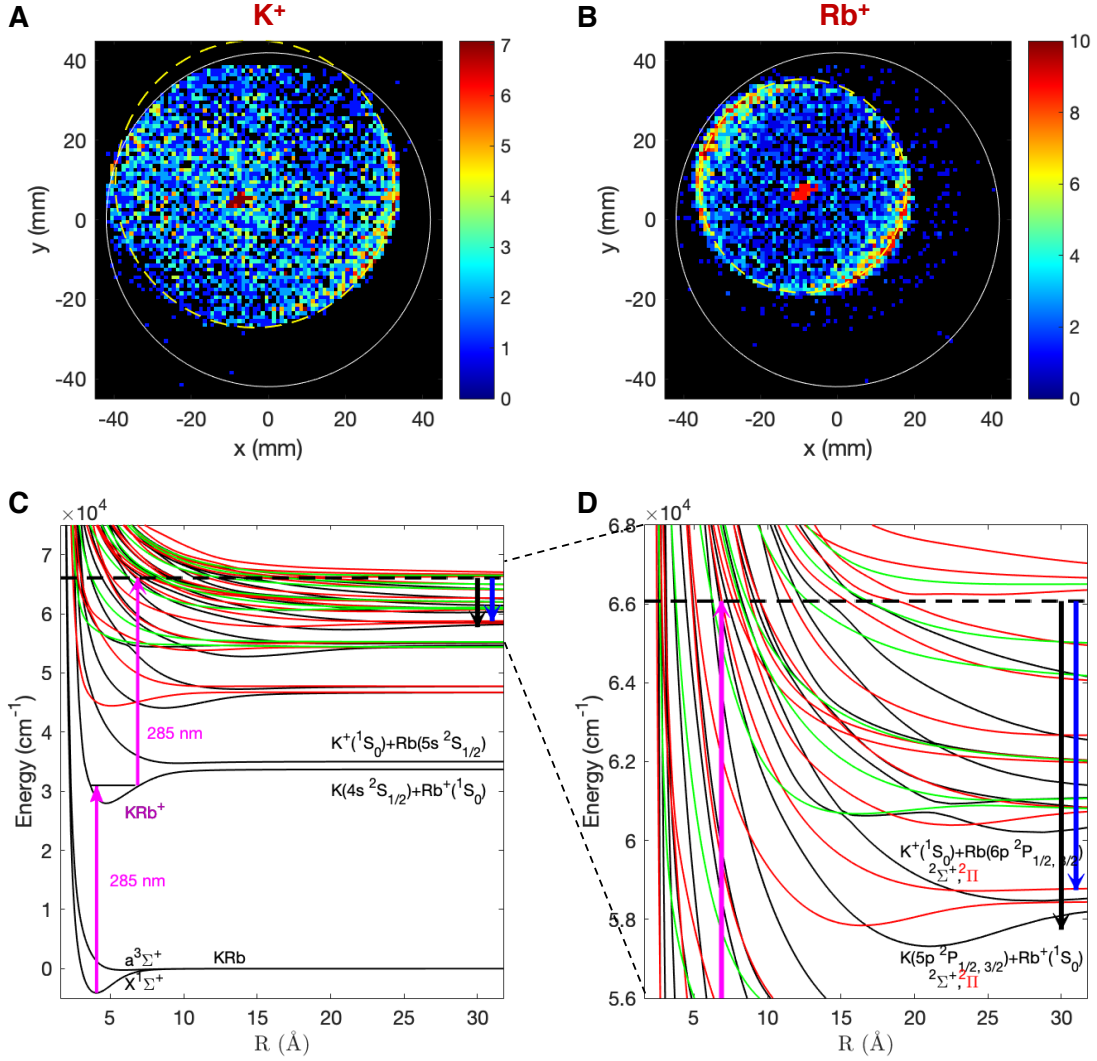
Figure 5.4: Photoionization of GS KRb molecules. (**A-B**) Measured VMI signals of K^+ and Rb^+ ions at 285 nm and $V_R = 1000$ V. The white circles represent the detector active area. The yellow dashed circles correspond to the momenta of the K^+ and Rb^+ ions acquired during the dissociative ionization of ground state KRb molecules. The radius of the yellow circle for the K^+ (Rb^+) ions is 37 mm (26 mm) corresponding to TER of 0.73×10^4 cm^{-1} (0.83×10^4 cm^{-1}). (**C-D**) Energy diagram for KRb and KRb$^+$ molecules. The potential energies of the electronic states of molecular KRb$^+$ ions are taken from [122]. The magenta arrows represent the photon energy of the ionization laser. KRb$^+$ ions are generated via single-photon ionization. In addition, K^+ and Rb^+ ions are generated via two-photon dissociative ionization, during which the released energy is distributed between Rb$^+$ (Rb) and K (K^+) according to their mass ratio. The measured TER, 0.73×10^4 cm^{-1}, from the VMI signal of K^+ ions in (**A**) is drawn as the blue arrow above, which matches the energy of the dissociative ionization channels, $K^+(^1S_0) + Rb(6p\ ^2P_{1/2,3/2})$. The measured TER, 0.83×10^4 cm^{-1}, from the VMI signal of Rb$^+$ ions in (**B**) is drawn as the black arrow above, which matches the energy of the dissociative ionization channels, $K(5p\ ^2P_{1/2,3/2}) + Rb^+(^1S_0)$.

174

originate from residual ultracold atoms from the molecule creation process after the cleanup pulses. Based on the known ionization cross sections and estimated ion detection efficiencies (Tab. 4.1), we put an upper bound of 250 atoms of each species in the trap. These populations are small compared to KRb, ensuring that the dominant reaction in the subsequent study is the desired bimolecular reaction. The sensitivity of ionization detection allowed us to quantify the small number of residual atoms in the ODT, which are not seen using absorption imaging. To analyze the Rb^+ ions forming the ring pattern, we extracted the kinetic energy release (KER) from the diameter of the ring to obtain a KER of 8.3×10^3 cm^{-1}. By comparing this KER to the calculated molecular potentials of KRb and KRb$^+$ [122] (Fig. 5.4(c,d)) we identified a two-photon dissociative ionization pathway that contributes to this atomic ion signal. The same analysis also applies to the ring pattern of the K^+ ions (Fig. 5.4(b)).

Zooming in on the vertical scale in Fig. 5.2(a) to examine ion signals near the noise floor, we obtain the mass spectrum in Fig. 5.2(b). In the signal spectrum (gray), we observe many more mass peaks, most of which are identically reproduced in the background spectrum (cyan) and are therefore attributed to background ions. Besides these, we identify two strong peaks found only in the signal and not the background spectrum, located at 80 and 174 amu. These peaks, highlighted in red and blue, correspond to the masses of K_2^+ and Rb_2^+ ions, respectively.

We postulate that K_2^+ and Rb_2^+ come from direct ionization of reaction products, K_2 and Rb_2. To support such an assignment, we draw evidence from the TOF distributions and the ion images. As we have discussed in section 4.3, the TOF distribution of an ion species characterizes its spatial origin. The KRb$^+$ distribution (Fig. 5.3(a)) is sharp in time and described well by a time-resolution limited Gaussian, corresponding to ions that originate from within the XODT. In comparison, the K_2^+ and Rb_2^+ distributions, as shown in Figs. 5.3(b) & (c), are much wider than that of KRb$^+$. The unique shapes of these distributions, characterized by peaks on the edges and a dip in between, are matched well by simulated distributions for ions that originate from the

175

high intensity portions of the hollow-bottle beams (see Appendix C for details). This supports the assignment of the origin of these signals as reaction products escaping the KRb cloud and ionized by the crossed hollow-bottle beams. The presence of a center peak in both Fig. 5.3(b) and (c) that is not captured by the simulated curve is likely due to the product ionization at the "dark" center of the hollow beams, where the product density is very high (see 4.2.1).

In addition to TOF distribution, we also analyzed the translational kinetic energy (KE) distribution of K_2^+ and Rb_2^+ using their ion images (Figs. 5.3(e) & (f)). To characterize the radius of the distribution, we performed simple Gassuain fits to the images. The 1σ radius of K_2^+ (Rb_2^+) corresponds to a translational energy of 0.59 cm^{-1} (0.29 cm^{-1}). The ionization process of K_2 (Rb_2) would impart to the resulting ion a photon recoil energy of 0.0159 cm^{-1} (0.0112 cm^{-1}), too small to significantly impact the momentum distribution of the ions. Therefore, the measured K_2^+ and Rb_2^+ translational energies closely resemble that of their parent neutrals. The sum of measured translational energies is smaller than the exothermicity, 9.53(7) cm^{-1}, of the reaction. Further, their translational energy ratio, 0.49 ± 0.06, is consistent with the expected ratio, 0.46, originating from two different mass products flying apart with zero center-of-mass momentum (see section 7.4.2). This provides further evidence that supports the identification of K_2^+ and Rb_2^+ ions as arising from ionization of the products of the KRb + KRb chemical reaction. More detailed analysis to extract the actual KE distributions of the K_2^+ and Rb_2^+ ions is reserved for later experiments, the repeller voltage is lowered to $V_R = 100$ V to magnify their images (see section 7.4.1).

The unambiguous detection of the reaction products here provides the first direct evidence for the KRb + KRb reaction observed a decade ago, and enables further explorations of its dynamics in the ultracold regime.

176
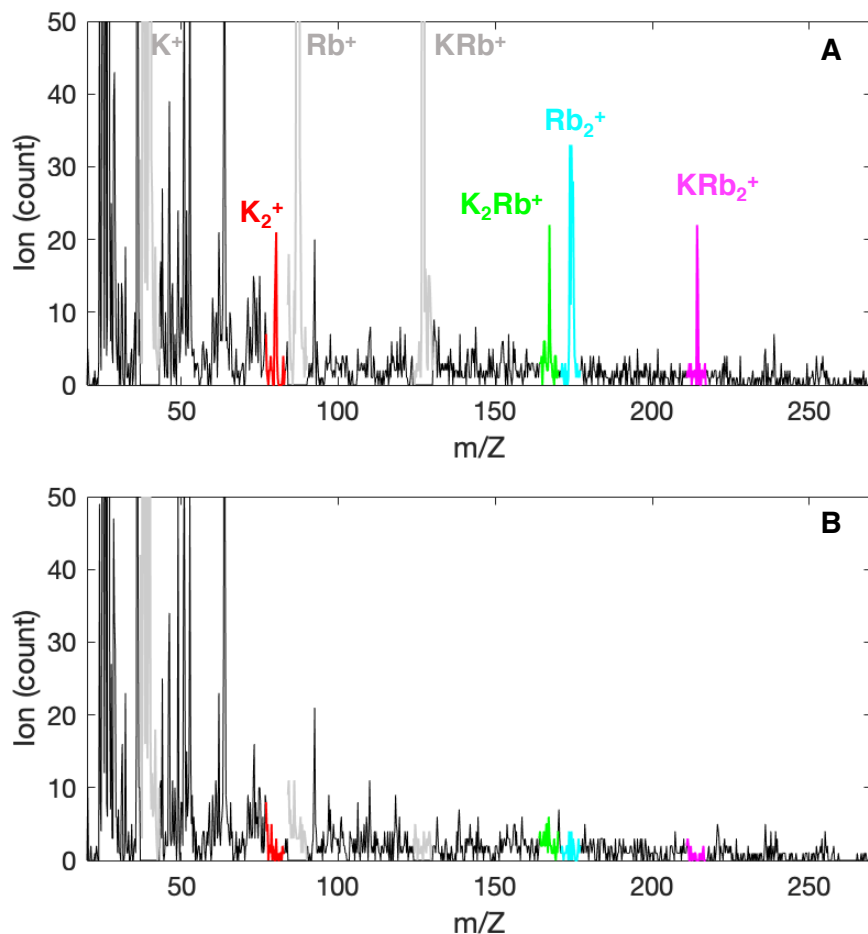
Figure 5.5: Mass spectra recorded as the reaction is probed by a 285 nm UV laser with a Gaussian beam profile. (A) Signal spectrum. (B) Background spectrum. Peaks corresponding to species of interest are color-coded and labeled. Besides the previously observed K_2^+ and Rb_2^+ peaks, clear signals associated with the triatomic ions are observed.

5.2   Understanding triatomic ion signals

After identifying the reaction products, we turned our attentions to other signals observed in mass spectroscopy whose origins are less obvious. Fig. 5.5 shows the signal (a) and background (b) mass spectra obtained using a detection scheme identical to that described in the previous
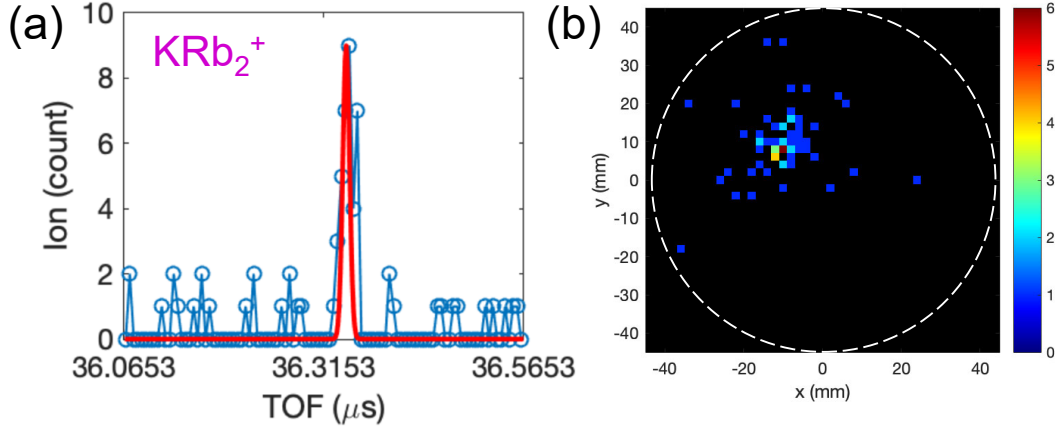
Figure 5.6: KRb_2^+ ion signal in the TOF and spatial domain. (a) TOF distribution of the triatomic ions, showing a resolution limited width similar as that associated for the KRb^+ ions (Fig. 5.3(a)), indicating that the ions originate from within the ODT; (b) The spatial image of the ions showing an extended distribution that corresponds to a characteristic kinetic energy of $\overline{KE} = 58 \pm 10$ cm^{-1}.

section, but with higher UV fluence present at the location of the KRb cloud. The stronger UV lead to higher KRb depletion and therefore lower data collection rate. Nevertheless, after several days of accumulation, we observed strong signals associated with not only the previously identified species, but also triatomic ions K_2Rb^+ and KRb_2^+. The detection of these ions was quite surprising, as the formation of their neutral counterparts, K_2Rb and KRb_2, are energetically forbidden at ultralow temperatures (see Fig. 1.4).

To investigate the origins of these ions, we turned again to their TOF and spatial distributions, as shown in Fig. 5.6. We focus our quantitative analysis on the KRb_2^+ distributions due to its relatively better signal-to-noise ratio (SNR), and note that the K_2Rb^+ distributions are quite similar. Fig. 5.6(a) shows a narrow distribution of KRb_2^+ in TOF, with a width comparable to that associated with the KRb^+ ions (Fig. 5.3(a)), indicating that they are generated from within the XODT. The ion image in Fig. 5.6(b), on the other hand, shows an very broad distribution, indicating that the ions carry substantial KE. Due to the low ion count in the image and presence

178

of substantial background ions, we cannot apply the inverse Abel analysis discussed in section 4.4 to extract the the radial and the corresponding KE distributions. Instead, we quantify the characteristic radius, $\overline{R}$, of the ion distribution by performing a Gaussian fit to the image with the assistance of Bayesian analysis (see details in Appendix E). While $\overline{R}$ can be straightforwardly obtained from the standard deviation of the ion distribution, the presence of background ions at large distances from the center can significantly skew the result. Bayesian analysis, on the other hand allows us to screen for signal ions based on "prior" knowledge of the characteristics of our ionization and detection system, and obtain a much more sensible $\overline{R}$. For the KRb_2^+ image in Fig. 5.6(b), we find $\overline{R} = 3.68 \pm 0.37$ mm. Given the calibration of our ion spectrometer (section 4.4.2), this corresponds to a characteristic kinetic energy of $\overline{KE} = 58 \pm 10$ cm^{-1}.

The characteristics of the TOF and spatial distributions of the triatomic ions led us to speculate that they come from dissociative photoionizations (Fig. 4.1(d)) of the $K_2Rb_2^*$ intermediate complex that is transiently-formed during the reaction, specifically

$$K_2Rb_2^* \xrightarrow{h\nu} K_2Rb^+ + Rb(5S) \quad \text{and} \quad K_2Rb_2^* \xrightarrow{h\nu} KRb_2^+ + K(4S). \tag{5.3}$$

Fig. 5.7(a) schematically illustrates the energy structure of $K_2Rb_2^+$, including its various dissociation channels, with the energy of the $K_2Rb_2^*$ complex on the ground-state potential energy surface defined as zero. All energy values here are calculated by O. Dulieu and collaborators, and specified in Fig. 5.7(a) in terms of the corresponding photon wavelength $\lambda_{UV}(E_{UV} = hc/\lambda_{UV})$, accurate to within ± 2 nm. Details of the calculation can be found in Ref.[107]. The minimum photon energy required to ionize $K_2Rb_2^*$ corresponds to a wavelength of 385.0 nm. As energy is increased above this level, multiple channels for dissociation into ion plus neutral fragments open up, including the triatomic ion plus atom processes described in Eq. 5.3, with threshold energies corresponding to 345.4 and 346.0 nm, respectively. UV light with photon energies
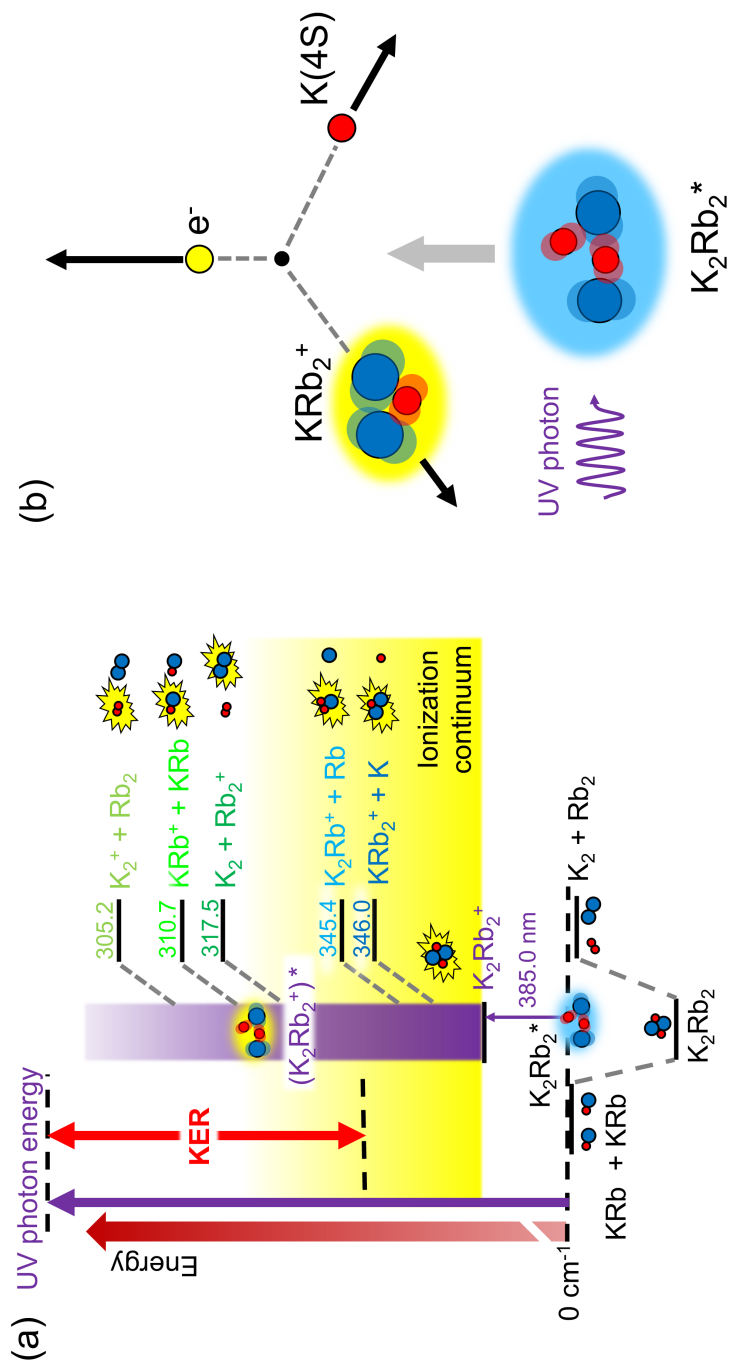
Figure 5.7: Ionization pathways of the intermediate complex. (a) Calculated threshold wavelengths of the direct photoionization and dissociative ionization of $K_2Rb_2^*$. The energies for the dissociative ionization thresholds are those corresponding to the equilibrium geometry of the ionic complex 4.1 and are therefore lower bounds on the ionization energy. (b) Schematic representation of the fragmentation of $K_2Rb_2^*$ in a dissociative ionization event. The excess photon energy is partitioned into the translational energies of the triatomic ion, the neutral atom, and the electron, as well as the internal energy of the triatomic ion (Eq. 5.4).

180
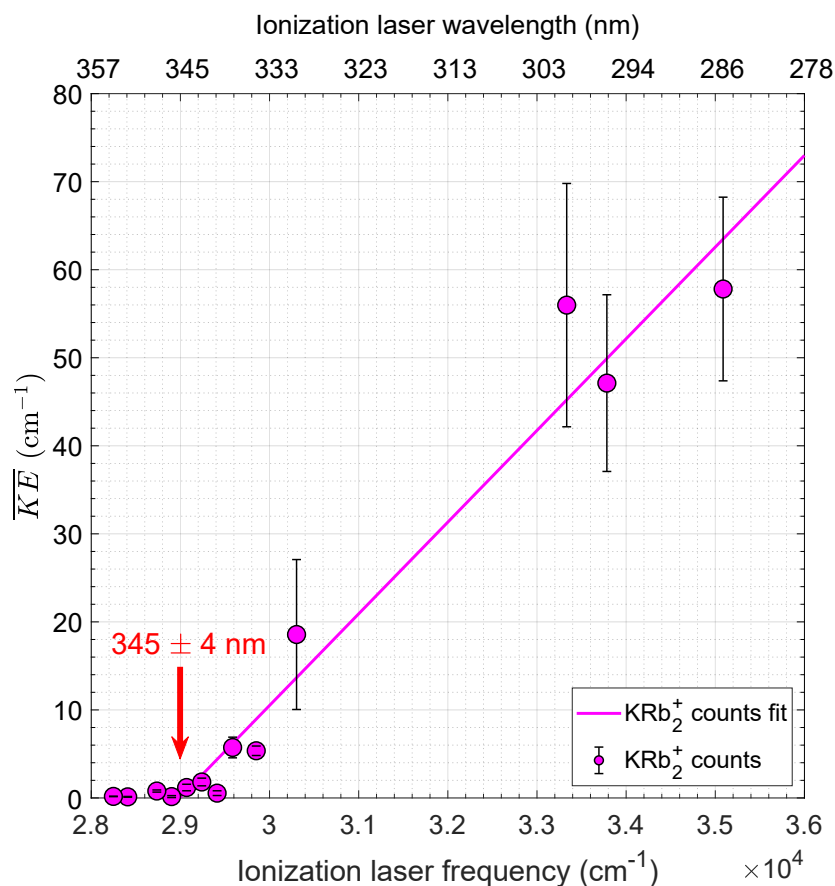
Figure 5.8: The characteristic translational energy ($\overline{KE}$) of the KRb$_2^+$ ions as a function of the ionization laser's wavelength (upper horizontal axis) or spatial frequency (lower horizontal axis). At each laser frequency, $\overline{KE}$ for the ions is determined from Bayesian fits described in Appendix E. Error-bars denote the standard deviation of the mean (standard error). The solid line is an unweighted linear fit to the data above 2.9×10^4 cm^{-1} with the RMSE being 1.44, from which an experimental dissociative ionization threshold wavelength of 345 ± 4 nm is determined.

exceeding these thresholds, *i.e.* the 285 nm light used to observe the triatomic ions, can lead to the dissociative ionization process as illustrated in Fig. 5.7(b). In this example, K$_2$Rb$_2^*$ is fragmented into KRb$_2^+$, K, and an electron (e^-). Here, the excess energy of the photon can be deposited into the kinetic energies (KE) of the fragments, as well as the internal (rovibrational)

energy (IE) of the triatomic ion, according to the relation

$$E_{\text{UV}} - E_{\text{th}} = KE(\text{KRb}_2^+) + IE(\text{KRb}_2^+) + KE(\text{K}) + KE(e^-) \qquad (5.4)$$

As such, we expect, in general, a distribution in kinetic energy for the KRb$_2^+$ fragment. The exact partitioning of energies into the various degrees of freedom is a complication question which we do not attempt to address in this work. Despite the lack of this information, we can expect that: 1. the majority of the excess energy should be carried away by the electron and the K atom, as dictated simultaneous energy and momentum conservation of the fragments; 2. the characteristic KE of KRb$_2^+$ should increase monotonically as a function of the excess photon energy.

To determine the behavior of the KE of KRb$_2^+$ as a function of the photon energy, we acquired images for the triatomic ions at different wavelength of the ionization laser, As shown in Fig. 5.8, the $\overline{KE}$ of the KRb$_2^+$ ions decrease monotonically as a function of the photon energy of the ionization laser, reaching zero at around 2.9×10^4 cm^{-1}, or 345 nm. This is consistent with photodissociative behavior. To extract the threshold of dissociation, we apply a linear fit to all data points in 5.8 with energy above 2.9×10^4 cm^{-1}, and obtain an x-intercept of 345 ± 4 nm, which agrees with the calculated value of 346 ± 2 nm for the K$_2$Rb$_2^*$ $\xrightarrow{h\nu}$ KRb$_2^+$ +K process. The $\overline{KE}$ obtained here are indeed small fractions of the corresponding excess photon energies. At 285 nm, for example, the excess energy is 6.2×10^3 cm^{-1}, whereas $\overline{KE} = 58 \pm 10$ cm^{-1}. The results here strongly support our hypothesis that the triatomic ions result from the dissociative photoionization of the transient intermediate complex.

Finally, we address the presence of KRb$_2^+$ ion signals even at photon energies below the dissociation threshold for K$_2$Rb$_2^*$ $\xrightarrow{h\nu}$ KRb$_2^+$ + K (Fig. 5.8), at which point this process becomes energetically forbidden. The images associated with these ions display resolution-limited spots,

indicating that they are generated by single-photon rather than dissociative ionization. Further-more, we find the amount of KRb_2^+ to have approximately a linear dependence on the amount of residual Rb atoms co-trapped in the XODT with the KRb molecules. These evidences led us to hypothesize that a small amount of KRb_2 is present inside our sample, formed by colli-sions between Rb and KRb, and the observed ions result from their single-photon ionization. These triatomic molecules can either be transient intermediates during the Rb + KRb collision, or weakly-bound KRb_2 complexes as a result of three-body processes, *i.e.* Rb + Rb + KRb. Systematic investigations of these possibilities are reserved for future experiments.

5.3   Detection of the intermediate complex

According to the understanding of the ionization and dissociation pathways as depicted in Fig. 5.7(a), it should be possible to covert $K_2Rb_2^*$ into an intact $K_2Rb_2^+$ ion using UV photons with energy below any dissociation thresholds for the tetratomic ion. To this end, we probed the reaction using an ionization wavelength of 356 nm. Since in this case the photon energy is below the IP of KRb (310.0 nm), we can afford to use much higher time-averaged UV powers ($7\,\text{kHz} \times 14\,\mu\text{J}$ per pulse $\sim 100\,\text{mW}$) to improve the data collection rate. After 300 experimental cycles of data accumulation, we obtain the mass spectrum as shown in Fig. 5.9. We identify strong signals at $m = 254$ amu, corresponding to the $K_2Rb_2^+$ ion. The kinetic energy associated with these ions is zero to within the resolution of our ion imaging, supporting the hypothesis that they originate from low COM velocity $K_2Rb_2^*$ complexes formed by collisions of ultracold KRb molecules. With a relatively high count rate of 0.3 ions per experimental cycle (later improved to 1 per cycle), the $K_2Rb_2^+$ signal observed here provides a direct and efficient proxy for the transient $K_2Rb_2^*$ complex, which we exploited in later experiments to study their dynamics (Chapter 6).

We also investigated and understood the origins of other ion signals present in Fig. 5.9. Both
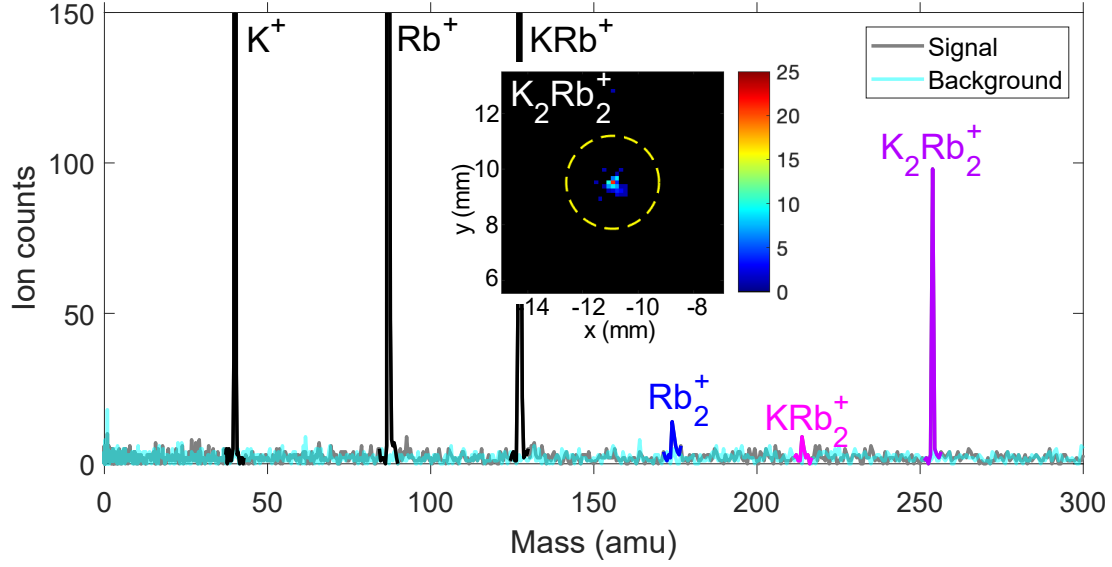
Figure 5.9: TOF mass spectrum produced using an ionization laser wavelength of 356 nm, which shows signals corresponding to $K_2Rb_2^+$. The presence of other species are explained in the main text. (Inset) The corresponding VM image of the detected $K_2Rb_2^+$ ions. The yellow dashed circle corresponds to 10.4 cm^{-1}. We do not observe any species heavier than K_2Rb_2, up to 1500 amu.

the K^+ and Rb^+ ions have anisotropic ring distributions characteristic of the photodissociation followed by ionization process described in section 4.4.2. Based on the corresponding kinetic energies, we assign the K^+ ions to the $KRb \xrightarrow{h\nu} K(3D)+Rb(5S)$ threshold, and Rb^+ to $KRb \xrightarrow{h\nu} K(4S) + Rb(6P)$. Two-photon ionizations of KRb ($KRb \xrightarrow{2h\nu} KRb^+$) and Rb_2 ($Rb_2 \xrightarrow{2h\nu} Rb_2^+$) resulted in the KRb^+ and Rb_2^+ ion signals in the spectrum. We make these assignments on the basis of that the sizes of their spatial distributions are consistent with photon-recoil-broadening (see section 4.4). The weak nature of these processes is compensated by the high density of KRb and Rb_2 present inside the XODT to yield observable signals. Finally, the KRb_2^+ signal arises from the single-photon ionization of KRb_2 in the trap, as discussed in the previous section.

The $K_2Rb_2^+$ signal can be obtained at a range of UV wavelengths around the thresholds for dissociating into triatomic ions (Fig. 5.7(a)). As example, we show the mass spectrum acquired with a UV wavelength of 335 nm, which corresponds to a photon energy above the dissociation

184
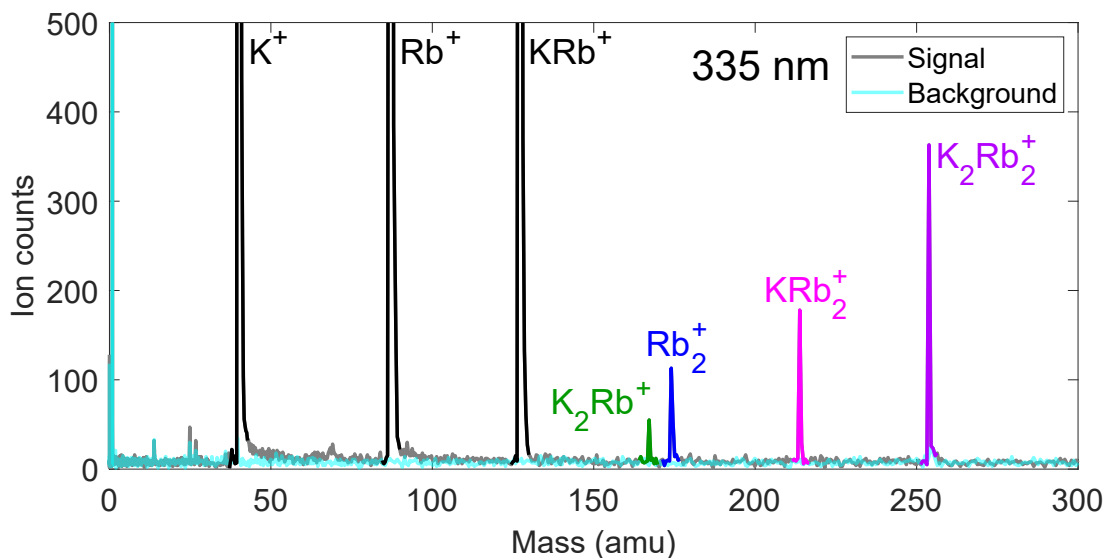
Figure 5.10: TOF mass spectrum produced using an ionization laser wavelength of 335 nm. The triatomic and tetratomic ions now coexist, due to competitions between direct and dissociative ionization pathways for K_2Rb^*.

thresholds. Here, we detect $K_2Rb_2^+$ as well as the triatomic ions K_2Rb^+ and KRb_2^+, indicating the coexistence of the direct and dissociative ionization pathways for the K_2Rb^* complex. This observation highlights an important point that ionization at above dissociation thresholds does not necessarily lead to dissociation, since the system can choose to partition the excess energy into the electron, to a point which there is not enough left for $K_2Rb_2^+$ to dissociate.

For subsequent experiments aimed at studying the K_2Rb^* complex, it is advantageous to choose a UV wavelength that maximizes the ionization efficiency. To this end, we measured the K_2Rb^+ counts per experimental cycle at different UV wavelengths between 356 and 335 nm. Since both the laser pulse energy and the degree of KRb depletion* varies as a function of the UV wavelength, we normalized the measured K_2Rb^+ counts by the laser output and the

---

*While we know now that KRb depletion can be largely avoided by fine-tuning the UV wavelength to avoid resonant transitions (see section 4.2.3), we were not aware of the fact at the time of this measurement.
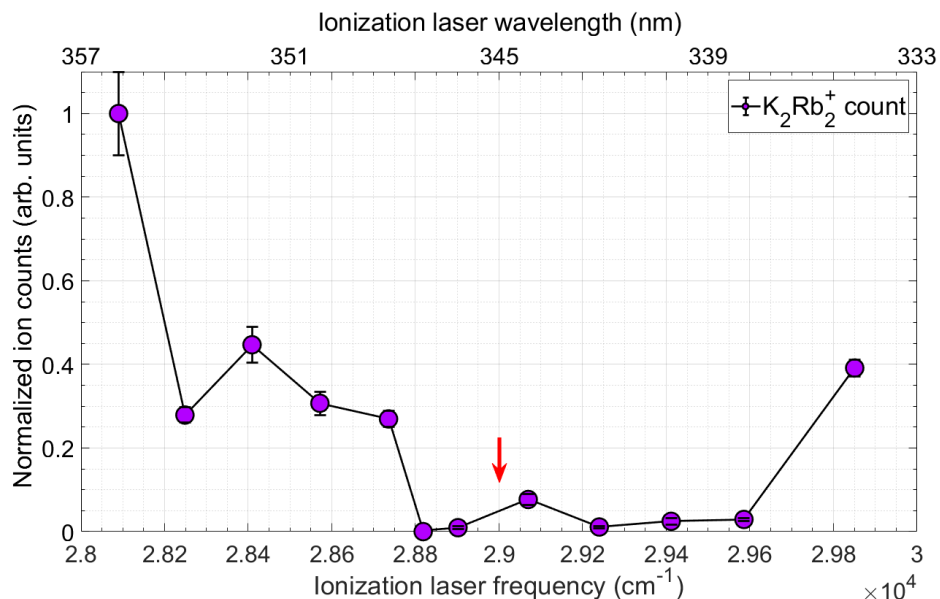
Figure 5.11: $K_2Rb_2^+$ ion counts as a function of ionization laser spatial frequency (wavelength) over the range of 28000 - 30000 cm^{-1} (357 - 333 nm). The ion counts are normalized against variations in UV wavelength dependent parameters including UV pulse energy and the degree of KRb depletion. Error bars represent shot noise. The red arrow indicates 345 nm, the threshold wavelength for the process $K_2Rb_2^* \xrightarrow{h\nu} KRb_2^+ + K$ (see Fig. 5.8).

amount of KRb available in the sample to form complexes. The normalized counts, which proportionally reflect the cross section for the process $K_2Rb^* \rightarrow K_2Rb^+$, are plotted against UV wavelength in Fig. 5.11. Here, we observe a marked increase in the K_2Rb^+ counts going from above the previous determined dissociation thresholds at 345 nm (red arrow) to below it. This is consistent with the closing up of dissociative ionization channels, at which point the direct ionization becomes dominant. On the other hand, we also observe an increase in counts towards higher photon energies, which cannot be accounted for based on simple arguments.

A detailed understanding of the ionization of K_2Rb^* requires not only probing a wider spectral range, but also knowledge of the ground and excited electronic structure of K_2Rb^+, and is reserved for future work. Extending the above measurements to longer UV wavelengths will

allow us to measure depth of the the ground potential well of the K_2Rb^+ ion, and assess the accuracy of the calculated ionization potential of 384.9 nm. Currently, this is not possible due to the limited tuning range of the frequency doubling crystal in our dye laser. Amount the accessible range of UV wavelengths, we determine that the optimum value to ionize K_2Rb^* to be around 356 nm.

5.4   Origin of the detected complex

The results and discussions presented in sections 5.2 and 5.3 have led us to establish the origin of the measured K_2Rb^+ ions as the transient K_2Rb^* complex formed during reactions. While this seems to be the simplest explanation for our observations, there are mechanisms that can potentially lead to similar signals. These will be this section's subjects of discussion.

The dissociative ionization measurement, as shown in Fig. 5.8, tells us that the complexes we convert to ions lived near the collisional threshold of two KRb molecules in terms of energy. However, our knowledge of the absolute energy scale in the system, as informed by the dissociation threshold energy obtained from the fit, is accurate only to ± 300 cm^{-1}. Therefore on the basis for this measurement alone, we cannot distinguish transient complexes that are formed by KRb + KRb reactions from near threshold ones that may come from other sources.

Sticking-amplified three-body loss, first proposed by Ref.[139] in the context of ultracold molecule gases, is one possible mechanism that can result in the formation of near-threshold complexes (see Fig. 5.12(a)). In this hypothesis, the transient complex, once formed by the "sticking" of two KRb molecules, collides with another KRb molecule inside the sample. This results in the vibrational quenching of the complex, which converts a portion of its rich internal energy into the translational kinetic energy (KE) of both the complex and the molecule. Such energy should lead to an observable spread in the ion image of K_2Rb^+. However, the image we observe (Fig.
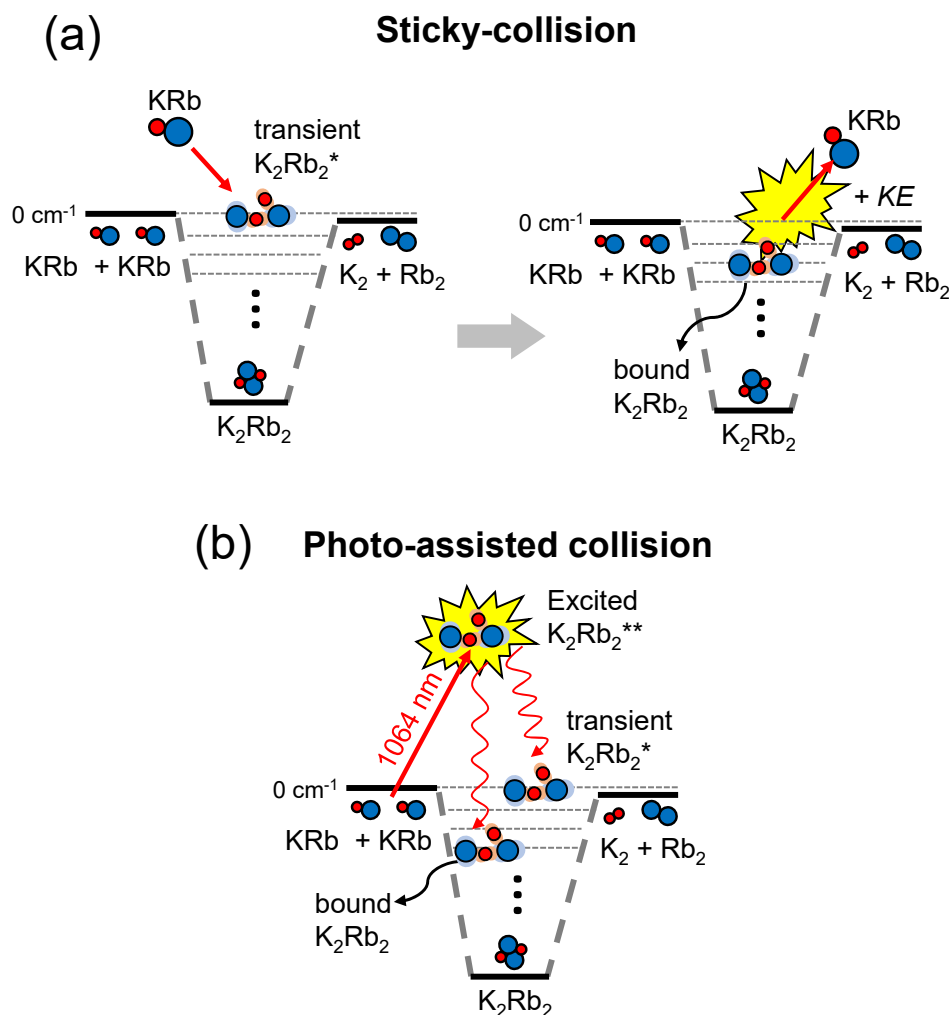
Figure 5.12: Mechanisms other than two-body reaction that can potentially lead to the observed $K_2Rb_2^+$ signal. (a) The sticky collision hypothesis. The transient $K_2Rb_2^*$, once formed from KRb - KRb collision, may collide with another molecule in the bulk gas, leading to a quench in its rich internal energy, resulting in a more deeply-bound complex and an energy release in the form of the relative translation between the complex and the molecule. (b) The photo-assisted collision hypothesis. As a pair of colliding KRb molecules approach each other, the trap light may photoassociate them into a bound complex on an excited PES, which then proceeds to spontaenously decay, into either open or closed channels on the ground PES, resulting respectively in another transient complex or a bound one.

5.9 inset) displays a VMI-resolution limited spot, and we can therefore rule out the role of amplified three-body loss in the formation of all complexes except those with a binding energy of
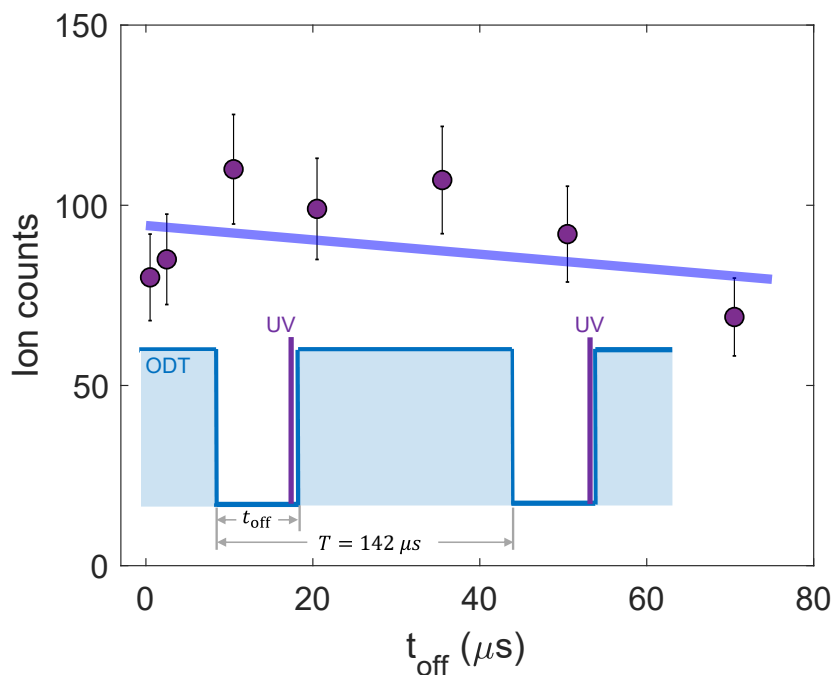
Figure 5.13: Verifying the origin of the detected $K_2Rb_2^+$ signal. The $K_2Rb_2^+$ ion counts are plotted against t_{off}, where t_{off} denotes the length of ODT off time before UV photoionization. Error bars include shot noise and 10% molecule number fluctuations. A weighted linear fit (blue line) with the RMSE being 1.17 determines a slope of -0.2 ± 0.2, consistent with zero. No monotonic trend in the ion signal as a function of ODT off time is observed, excluding the two mechanisms illustrated in Fig. 5.12 as possible explanations for the observed $K_2Rb_2^+$ signal.

~ 0.1 cm^{-1} below the threshold. While the ion image alone does not rule out the formation of very weakly-bound complexes, our measurements in Chapter 6 will demonstrate unambiguously that the complexes we detect are in fact transient, not bound.

Another mechanism that can potentially result in complex formation is photo-assisted collision of two KRb molecules due to the 1064 nm ODT light used to trap them (see Fig. 5.12(b). In this case, a pair of KRb molecules are photo-associated into an electronically-excited complex, which can then spontaneously decay to the ground-state. This leads to the formation of either transient or bound complexes depending on whether the excited complexes decay into open or closed channels. The prior possibility is immediately excluded by the fact that all K_2Rb^+ signals

we detected occured during the dark phases of the ODT modulation, where no photo-assisted collisions can occur. Bound complexes, on the other hand, can linger in the detection region for up to several milliseconds after formation by the ODT, and be detected even during the dark phases. To examine this possibility, we varied the length of time that the ODT was switched off prior to ionization, from 1 μs to 70 μs (Fig. 5.13 inset). If the ODT contributed to the formation of bound K_2Rb_2 molecules, the K_2Rb_2 would steadily build up in concentration in the presence of the ODT. As a result, the concentration of K_2Rb_2 should decrease monotonically as we increase the ODT off duration. Instead, we find the yield of $K_2Rb_2^+$ ions has no monotonic trend with the ODT off duration (see Fig. 5.13). This result is evidence that the complexes we observed are not formed by the ODT.

The exclusion of both sticky and photo-assisted collisions as contributors to the $K_2Rb_2^+$ signals we observed in section 5.3 further support their origin as transient $K_2Rb_2^*$ complexes formed during bimolecular reactions of KRb.

5.5   Conclusion and outlook

In this chapter, we have described the direct observation of the reaction KRb + KRb $\rightarrow$ K_2 + Rb_2, including its products as well as the transient intermediate complex. These results not only help resolve a long-standing mystery of losses observed in ultracold gases of KRb molecules, but also pave the way to studying chemical dynamics in the unexplored ultracold regime. From the stand point of traditional physical chemistry, our detection of the reaction complex using laser pulses that are $\sim$10 nanoseconds long is highly unusual, as they typically live for a duration that is several orders of magnitude shorter. This suggests that $K_2Rb_2^*$ live for quite a bit longer than its counterparts in other reactions, a point which we explore further in chapter 6. In chapter 7, we turn our attention to the reaction products, and study their quantum state distribution which

characterizes the outcome of the reaction.

Chapter 6

Probing the long-lived complex: lifetime and photo-excitation properties

The KRb + KRb reaction is an example of complex forming reactions – an important class of reactions that is widely found in interstellar, atmospheric, and combustion processes. As such, intermediate complexes have been extensively studied since the early days of chemistry[133,101,200], and continue to be an important subject of research today[94,194,24,50,160]. As the bridge between reactants and products, their structures, energetics, and dynamics directly determine the rates and outcomes of the reactions in which they are involved. In gas phase chemistry, intermediate complexes are characterized by their fleeting nature – typically lasting on the order of 10 ps or less in systems consisting of a handful of atoms. In order to detect and study these highly transient objects, physical chemists have developed two general classes of methods: follow the complexes' motions using femtochemistry (or ultrafast) techniques[30,223], or stop their motions

using collisional stablization techniques. In femtochemistry experiments[181,91,187,170], all reactions within a sample, typically in the form of molecular beams, are initiated with a sharply-defined zero-of-time using a femtosecond laser pulse, and their outcomes are probed after some time delay using another femtosecond pulse. The delayed appearance of products with respect to the start of the reactions indicate the existence of intermediate complexes, and the delay time directly provides the complex lifetime – an important metric characterizing the dynamics of the complex. In collisional stabilization experiments[213,24,34], the energy-rich intermediate complexes are quenched via collisions with another particle into a stable bound-state, which can then be studied spectroscopically and help elucidate the struture of the complex.

Notably, our detection of the transient $K_2Rb_2^*$ complex required neither of the above techniques. Instead, by simply shinning in a nanosecond-scale pulsed laser at the reacting cloud of KRb molecules, we observed rather efficient conversion of $K_2Rb_2^*$ into detectable $K_2Rb_2^+$ ions. This indicates that the lifetime of the $K_2Rb_2^*$ complex is significantly longer compared to its counterparts in other chemical reactions. But just how long *does* it live? Given the amount of $K_2Rb_2^+$ ions we detected, the amount of KRb molecules we prepared, and other know experimental parameters, we actually have most of the ingredients to estimate the lifetime of the complex. The only missing piece is the ionization cross section for $K_2Rb_2^* \xrightarrow{h\nu} K_2Rb_2^+$, which has not been reported in the literature to our best knowledge. However, if we assume a reasonable cross section of 1 Mb* (10 Mb)†, we obtain a complex lifetime of ~ 350 ns ($\sim 3\mu$s). In either case, the lifetime for $K_2Rb_2^*$ is many orders of magnitude longer than the typical picosecond-scale lifetime for complexes studied in other gas-phase reactions.

---

*Mb stands for megabarn, which is equal to 10^{-18} cm^2.

†Based on typical photoionization cross sections for clusters of alkali atoms, see for example Ref.[75].
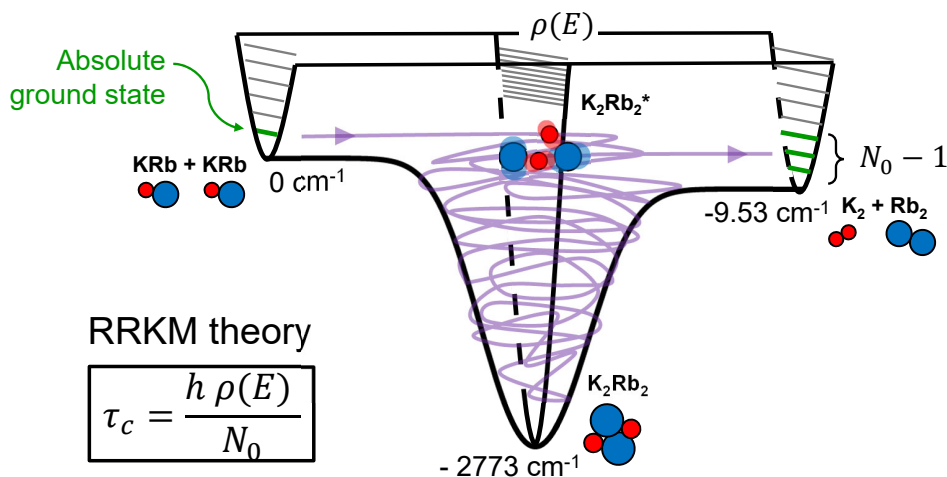
Figure 6.1: Schematic potential energy surface for the KRb + KRb reaction illustrating key elements of the RRKM theory. Inside the deep potential well, the intermediate complex ergodically explores the available reaction phase space, following a complicated classical trajectory (purple trace). After some time, the complex finds its way out of the well as either reactants or products. Under ultracold conditions, the number of exit channels is energetically minimized, resulting in the longest lifetime that can be achieved in this system.

6.1 RRKM theory and complex lifetime

To understand the origin for the exceptionally long lifetime of $K_2Rb_2^*$, we turn to the Rice-Ramsperger-Kassel-Marcus (RRKM) theorem[129], which describes complex-forming reactions and their rates in an elegant and universal way. The physical picture and essential elements for the theory are illustrated in Fig. 6.1, using a schematic potential energy surface that describes the KRb + KRb reaction. Here, reactants collide at an incident energy of E_0 to form an energy-rich intermediate complex, which possesses $3m - 6^*$ vibrational degrees of freedom, where m is the number of constituent atoms. In a properly transformed coordinate system, one of the degree of freedom lies along the reaction coordinate, and takes the reaction from reactants to products, while the rest $3m - 7$ are orthogonal to the reaction coordinate and simply cause

---

*For non-linear molecules (*e.g.* H_2O); becomes $3m - 5$ for linear molecules (*e.g.* CO_2).

194

the complex to vibrate. In general, the energy of the complex can be mixed into all degrees of freedom, while a dissociation can occur only if there is a sufficient fraction along the reaction coordinate to overcome the energy barrier to product formation. As such, the complex makes repeated attempts at escaping while it vibrates within the potential well, and only succeeds in a rare event, typically after many vibrational periods. Classically, this corresponds to a long and snarled trajectory through the reaction phase space[189], as illustrated in Fig. 6.1.

The RRKM hypothesis assumes that the complex behaves statistically, where the energy is equally mixed into all energetically allowed internal modes, in which case the rate for the complex dissociation is given by the celebrated equation

$$\Gamma_c = \frac{N_0(E_0)}{h\rho(E_0)} = \tau_c^{-1},$$

(6.1)

where $\rho(E_0)$ represents the density of states of the complex at the incident energy E_0, and $N_0(E_0)$ is the number of quantum states available for the complex to dissociate, i.e. exit channels. The lifetime of the complex, τ_c, is simply the inverse of its dissociation rate. Note that the RRKM theory makes no distinction between complex dissociation into either reactants or products, and N_0 include exit channels on both sides.

Eqn. 6.1 tells us that the larger the number of exit channels, the faster the complex dissociates, while the higher its density of state, the longer it will linger as a complex. This allows us to rationalize the long complex lifetime in the reactions we probed as a consequence of the ultracold initial condition: by preparing KRb molecules in their absolute rovibronic ground state and with ultralow collision energies, the number of exit channels is energetically minimized to a number that is significantly reduced compared to higher temperature reactions. Besides the ultracold preparation, two other factors that contribute to the long lifetime are: 1. the high density-of-state of the $K_2Rb_2^*$ complex due to the heaviness of the constituent atoms and the large depth of

195

the potential well; and 2. the fact that the reaction is nearly thermal neutral, thus allowing the number of exit channels to be small under ultracold conditions.

While the RRKM theory provides a nice physical picture to understand complex dissociation, its real power is in predicting the value for the complex lifetime. The theory, despite its simplicity, has been applied to a wide range of chemical systems and, in many cases, yielded estimates of lifetimes that are quantitatively matched by experimental results[99,132]. In other cases, non-RRKM behavior, where the measured lifetime is significantly shorter than the RRKM estimate, were observed[35,206,138]. This usually indicates the existence of interesting reaction dynamics which does not equally sample all available internal modes, leading to a non-statistical behavior of the complex. As a general principle, systems with fewer atoms form short-lived complexes whose lifetimes ($\tau_c < 10$ ps) start to approach rotational or vibrational periods, whereas those with more atoms form longer-lived complexes ($\tau_c > 10$ ns). There is (not) sufficient time for efficient energy re-distribution in the former (latter) case, leading to statistical (non-statistical) behavior[40].

Given the roughly estimated lifetime of 350 ns – 3 μs for the K$_2$Rb$_2^*$ complex from our previous experiments, the ultracold KRb + KRb reaction seems like a case where RRKM would apply. Actual calculation of the complex lifetime, on the other hand, is easier said than done. The difficulty stems mostly from estimating the complex's density of state, which amounts to a proper counting of the number of modes available for energy deposition. Theory works that used different criteria for mode counting differently yielded widely different estimates for the lifetime, with Mayle et al.[139] reporting 3.5 μs, and Christianen et al.[46] estimating approximately 100 ns based on parameters extrapolated from NaK + NaK calculations. As such, an experimental measurement of the lifetime is highly desirable.

6.2 Consequences of long-lived complexes

Long-lived complexes have important ramifications for ultracold gases of bialkali molecules (AB), for which the $AB + AB \rightarrow A_2 + B_2$ is endothermic, and are therefore supposed to be stable against two-body chemical reactions. As we have discussed in the beginning of Chapter 5, two-body losses at near-universal rates were still experimentally measured for these molecules[196,220,88,165], and it was suspected that transient complexes, $A_2B_2^*$, formed upon the pairwise collisions of AB, led to the observed losses. The hypothesis is that while each complex by itself has no apparent loss channel and must return as the original molecule pair upon its dissociation*, interactions with another entity during the complex lifetime can quench the complex and lead to pairwise molecule loss. Calculations show that for all AB + AB collisions, the ground potential energy surface feature deep wells ($\mathcal{O}(10^3)$ cm^{-1}) that support the formation of $A_2B_2^*$ complexes. These complexes can actually be substantially longer-lived compared to $K_2Rb_2^*$, since in these cases the number of exit channels available for complexes to dissociate is reduced to $N_0 = 1$ – the same channel by which the two AB molecules enter the complex (see Eqn. 6.1). Using the RbCs molecule as an example, Mayle et al.[140] estimted a complex lifetime of 45 ms. This is comparable for the average time it would take for the complex to run into another molecule in the trap, which is $\sim$ 10 - 100 ms for average molecule densities of 10^{11} - 10^{10} cm^{-3}, resulting in the "sticky collision" loss discussed in section 5.4. This mechanism was used in Ref.[88] to explain the two-body losses observed for a sample of ground-state RbCs molecules.

More recently, Christanen et al.[46] claims to have identified a error in the state-counting method of Mayle et al., one which resulted in an overestimate of the complex's density of state, and correspondingly its lifetime, by several orders of magnitude. Using the NaK + NaK system

---

*This is only true if the AB molecules are prepared in their absolute rovibronic ground state, which is indeed the case for all experimental studies where two-body losses were observed.

as an example, the authors estimate a complex lifetime of 18 μs. Extrapolating their results to the case of RbCs, they find a complex lifetime of 253 μs, making its collision with another molecule before its dissociation exceedingly unlikely. Instead, the authors propose that the observed losses are due to electronic excitations of the complexes caused by the optical dipole trap in which the molecules are confined[47]. Their calculations for the NaK system not only demonstrate the existence of excitation pathways at the commonly used ODT wavelength of 1064 nm, but also that the rate for such excitations is almost two orders of magnitude faster than the rate of complex dissociation at the ODT intensity used during experiments. They further speculate, on the basis of the similarity between the electronic structures of alkali systems, that photoexcitation is the dominant loss mechanism in all endothermic gases of bialkali molecules. However, at the time of this proposal, direct experimental evidences supporting this photo-induced loss mechanism are lacking.

With competing theories based on widely different estimated complex lifetimes, the loss of bialkali molecules once thought to be chemically stable remained a mystery in the field for over a decade. Despite the fact that the KRb + KRb reaction is exothermic, the ability to directly detect the long-lived complex puts us in a unique position to investigate both the lifetime of the complex, and its possible interactions with the trapping light. A direct measurement of the complex lifetime would provide the much needed benchmark for theory, and shed light on the origin of losses that have plagued ultracold molecule experiments.

6.3 Ultracold reactions in the presence of light

Our first task is to investigate possible effects of the 1064 nm light on the KRb + KRb reaction, including its complex and products. Each experiment begins with a gas of ~ 5000 rovibronic ground state KRb molecules prepared at a temperature of 500 nK and an average number density
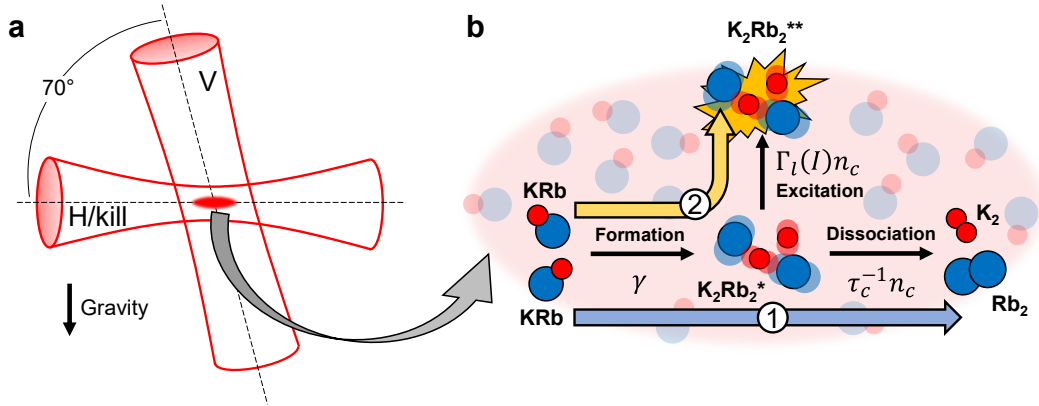
Figure 6.2: Ultracold reactions in an optical dipole trap. (a) Optical trapping of a gas of KRb molecules. "H" and "V" are Gaussian beams with $1/e^2$ diameters of 60 and 200 μm, respectively. The "kill" beam, introduced for the purpose of complex lifetime measurement, shares the same optical path with "H", but has independent timing control. (b) Two pathways for bimolecular KRb reactions. Both pathways involve the formation of a long-lived intermediate complex $K_2Rb_2^*$. ① indicates the ground state pathway KRb + KRb $\rightarrow$ $K_2Rb_2^*$ $\rightarrow$ K_2 + Rb_2, which is the only pathway in the absence of ODT light; ② indicates the excited state pathway KRb + KRb $\rightarrow$ $K_2Rb_2^*$ $\rightarrow$ $K_2Rb_2^{**}$, which is dominant at high ODT intensity. The rates for $K_2Rb_2^*$ formation, dissociation, and excitation are labeled as γ, $\tau_c^{-1} n_c$, and $\Gamma_l(I) n_c$, respectively.

of 3.5×10^{11} cm^{-3} inside the XODT (section 2.3.2) formed by two 1064 nm laser beams ("H" and "V"), as illustrated in Fig. 6.2(a). Previously, we studied the reaction in the absence of the ODT light, probing the complex and products during the dark phase of the ODT intensity modulation (sections 5.1 & 5.3). Here, the goal is to subject the reaction to a controllable amount of ODT light. A simple change in the overall intensity of the ODT, however, would modify the confining potential felt by the KRb molecules and therefore the temperature and density of the gas, resulting in changes in the rate of reaction that confounds our measurements. To circumvent this issue, we apply a square wave modulation with an adjustable contrast (Fig. 6.4(a) inset). This creates two phases with variable instantaneous intensity levels, I and I', while keeping the time-averaged intensity, $(I + I')/2$, constant. As long as the modulation frequency, f_{mod}, is much higher than the trapping frequencies of the gas, f_{trap}, the molecular motions are unaffected, and therefore the density, temperature, and two-body loss rate of the gas remain unchanged. We
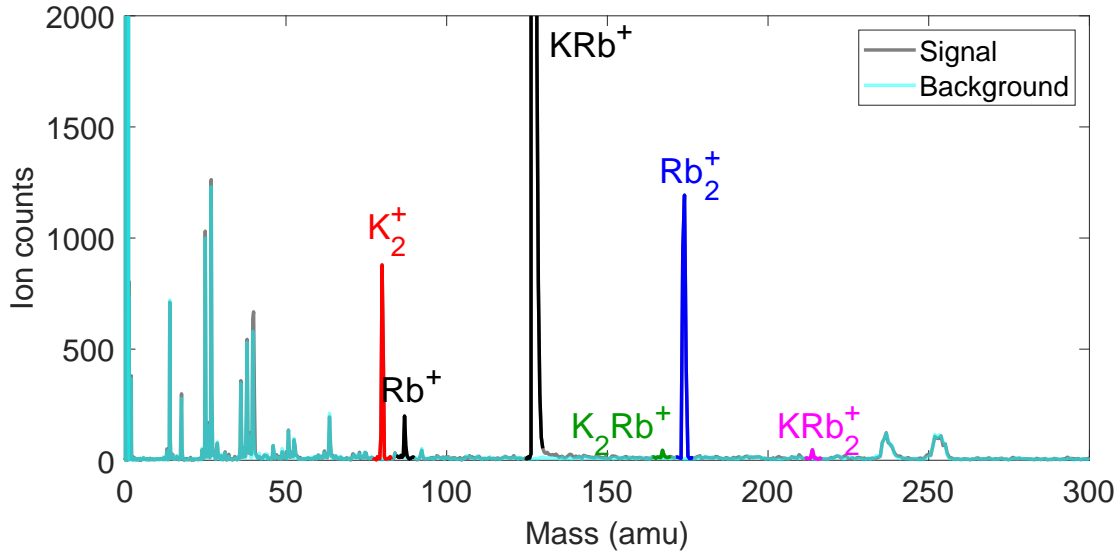
Figure 6.3: The TOF mass spectrum of the reaction products ionized by 305 nm UV laser pulses. Black and cyan traces the signal and background spectra, recorded respectively in the presence of absence of reactant molecules. The presences of other ion species are explained in the main text.

fulfill this requirement by choosing $f_{mod} = 3$ kHz, where $f_{trap} \leq 0.4$ kHz along all three axes of the trap.

We first probe for changes in the amount of reaction products (K_2 and Rb_2) formed while the KRb cloud is exposed to varying intensities of ODT light. As the reaction proceeds, we sample the product population using ion time-of-flight mass spectrometry (TOF-MS), the details of which were described in chapter 4. In brief, the ROI surrounding the KRb cloud is exposed to a pulsed UV ionization laser with a wavelength of 305 nm, a pulse duration of 7 ns, and a hollow-bottle beam profile depicted in Fig. 2.32. Photoionized products are then accelerated onto a time and position sensitive ion detector and counted. The resulting mass spectrum is shown in Fig. 6.3, where signal peaks associated with K_2^+ and Rb_2^+ can be clearly identified. The total ion counts associated with each product species serves as a proxy for its steady-state population at the instances of the UV pulses (see section 4.2.1). The repetition of the UV pulses is synchronized to the ODT intensity modulation such that the reaction is always probed towards

200

the end of the I-phase, allowing the product distribution within the ROI to settle into steady state after the previous I'-phase (see Appendix F).

We accumulated ion data at 10 different values of I between 0 and 22.6 kW/cm^2, with a fixed time-averaged intensity of 22.6 kW/cm^2. The counts of K$_2^+$ and Rb$_2^+$, plotted in Fig. 6.4(a), decrease monotonically with increasing values of I, indicating a reduction in the amount of products formed as the ODT becomes more intense. We rule out electronic excitation of the products by the 1064 nm light as the cause of this reduction, because the light is far-detuned from any relevant molecular transitions in K$_2$[204] and Rb$_2$[66]. Additionally, we observe that the ion counts plateau at high ODT intensities to a value $\sim 25\%$ of the maximum signal, an effect which persists up to at least 45.2 kW/cm^2, as we have verified in a separated measurement (see Appendix G).

Because products are formed from the dissociation of the K$_2$Rb$_2^*$ complexes, it is natural to question how the complexes are affected by the ODT light. To this end, we probe the complex population at different ODT intensities using an experimental protocol similar to that used for the products (Fig. 6.4(b) inset). Here, the UV ionization laser is tuned to 354.77 nm, a wavelength that results in the photoionization of K$_2$Rb$_2^*$ into K$_2$Rb$_2^+$ (see sections 4.2.3 & 5.3). The intensity of the ODT is then modulated at $f_{\mathrm{mod}} = 7$ kHz with a time-averaged value of 11.3 kW/cm^2. K$_2$Rb$_2^+$ ion counts are accumulated at 10 different values of I between 0 and 22.6 kW/cm^2, as shown in Fig. 6.4(b).

Similar to the products, the complex population also decreases with increasing intensity of the 1064 nm light. This observation points to photo-induced complex loss, as postulated in Ref.[47] (section 6.2). To verify this hypothesis, Tijs Karman (ITAMP) helped compute the energies and rates of electronic excitations of K$_2$Rb$_2$ using an *ab initio* method. The results show that multiple excited states can be reached by the absorption of a single 1064 nm photon, with an appreciable transition rate at most of the ODT intensities explored here (Fig. 6.5). This indicates that, in
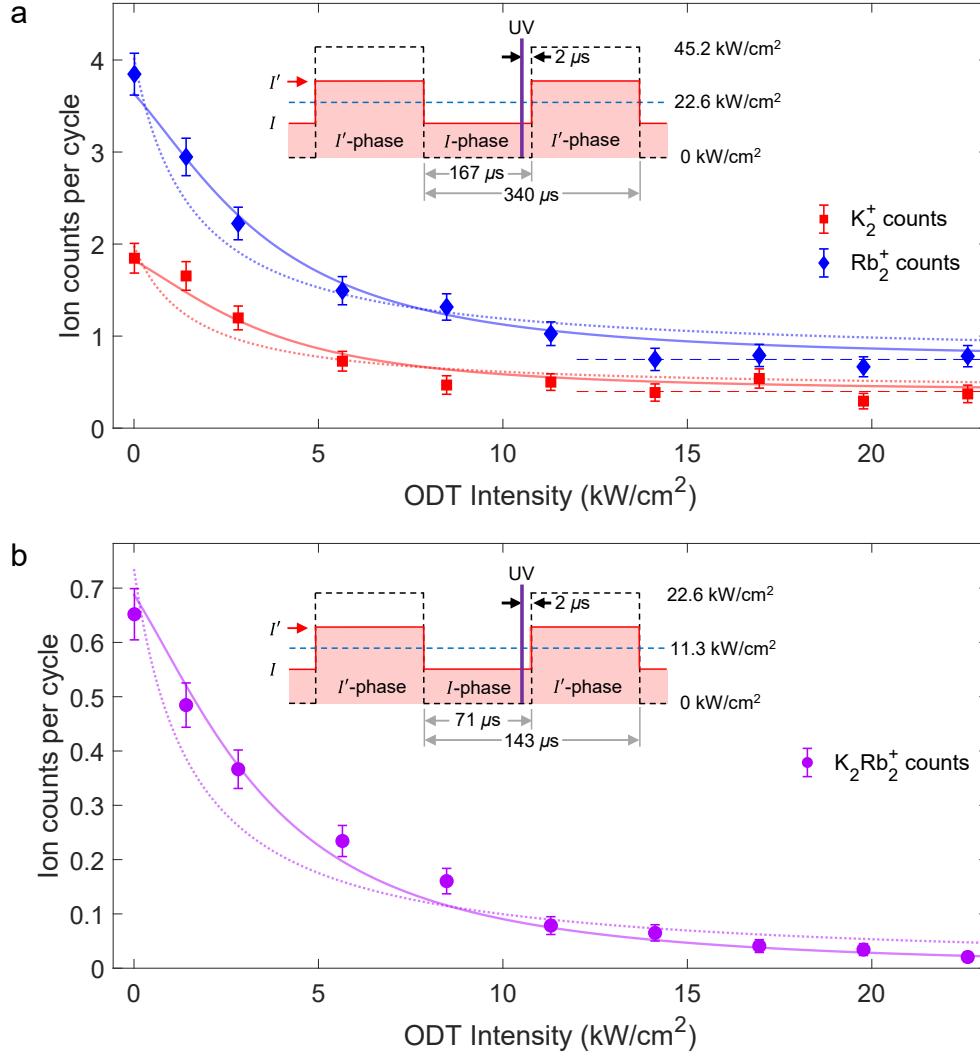
Figure 6.4: Trap light induced excitation of the intermediate complex. (a) Steady-state K_2^+ (red squares) and Rb_2^+ (blue diamonds) ion counts at various ODT light intensities, normalized by the number of experimental cycles (~ 80 for each data point). The error bars represent shot noise. The dashed lines indicate the offset levels $C_{K_2^+}$ and $C_{Rb_2^+}$. (b) Steady-state $K_2Rb_2^+$ (purple circles) ion counts at various ODT light intensities, normalized by the number of experimental cycles (~ 290 for each data point). The solid lines are simultaneous fits to the data in **a** and **b** using Eq. 6.5 with B_1 and B_2 as free parameters, and the dotted lines are fits with B_2 set to zero and only B_1 as a free parameter. The fits are weighted by the inverse of the ion counts. (Insets) Timing schemes for the ODT (red) and the pulsed UV ionization laser (purple) used for the product and complex measurements. The blue dashed line represents the time-averaged intensity level, while the black dashed line represents the ODT intensity envelope for full depth modulation.

addition to the previously observed ground state pathway, there is a competing excited-state pathway (Fig. 6.2(b)),

$$\text{KRb} + \text{KRb} \rightarrow \text{K}_2\text{Rb}_2^* \xrightarrow{h\nu} \text{K}_2\text{Rb}_2^{**}. \tag{6.2}$$
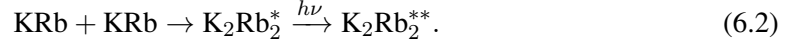
The photo-excited complex, $\text{K}_2\text{Rb}_2^{**}$, is the likely source of the offset observed at high ODT intensities in the product data of Fig. 6.4(a). Possible channels for the formation of K_2 and Rb_2 from $\text{K}_2\text{Rb}_2^{**}$ include dissociation via crossings with repulsive potentials, and decay via spontaneous emission into product-forming channels on the ground-state PES. Products resulting from these processes will in general have different translational energy distributions from those formed via the ground state reaction pathway, which provides an avenue for future investigations into their origins.

We include both pathways to model the data in Fig. 6.4 using the rate equation

$$\dot{n}_c(t) = \gamma - \tau_c^{-1} n_c(t) - \Gamma_l(I) n_c(t), \tag{6.3}$$

where n_c is the complex density, $\gamma = -\dot{n}_r/2$ is the rate of KRb + KRb collisions, τ_c is the complex lifetime, and Γ_l is the intensity-dependent photo-excitation rate. In steady state, the formation of the complex from reactants is balanced by its dissociation into products, and its photo-excitation, so that $\dot{n}_c = 0$. In this case, the complex density is given by

$$n_c = \frac{\gamma}{\tau_c^{-1} + \Gamma_l(I)}. \tag{6.4}$$

We model the excitation rate as $\Gamma_l = \beta_1 I + \beta_2 I^2$, where the linear term represents single-photon excitation of the complex, and the quadratic term represents possible second-order contributions. Equation 6.4 then becomes $n_c = \gamma\tau_c \left(1 + B_1 I + B_2 I^2\right)^{-1}$, where $B_{1,2} = \beta_{1,2}\,\tau_c$. Since both the product and the complex ion counts are proportional to the steady-state density of the

203
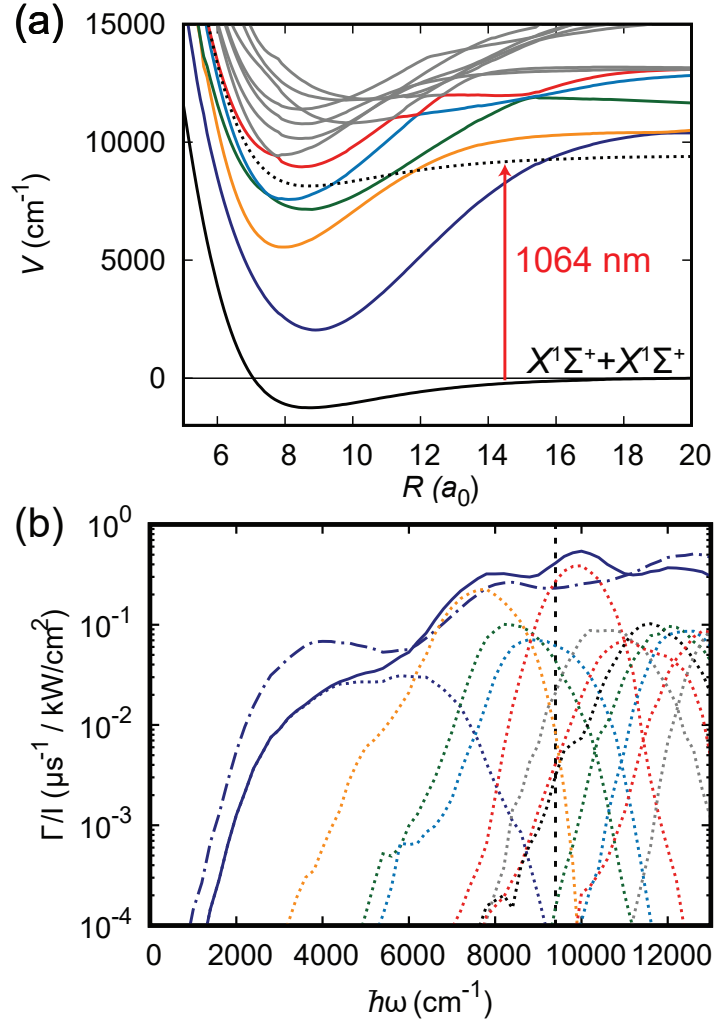
Figure 6.5: Energies and rates of the electronic excitations of the complex. (a) Potential energy curves for the ground state and low-lying excited states of KRb+KRb as a function of the distance between the molecules, R, in units of the Bohr radius, a_0, for fixed orientation and monomer bond lengths. The black dotted curve shows the ground-state potential shifted vertically by the energy of a 1064 nm photon. This crosses various excited state potentials, indicating these are accessible through one-photon excitation of the complex. (b) Calculated excitation rates as a function of the excitation photon energy, with the 1064 nm ODT marked by the vertical dashed line. Dotted lines show the contribution of various adiabatic electronic states, color-coded accordingly with the potential curves in (a). The blue solid line shows the corresponding total excitation rate, whereas the dashed-dotted line shows the excitation rate obtained assuming the total dipole moment is equally distributed over all excited states. The difference between the two serves as an indication of the uncertainty in the calculated transition dipole moments.

204

complex, their dependence on the 1064 nm light intensity can be modeled as

$$N_s = \frac{A_s}{1 + B_1 I + B_2 I^2} + C_s,$$

(6.5)

where $s = \mathrm{K_2^+}, \mathrm{Rb_2^+}$, or $\mathrm{K_2 Rb_2^+}$, and C_s is introduced to account for any offsets in the data. We apply Eq. 6.5 to simultaneously fit the product and complex ion data, as shown in Fig. 6.4(a) and (b). For the product data, C_s is fixed to be the average value of the respective set of four data points at the highest ODT intensities, while for the complex data, C_s is set to zero. We allow the amplitudes A_s to be independent free parameters, whereas B_1 and B_2 are shared parameters across the data sets. The fit adequately captures the data in all three sets, and yields $B_1 = 0.15 \pm 0.03$ cm^2/kW and $B_2 = 0.050 \pm 0.004$ $\left(\mathrm{cm}^2/\mathrm{kW}\right)^2$, with a mean-squared-error (MSE) of 1.2. Alternatively, we fit the three data sets in Fig. 6.4 with B_2 set to zero, representing an excitation rate model that is purely linear in the intensity. In this case we find that $B_1 = 0.64 \pm$ 0.05 cm^2/kW, but that the fit yields a larger MSE of 4.0, and systematically underestimates the lower intensity data points while overestimating the higher ones. This indicates that the linear rate model is insufficient to fully describe the observed photo-excitation of the complex.

We note that the term $B_1 I + B_2 I^2$ physically represents the ratio between the rates of complex excitation and dissociation. Given the values for $B_{1,2}$ obtained from the fit with the smaller MSE, we find that, at a typical ODT intensity of 11.3 kW/cm^2, the reaction is ~ 8 times as likely to proceed via the excited-state pathway as the ground-state pathway. In contrast, if the complex lifetime were to be of order 10 ps or less, as is typically found in higher temperature reactions, effects of the photo-excitation would become insignificant at any reasonably achievable optical power.

6.4 Direct measurement the complex lifetime

The lifetime of the intermediate complex has been measured for a variety of chemical systems[180,158,181], where the use of ultrafast lasers and molecular beam techniques establishes a well-defined zero-of-time for all individual reaction events, allowing the process of complex formation and dissociation to be monitored in real time. In our experiment, the bulk nature of the ultracold KRb sample makes establishing a zero-of-time challenging, as individual reactions occur stochastically. Fortunately, the observed optical excitation of the complex described in the previous section makes it possible to use light to set a zero-of-time. Specifically, we first strongly reduce the complex population by exposing the KRb cloud to intense 1064 nm light, and then monitor its growth to a new steady-state value after the light is quickly switched off. In this situation, the kinetics of the complex density can be understood by solving Eq. 6.3 with the initial condition $n_c(t = 0) = n_0$, where $t = 0$ is the time at which the light turns off, and n_0 is the suppressed complex density at and before the turn-off. The solution is given by

$$n_c(t) = \gamma \tau_c \left[1 - \left(1 - \frac{n_0}{\gamma \tau_c} \right) \mathrm{e}^{-t/\tau_c} \right], \tag{6.6}$$

where the $1/e$ saturation time is the complex lifetime τ_c. Note that Eq. 6.6 is exact if the light turns off instantaneously, and is a good approximation if the characteristic turn-off time $t_{\mathrm{off}} \ll \tau_c$. To minimize t_{off}, we introduce a "kill" beam whose wavelength and optical path are identical to the "H" beam (Fig. 6.2(a)), but whose timing and intensity are independently controlled. This "kill" beam has a 90 - 10% fall time of 30 ns, compared to > 200 ns for the "H" and "V" beams.

As the reaction proceeds, the intensities of the ODT beams are modulated with 100% depth at 7 kHz. During the dark phase of the modulation, the "kill" beam is pulsed on for 10 μs with an intensity of 12.7 kW/cm^2, and the UV pulse probes the complex population at various delay
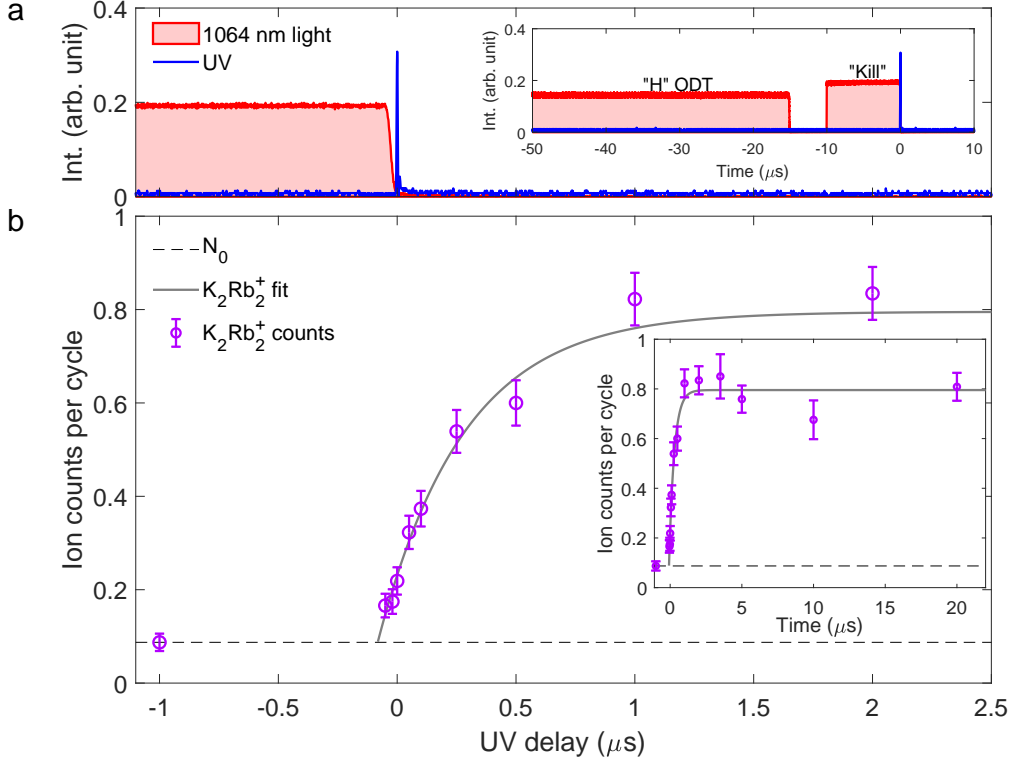
Figure 6.6: Lifetime of the intermediate complex. (a) Measured time traces of the 1064 nm light (red) and the UV ionization pulse (blue) intensities. The UV pulses probe the complex population around the off edge of the "kill" pulse, which provides a zero-of-time for the measurements. (Inset) The same traces displayed over a wider time window showing the relative timing between the "H" and "kill" beams. The "V" beam, not shown here, shares the same timing as the "H" beam. With the addition of the "kill" beam, the "H" beam power is adjusted such that the time-averaged intensity of the ODT is maintained at 11.3 kW/cm^2. (b) K$_2$Rb$_2^+$ ion counts (purple circles) measured at different UV delays with respect to the off edge of the "kill" pulse. The dashed line indicates the baseline from which the ion counts grow after the light is turned off. The level for this baseline is given by the ion counts at -1μs, N_0. The solid line shows a fit to the entire data set (see inset) using the function $A\left[1-(1-N_{\mathrm{K_2Rb_2^+}}^{(0)}/A)\mathrm{e}^{-(t-t_0)/\tau_c}\right]$, which is derived from Eq. 6.6. The fit yields a complex lifetime $\tau_c = 360 \pm 30$ ns, and a timing offset $t_0 = -82 \pm 7$ ns. This offset accounts for a systematic uncertainty in the relative timing between the 1064 nm light and the UV. The MSE for the fit is 0.85.

times around the off edge of the "kill" pulse (Fig. 6.6(a)). Here we define $t = 0$ as the time when the UV pulse is 27 ns delayed with respect to the midpoint of the "kill" pulse turn-off. The $K_2Rb_2^+$ counts are plotted against the UV delay in Fig. 6.6(b) and fitted using the function $N_{K_2Rb_2^+} = A \left[1 - (1 - N_{K_2Rb_2^+}^{(0)}/A)e^{-(t-t_0)/\tau_c} \right]$, derived from Eq. 6.6, with A, t_0, and τ_c as free parameters. Here, t_0 is introduced to account for a systematic timing uncertainty; N_0 is fixed to the ion counts measured at a UV delay of -1 μs, when the "kill" pulse is still on, which serves as a proxy for n_0. The complex lifetime given by the fit is 360 ± 30 ns.

Having measured both τ_c and $B_{1,2} = \beta_{1,2}\tau_c$, we can determine the first- and second-order rate constants, β_1 and β_2, for complex excitation by 1064 nm light. For $B_1 = 0.15 \pm 0.03$ cm^2/kW and $B_2 = 0.050 \pm 0.004$ (cm^2/kW)^2 extracted from the fit to the data in Fig. 6.4, we obtain $\beta_1 = 0.42 \pm 0.09$ μs^{-1}/(kW/cm^2) and $\beta_2 = 0.14 \pm 0.02$ μs^{-1}/$\left(\text{kW/cm}^2\right)^2$.

6.5   Theory and comparison

Finally, we compare the measured lifetime and the photo-excitation rate of the complex and compare them to theoretical calculations performed by our collaborators Tijs Karman (ITAMP) and Hua Guo (UNM). The complex lifetime was estimated using the RRKM theory introduced at the beginning of the chapter (section 6.1), $\tau_c = 2\pi\hbar\rho_c/N_0$. Here, ρ_c is the density of states (DOS) of the complex, and N_0 is the number of open product channels via which the complex can dissociate. We also assume that, over the course of the reaction, the total angular momentum* of the system ($J = 1$) † is conserved, and the spins of the nuclei remain unchanged. N_0 is counted

---

*Here and throughout this thesis, the term "total angular momentum" refers to the vector sum of all angular momenta of the system except for the nuclear spins. The reason for making such a distinction will become clear in Chapter 7.

†The reactant KRb molecules, which are prepared in a single hyperfine quantum state, are identical fermions. Therefore, their collisions at ultralow temperatures are restricted to p-wave, with angular momentum $L = 1$. Since the KRb molecules are in the rotational ground state ($N = 0$), the total angular momentum ($\mathbf{J} = \mathbf{N} + \mathbf{L}$) for the KRb + KRb system is $J = 1$

using known values for the exothermicity* of the reaction[162] and the rotational constants of K$_2$[109] and Rb$_2$[5] (see details in Appendix H) to be 745. Computing ρ_c requires knowledge of the ground-state PES for the KRb + KRb system, which we calculate in full dimensionality using the Molpro package[210]. A one-dimensional cut of the PES is shown in Fig.[46]. The minimum energy structures agree with Byrd *et al.*[37], and the corresponding binding energies differ by less than 15%, which was taken to be the uncertainty of the energy calculation. Using this PES and following the quasi-classical method developed in Ref.[46], ρ_c was calculated to be $2.6 \pm 0.8\,\mu\mathrm{K}^{-1}$. The resulting RRKM lifetime is 170 ± 60 ns, which is remarkably similar to the measured value. More recently, Yang et al.[216] performed an independent calculation of the PES at the CCSD(T) level, and find a similar ρ_c of $3.5\,\mu\mathrm{K}^{-1}$, which corresponds to a complex lifetime of 227 ns.

We note that while the above theory calculations have assumed the conservations of both nuclear spins and total angular momentum, the calculated lifetime is expected to be comparable even if they do, because any additional channels that result from the violation of these conservation laws will increase both ρ_c and N_0 by similar proportions, whereas the RRKM lifetime depends only on the ratio of the two. Detailed discussions regarding the behaviors of nuclear spin and angular momentum throughout the reaction are offered in Chapter 7.

We note also that both theory studies underestimate the lifetime with respect to the measured value. Within the framework of RRKM (section 6.1), this could mean an underestimate of complex's density of states†, and/or that the number of exit channels that actually participate in complex dissociation is smaller than the total allowed channels. Understanding this discrepancy may help improve the accuracy of statistical theory models developed for ultracold reactions as well as complex-forming reaction in general.

---

*At the time of this work, the reaction exothermicity was assumed to be -10.4 cm^{-1}[162]. Later estimates updated this value to -9.53 cm^{-1} (see Appendix I). With the later value, we count $N_0 = 688$, which is $\sim 8\%$ lower than the stated value of 745, leading an increase by the same proportion in the lifetime estimate. The change, however, is well below the uncertainty associated with ρ_c.

†Both studies implemented the phase-space integration method from Ref.[46] to calculate ρ_c.

To calculate the first-order photo-excitation rate constant, our collaborators computed excitation energies and transition dipole moments for the lowest twelve excited states. The single-photon excitation rate of the complex from the ground state, i, to a particular excited state, f, is computed as $\Gamma_{i \to f} = c^{-1} \langle b_{i \to f}(\omega) \rangle I$. Here, c is the speed of light, I the optical intensity, ω the excitation frequency, and b the Einstein B-coefficient for state f. Under the assumption that the complex ergodically explores the ground PES, b can be calculated by averaging the squared transition dipole moment over the local DOS[47]. Contributions from different excited states are then summed to obtain the total excitation rate Γ_l. The rate constant, $\beta_1 = \Gamma_l / I$, is shown in Fig. 6.5(b) as a function of the excitation photon energy. At 1064 nm this excitation rate is $\beta_1 = 0.4^{+0.4}_{-0.2} \ \mu s^{-1}/(kW/cm^2)$, which agrees well with the measured first-order excitation rate of $0.42 \pm 0.09 \ \mu s^{-1}/(kW/cm^2)$. Calculation of the second-order rate constant, β_2, requires an understanding of higher-order excitation processes in the complex, which is beyond the scope of the current work.

6.6 Conclusion and outlook

In this chapter, we have described our discovery and characterization of an excited-state pathway for the bimolecular reaction between ultracold KRb molecules, one that is mediated by the trap light photo-excitation of the transient $K_2Rb_2^*$ complex. We further prove that the complex is indeed exceptionally long-lived as we have previously speculated (Section 5.5), this time through a time-domain measurement of its lifetime. These results brings new understanding to the origin of molecular loss in this much-studied system [162,61,60] – while it is certainly true that the ground-state pathway leads to the loss of KRb, the excited-state pathway completely dominants at the level of optical intensity typically used for molecule trapping. One obvious question is that why was this pathway never considered in prior works with regard to the loss of KRb. The answer is

that because both pathways involve first the formation of the $K_2Rb_2^*$ complex, the rate of which is determined by the long-range attraction between KRb molecules, they manifest in the same two-body loss rate for KRb molecules. This highlights the importance of direct, multi-species detection to the studies of ultracold chemistry.

Beyond the KRb system, our results also have important implications for the losses observed in other ultracold bialkali species whose ground state reactive pathways are energetically forbidden[196,220,88,165]. Because the electronic structures of these systems are comparable to KRb, the complexes formed from bimolecular collisions are likely also susceptible to excitations and losses induced by the trapping light. Furthermore, the good agreement between the measured complex lifetime and the RRKM estimate validates the methods developed in Ref.[46] for calculating the complex density of states and lifetimes of various ultracold bialkali species. Taken together, this work supports the proposal by Ref.[47] that the leading cause of molecular loss in these systems is the photo-excitation of collision complexes, and not the previously proposed mechanism of sticking-amplified three-body loss. Such an understanding is further solidified by recent work carried out on a gas of ultracold RbCs molecules[87], where by trapping the molecules using a low-duty cycle, time-modulated ODT, the authors observed suppressed molecular loss – by partially hiding the gas in the dark, some of the $Rb_2Cs_2^*$ complexes are allowed to revive back into RbCs molecules. Based on the degree of this revival, the authors extracted a photo-excitation rate of 3^{+4}_{-2} $\mu s^{-1}/(kW/cm^2)$, which is quite comparable to what we observed for $K_2Rb_2^*$, and found the lifetime of the $Rb_2Cs_2^*$ complex to be 530 ± 60 μs, which is 3 orders of magnitude longer than what we measure for $K_2Rb_2^*$. This can be directly correlated to the fact that the number of exit channels in the exothermic KRb + KRb case, which is $N_0 = 745$, is about 3 orders of magnitude higher than that for the endothermic RbCs + RbCs case, which is $N_0 = 1^*$ (see Eqn. 6.1).

---

*The densities of states of the two systems are quite similar, to within a factor of 2.

For the "chemically stable" bialkali species, avoiding trap light induced loss will facilitate the creation of molecular gases with higher phase space densities and the exploration of the many new scientific directions such systems promise[33,129,18,219]. To this end, one may consider alternative trapping schemes such as blue-detuned repulsive optical traps and electrostatic traps, or engineer repulsive potentials between the molecules via dipolar interactions or microwave-dressing. On the other hand, collisional losses are naturally suppressed in applications where the molecules are kept apart from each other, such as quantum simulation or computation using molecules trapped optical lattices or tweezers.

The ability to initialize ultracold reactants in single quantum states provides a unique opportunity to test RRKM scaling laws in a chemical reaction with unprecedented precision. In particular, by preparing KRb molecules with well-defined rovibrational excitations and measure the resulting lifetime of the complex, one could understand how the density of states of the complex and number of open channels impact the complex lifetime in a highly systematic fashion.

From the perspective of controlling chemical reactions, the long-lived complex formed from ultracold molecular collisions provides a new handle to steer the reaction dynamics. This is in contrast to the more traditional gas-phase reactions, where control over the pathways and outcomes of reactions are typically achieved by manipulating the reactants – e.g. their translational energy[173], orientation[163], and internal quantum state[172] – as the intermediate complexes are simply to short-lived to be affected by external processes. In the future, a detailed understanding of the fate of the optically excited complex, including possible decay pathways, may allow for the direct control of reaction outcomes using light. Furthermore, the long complex lifetime, coupled with the observed photo-excitation pathway, opens up the possibility to perform high resolution spectroscopy on the complex. Such a study may provide critical information on the rovibrational and electronic structure of the complex, bringing us closer to a microscopic picture

212

of the reaction dynamics.

Chapter 7

Quantum state distribution of the products

The direct measurement of the complex lifetime described in the last chapter provides a first-order characterization of the dynamics of the KRb + KRb reaction. To understand the reactive process with greater details, we turn attention once again to the reaction product, with the goal of resolving the quantum states with which they emerge from the reaction, and measuring the population distribution among these states. As we have discussed in the opening chapter, product state distributions contain valuable information that help elucidate reaction mechanisms[129], and has been widely and successfully applied in physical chemistry to study reactions in the gas-phase[15]. As such, the importance of product state detection and analysis have been recognized by many in the emerging field of cold and ultracold chemistry[64,151,27,135,199]. Such a capability, when coupled with the ability to control all quantum degrees of freedom of the reactants afforded by the low temperatures, promises state-to-state chemistry at an unprecedented level of resolution.

A central theme of state-to-state chemistry is that by measuring the product state distribution given a certain reactant state preparation, one could learn something about the PES which underlies the reaction as well as the dynamics thereon. For example, the degree of product vibrational excitation can inform the location of the chemical barrier on the reaction path[169], and rotational distributions of the products reveals the anisotropy of the short-range interactions[182]. While such analyses can be carried out for reactions that occur via direct pathways, they become much more challenging for those that feature complex-forming pathways, such as the vast majority of low temperature reactions[20]. As we have discussed in section 6.1, intermediate complexes found in such reactions can live for a duration that is many times longer than the characteristic rovibrational timescale of the system, leading to a mixing of the energy of the complex into its various degrees of freedom. This effect is expected to result in a statistical distribution of the reaction products, *i.e.* every product channel, so long as allowed by conservation laws, is equally likely to be populated. In such an event, the effect of the reactant state preparation will be strongly suppressed, and extracting details about the underlying PES becomes much more difficult[129]. Given this understanding, an exciting prospect for studying state-to-state chemistry in the ultracold setting then becomes the search for non-statistical behaviors which may manifest in the product state distribution. Such is what we set out to do.

The content of this chapter is structured as follows. In section 7.1, we identify product quantum states that are relevant for the ultracold KRb + KRb reaction. in section 7.2, we demonstrate detection of these states and the populations therein using resonance-enhanced multi-photon ionization spectroscopy. In section 7.3.1, we report observations of a strong parity preference in the rotational state distribution of products which clearly deviate from a statistical behavior, and attribute such a phenomenon to the conservation of nuclear spins throughout the reaction. Leveraging this effect, we demonstrate, in section 7.3.3, the ability to control the product state distribution via an external magnetic field. Finally, in section 7.4, we provide an outlook on

additional non-statistical effects which may govern the reaction and how to search for them.

7.1 Quantum states of products

Since the reaction we study occurs on the ground electronic surface, the relevant degrees of freedom of the products include molecular vibration, rotation, orbital motion, and spins (see Fig. 1.2 in Chapter 1). In this section, we discuss restrictions imposed on states associated with these degrees of freedoms by various conservation laws, and eventually identify those that can be populated by the reaction given our ultracold, ground-state reactant preparation. We pay particular attention to the rotation and vibrations of the products, since these are the only degrees of freedom for which the associated quantum states can be experimentally detected (section 7.2).

7.1.1 Rovibrational states

We begin by considering the rotational and vibrational states of the products. In a generic reactive collision event, two reactant KRb molecules in rovibrtaional states $|N_{\text{KRb}(1)}, v_{\text{KRb}(1)}, N_{\text{KRb}(2)}, v_{\text{KRb}(2)}\rangle$ collide with each other with a negligible translational energy and an orbital angular momentum of $\mathbf{L}_{\text{reac}}$, resulting in products in states $|N_{\text{K}_2}, v_{\text{K}_2}, N_{\text{Rb}_2}, v_{\text{Rb}_2}\rangle$ with a total translational energy of KE and an orbital angular momentum of $\mathbf{L}_{\text{prod}}$. Here, N and v denote the rotational and vibration quantum numbers, respectively. Product states that are allowed to be populated at the end of the reaction are restricted, first and foremost, by energy conservation, *i.e.*

$$
\begin{aligned}
E_{\text{tot}} = {} & B_{\text{KRb}} N_{\text{KRb1}}(N_{\text{KRb}(1)} + 1) + B_{\text{KRb}} N_{\text{KRb}(2)}(N_{\text{KRb}(2)} + 1) + \omega_{\text{KRb}} v_{\text{KRb}(1)} + \omega_{\text{KRb}} v_{\text{KRb}(2)} + |\Delta E| \\
= {} & KE + B_{\text{K}_2} N_{\text{K}_2}(N_{\text{K}_2} + 1) + B_{\text{Rb}_2} N_{\text{Rb}_2}(N_{\text{Rb}_2} + 1) + \omega_{\text{K}_2} v_{\text{K}_2} + \omega_{\text{Rb}_2} v_{\text{Rb}_2}.
\end{aligned}
\tag{7.1}
$$

Table 7.1: Parameters relevant for calculating the energy levels of reactant and product rovibrational states. All values quoted to their reported precision.

Quantity	Symbol	Value (cm^{-1})	Reference
^{40}K^{87}Rb rotational constant	B_{KRb}	3.7156×10^{-2}	156
^{40}K$_2$ rotational constant	B_{K_2}	5.46785×10^{-2}	6
^{87}Rb$_2$ rotational constant	B_{Rb_2}	2.18894×10^{-2}	185
^{40}K^{87}Rb vibrtaional constant	ω_{KRb}	74.915†	8
^{40}K$_2$ vibrational constant	ω_{K_2}	91.032‡	72
^{87}Rb$_2$ vibrational constant	ω_{Rb_2}	57.121	185
Reaction exothermicity	ΔE	-9.53 ±0.07	appendix I

† Scaled by mass from the measured value for ^{39}K^{85}Rb

‡ Scaled by mass from the measured value for ^{39}K$_2$

Here, ΔE is the exothermicity of the reaction, and B and ω represent rotational and vibrational constants, respectively. The values for these constants are listed in Tab 7.1, while the relevant energies are labeled in Fig. 7.1. Note that for collisions between ground state KRb molecules ($|N_{KRb(1)} = 0, v_{KRb(1)} = 0, N_{KRb(2)} = 0, v_{KRb(2)} = 0\rangle$), the reaction exothermicity does not allow for vibrational excitations in the products, but rotational excitation of up to $N_{K_2} = 12$ and $N_{Rb_2} = 20$.

For each product pair, labeled by their rotational states as $\{N_{K_2}, N_{Rb_2}\}$, the associated total translational energy, KE, is partitioned into the translational energies for K$_2$ and Rb$_2$ according to momentum conservation as

$$KE_{K_2} = KE \frac{\mu(K_2, Rb_2)}{m_{K_2}}, \qquad (7.2)$$

and

$$KE_{Rb_2} = KE \frac{\mu(K_2, Rb_2)}{m_{Rb_2}}, \qquad (7.3)$$

where $\mu(K_2, Rb_2) = m_{K_2} m_{Rb_2} / (m_{K_2} + m_{Rb_2})$ is the reduced mass of the K$_2$–Rb$_2$ pair.

We now consider the various rotational degrees of freedom of the reactants and products, and
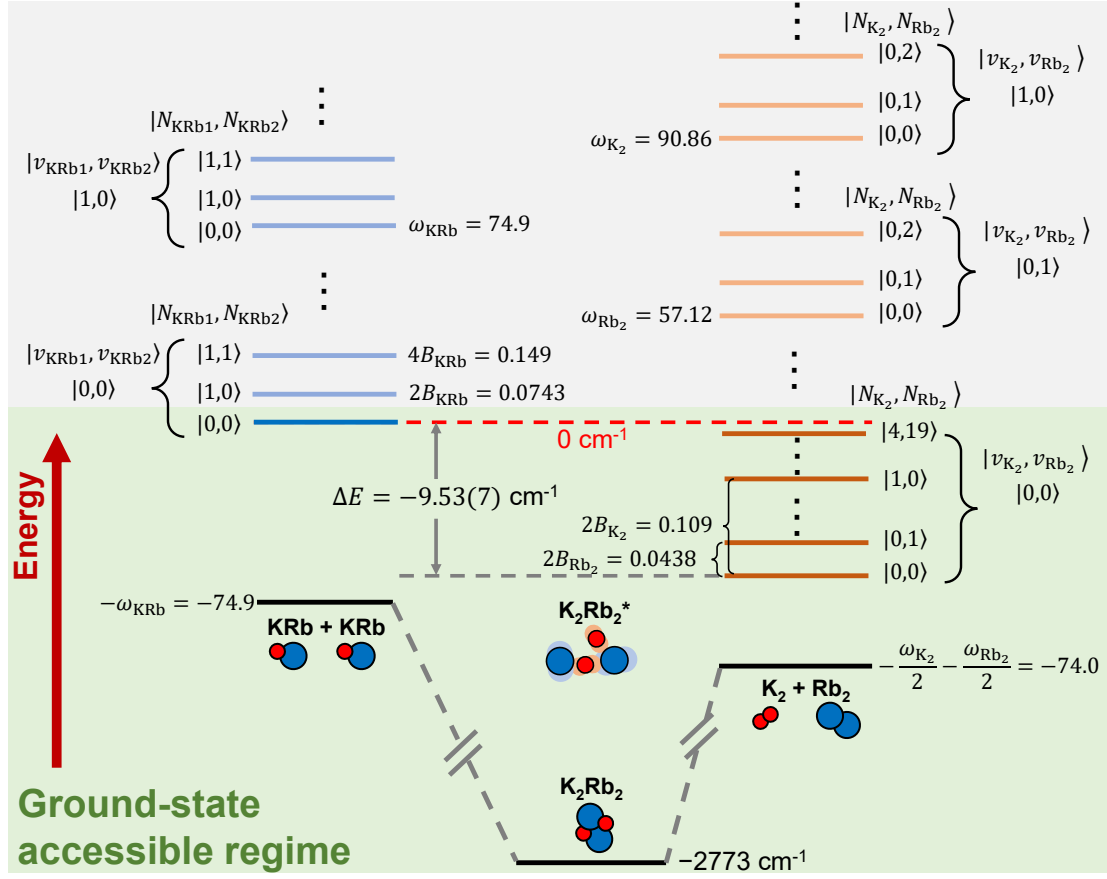
Figure 7.1: Reactant and product rovibrational states and their energies. All energy values are specified in units of cm^{-1}. See main text for definitions of different symbols, and Tab. 7.1 for tabulated values of the rotational and vibrational constants. Each vibrational state pair is associated with a stack of rotational state pairs. The red dashed line marks the energy zero, defined as the energy of two KRb molecules in their ground state with no translational energy. The energy range accessible for the reaction in the case of ground-state, ultracold reactants is marked by the light green shaded region.

restrictions placed upon the associated angular momenta. In the absence of external electric and magnetic fields, the total angular momentum of the system is conserved, *i.e.*

$$\mathbf{J}_{\text{tot}} = \mathbf{N}_{\text{reac}} + \mathbf{L}_{\text{reac}} = \mathbf{N}_{\text{prod}} + \mathbf{L}_{\text{prod}}, \tag{7.4}$$

where

$$\mathbf{N}_{\text{reac}} = \mathbf{N}_{\text{KRb}(1)} + \mathbf{N}_{\text{KRb}(2)}$$

$$\mathbf{N}_{\text{prod}} = \mathbf{N}_{\text{K}_2} + \mathbf{N}_{\text{Rb}_2} \tag{7.5}$$

The vectorial relationships between these angular momenta are schmatically illustrated in Fig. 7.2. Given this conservation law, the angular momentum states of the reactants and products are denoted, by sets of good quantum numbers, as

$$\Psi_J^{\text{reac}} = \left| J_{\text{tot}}, M_{\text{tot}}; N_{\text{KRb}(1)}, N_{\text{KRb}(2)}; N_{\text{reac}}, L_{\text{reac}} \right\rangle, \tag{7.6}$$

$$\text{and} \quad \Psi_J^{\text{prod}} = \left| J_{\text{tot}}, M_{\text{tot}}; N_{\text{K}_2}, N_{\text{Rb}_2}; N_{\text{prod}}, L_{\text{prod}} \right\rangle. \tag{7.7}$$

The relations between these quantum numbers are constrained by the quantum mechanical versions of equations 7.4 and 7.5, *i.e.* a set of triangular inequalities

$$\left| N_{\text{KRb}(1)} - N_{\text{KRb}(2)} \right| \leq N_{\text{reac}} \leq \left| N_{\text{KRb}(1)} + N_{\text{KRb}(2)} \right|,$$

$$\left| N_{\text{K}_2} - N_{\text{Rb}_2} \right| \leq N_{\text{prod}} \leq \left| N_{\text{K}_2} + N_{\text{Rb}_2} \right|,$$

$$\left| N_{\text{reac}} - L_{\text{reac}} \right| \leq J_{\text{tot}} \leq \left| N_{\text{reac}} + L_{\text{reac}} \right|,$$

$$\left| L_{\text{prod}} - N_{\text{prod}} \right| \leq J_{\text{tot}} \leq \left| L_{\text{prod}} + N_{\text{prod}} \right|. \tag{7.8}$$

For a given $\{J_{\text{tot}}, M_{\text{tot}}\}$ defined by the input state of the reactants, each Ψ_J^{prod} is uniquely specified by $\{N_{\text{K}_2}, N_{\text{Rb}_2}; N_{\text{prod}}, L_{\text{prod}}\}$. Experimentally, however, only N_{K_2} and N_{Rb_2} can be directly resolved (see section 7.2). Thus, each product rotational state pair $\{N_{\text{K}_2}, N_{\text{Rb}_2}\}$ has a degeneracy given by the number of allowed $\{N_{\text{prod}}, L_{\text{prod}}\}$ pairs, to which we refer to as the "L-degeneracy".

Besides conservation, a further constraint on the angular momentum quantum numbers is

Reactants	Intermediate	Products

$\mathbf{J}_{tot} = \mathbf{L}_{reac}$

$\mathbf{J}_{tot}$

$\mathbf{L}_{prod}$ $\mathbf{J}_{tot}$

$\mathbf{N}_{K_2}$

$\mathbf{N}_{Rb_2}$

$\mathbf{N}_{prod}$

$\mathbf{N}_{KRb(1)} = \mathbf{N}_{KRb(2)} = 0$

$J_{tot} = L_{reac} = 1$ (*p*-wave)

$\mathbf{J}_{tot} = \mathbf{L}_{reac} = \mathbf{N}_{K_2} + \mathbf{N}_{Rb_2} + \mathbf{L}_{prod}$
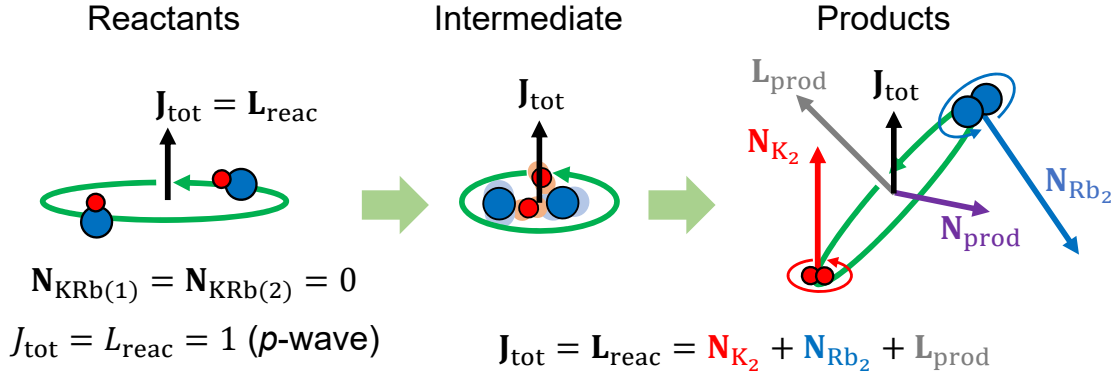
Figure 7.2: Schematic illustration of the relations between various angular momentum vectors involved in the KRb + KRb reaction. Here, we consider the initial condition in our experiments, where reactant KRb molecules prepared in their rovibrational ground states ($N_{KRb(1)} = N_{KRb(2)} = 0$), and colliding via *p*-wave collisions (L_{reac}). In this case, the total angular momentum of the system is simply $\mathbf{J}_{tot} = \mathbf{L}_{reac}$. The product angular momenta, $\mathbf{N}_{K_2}$, $\mathbf{N}_{Rb_2}$, and $\mathbf{L}_{prod}$, can each take on a range of values within the energy conservation limit, but restricted to a vectorial sum of $\mathbf{J}_{tot}$ if total angular momentum of the system is conserved throughout the reaction 7.4.

imposed on the conservation of total parity, *i.e.*

$$(-1)^{N_{KRb1}}(-1)^{N_{KRb1}}(-1)^{L_{reac}} = (-1)^{N_{K_2}}(-1)^{N_{Rb_2}}(-1)^{L_{prod}}. \tag{7.9}$$

We now consider effects of external fields on angular momentum conservation. In the presence of electric and/or magnetic field along some lab-frame axis z, J_{tot} is no longer rigorously conserved, but its projection M_{tot} still is, i.e.,

$$M_{tot} = M_{N_{reac}} + M_{L_{reac}} = M_{N_{prod}} + M_{L_{prod}},$$

$$M_{N_{reac}} = M_{N_{KRb(1)}} + M_{N_{KRb(2)}}, \tag{7.10}$$

$$M_{N_{prod}} = M_{N_{K_2}} + M_{N_{Rb_2}},$$

The consequence is that for each Ψ_{Ang}^{prod}, there opens up $2\min(L_{prod}, N_{prod}) + 1$ additional degenerate sublevels, to which we refer to as the "*m*-degeneracy". For reactions between ground

state KRb molecules, this leads to a approximately twenty-fold increase in the total number of product channels. In the case of nonparallel electric and magnetic external fields, the cylindrical symmetry of the reactive system is broken, further removing the restrictions on the projections. This changes the number of degenerate sublevels for each $\Psi_{\mathrm{Ang}}^{\mathrm{prod}}$ to $(2N_{\mathrm{prod}} + 1)(2L_{\mathrm{prod}} + 1)$, increasing the number of channels by roughly another thirty-fold.

Our experiments are carried out in the presence of orthogonal electric and magnetic fields (Fig. 6.2(a)). The magnitudes of these fields, however, are quite small, with $E = 17$ V/cm and $B = 5 - 50$ G. So which angular momentum conservation law actually governs the allowed product channels? The answer will depend largely on the intermediate complex, and in particular the structure of its quantum states, and how external fields couple these states to each other. While this is a subject of ongoing theoretical investigation, we shall proceed under the working assumption that there exists total angular momentum conservation (Eq. 7.4) for our system. We note that such an assumption does not affect the experimental investigations of the role of nuclear spins in ultracold chemistry described in section 7.3, but will impact future studies of state-to-state chemistry as we will discuss in the outlook (section 7.4).

Beyond those chracterized by Eqns. $7.1 - 7.9$, an additional and final restriction on the product states results from the homonuclear nature of K_2 and Rb_2, which we discuss next.

7.1.2 Nuclear spin states

We now discuss the spin degree of freedom of the products, and quantum states associated with it. Since both K_2 and Rb_2 emerge in the $X^1\Sigma^+$ electronic state, with no net orbital or spin angular momentum associated with the electrons, we need only to consider the spins associated with the nuclei. The eigenstates of the product nuclear spins are given by

$$\Psi_{\mathrm{nuc}}^{K_2/Rb_2} = |I_{K_2/Rb_2}, M_{K_2/Rb_2}; i_{K(1)/Rb(1)}, i_{K(2)/Rb(2)}\rangle. \tag{7.11}$$

Here, i represents the spin quantum number of each nucleus; I represents the total spin quantum number of the diatomic molecule, and is vectorially related to i as $\mathbf{I}_{K_2/Rb_2} = \mathbf{i}_{K/Rb(2)} + \mathbf{i}_{K/Rb(1)}$; M represents the projection quantum number associated with I. Since $i_{40K} = 4$, the nuclear spin states of K_2 can have $I_{K_2} = 8, 7, ..., 1, 0$, with $M_{K_2} = -I, -I+1, ...I-1, I$ for each value of I, making a total of 81 states. In the case of Rb_2, $i_{87Rb} = 3/2$, and we have $I_{Rb_2} = 3, 2, 1, 0$, with a total of 16 states.

Each nuclear spin state has a well-defined symmetry with respect to particle exchange – those that remain positive upon swapping nuclei (1) and (2) are symmetric (S), while those that acquire a negative sign are antisymmetric (A). $S(A)$ states are characterized by even (odd) values of the quantity $i_{(1)} + i_{(2)} - I$. As such, $I_{K_2} = 8, 6, 4, 2, 0$ and $I_{Rb_2} = 3, 1$ are S states, while $I_{K_2} = 7, 5, 3, 1$ and $I_{Rb_2} = 2, 0$ are A. In homonuclear diatomic molecules where the nuclei are identical particles, the symmetry of the nuclear spins under particle exchange is linked to the symmetry of their rotational states by the relation

$$\Psi_{\text{tot}} = \Psi_{\text{nuc}} \otimes \Psi_{\text{rot}}, \tag{7.12}$$

where Ψ_{tot}, Ψ_{nuc} and Ψ_{rot} represent the total, nuclear, and rotational wave functions of the nuclei, respectively. Now, since the nuclei of $^{40}K_2$ are bosonic particles, Ψ_{tot} must be symmetric under their exchange. As a result, a symmetric Ψ_{nuc} requires Ψ_{rot} to have even parity, while an antisymmetric one requires the Ψ_{rot} to be odd. In $^{87}Rb_2$, where the nuclei are fermionic, this symmetry-parity correspondence is swapped.

The spin-rotation symmetry relations in the product molecules has two important implications. First, any rules that govern the symmetry of the product nuclear spins will determine the parity of the product rotations, placing further constraints on the allowed rovibrational states. This will be discussed in detail in the next section as we consider the behaviors of nuclear spins

throughout chemical reactions. Secondly, while nuclear spin states are not easily resolved spectroscopically due to their small energy splittings, their correspondence to molecular rotations makes it possible to probe them by measuring the product rotational states, which can be resolved.

7.1.3   Behaviors of nuclear spins

While most degrees of freedom associated with a chemical reaction become strongly coupled to each other at short-range, nuclear spins, which remains weakly coupled[174,159], represent a notable exception. This is evidenced by the tendency of the spins of nuclei to remain unchanged throughout reactions, a phenomenon observed in both complex-forming[203,52] and direct[78,147] bimolecular reactions, as well as in photodissociations[183,209]. These observations helped establish the now well-accepted rule of nuclear spin conservation in gas-phase chemistry[159], which forms the basis for the studies of interstellar[92,73] and atmospheric[93] chemical processes that involve species with different nuclear spin isomers.

Compared to those studied in prior works, reactions that occur at ultralow temperatures display unique characteristics that may challenge the robustness of nuclear spin conservation. Specifically, the nuclei involved can possess spins many times larger than those found in prior works, which were typically protons with spin of $I = 1/2$. This can result in stronger couplings between the spins and other degrees of freedom. Furthermore, the intermediate complex involved in these reactions can be exceptionally long-lived, providing ample time for these couplings to alter the spins. Thus far, however, experimental evidence for the behavior of nuclear spin in cold and ultracold reactions remains lacking, while competing assumptions regarding the subject have been made in theoretical studies[140,139,151,85].

Testing the conservation of nuclear spins in reactions requires two technical ingredients –

the ability to prepare reactants with known nuclear spins, and the ability to measure the spin composition of the products. In prvious works, the prior is accomplished by the use of reactant samples with known abundance ratios of nuclear spin isomers*, while the latter by spectroscopically probing the product population in different rotational states, which are coupled to the spins of the protons as per our discussion in the previous section. In recent years, controls over nuclear spins have been significantly advanced by ultracold techniques. Preparation of molecules in single nuclear spin states is now experimentally achievable, and has enabled robust storage of quantum information [166] and studies of hyperfine-state-dependent chemistry [162,118,218]. Such controllability, combined with the fact that ultracold matters are dilute enough to prevent secondary collisions, makes ultracold molecules a unique platform to cleanly probe the behavior of nuclear spins in chemical reactions.

We now consider specifically how nuclear spin conservation will manifest in the ultracold KRb + KRb reaction, where the reacant KRb molecules are identically prepared in a single nuclear spin eigenstate

$$\Psi_{\text{nuc}}^{\text{KRb}} = |i_{\text{K}} = 4, i_{\text{Rb}} = 3/2; m_{\text{K}}, m_{\text{Rb}}\rangle. \tag{7.13}$$

Formally, conservation means that the states of the ^{40}K and ^{87}Rb nuclei in the reactants are directly inherited by those in the products. In that case, products emerge with states

$$\Psi_{\text{nuc}}^{\text{K}_2} = |i_{\text{K}(1)} = 4, i_{\text{K}(2)} = 4; m_{\text{K}(1)}, m_{\text{K}(2)}\rangle,$$
$$\text{and} \quad \Psi_{\text{nuc}}^{\text{Rb}_2} = |i_{\text{Rb}(1)} = 3/2, i_{\text{Rb}(2)} = 3/2; m_{\text{Rb}(1)}, m_{\text{Rb}(2)}\rangle, \tag{7.14}$$

---

*Two molecules are nuclear spin isomers if they are of the same chemical composition and arrangements, but different nuclear spin quantum states. These states are often referred to in the chemistry literature as "para-", "ortho-", and "meta-", in increasing order of their total nuclear spin quantum number I. H_2 for example, has para ($I = 0$) and ortho ($I = 1$) spin isomers that exist in a 3:1 ratio under thermal equilibrium at room temperature. This abundance ratio is determined by the multiplicities of the two nuclear spin states.

both of which are evidently of S character. As such, the spin-rotation symmetry relation for K_2 and Rb_2 demand that N_{K_2} take on only even values, and N_{Rb_2} only odd, *i.e.*

$$(-1)^{N_{K_2}} = 1, \quad \text{and} \quad (-1)^{N_{Rb_2}} = -1. \tag{7.15}$$

In the absence of the conservation rule, on the other hand, A states become accessible, allowing N_{K_2} and N_{Rb_2} to take on both even and odd values. In the extreme case where the spin states are statistically populated*, the population ratio between even and odd rotational states, $R_{e/o}$ or $R_{o/e}$, would be determined by the numbers of S and A spin states in each product species (see previous section). In such a case, we expect $R_{e/o} = 45/36 = 1.25$ for K_2 and $R_{o/e} = 10/6 = 1.67$ for Rb_2.

The above comparison shows that the behavior of nuclear spin throughout the reaction can be examined by investigating the parity preference of the product rotational states, at least for the case where the reactants are in a single spin eigenstate. This is still possible, albeit quantitatively more complex, in the general case where the reactant nuclear spin is in a superposition of many eigenstates. We will delve into this subject in section 7.3.2.

7.1.4   Allowed product states

Having considered the restrictions placed on the product states by energy (Eq. 7.1), angular momentum (Eq. 7.4), total parity (Eq. 7.9), and nuclear spin conservation laws (sections 7.1.2 & 7.1.3), we are now in a position to identify the entire set of allowed rovibrational states for the products. To this end, we implemented a state counting and sorting algorithm in Mathematica, the details of which are provided in Appendix H. For a given input condition specified by the set reactant quantum numbers $\{v_{KRb(1)}, v_{KRb(2)}, N_{KRb(1)}, m_{N_{KRb(1)}}, N_{KRb(2)}, m_{N_{KRb(2)}}, L_{\text{reac}}, m_{L_{\text{reac}}}\}$,

---

*<i>i.e.</i>, all allowed spin states are equally likely to be populated

the algorithm tests whether a given product state, $|N_{K_2}, v_{K_2}, N_{Rb_2}, v_{Rb_2}\rangle$, statisfies Eq. 7.1 – 7.9 and 7.15, starting with the ground state $|0,0,0,0\rangle$ and ends when it reaches the state with the highest allowed rovibrational energy. We shall tentatively also assume the conservation of nuclear spins, in which case the rotational states are subjected to the parity requirements set by Eq. 7.15. For each rovibrational state, the number of allowed $|L_{prod}, N_{prod}\rangle$ states are counted towards its L-degeneracy.

We apply the above algorithm to identify the allowed product rovibrational states given the reactant state preparation used in our experiments – all KRb molecules are identically prepared in the ground rovibrational state $|N_{KRb} = 0, v_{KRb} = 0\rangle$, and the hyperfine state $|m_K = -4, m_{Rb} = 1/2\rangle$, in the presense of a quantization magnetic field $\mathbf{B}$. Under such conditions, the identical fermionic nature of the reactants restricts the partial wave of collision to those with odd values of L_{reac}. At ultralow temperatures, only $L_{reac} = 1$, which corresponds to p-wave collisions, is permitted[162]. Thus, the total angular momentum of the reaction is $J_{tot} = L_{reac} = 1$, with projections $M_{tot} = m_{L_{reac}} = 0, \pm1^*$. In this case, energy conservation allows no vibrational excitations in the products[†], but rotational excitations of up to $N_{K_2} = 13$ and $N_{Rb_2} = 21$ (see Fig. 7.1). Among the $(13+1) \times (21+1) = 308$ possible $|N_{K_2}, N_{Rb_2}\rangle$ state pairs, 56 survive the screening by the rest of the conservation laws. These allowed rotational state pairs, along with their corresponding kinetic energy (KE), L-degeneracy, and m-degeneracy[‡], are documented in Tab. 7.2.

Note that the assumptions of nuclear spin conservation and weak coupling between nuclear spins and other degrees of freedom drastically reduce the number of states that we need to consider in studying the product state distribution. The validity of these assumptions, however,

---

*Since there is no preferred orientations for KRb-KRb collisions in our experiment, the three possible values of M_{tot} are expected to participate equally.

†For this reason, we will suppress the vibrational quantum number in subsequent state notations.

‡In the m-degeneracy for each state is counted for a given value of M_{tot}, which can be 0 or ±1; the number total allowed m degenerate states is higher by a factor of 3.

Table 7.2: Allowed product states in a reaction between ground-state ultracold KRb molecules. Each allowed state is labeled by the rotational state pair $\{N_{K_2}, N_{Rb_2}\}$, and is associated with a kinetic energy (KE) that is given by the difference between the reaction exothermicity and the internal (rotational) energy of that state. Also given in the table are the L- and m-degeneracies of each state pair, which arise from two different assumptions about total angular momentum conservation throughout the reaction. See main text for details. The sums of the L- and m-degeneracies respectively represent the total numbers of unique product channels under the two aforementioned assumptions.

N_{K_2}	N_{Rb_2}	KE	L-deg.	m-deg.	N_{K_2}	N_{Rb_2}	KE	L-deg.	m-deg.
0	1	9.49	2	4	4	17	1.74	14	480
0	3	9.27	2	12	4	19	0.12	14	536
0	5	8.87	2	20	6	1	7.19	5	61
0	7	8.30	2	28	6	3	6.97	11	135
0	9	7.56	2	36	6	5	6.58	17	209
0	11	6.64	2	44	6	7	6.01	20	286
0	13	5.55	2	52	6	9	5.26	20	366
0	15	4.28	2	60	6	11	4.34	20	446
0	17	2.83	2	68	6	13	3.25	20	526
0	19	1.21	2	76	6	15	1.98	20	606
2	1	9.16	5	21	6	17	0.54	20	686
2	3	8.94	8	50	8	1	5.55	5	81
2	5	8.55	8	82	8	3	5.33	11	179
2	7	7.98	8	114	8	5	4.94	17	277
2	9	7.23	8	146	8	7	4.37	23	375
2	11	6.31	8	178	8	9	3.62	26	476
2	13	5.22	8	210	8	11	2.70	26	580
2	15	3.95	8	242	8	13	1.61	26	684
2	17	2.50	8	274	8	15	0.34	26	788
2	19	0.88	8	306	10	1	3.47	5	101
4	1	8.39	5	41	10	3	3.25	11	223
4	3	8.17	11	91	10	5	2.86	17	345
4	5	7.78	14	144	10	7	2.29	23	467
4	7	7.21	14	200	10	9	1.55	29	589
4	9	6.47	14	256	10	11	0.63	32	714
4	11	5.55	14	312	12	1	0.96	5	121
4	13	4.45	14	368	12	3	0.74	11	267
4	15	3.18	14	424	12	5	0.34	17	413
							total	688	14876

remains to be experimentally tested, which is our next subject.

7.2 Rotational spectroscopy of K_2 and Rb_2

In the previous section, we have identified the target states for investigating the outcomes of the ultracold KRb + KRb reaction as the low-lying rotational states of K_2 and Rb_2 in their ground rovibronic manifold ($|X^1\Sigma^+, v = 0\rangle$). To detect these states and their associated populations, we use $1 + 1'$ resonance-enhanced multiphoton ionization (REMPI), schematically illustrated in Fig. 7.3 along with the electronic energy diagram for K_2 and Rb_2. This two-photon scheme consists of an initial bound-to-bound transition from a target state $|X^1\Sigma^+, v = 0, N = 0\rangle$ to an electronically excited intermediate-state* $|\Lambda, v' = 0, N'\rangle$, followed by a bound-to-continuum transition that ionizes the molecule. Since these target states have not been studied in the literature, our first task is to identify suitable transitions for the bound-to-bound leg.

To maximize the detection efficiency, it is important to select transitions with large transition dipole moments (TDM). For a molecular rovibronic transition $|\Lambda, v, N\rangle \rightarrow |\Lambda', v', N'\rangle$, the TDM is expressed as

$$D(\Lambda, \Lambda', v, v', N, N') = R(\Lambda, \Lambda')F(v, v')S(N, N'). \tag{7.16}$$

In the above expression, $R(\Lambda, \Lambda') = e\langle\Lambda|\mathbf{x} \cdot \mathbf{E}|\Lambda'\rangle$ represents the electronic part of the TDM, $F(v, v') = \langle v|v'\rangle$ is the Franck-Condon factor that characterizes the overlap between the vibrational wave functions of the two states, and $S(N, N') = \langle N|N'\rangle$ is the Hönl-London factor that characterizes the overlap between their rotational wave functions, which are spherical harmonics. Aided by the K_2 and Rb_2 spectroscopy literature[23] and calculations provided by O. Dulieu

---

*While Λ typically represents the projection of the electron's orbital angular momentum along the internuclear axis, here we use it to label the electronic state.

and his team[108], we identify the low-lying vibrational levels ($v = 0 - 6$) of the $B^1\Pi_u$ electronic state in both molecules to have particularly favorable TDM from their respective ground states, with $R \sim 3.6\ ea_0$ for Rb_2 and $3.5\ ea_0$ for K_2, and F in the range of $0.05 - 0.2$ for their different vibrational states. The frequencies for these transitions correspond to laser wavelengths of 642 - 660 nm in K_2 668 - 670 nm Rb_2 both of which are accessible by diode lasers. For subsequent rotational spectroscopy studies, we drive $v = 0 \to v' = 1$ for K_2 $v = 0 \to v' = 4/6$ or Rb_2. Transitions between rotational states are subjected to the selection rule $\Delta N = N' - N = -1, 0,$ or 1, commonly referred to in spectroscopy literature as P-, Q-, and R-branch transitions. For $\Sigma \to \Pi$ electronic transitions, the Hönl-London factors for the three branches are given by[22]

$$S_P(N) = \frac{N-1}{2N+1}, \quad S_Q(N) = 1, \quad \text{and} \quad S_R(N) = \frac{N+2}{2N+1}. \tag{7.17}$$

Note that Q-branch transitions, for which $N' = N$, are the overall strongest and are uniform for different values of N, making them particularly suitable for mapping population in different rotational states into ion counts.

We begin our spectroscopic search by looking for P-,Q-, and R-branch rotational transitions from $N_{Rb_2} = 0 - 21$ within the $X^1\Sigma_g^+(v = 0) \to B^1\Pi_u(v' = 6)$ vibronic band. Our initial search is guided by transition frequencies calculated by O. Dulieu and coworkers based on molecular potentials fitted by prior spectroscopic data[185,39,7]. From their results, we identify 447560 – 447685 GHz (669.854 – 669.667 nm) as the spectral region of interest. Using the laser systems and optical setup described in section 2.5.1, we attempt to drive the $1 + 1'$ REMPI transition (Fig. 7.3) to ionize Rb_2 molecules emerging from reactions towards the end of each experimental cycle. A 5 G quantization magnetic field is present during ionization and detection. Because the trap light can alter the outcome of the reaction (section 6.3), we apply a 7 kHz square wave modulation to its intensity, and probe the products during the dark phases of the
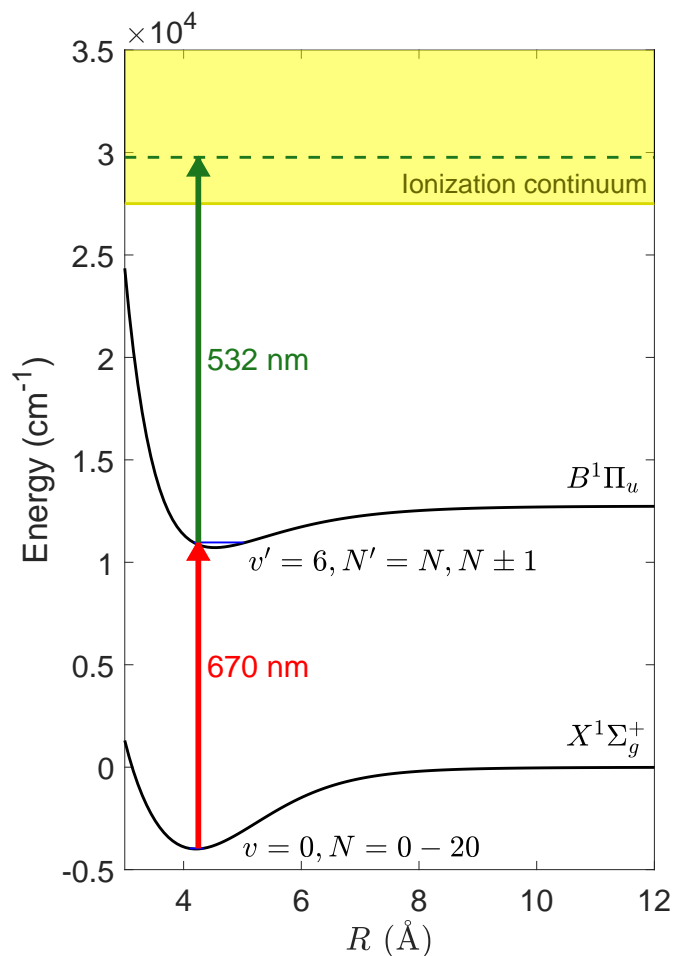
Figure 7.3: Resonance-enhanced two-photon ionization of Rb_2. Product Rb_2 molecules emerging from the reaction with $v = 0$ and $N = 0 - 20$ on the ground electronic potential ($X^1\Sigma_g^+$) are resonantly excited by 670 nm light to the $v' = 6$, $N' = N - 1, N$ or $N + 1$ state on an excited potential ($B^1\Pi_u$) via a P-, Q-, or R-branch rovibronic transition, and subsequently ionized by 532 nm light. Molecular potentials are taken from Ref.[192].

modulation. The relative timing between the REMPI and trap lights are shown in Fig. 7.4 inset.

We scanned the frequency of the 670 nm diode laser driving the bound-to-bound transition and monitored the variation in ion counts accumulated over a fixed amount of experimental cycles. We observed many resonances within the expected spetral region, as displayed in Fig.
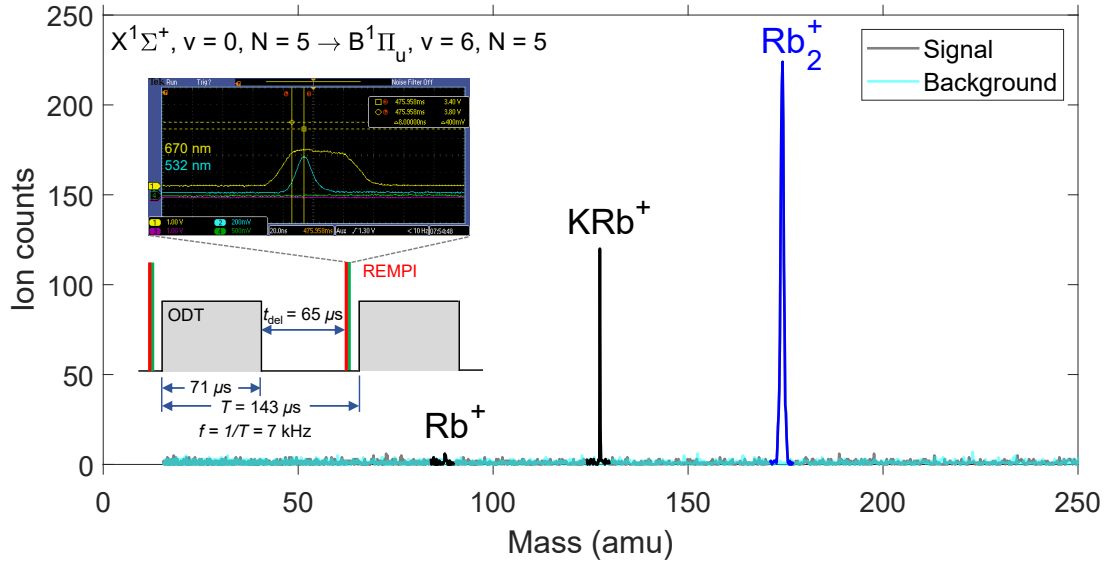
Figure 7.4: TOF mass spectrum acquired via REMPI that targets Rb_2^+ in the $v = 0, N = 5$ rovibrational state. The presence of KRb^+ and Rb^+ signals is due to two photon ionization of Rb and KRb within the trapped gas at 532 nm. The large width associated with the Rb_2^+ signal is due to the sampling geometry of the REMPI beams (Fig. 2.33). Inset: relative timing between the REMPI and ODT lights used during this measurement as well as all other REMPI measurements reported in this chapter.

7.6. As an example, Fig. 7.4 shows the TOF mass spectrum associated with one such resonance that occurs at 447747.13 GHz. Besides a clear signal of Rb_2^+ ions, we also observe signals corresponding to Rb^+ and KRb^+, which result from two-photon ionization by the finite amount of 532 nm light present at the cloud location. The Rb_2^+ peak has a broad characteristic TOF distribution of ~ 350 ns, consistent with the behavior described in section 4.3. Fig. 7.4 shows the spectral lineshape of the same resonance. We find a 1σ Gaussian width of 42.4 ± 1.5 MHz, which arises from a combination of natural linewidth of the excited state (13.9 MHz), Doppler broadening due to product velocity $(0 - 20$ MHz$)$, power broadening $(\sim 35 - 40$ MHz$)$, and residual frequency fluctuation of the 670 nm laser $(\sim 25$ MHz$)$.

To assign the resonances, we compare the observed frequencies to those calculated by O. Dulieu and coworkers for the target transitions. Besides an overall underestimation of 2.13 GHz
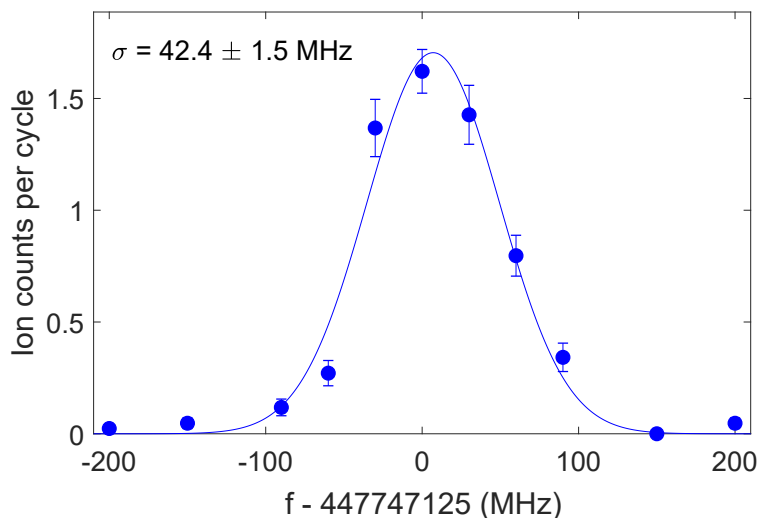
Figure 7.5: A resonance signal obtained through REMPI spectroscopy for the transition $N_{K_2} = 6 \rightarrow N'_{K_2} = 6$; the Gaussian width is $\sigma = 46 \pm 4$ MHz, and the error bars denote shot noise associated with ion counting.

by the theory*, we find excellent agreements between the measurements and predictions, to within ± 15 MHz. We therefore apply a 2.13 GHz offset to the entire set of predictions, and superimpose them with the measured spectrum in Fig. 7.6. Each theory line is labeled by the associated P-,Q-, or R-branch transition. This allows us to assign all observed resonances. The numerical values of the corrected theory frequencies are reported in Appendix J, along with a detailed explanation of how the corrections to theory values are applied.

From the fully assigned spectrum, we identify transitions from $N_{Rb_2} = 0 - 19$ of the ground vibronic state, indicating the existence of product populations among them. Notably, transitions from $N_{Rb_2} > 19$ are missing, consistent with what is required by the reaction exothermicity[†] of -9.53(7) cm^{-1}. We note the amplitudes of the resonances in spectrum in Fig. 7.6 do not directly correspond to the population among different rotational states due to lack of proper

---

*The discrepency likely arises from uncertainties in the rovibronic energy calculation.

[†]see further discussions in Appendix I
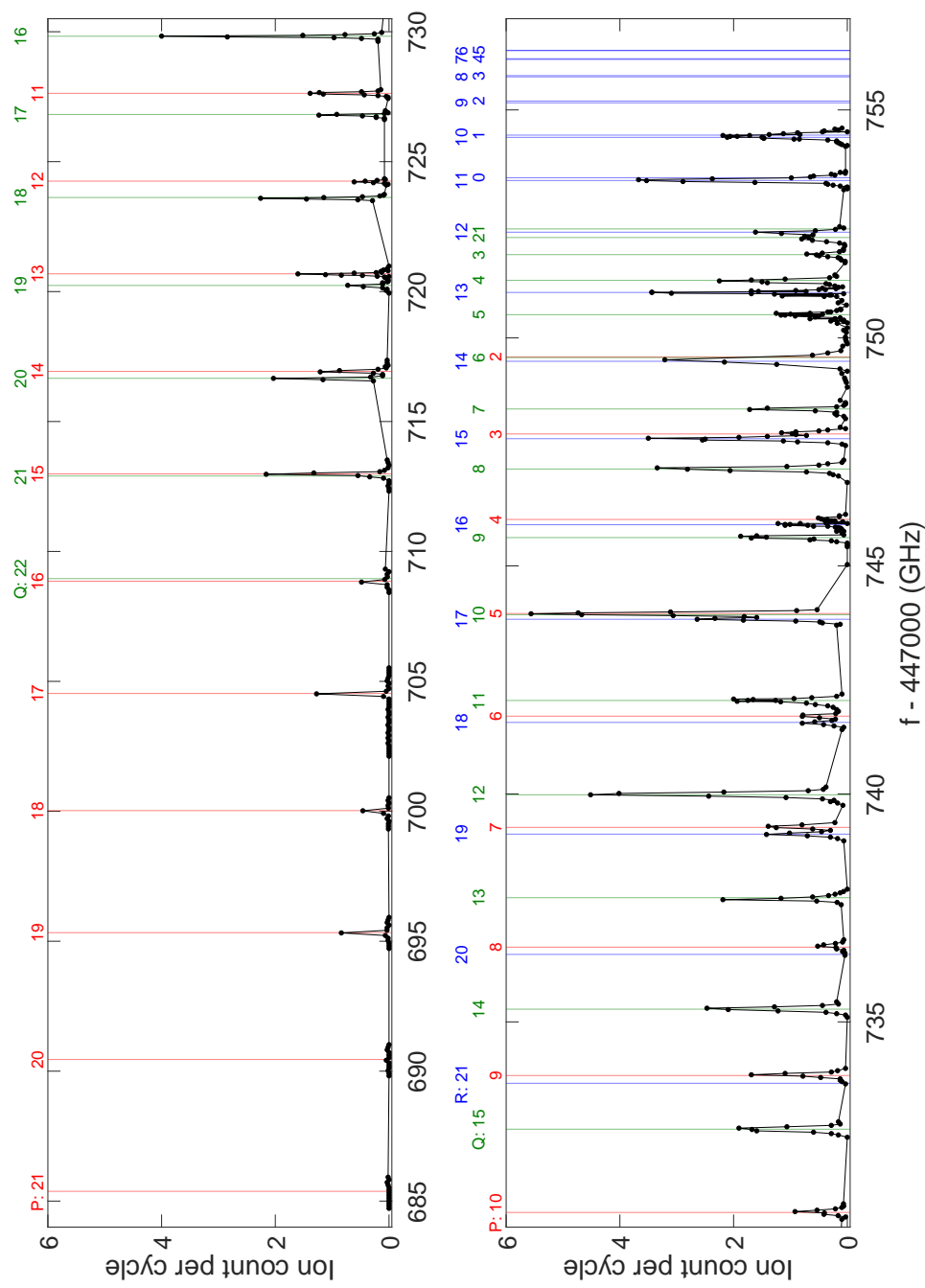
Figure 7.6: Spectorscopic search for rotational transitions in Rb_2 via the REMPI scheme described in Fig. 7.3. Black circles represent experimentally measured ion counts at different frequencies of the bound-to-bound transition laser; red, green, and blue lines represent theoretically predicted frequencies for P-, Q-, or R-branch transitions from low-lying rotational states of Rb_2. All observed resonances are assigned. Some resonances (*e.g.* R11 and R0) are too close to be resolved.

normalization, which we will discuss towards the end of the the chapter.

7.3 Behavior of nuclear spins in ultracold reactions

7.3.1 Product state occupations at 30 G vs. 5 G

The REMPI spectroscopy described in the previous section lays the groundwork for studying the product state distribution of the ultracold KRb + KRb reaction. As we have discussed in section 7.1.3, the first goal of such a study is to probe the behavior of nuclear spins throughout the reaction, which manifests in the relative occupation of rotational states of different parities. In particular, for reactant KRb molecules identically prepared in single Zeeman states $|m_K, m_{Rb}\rangle$ of the uncoupled basis, the conservation of nuclear spins would lead to a highly non-statistical outcome, where populations are allowed in only even rotational states of K_2 and odd of Rb_2. To this end, we set up the experiment with the reactant KRb molecules identically prepared via STIRAP in the $|m_K = -4, m_{Rb} = 1/2\rangle$ nuclear spin state within the hyperfine manifold of the ground rovibronic state[162], at a magnetic field of $B = 550$ G near the interspecies Feshbach resonance (section 3.7). We then ramp the magnetic field over a period of 30 ms to $B = 30$ G, a value sufficiently low for ion imaging (see section 4.5).

As the magnetic field lowers, states other than $|-4, = 1/2\rangle$ but satisfy $m_K + m_{Rb} = -7/2$ begin mixing in, resulting in a superposition of three Zeeman components

$$\Psi^{nuc}_{KRb} = \alpha \left| 4, \frac{3}{2}, -4, \frac{1}{2} \right\rangle + \beta \left| 4, \frac{3}{2}, -3, -\frac{1}{2} \right\rangle + \gamma \left| 4, \frac{3}{2}, -2, -\frac{3}{2} \right\rangle. \qquad (7.18)$$

To investigate the effect this has on our state preparation, we characterized the composition of the KRb nuclear spin state as a function of the magnetic field. The values for the admixture

234

coefficients α, β, and γ are calculated for $B = 0 - 50$ G by direct diagonalization of the KRb hyperfine Hamiltonian. Details of the calculation are provided in Appendix K. We find that the mixing of the $|-3, -1/2\rangle$ and $|-2, -3/2\rangle$ components become significant only for $B \lesssim 20$ G due to a competition between the Zeeman energy and the nuclear spin-spin interaction[4]. In particular, at $B = 30$ G used in this experiment, the state is dominated by the $|-4, 1/2\rangle$ component, with $|\alpha|^2 = 0.982$.

To probe the state occupation of the reaction products, we performed rotational spectroscopy on K_2 and Rb_2 via the $|X^1\Sigma_g^+, v = 0, N\rangle \rightarrow |B^1\Pi_u, v' = 1, N'\rangle$ and $|X^1\Sigma_g^+, v = 0, N\rangle \rightarrow |B^1\Pi_u, v' = 4, N'\rangle$ rovibronic transitions, respectively, using schemes otherwise identical to that described in the previous section. Both transitions enjoy high Franck-Condon factors ($>$ 0.1), and correspond to wavelengths readily accessible with the diode laser systems we already constructed (section 2.5.1). We drive primarily Q-branch ($N' = N$) transitions, for which transition dipole moments are independent of N and are therefore most suited for probing the underlying state occupations. For states with $N = 0$ for which Q-branch transition is forbidden, and we drive the R-branch transition $N = 0 \rightarrow N' = 1$ instead. The resulting spectra are shown in Fig. 7.7 for 7.8, for K_2 and Rb_2 respectively. We observe resonant signals corresponding to the states $N = 0 - 12$ for K_2 and $0 - 19$ for Rb_2, at frequencies that match the calculated values to within our measurement precision up to an overall offset of 8.30 GHz for K_2 and 1.78 GHz for Rb_2. We again document the theory frequencies in Tab J.3 and J.2 of Appendix J. We also targeted resonances corresponding to $N_{K_2} > 12$ and $N_{Rb_2} > 19$, and detected no significant ion signals, consistent with what is required by the reaction exothermicity* of 9.53(7) cm^{-1}.

In order to compare the signals from different rotational states for each product species, we fit each of the measured resonances with a Gaussian function (see Fig. 7.7 and 7.8 insets), from which we obtain the total integrated signal of a given rotational state. The resulting signal dis-

---

*see further discussions in Appendix I
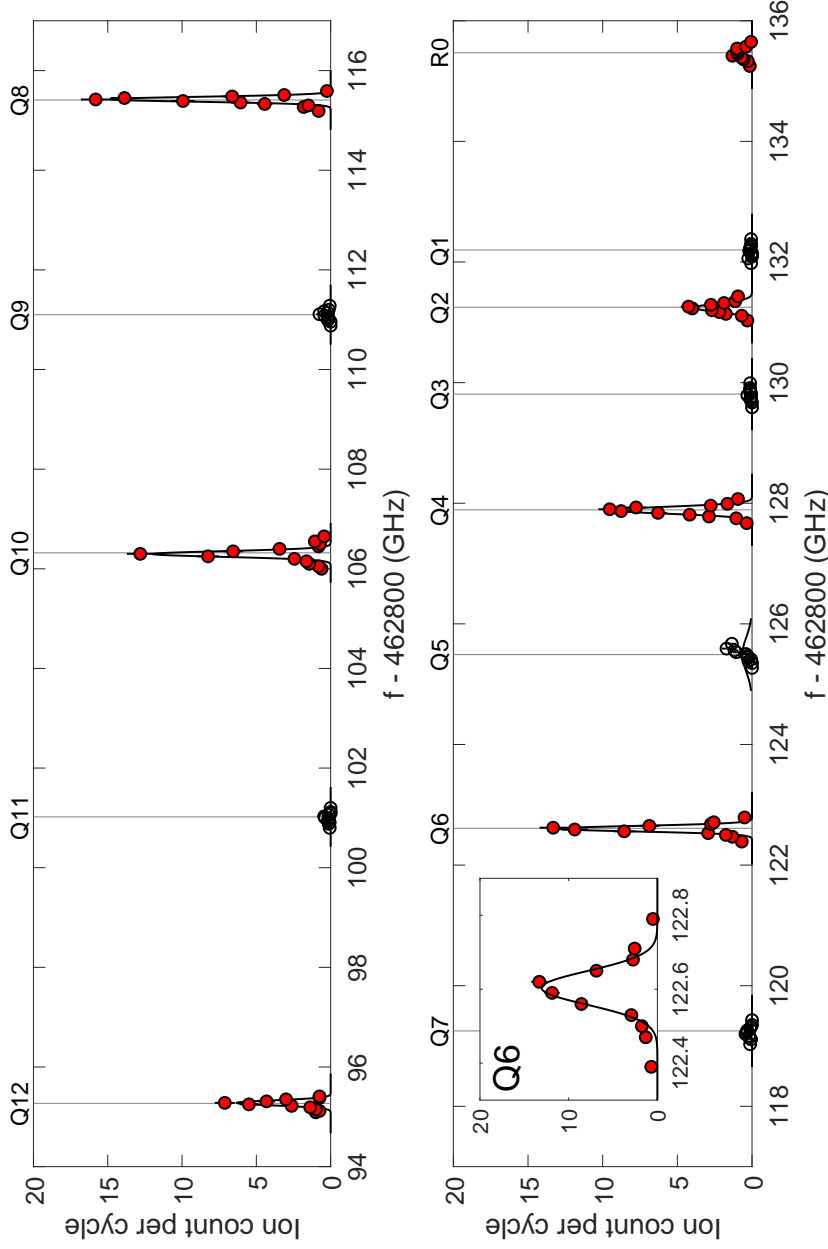
Figure 7.7: **REMPI spectrum for ^{40}K$_2$ product molecules at 30 G.** We scan the 648 nm laser frequency to search for rotational lines within the $X^1\Sigma_g^+(v=0, N_{K_2}=0, N_{K_2}') \rightarrow B^1\Pi_u(v'=1, N_{K_2}')$ vibronic band. By scanning the 648 nm laser frequency to search for rotational lines within the $X^1\Sigma_g^+(v=0, N_{K_2}) \rightarrow B^1\Pi_u(v'=1, N_{K_2}')$ vibronic band, we observe strong K$_2^+$ signals at frequencies corresponding to rotational states with even values of N_{K_2} (red filled circles), and highly suppressed signals for odd values (black open circles). The ion count for each data point is normalized by the corresponding number of experimental cycles (~ 16); the error bars denote shot noise. For $N_{K_2} > 0$ we drive transitions with $N_{K_2}' - N_{K_2} = 0$ (Q branch), whereas for $N_{K_2} = 0$, we drive the only allowed transition, with $N_{K_2}' - N_{K_2} = 1$ (R branch). Blue dashed lines indicate the predicted transition frequencies. The relatively strong asymmetric signal associated with $N_{K_2} = 5$ is due to the nearby $N_{K_2} = 2 \rightarrow N_{K_2}' = 1$ (P branch) transition at 462925.68 GHz. We do not observe any signals at frequencies corresponding to states with $N_{K_2} > 12$. Gaussian fits (black curves) are applied to each signal peak, yielding a typical spectral linewidth (1σ) of ~ 50 MHz. (Inset) Lineshape for the transition $N_{K_2} = 6 \rightarrow N_{K_2}' = 6$; the Gaussian width is $\sigma = 46 \pm 4$ MHz.

236
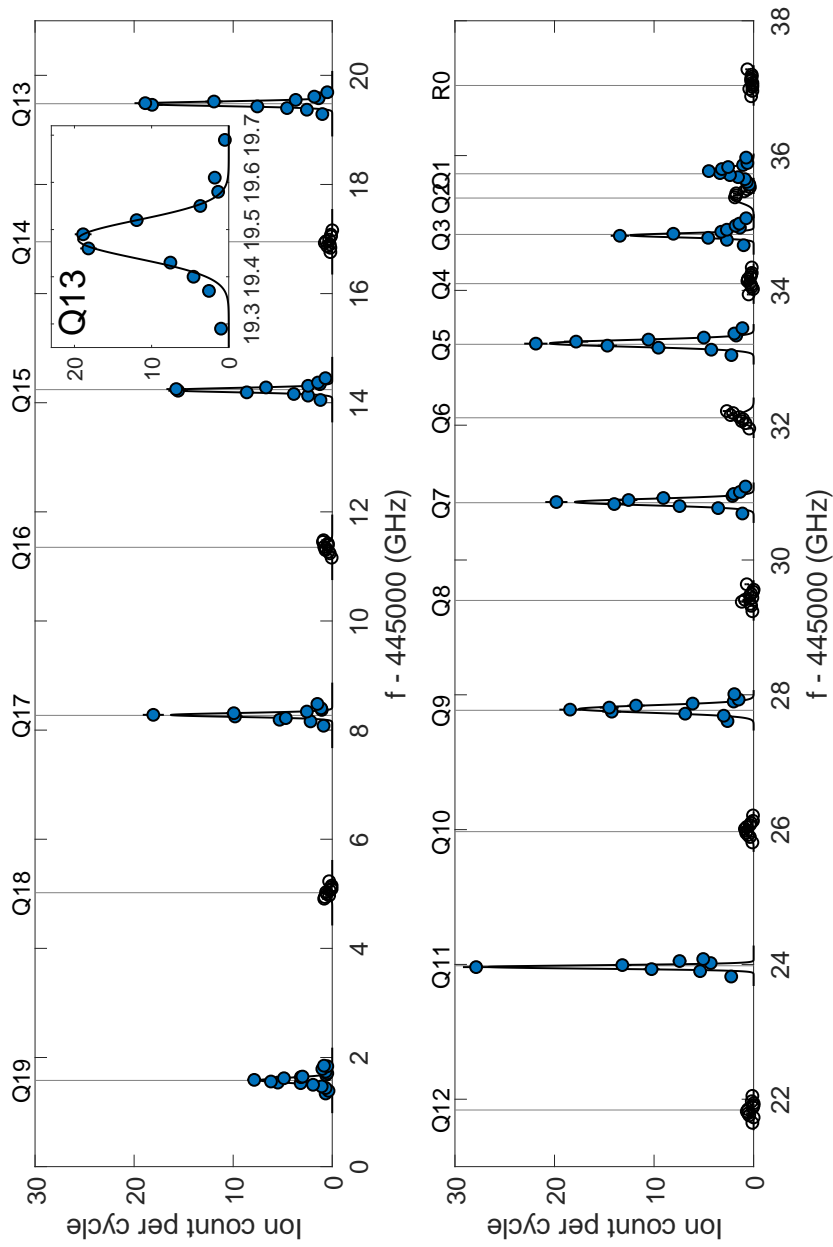
Figure 7.8: **REMPI spectrum for ^{87}Rb$_2$ product molecules at 30 G.** The frequency of the 674 nm laser is scanned within the $X^1\Sigma_g^+(v = 0, N_{\mathrm{Rb}_2}) \to B^1\Pi_u(v' = 4, N'_{\mathrm{Rb}_2})$ vibronic band. We observe strong Rb$_2^+$ signals for transitions from odd rotational states (blue filled circles), and highly suppressed signals from even ones (black open circles). The ion count for each data point is normalized by the corresponding number of experimental cycles (~ 16); the error bars denote shot noise. We drive Q branch transitions for $N_{\mathrm{Rb}_2} > 0$, and R branch for $N_{\mathrm{Rb}_2} = 0$. Blue dashed lines indicate the predicted transition frequencies. The relatively strong asymmetric signal associated with $N_{\mathrm{Rb}_2} = 6$ is due to the nearby $N_{\mathrm{Rb}_2} = 15 \to N'_{\mathrm{Rb}_2} = 16$ (R branch) transition at 445032.31 GHz, while that with $N_{\mathrm{Rb}_2} = 2$ is due to the $N_{\mathrm{Rb}_2} = 13 \to N'_{\mathrm{Rb}_2} = 14$ (R branch) transition at 445035.30 GHz. We do not observe any signals at frequencies corresponding to states with $N_{\mathrm{Rb}_2} > 19$. Gaussian fits (black curves) are applied to each signal peak, yielding a typical spectral linewidth (1σ) of ~ 40 MHz. (Inset) Lineshape for the transition $N_{\mathrm{Rb}_2} = 13 \to N'_{\mathrm{Rb}_2} = 13$; the Gaussian width is $\sigma = 43 \pm 3$ MHz.

237

tributions are shown in Fig. 7.9(a) for K_2 and (b) for Rb_2 as functions of N. Among those states that are energetically accessible, we find populations predominantly in the even-numbered rotational states of K_2 and odd-numbered rotational states of Rb_2. This significantly deviates from statistical behavior, and provides direct evidence for the conservation of nuclear spins in a reaction involving high-spin nuclei and a long-lived intermediate complex. We note here, however, that the relative signal heights in Fig. 7.9 are not yet sufficient to directly reconstruct the intrinsic product state distribution governed by the reaction dynamics, as the signals have not been normalized by the ionization efficiency associated with each state. This state-dependent efficiency arises from the fact that there is a unique velocity distribution associated with products with a given N_{K_2} or N_{Rb_2}, and the velocity-dependent fashion in which we are sampling them (see section 4.2.2). Further discussions on normalization of ion signals are offered towards the end of the chapter (section 7.4.1). Such normalizations, however, are not expected to qualitatively change the data presented in Fig. 7.9 and the strong parity preferences observed therein.

Given the strong rotational parity preference observed for a simple hyperfine state of the reactants, *i.e.* $\Psi^{nuc}_{KRb} = |-4, 1/2\rangle$, we now consider how nuclear spin conservation manifests itself for the more general case where all three Zeeman components participate (Eq. 7.18). To this end, we analyze the Rb_2 rotational spectrum shown in Fig. 7.6, acquired at a lower field of $B = 5$ G where the state admixture probabilities are given by $|\alpha|^2 = 0.354$, $|\beta|^2 = 0.517$, and $|\gamma|^2 = 0.129$. To extract the rotational state occupation, we select signals associatied with Q-branch transitions for $N_{Rb_2} = 1 - 19$ and R-branch transition for $N_{Rb_2} = 0$, normalize them by the different KRb molecule numbers associated with each measurement, and plot them in Fig. 7.10. Each resonance is then fitted to a Gaussian function, which is then integrated to produce the distribution shown in Fig. 7.11. Clear deviations from the 30 G distribution are observed, as evidenced by the establishment of a significant population in even-numbered rotational states of Rb_2 at 5 G.
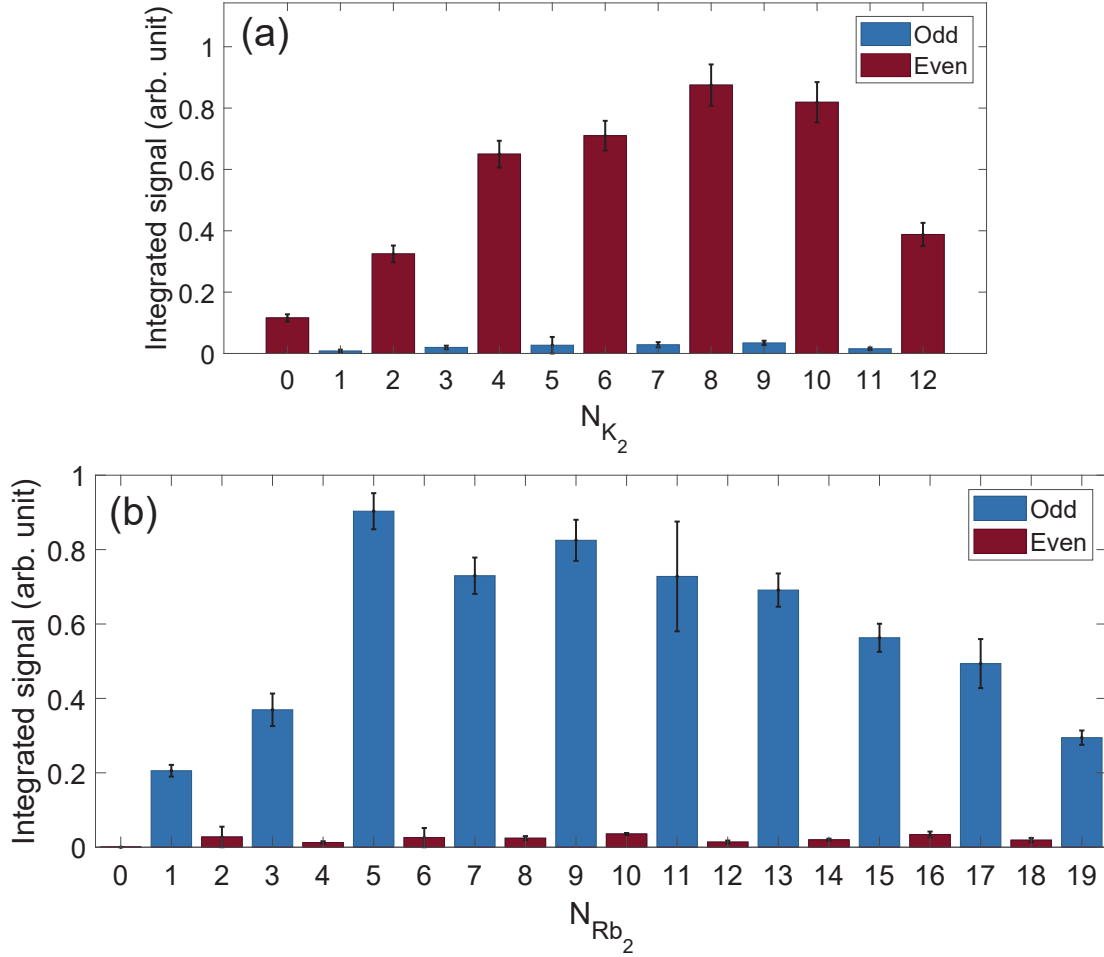
Figure 7.9: Rotational state occupation of the $^{40}K_2$ (a) and $^{87}Rb_2$ products in a 30 G magnetic field. Each bar is color-coded by the parity of the corresponding rotational state (crimson for even and blue for odd); its height is obtained by integrating the corresponding resonance in Fig. 7.7 or Fig. 7.8; and the associated error bar denote the standard deviation of the mean (standard error). Strong but opposite parity preferences are observed for the two product species.

7.3.2 Nuclear spin selection rules

While the suppressed parity preference observed at $B = 5$ G naively seems to contradict the previous conclusion that nuclear spins are conserved throughout this ultracold reaction, we argue that it is, in fact, a manifestation the conservation for a superposition input spin state. To sub-
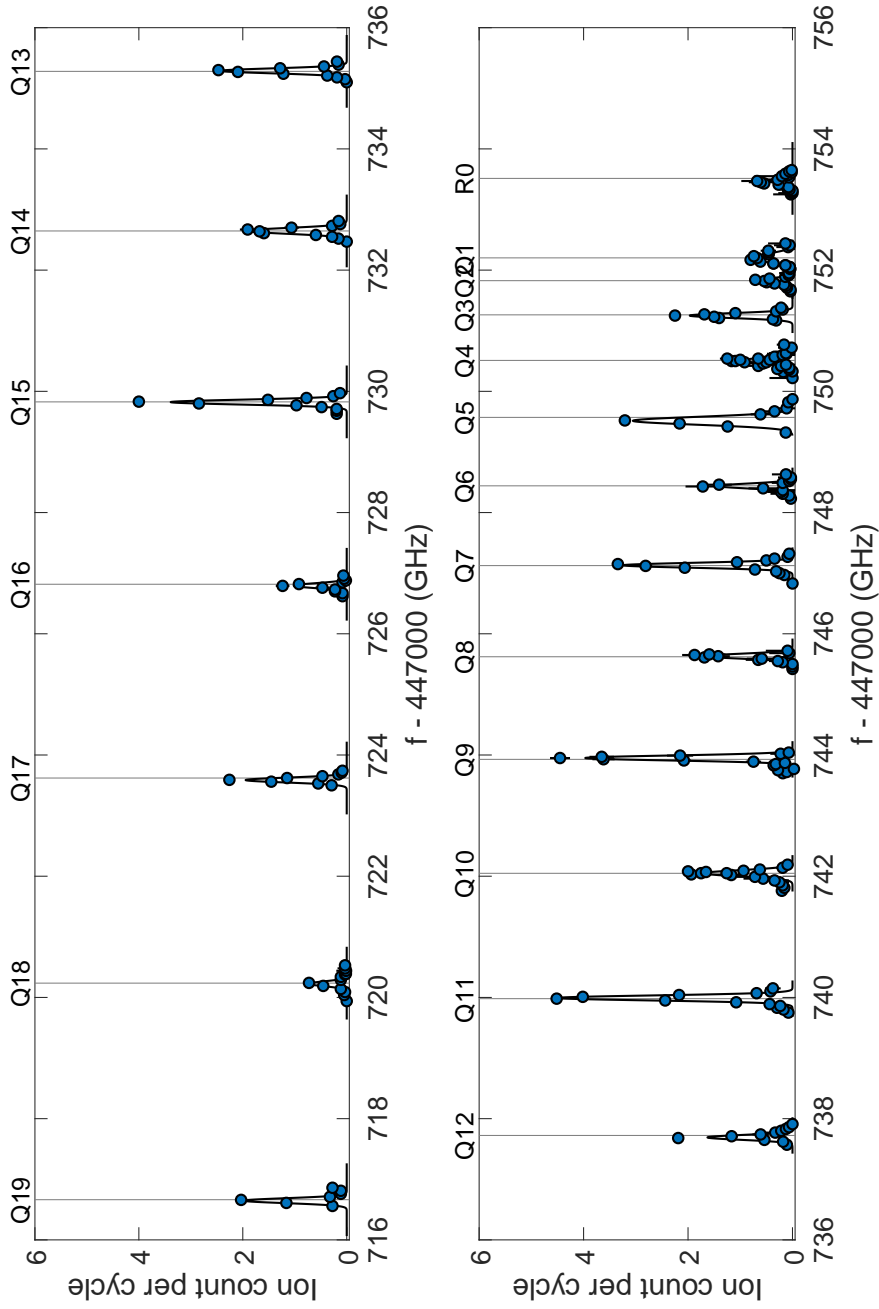
Figure 7.10: REMPI spectrum for $^{87}\mathrm{Rb}_2$ product molecules at 5 G. The frequency of the 674 nm laser is scanned within the $X^1\Sigma_g^+$ ($v = 0$, N_{Rb_2}) $\rightarrow B^1\Pi_u$ ($v' = 6$, N'_{Rb_2}) vibronic band. We observe strong Rb_2^+ signals for transitions from both even (red filled circles) and odd (blue filled circles) rotational states. The ion count for each data point is normalized by the corresponding number of experimental cycles (~ 20); the error bars denote shot noise. We drive Q branch transitions for $N_{\mathrm{Rb}_2} > 0$, and R branch for $N_{\mathrm{Rb}_2} = 0$. Gray vertical lines indicate the predicted transition frequencies. The relatively strong asymmetric signal associated with $N_{\mathrm{Rb}_2} = 6$ is due to the nearby $N_{\mathrm{Rb}_2} = 15 \rightarrow N'_{\mathrm{Rb}_2} = 16$ (R branch) transition at 445032.31 GHz, while that with $N_{\mathrm{Rb}_2} = 2$ is due to the $N_{\mathrm{Rb}_2} = 13 \rightarrow N'_{\mathrm{Rb}_2} = 14$ (R branch) transition at 445035.30 GHz. We do not observe any signals at frequencies corresponding to states with $N_{\mathrm{Rb}_2} > 19$. Gaussian fits (black curves) are applied to each signal peak, yielding a typical spectral linewidth (1σ) of ~ 40 MHz.

Figure 7.11: Rotational state occupation of $^{87}\text{Rb}_2$ products in a 5 G magnetic field. Each bar is obtained by integrating the corresponding resonance in Fig. 7.10. The associated error bars denote the standard deviation of the mean (standard error). In contrast to the 30 G case (Fig. 7.9(b)), Both even (crimson) and (blue) odd rotational states are significantly occupied.

stantiate this claim, we develop a model to characterize the product nuclear spin states given the two-particle reactant spin state, expressed in the uncoupled basis $\left| i_{\text{K}(1)}, i_{\text{Rb}(1)}, m_{\text{K}(1)}, m_{\text{Rb}(1)} \right\rangle \otimes \left| i_{\text{K}(2)}, i_{\text{Rb}(2)}, m_{\text{K}(2)}, m_{\text{Rb}(2)} \right\rangle$ as

$$\Psi_{\text{nuc}}^{\text{KRb}(1)} \otimes \Psi_{\text{nuc}}^{\text{KRb}(2)} = \alpha^2 \left| 4, \frac{3}{2}, -4, \frac{1}{2} \right\rangle \otimes \left| 4, \frac{3}{2}, -4, \frac{1}{2} \right\rangle + \beta^2 \left| 4, \frac{3}{2}, -3, -\frac{1}{2} \right\rangle \otimes \left| 4, \frac{3}{2}, -3, -\frac{1}{2} \right\rangle$$
$$+ \gamma^2 \left| 4, \frac{3}{2}, -2, -\frac{3}{2} \right\rangle \otimes \left| 4, \frac{3}{2}, -2, -\frac{3}{2} \right\rangle + \{\cdots\}.$$

$$(7.19)$$

Here, $\{\cdots\}$ represents the six cross terms resulting from the product of $\Psi_{\text{nuc}}^{\text{KRb}(1)}$ and $\Psi_{\text{nuc}}^{\text{KRb}(2)}$. Similar as before (section 7.1.3), we treat nuclear spin conservation formally as a direct projec-

241

tion of the state of the reactants onto that of the products, *i.e.*

$$\Psi_{\text{nuc}}^{K_2} \otimes \Psi_{\text{nuc}}^{Rb_2} = \alpha^2 \left|4, 4, -4, -4\right\rangle \otimes \left|\frac{3}{2}, \frac{3}{2}, \frac{1}{2}, \frac{1}{2}\right\rangle + \beta^2 \left|4, 4, -3, -3\right\rangle \otimes \left|\frac{3}{2}, \frac{3}{2}, -\frac{1}{2}, -\frac{1}{2}\right\rangle$$
$$+ \gamma^2 \left|4, 4, -2, -2\right\rangle \otimes \left|\frac{3}{2}, \frac{3}{2}, -\frac{3}{2}, -\frac{3}{2}\right\rangle + \{\cdots\}.$$

$$(7.20)$$

Note that in the above expression, spin states of K_2 and Rb_2 are given in the uncoupled basis $\left|i_{K(1)}, i_{K(2)}, m_{K(1)}, m_{K(2)}\right\rangle \otimes \left|i_{Rb(1)}, i_{Rb(2)}, m_{Rb(1)}, m_{Rb(2)}\right\rangle$, which is not the eigen-basis for homonuclear molecules[3]. As such, the symmetry characteristic (section 7.1.2) of each state is not immediately apparent. To this end, we transform the expression into the coupled basis $\left|I_{K_2}, M_{K_2}; i_{K(1)}, i_{K(2)}\right\rangle \otimes \left|I_{Rb_2}, M_{Rb_2}; i_{Rb(1)}, i_{Rb(2)}\right\rangle$, using the general formula for angular momentum addition

$$\left|i_{(1)}, i_{(2)}, m_{(1)}, m_{(2)}\right\rangle = \sum_{I=|i_{(1)}-i_{(2)}|}^{i_{(1)}+i_{(2)}} \left\langle I, M; i_{(1)}, i_{(2)} | i_{(1)}, i_{(2)}, m_{(1)}, m_{(2)}\right\rangle \left|I, M; i_{(1)}, i_{(2)}\right\rangle.$$

$$(7.21)$$

Here, $M = m_{(1)} + m_{(2)}$ and $\left\langle I, M; i_{(1)}, i_{(2)} | i_{(1)}, i_{(2)}, m_{(1)}, m_{(2)}\right\rangle$ is the Clebsch-Gordan (CG) coefficient.

$$\left|4, 4, -3, -3\right\rangle \otimes \left|\frac{3}{2}, \frac{3}{2}, -\frac{1}{2}, -\frac{1}{2}\right\rangle$$
$$= \left(-\sqrt{\frac{7}{15}}|I_{K_2} = 6, M_{K_2} = -6\rangle + \sqrt{\frac{8}{15}}|I_{K_2} = 8, M_{K_2} = -6\rangle\right)$$
$$\otimes \left(\sqrt{\frac{3}{5}}|I_{Rb_2} = 3, M_{Rb_2} = -1\rangle - \sqrt{\frac{2}{5}}|I_{Rb_2} = 1, M_{Rb_2} = -1\rangle\right).$$

$$(7.22)$$

Here, in the interest of simplicity, we have dropped from the coupled state label the individual nuclear spin quantum numbers $i_{K(1)}$, $i_{K(2)}$, $i_{Rb(1)}$, and $i_{Rb(2)}$, since they do not vary. Applying the basis transformation to all nine terms in Eqn 7.20, we arrive at Eqn L.3–L.11 in Appendix L.

242

Recall from the discussion in section 7.1.2 that states for which the quantity $i_{(1)} + i_{(2)} - I$ is even (odd) are symmetric (antisymmetric) under the exchange of nuclei (1) and (2). Take, for instance, the state in Eq. 7.22. Since $I_{K_2} = 6, 8$, and $I_{Rb_2} = 3, 1$, both products are in S states. Applying this criterion to all nine terms, we find that three of them consist of antisymmetric-antisymmetric combinations of K_2 and Rb_2 nuclear spin states, which we shall refer to as $A \otimes A$. The admixture coeffcients of these states are given by $\alpha\beta$, $\alpha\gamma$, and $\beta\gamma$, respectively. The remaining six terms, on the other hand, are symmetric-symmetric, or $S \otimes S$ combinations. The total probabilities for products to scatter into $A \otimes A$ and $S \otimes S$ states are given by the sums of the admixture probabilities for the individual terms, as

$$P_{A \otimes A} = |\alpha\beta|^2 + |\alpha\gamma|^2 + |\beta\gamma|^2,$$

$$P_{S \otimes S} = 1 - P_{A \otimes A}.$$

$$(7.23)$$

The above results constitute what is typically referred to in the chemistry literature as nuclear spin selection rules[159] (see Appendix L for details). As a result of the spin-rotation symmetry correspondence (section 7.1.2), these selection rules govern the probabilities of scattering into different rotational states based on their parities. Such probabilities are, of course, also determined by the dynamics of the reaction. Thus for a given N_{K_2} or N_{Rb_2} state, we have

$$P_{N_{K_2}} = A_{N_{K_2}} P_{A \otimes A} \quad \text{if } N_{K_2} \text{ is odd,}$$

$$P_{N_{K_2}} = A_{N_{K_2}} P_{S \otimes S} \quad \text{if } N_{K_2} \text{ is even,}$$

$$P_{N_{Rb_2}} = A_{N_{Rb_2}} P_{S \otimes S} \quad \text{if } N_{Rb_2} \text{ is odd,}$$

$$\text{and} \quad P_{N_{Rb_2}} = A_{N_{Rb_2}} P_{A \otimes A} \quad \text{if } N_{Rb_2} \text{ is even,}$$

$$(7.24)$$

243

Table 7.3: Relative occupation of even and odd rotational states of Rb_2 when the reactions are operated under a 30 or 5 G magnetic field. $R_{o/e}$ represents the measured ratio between even and odd states, and $P_{S\otimes S}$ and $P_{A\otimes A}$ represent the predicted probabilities of scattering into symmetric and anti-symmetric product nuclear spin states, the values of which are related to the reactant nuclear spin state admixture coefficients (Eq. 7.18) α, β, and γ according to Eq. 7.23.

B field (G)	$|\alpha|^2$	$|\beta|^2$	$|\gamma|^2$	$P_{S\otimes S}$	$P_{A\otimes A}$	$P_{S\otimes S}/P_{A\otimes A}$	$R_{o/e}$
30	0.982	0.018	0.000	0.982	0.018	54.6	40^{+20}_{-10}
5	0.354	0.517	0.129	0.684	0.316	2.16	$2.5^{+0.2}_{-0.3}$

where $\{A_{N_{K_2}}\}$ and $\{A_{N_{Rb_2}}\}$ represent the amplitudes of scattering into N_{K_2} or N_{Rb_2} due to the reaction dynamics, which, by the conservation of total probability, must satisfy the relations

$$P_{K_2}^{\text{odd}} + P_{N_{K_2}}^{\text{even}} = \left(\sum_{\text{odd}} A_{N_{K_2}}\right) P_{A\otimes A} + \left(\sum_{\text{even}} A_{N_{K_2}}\right) P_{S\otimes S} = 1,$$

$$\text{and} \quad P_{Rb_2}^{\text{odd}} + P_{Rb_2}^{\text{even}} = \left(\sum_{\text{odd}} A_{N_{Rb_2}}\right) P_{S\otimes S} + \left(\sum_{\text{even}} A_{N_{Rb_2}}\right) P_{A\otimes A} = 1,$$

(7.25)

where $P_{K_2/Rb_2}^{\text{odd/even}}$ represents the summed probability to scatter into odd or even states of K_2 or Rb_2. Direct measurements of $\{A_{N_{K_2}}\}$ and $\{A_{N_{Rb_2}}\}$ are reserved for future studies aimed at probing the dynamics of the KRb + KRb reaction, and we provide some outlook on this topic at the end of the chapter. Now, under the reasonable assumption that the reaction dynamics do not intrinsically prefer even or odd rotational states in products, we have $\sum_{\text{odd}} A_{N_{K_2}/N_{Rb_2}} \approx \sum_{\text{even}} A_{N_{K_2}/N_{Rb_2}} \approx 1$, and therefore

$$\frac{P_{K_2}^{\text{even}}}{P_{K_2}^{\text{odd}}} = \frac{P_{Rb_2}^{\text{odd}}}{P_{Rb_2}^{\text{even}}} = \frac{P_{S\otimes S}}{P_{A\otimes A}}.$$

(7.26)

Having established the relationships between the reactant spin states, the product spin states, and the product rotational states, we are now in a position to explain the markedly different product state distributions observed at $B = 30$ G (Fig. 7.9) and $B = 5$ G (Fig. 7.11). Using

the calculated values of the state admixture probabilities $|\alpha|^2$, $|\beta|^2$, and $|\gamma|^2$ at each field value, we obtain the expected probabilities for scattering into odd or even rotational states of Rb$_2$, as well as their ratio (Tab. 7.3). Comparing the ratios between summed signal strengths of odd and even states from our measurements, $R_{o/e}$, to the calculated values of $P_{S\otimes S}/P_{A\otimes A}$, we find good agreements given experimental uncertainties. Notably, both cases differ significantly from the completely statistical outcome, for which the expected odd-to-even ratio is 1.67 (section 7.1.2). These results demonstrate that the observations of significant population in even rotational states of Rb$_2$ at $B = 5$ G and the lack thereof at $B = 30$ G are both manifestations of nuclear spin conservation throughout the ultracold KRb + KRb reaction, albeit for two qualitatively different forms of input spin state of the reactants.

7.3.3   Continuous control of product occupations

The significant change in the parity preference of product rotational states resulting from the variation of an external magnetic field represents a new mechanism for controlling the product state distribution at the quantum state level. To further explore this control, we probe the outcome of the reaction for different values of B in the range $5 - 50$ G*. Without loss of generality, we measure changes in the amplitudes of the resonances corresponding to the rotational states $N = 6, 7$ for K$_2$ and $N = 4, 5, 13, 14$ for Rb$_2$ (Fig. 7.12c,d). We observe that the odd (even) states of K$_2$ (Rb$_2$), which are unoccupied at higher magnetic fields, acquire significant population as B decreases, while the population in the even (odd) states is suppressed. This shows that the relative occupation of odd and even parity states of the products can be altered continuously by controlling the nuclear spin state of the reactants via an external field.

---

*Extending the range of this measurement below 5 G is an interesting future direction. As we have demonstrated in section 4.5, the external field can be as low as 2 G without the KRb molecules loosing their magnetic quantization, at which point the reactions become s-wave dominated.
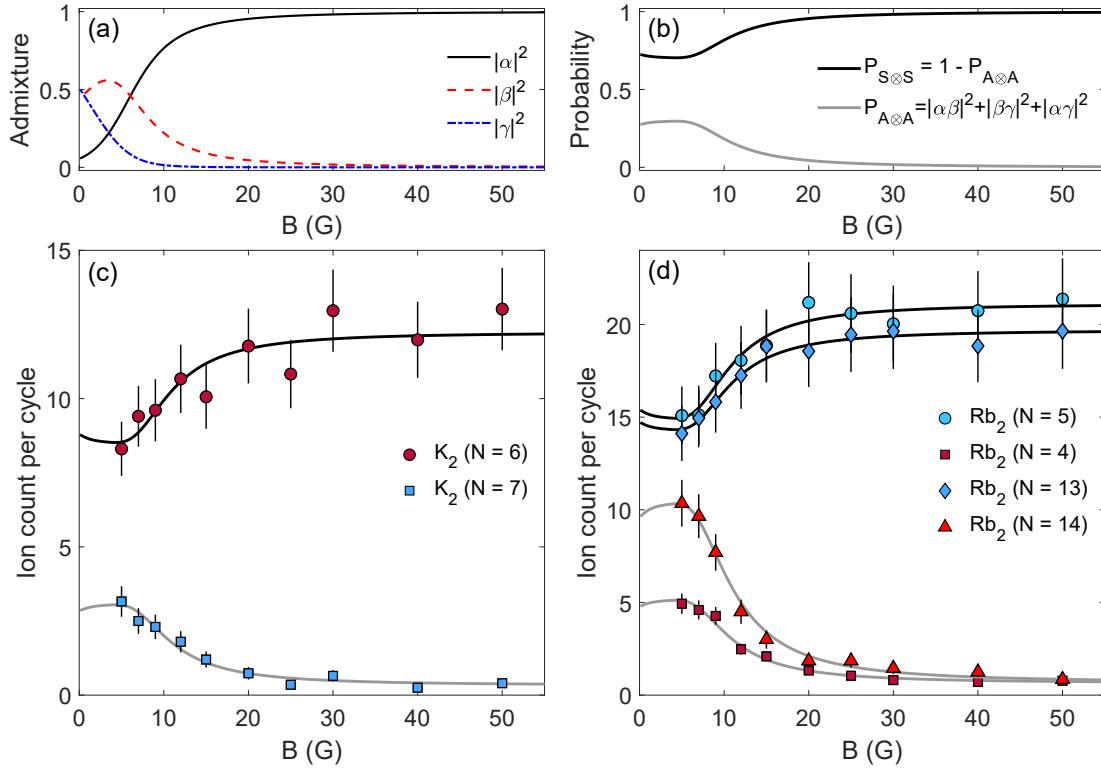
Figure 7.12: Continuous control of product rotational state occupations with a magnetic field. (a) Calculated admixture probabilities $|\alpha|^2$, $|\beta|^2$, and $|\gamma|^2$ for the reactant spin superposition (Eq. 7.18) as a function of magnetic field. (b), Probabilities for scattering into the symmetric (P_S) and antisymmetric (P_A) nuclear spin states of K_2 or Rb_2 based on the conservation of nuclear spins. (c–d), Product ion counts associated with the rotational states $N = 6, 7$ for K_2 (c) and $N = 4, 5, 13, 14$ for Rb_2 (d) obtained at different magnetic field values between 5 and 50 G. For each data set, the 648/674 nm laser frequency is fixed to be resonant with the corresponding transition, as identified from the spectra in Fig. 7.7 and 7.8. The ion count for each data point is normalized by the corresponding number of experimental cycles (~ 20). Error bars include shot noise and 10% ion number fluctuation due to the REMPI laser frequency uncertainty (~ 25 MHz). Black (grey) curves are fits to the function $a \cdot P_{S(A)} + b$, where a and b are fit parameters representing the state-dependent proportionality constant and the offset arising from the detection noise floor, respectively. The typical root-mean-square error (RMSE) for the fit is 0.35.

To understand the observed variations in even and odd populations, we examine the magnetic field dependence of the reactant nulcear spin state composition (7.12(a)), as well as that of the corresponding scattering probabilities into S and A product states (7.12(b)). We see that while Ψ_{KRb}^{nuc} is well-approximated by the single $|-4, 1/2\rangle$ state for $B \gtrsim 20$ G, significant mixing of

$|-3, -1/2\rangle$ and $|-2, -3/2\rangle$ start to occur for $B \lesssim 20$ G. Since the detected populations of even (odd) rotational states are proportional to $P_{S \otimes S}$ ($P_{A \otimes A}$) for K_2 and $P_{A \otimes A}$ ($P_{S \otimes S}$) for Rb_2 (Eq. 7.24), we can fit each data set in Fig. 7.12(c,d) to the function $a \cdot P_{S/A} + b$, with free parameters a and b. Here, a represents the proportionality between the measured signal strength and scattering probabilities, which include scattering amplitudes due to the reaction dynamics (*i.e.* $\{A_{N_{K_2}}\}$ and $\{A_{N_{Rb_2}}\}$), as well as the detection efficiency of products in particular rotational states; b is an offset arising from the noise floor of ion detection. The fitted curves (Fig. 7.12(c,d)) show that the selection rules (Eq. 7.23), derived in accordance with nuclear spin conservation, describes well the magnetic field dependence of the rotational state populations.

7.3.4 Conclusion and outlook

In this section, we studied the quantum state distribution of the products formed in the ultracold $KRb + KRb \rightarrow K_2 + Rb_2$ reaction using REMPI spectroscopy. By examining the relative proportions of products in even and odd rotational states for different forms of reactant nuclear spin states, we concluded that spins of the nuclei involved remain unchanged throughout the reaction. This result testifies to the robustness of the widely accepted concept of nuclear spin conservation[159], even in a case involving high spin nuclei and a long-lived intermediate complex. It implies that nuclear spins are effectively decoupled from the other degrees of freedom of the system and their complicated dynamics within the intermediate complex. This means that the spins, besides introducing a parity-dependent weighing factor to the rotational state populations, can in general be ignored in future studies of state-to-state reaction dynamics, greatly simplifying both the theoretical and experimental treatments of the reaction.

To quantitatively explain the magnetic field dependence of the product rotational state distributions, we formulated a set of nuclear spin selection rules (Eq. 7.23) using standard angular

momentum algebra. While these rules were established for a specific input state (Eq. 7.18), the methodology does not depend on the particular form of the state, and can be generalized to account for arbitrary states of the reactant nuclear spins. Experimentally, such states may be realized using a combination of external magnetic fields and microwave control techniques[161,166]. We also note that the sensitivity of the rotational state occupation to external fields observed here is not a feature that is unique to the KRb + KRb system, but can also play a significant role in other chemical reactions involving identical nuclei, such as those found in atmospheric[93] and interstellar processes[134]. Our results therefore indicate that the effects of ambient fields may warrant consideration in future studies of reactions in these environments.

Taking advantage of the weak-coupling between nuclear spins and other degrees of freedom, as well as the spin-rotation symmetry relation in homonulcear diatomic molecules, we demonstrated control over the product rotational state occupations by manipulating the reactant nuclear spins via an external magnetic field. This represents a new type of state-level control – one that bypasses the complexity of the underlying chemical dynamics. It stands in contrast to prior works that achieved control by manipulating the dynamics, through, for example, coherent control of molecular motion via optical pulses[186,28] or preparation of molecules in well-defined states of vibration[54]. As such, it shows that the complexity of complex-forming reactions does not fundamentally limit their controllability. An important advantage of our technique is that the quantum coherence between different spin-components of the reactants is inherited by the products. Such an effect can be utilized to engineer correlations between the states of product molecules originating from the same reaction, which can enable the generation of quantum entanglement between reaction products[84,131].

7.4 Toward state-to-state ultracold reaction dynamics

In the final section of this chapter, we delve into the state-to-state reaction dynamics of the ultracold KRb + KRb reaction. As this is a subject of ongoing investigation in the lab at the conclusion of this thesis work, we will present only an incomplete set of experimental data for the purpose of illustrating techniques for data acquisition and analysis. At the conclusion of this section, we will discuss the possibilities for non-statistical behaviors in a reaction that is expected to behave statistically, and how such effects may manifest in the fully-resolved product state distribution which will eventually be obtained.

Experimentally, studying the state-to-state dynamics amounts to measuring how the product populations are distributed among the allowed exit channels. To this end, the reader may note that such information is, in principle, already contained in rotational state occupations of K_2 and Rb_2 shown in Fig. 7.9. Directly extracting information on state-to-state dynamics from these data, however, is met with the issue of normalization, which will be discussed next.

7.4.1 Normalization of the product state distributions

As we discussed in section 7.3.1, in order for the raw ion signals presented in 7.9 to reflect proportionally the underlying population distribution, proper normalization must be applied. Recall from our discussions in sections 4.2.2 that such normalizations are necessary due to the fact that products with higher velocities are under-sampled by REMPI compared to those with lower velocities. This under-sampling stems from the finite repitition rate of the ionization lasers as well as the Doppler effect, resulting in the "velocity factors" $F_1(v)$ and $F_2(v)$. While we know precisely what these factors are for products belonging to single velocity classes from the models developed in section 4.2.2, here we are dealing with velocity distributions – due to the freedom

249

in the partitioning of the reaction exothermicity into the rotations of the two product molecules as well as their relative motion, each given rotational state of K_2 (Rb_2) is, in general, associated with multiple rotational states of Rb_2 (K_2), resulting in K_2 (Rb_2) molecules in multiple different kinetic energy (KE) or velocity classes (v_c) (see Tab. 7.2). As an example, the state $N_{Rb_2} = 3$ is associated with states $N_{K_2} = 0, 2, 4, 6, 8, 10$ and 12, resulting in Rb_2 products belonging to seven different velocity classes ranging from 5.7 to 20.0 m/s. As such, the total detected ion counts (per cycle) for a given N_{K_2} or N_{Rb_2}, $S_{N_{K_2}/N_{Rb_2}}$, is related to the number of product molecules for each velocity class (per cycle), $n_c(v_c)$, by

$$S_{N_{K_2}/N_{Rb_2}} = \eta_{\text{det}} \sum_{v_c} n_c(v_c) F_1(v_c) F_2(v_c). \tag{7.27}$$

For the purpose of normalization, the quantity we are interested in is $n_{N_{K_2}/N_{Rb_2}} = \sum_{v_c} n_c(v_c)$, which is the total product population belonging to the state N_{K_2} or N_{Rb_2}. This, however, will require knowledge of $n_c(v_c)$ for the entire set of velocity classes. The natural question is: how do we experimentally obtain this information?

In fact, the usefulness of obtaining $n_c(v_c)$ for each product state goes much beyond the normalization of state distributions – each $n_c(v_c)$ provides the population in a specific *pair* of product states $\{N_{K_2}, N_{Rb_2}\}$. Measuring $n_c(v_c)$ for all individual product rotational states will allow us to construct the *pairwise* population distribution for the reaction, which contains much more information about the reaction dynamics compared to the separate K_2 and Rb_2 distributions. As we will discuss at the end of this section (7.4.3), the search for non-statistical effects in the reaction dynamics would be very difficult, if not impossible, without the pairwise distribution.

In our investigations of reaction products thus far, we have not taken full advantage of the ion imaging capability of our ionization detection (section 4.4). By design, such a technique could help resolve products belonging to different velocity classes, thus allowing measure-

Figure 7.13: (a) Simulated image for the Rb_2^+ ions obtained from state-selective ionization of Rb_2 in the $N = 3$ rotational state; features are broadened to account for the finite resolution of the VMI. Detailed procedure for the simulation is given in the main text. Gray rings superimposed on the image represent the perimeter of Newton spheres associated with allowed product velocity classes. (b) The original, radially averaged, and reconstructed radial profiles corresponding to the image in (a). Blue lines represent radii of the different velocity classes.

ments of $n_c(v_c)$. To illustrate the basic ideas, we simulated an expected ion image for Rb_2 products in rotational state $N_{Rb_2} = 3$, for which the associated velocity classes are $v_c =$

$20.0, 19.7, 18.8, 17.3, 15.2, 11.9,$ and 5.7 m/s. For this simulation, we have assumed equal proportion of products belonging to each v_c, and applied the appropriate velocity factors $F_1(v_c)$ and $F_2(v_c)$ to account for the probability for Rb_2 in each v_c to be converted into Rb_2^+. We have ignored the anisotropy in the ion distribution due to Doppler shifts, which is in general a very small effect for Rb_2. As such, the products exist on seven concatenated Newton spheres, following the 1D probability distribution shown in Fig. 7.13(b). Note that in order to account for the finite resolution of our VMI (section 4.4) we have applied a Gaussian broadening with a 1σ width of 0.25 mm to each sphere. The ion image resulting from the 2D projection of the spheres is shown in Fig. 7.13(a), while its radially averaged ($f'(R)$) and inverse Abel reconstructed ($f(R)$) profiles are shown in Fig. 7.13(b). In principle, the value of n_c for each v_c can be extracted from $f(R)$ through fitting to the function

$$f(R) = \sum_{v_c} n_c(v_c) \exp\left[-\frac{(R - R_c(v_c))^2}{2\sigma^2}\right], \tag{7.28}$$

where $\{R_c\}$ are the radii of to the various Newton spheres, σ is the instrumentally broadened Gaussian width associated with each sphere, and $\{n_c\}$ are treated as free amplitude parameters whose values are to be determined by the fit. The reliable determination of $\{n_c\}$ from $f(R)$ hinges on one's ability to distinguish different velocity classes in ion imaging. From the above simulation, however, we see that, with the exceptions of two states with relatively low KE ($\{N_{K_2} = 12, N_{Rb_2} = 3\}$ and $\{N_{K_2} = 10, N_{Rb_2} = 3\}$), there are severe radial overlaps between products of different velocity classes, making it highly difficult to extract individual amplitudes. The problem is expected to be even worse for real ion images due to the presence of experimental noises.

Our expectations from the simulation are corroborated by the experimentally measured ion images for Rb_2 in the $N = 3$ rotational state, as shown in Fig. 7.14. Both the ion image itself
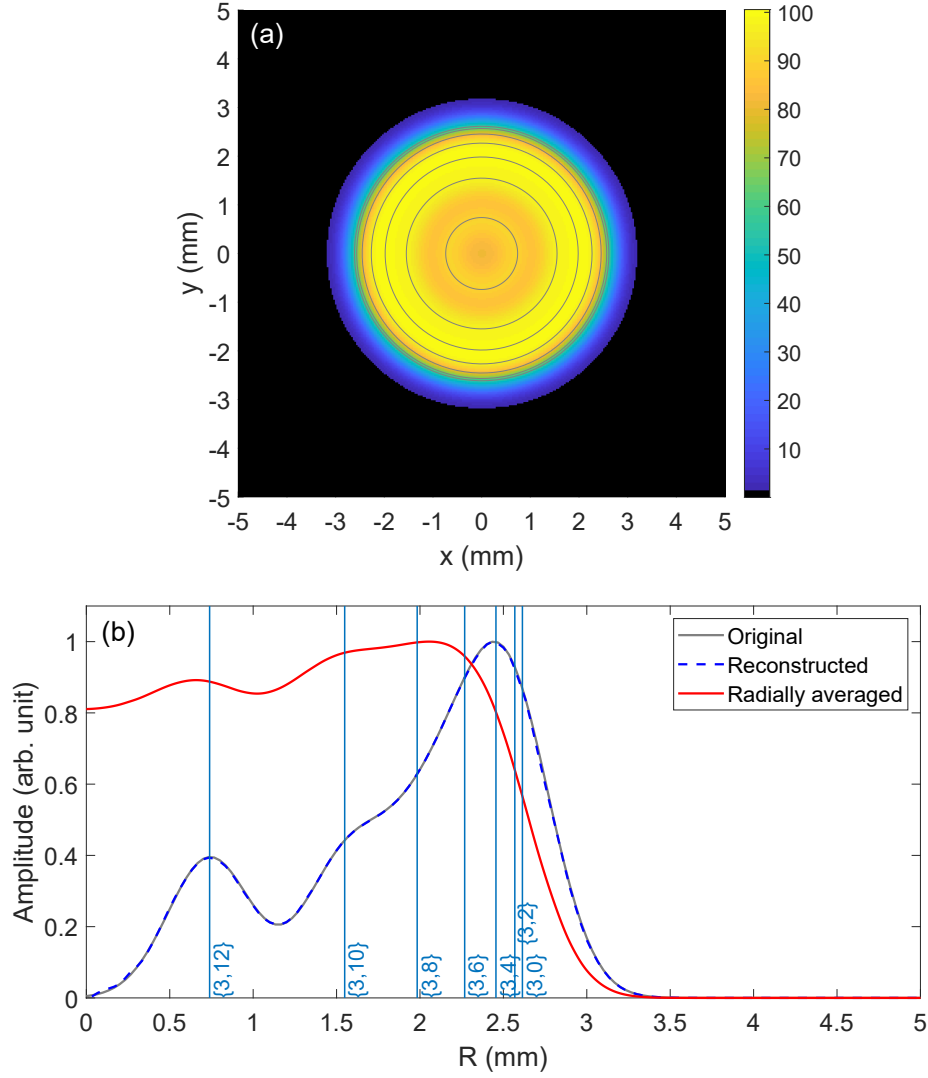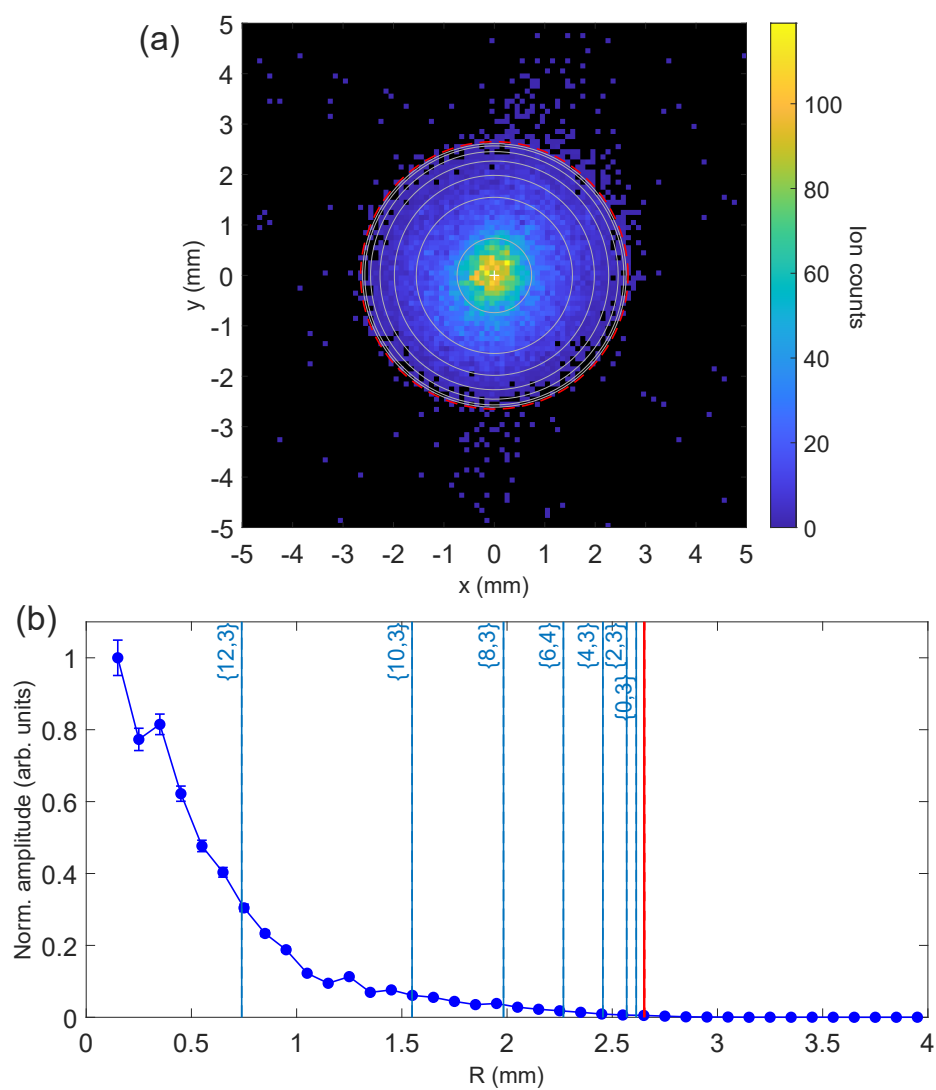
Figure 7.14: (a) Measured image for the Rb_2^+ ions obtained from state-selective ionization of Rb_2 in the $N = 3$ rotational state. Gray rings superimposed on the image represent the perimeter of Newton spheres associated with allowed product velocity classes. (b) The radial distributions of the ions obtained from radially averaging the ion image in (a) and applying an inverse Abel transform. Blue lines represent radii of the different velocity classes. The red line indicates the radius corresponding to the reaction exothermicity.

(a) and its reconstructed radial profile (b) lack any discernible structures. Thus we conclude that without fundamental improvements to our resolution, we cannot reliably determine the populations associated with pairs of product states through the combined use of REMPI and ion imaging.

Our preceding discussions makes clear that for the purpose of studying state-to-state dynamics, it is difficult to rely on individual state distributions such as the ones shown in Fig. 7.9. So is all hope lost? Fortunately, the answer is no. The solution is that instead of looking at the rotational states of K_2 and Rb_2 separately, we condition the detection on pairs of them *i.e.* coincidence detection. Since there is a single KE or v_c associated with each $\{N_{K_2}, N_{Rb_2}\}$ pair, we simply apply the corresponding velocity factors $F_1(v_c)$ and $F_2(v_c)$* to the measured coincidence signal to normalize it. As such, coincidence detection represents a viable option to obtaining the pairwise state distribution.

7.4.2 Coincidence product detection

In this section, we illustrate the procedure for coincidence product detection, using the sate pair $\{N_{K_2} = 6, N_{Rb_2} = 7\}$ as an example. Within a cloud of cold KRb molecules, each reactive event generates a pair of products in some rotational state $\{N_{K_2}, N_{Rb_2}\}$ that belong to the total of 56 possible exit channels (see Tab. 7.2)[†]. In order to selectively probe products belonging to $\{6, 7\}$, we simultaneously apply resonance-enhanced ionization to products in $N_{K_2} = 6$ as well as $N_{Rb_2} = 7$, and post-select for K_2^+ and Rb_2^+ counts that emerge from the same reactive event. To perform simultaneous REMPI, we combine light from the 650 and 674 nm diode lasers driving the bound-to-bound transitions in K_2 and Rb_2 on a dichroic mirror, overlap their pulses in

---

*Recall from the discussion in section 4.2.2 that F_2 can be approximated as 1.

[†]Technically, each product pair exist in a superposition of all possible exit channels. Each channel has an amplitude coefficient equal to the square root of the probability of scattering into that channel, as determined by the reaction dynamics as well as the nuclear spin statistics.
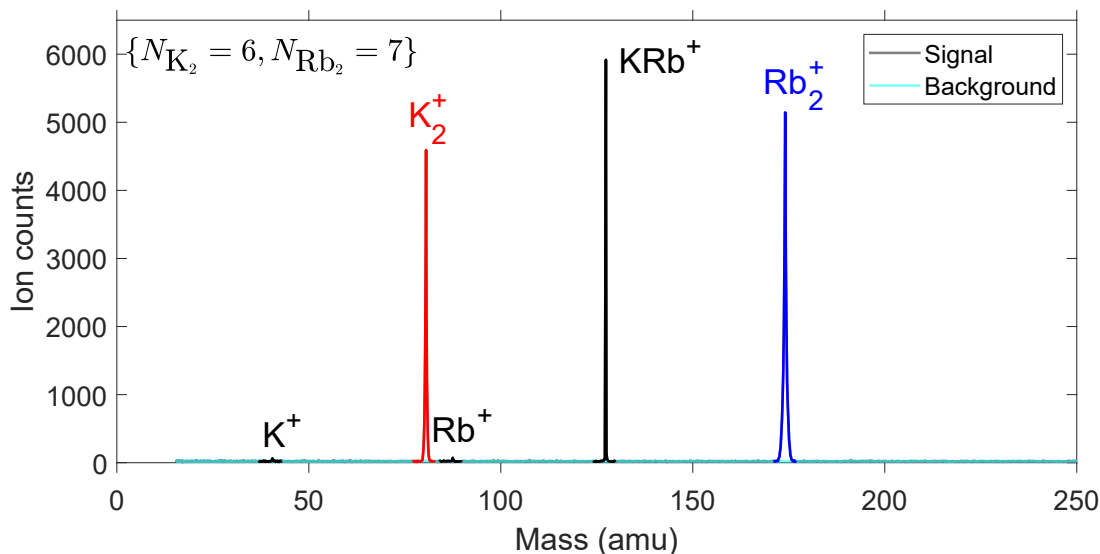
Figure 7.15: TOF mass spectrum obtained by simultaneous REMPI detection of K_2 products in $N = 6$ and Rb_2 in $N = 7$.

time, and synchronized them to the 532 nm pulses as well as ODT intensity modulation following the previously used timing scheme (see Fig. 7.4). In a given experiment, the frequencies for the diode lasers are tuned to be resonant with the $Q6$ and $Q7$ transitions in K_2 and Rb_2, respectively, such that products in those states are selectively ionized and subsequently detected.

After data accumulation for 1379 experimental cycles, we obtain the mass spectrum as shown in Fig. 7.15, which, as expected, displays peaks corresponding to both K_2^+ and Rb_2^+. Among the $\sim$16000 detected K_2^+ ions and $\sim$22000 Rb_2^+, only a small fraction correspond to $\{6, 7\}$, while the rest belong to the larger subsets $\{N_{K_2} = 6, N_{Rb_2} \neq 7\}$ and $\{N_{K_2} \neq 6, N_{Rb_2} = 7\}$. To screen out those that correspond to the state pair of interest, we apply two coincidence conditions. First, we pre-screen for pairs of K_2^+ and Rb_2^+ generated by the same set of REMPI pulses, and 176 such pairs are found within this dataset. Now, since each set of pulses exposes products from many reactive events, the pre-screened set of ions will contain "accidentals" – those that correspond products in the states of interest but are generated in different events. Therefore
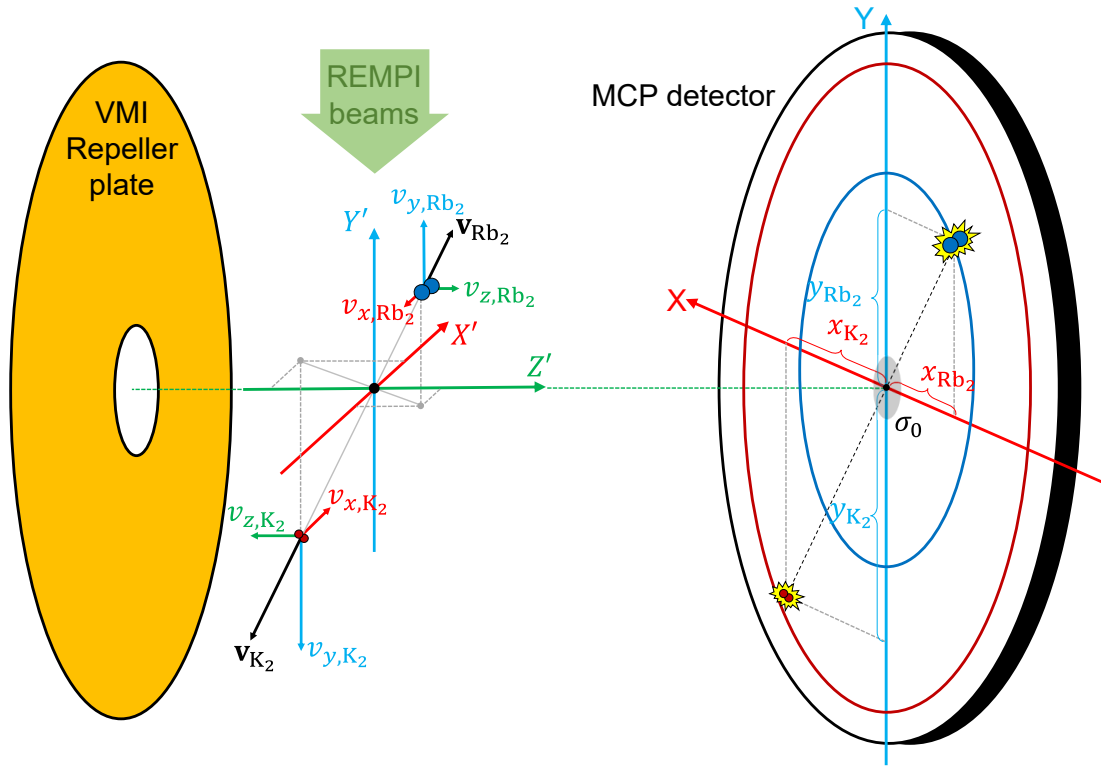
Figure 7.16: Coincidence product detection. Each reaction event generates a K_2–Rb_2 pair, in some rotational state pair $\{N_{K_2}, N_{Rb_2}\}$. The velocity vectors for the pair are constrained by momentum conservation (Eq. 7.31). Once ionized by REMPI, the pair is projected by VMI onto the MCP detector, where hit locations are recorded. The recorded locations are used to determined whether an experimentally observed ion pair is truly coincident (Eq. 7.33).

we apply additional screening based on the fact that products that emerge from the same event satisfy momentum conservation, *i.e.*

$$m_{K_2} v_{x/y/z,K_2} + m_{Rb_2} v_{x/y/z,Rb_2} = 0, \tag{7.29}$$

while those from different events in general do not. Here, v_z is the projection of the product velocity along the TOF axis, while v_x and v_y are the ones transverse to it, and in plane with the MCP detector (see coordinate system defined in Fig. 4.13).
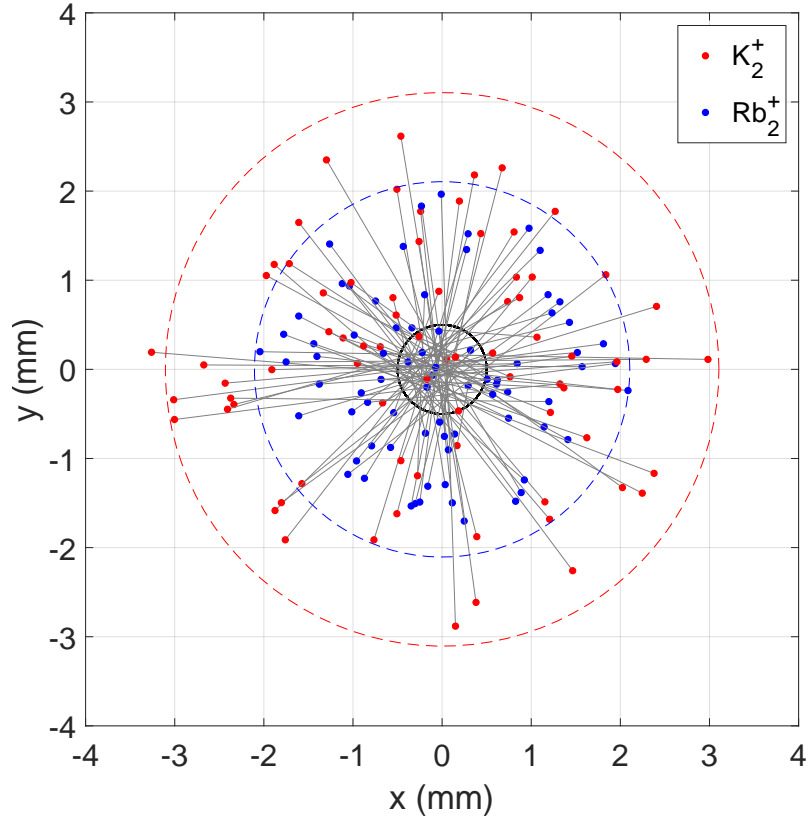
Figure 7.17: Hit locations of coincident ions, marked as red for K_2^+ and blue for Rb_2^+, with a gray line draw over each pair. Red (blue) dotted circles represent the expected perimeters of the Newton spheres associated with K_2^+ (Rb_2^+) ions, which has a well-defined translational energy of 4.12 (1.89) cm^{-1}.

To implementation of Eq. 7.29 for screening, we use spatial information of the ions to constrain their velocity projections in the xy-plane, $\vec{\nu}_{K_2} = \{v_{x,K_2}, v_{y,K_2}\}$ and $\vec{\nu}_{Rb_2} = \{v_{x,Rb_2}, v_{y,Rb_2}\}$, where $\nu_{K_2/Rb_2} = \sqrt{v_{x,K_2/Rb_2}^2 + v_{y,K_2/Rb_2}^2}$. For a given ion pair that survived the pre-screening process, we examine their hit locations on the detector, $\vec{\rho}_{K_2} = \{x_{K_2}, y_{K_2}\}$ and $\vec{\rho}_{Rb_2} = \{x_{Rb_2}, y_{Rb_2}\}$, where $\rho_{K_2/Rb_2} = \sqrt{x_{K_2/Rb_2}^2 + y_{K_2/Rb_2}^2}$. These coordinates are specified relative to the hit locations of zero-velocity K_2^+ and Rb_2^+ ions, O_{K_2} and O_{Rb_2}*. By design of the VMI (Eq. 4.14), the

_____

*O_{K_2} and O_{Rb_2} do not coincide due to the presence of the magnetic field

coordinates are related to the product velocity projections as

$$\vec{\rho}_{K_2/Rb_2} = A\sqrt{\frac{m_{K_2/Rb_2}}{2V_R}}\vec{v}_{x,K_2/Rb_2}. \tag{7.30}$$

For a true coincidence pair which obey momentum conservation, their coordinates will ideally satisfy the relations

$$\sqrt{m_{K_2}}\vec{\rho}_{K_2} + \sqrt{m_{Rb_2}}\vec{\rho}_{Rb_2} = 0 \quad \text{or} \quad \vec{\rho}_{K_2} + \sqrt{\frac{m_{Rb_2}}{m_{K_2}}}\vec{\rho}_{Rb_2} = 0. \tag{7.31}$$

Due to the finite spatial resolution of our ion imaging, however, we in practice define a circle with radius σ_0, and consider and ion pair to be coincident if it coordinates satisfy the condition

$$\left\|\vec{\rho_{K_2}} + \sqrt{\frac{m_{Rb_2}}{m_{K_2}}}\vec{\rho_{Rb_2}}\right\| < \sigma_0, \tag{7.32}$$

or, in terms of x and y coordinates

$$\left(x_{K_2} + \sqrt{\frac{m_{Rb_2}}{m_{K_2}}}x_{Rb_2}\right)^2 + \left(y_{K_2} + \sqrt{\frac{m_{Rb_2}}{m_{K_2}}}y_{Rb_2}\right)^2 < \sigma_0^2, \tag{7.33}$$

For the present dataset we choose σ_0 to be 0.25 mm, which is the working value of our detector resolution.

Applying the above criterion to the pre-screened ions, we find that 78 out of the 176 pairs survived the selection. Fig. 7.17 shows the hit locations of these ions, which are marked as red for K_2^+ and blue for Rb_2^+, with a gray line draw over each pair of ions that are deemed to be from the same event. Red (blue) dotted circles represent the expected perimeters of the Newton spheres associated with K_2^+ (Rb_2^+) ions, which has a well-defined translational energy of 4.12 (1.89) cm^{-1}. As expected, almost all coincident ions fall within these boundaries.

7.4.3 Statistical and non-statistical aspects of product state distributions

Having developed a pathway towards obtaining the pairwise product state distribution in the preceding sections, we now discuss what such a distribution may look like given different assumptions, and what can be learned about the reaction dynamics from it. As we have discussed in the introduction of this chapter, one likely outcome for the reaction, given the long complex lifetime which agrees well with RRKM, is that the system behaves completely statistically. In such a case, every product exit channel is equally likely to be populated by the reaction, and the probability of scattering into a given $\{N_{K_2}, N_{Rb_2}\}$ pair is proportional to its degeneracy (see section 7.1.4). The relevant degeneracy here depends on the nuclear spin state of the reactants (section 7.3.2), as well as whether the total angular momentum, J_{tot}, remains conserved throughout the reaction – a subject of ongoing investigation (section 7.1.1). For simplicity, we consider reactants prepared in a single nuclear spin Zeeman state, in which case only even-odd pairings of K_2 and Rb_2 rotational states are allowed (section 7.3.1). In this case, the number of states associated with each $\{N_{K_2}, N_{Rb_2}\}$ pair is given by its $L-$degeneracy if J_{tot} is rigorously conserved, or its $m-$degeneracy if J_{tot} is not conserved but its projection M_{tot} is.

The statistical product state distributions associated with the two scenarios above are shown in Fig. 7.18(a) and (d), in which we plot the $L-$ and $m-$degeneracies as functions of N_{K_2} and N_{Rb_2}, respectively. (b,e) and (c,f) show separate K_2 and Rb_2 distributions, obtained by summing over rows and columns of the pairwise distributions, respectively. Overall, the two pairwise distributions look very similar. Both show increases in population along rows and columns of constant N, with smoother gradients found in (d) compared to (a). The distributions peak towards $\{N_{K_2}, N_{Rb_2}\}$ pairs for which both rotational quantum numbers take on large values within the allowed state space, for which the number of N_{prod} and corresponding L_{prod} states are
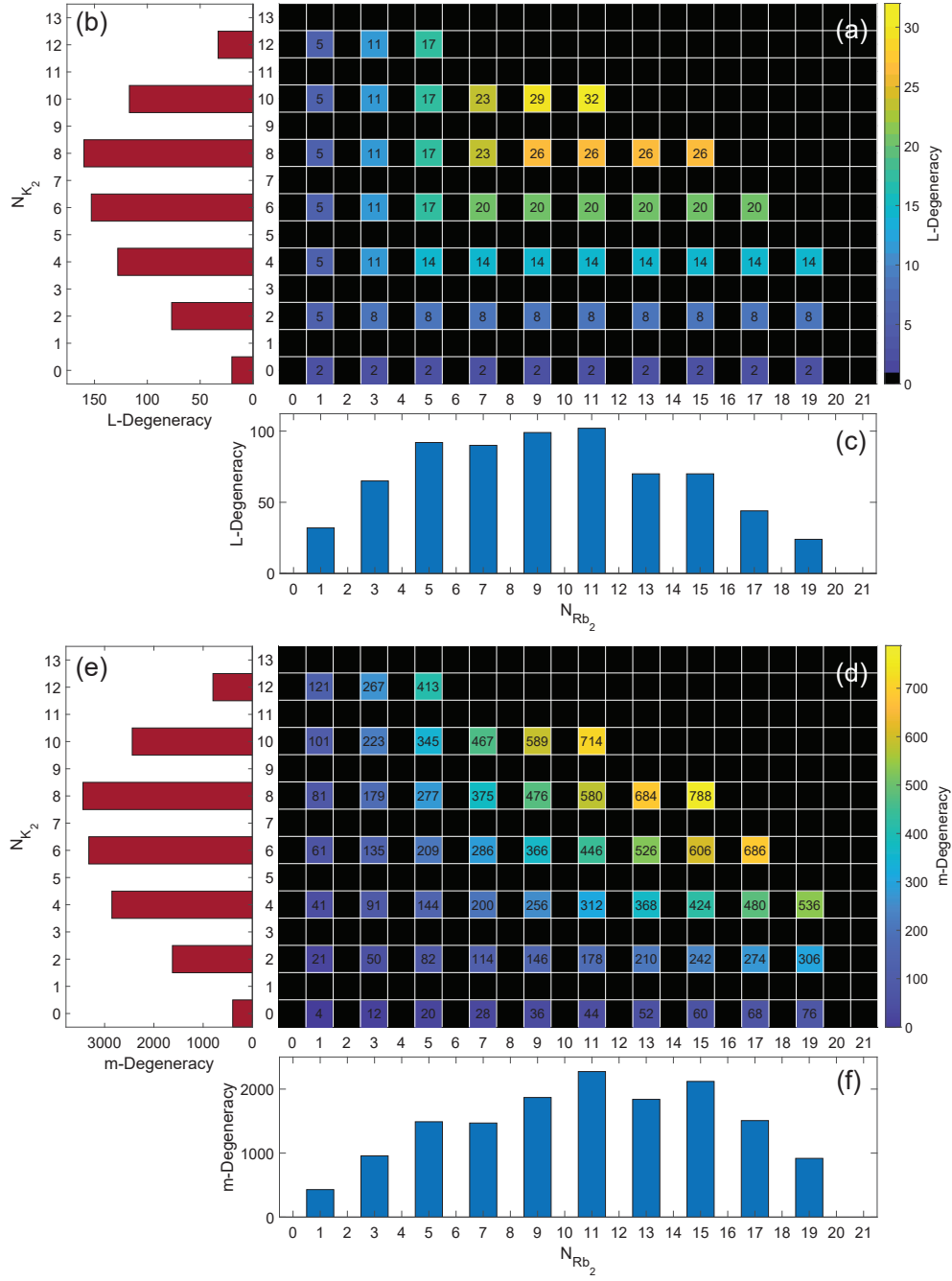
Figure 7.18: Statistical distributions of product populations. (a) $L-$degeneracy of all allowed $\{N_{K_2}, N_{Rb_2}\}$ pairs. (b,c) Degeneracies of N_{K_2} (b) and N_{Rb_2} (c) obtained by summing the $L-$degeneracies along rows and columns of (a), respectively. (d) $m-$degeneracy of all allowed $\{N_{K_2}, N_{Rb_2}\}$ pairs. (e,f) Degeneracies of N_{K_2} (e) and N_{Rb_2} (f) obtained by summing the $m-$degeneracies along rows and columns of (d), respectively.

maximized.

The statistical distributions discussed above provide a "baseline" to which we can compare the experimentally measured distribution. Such a comparison will allow us to critically examine the presence or absence of any non-statistical effects governing the reaction dynamics. To close out this chapter, we highlight two possible non-statistical behaviors, introduced to us by Nesbitt[151], to guide our future investigations. In this 2012 review article, the author draws on lessons learned from studying the quantum state distributions of fragments emerging from the photodissciations weakly-bound molecular complexes, and proposed the following two propensity rules that could govern product formation in ultracold reactions.

- **Energy deposition into the relative translation between the product pair should be minimized.** In other words, product internal states that are near-resonant with the reactants, which collide with near-zero translational energy, should be strongly favored.

- **Formations of product pairs with small translational energy (KE) AND large orbital angular momentum ($L_{\mathbf{prod}}$) should be disfavored.** The reason for this tendency, the author argues, is that a large L_{prod} corresponds to a large impact parameter*, b, which one would expect to not significantly exceed the physical size of the $K_2Rb_2^*$ complex, calculated to be ~ 4 Å[216]. As an example, the state $\{N_{K_2} = 4, N_{Rb_2} = 19\}$, which has a translational energy of $KE = 0.12$ cm^{-1} and an average allowed L_{prod} of 19, will have an average impact parameter of $b_{\mathrm{avg}} = 31$ Å, much larger compared to the complex size, making it highly unlikely to be populated.

To experimentally examine the propensity in a particular observable, such as the kinetic energy or impact parameter of a product state pair, it is helpful to display the statistical population

---

*The orbital angular momentum, $\mathbf{L}_{\mathrm{prod}}$, is related to the impact parameter, b, by the relation $\mathbf{L}_{\mathrm{prod}} = \mu\mathbf{v} \times \mathbf{b}$, where μ is the reduced mass of the product pair, and $\mathbf{v}$ is their relative velocity.
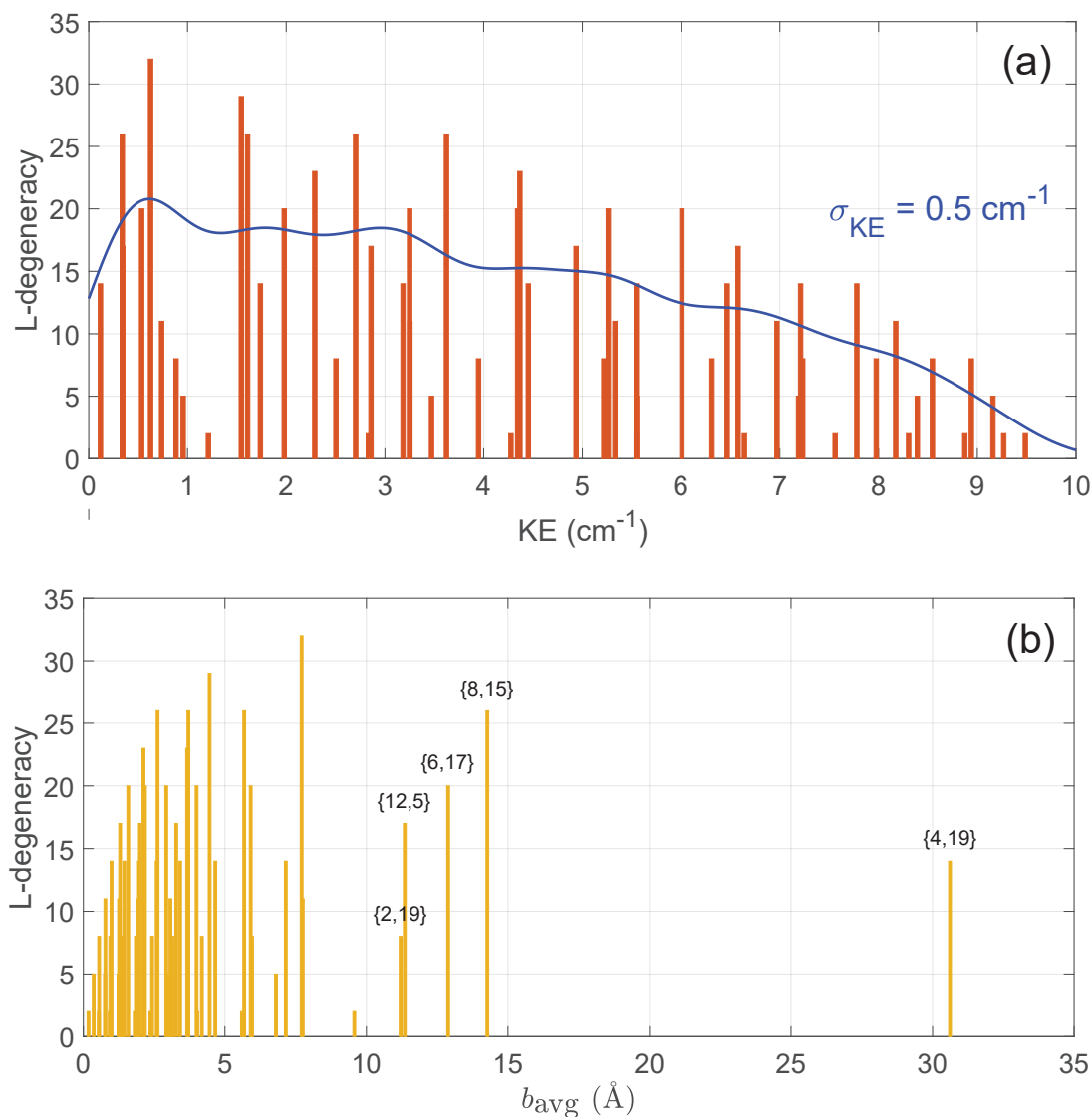
Figure 7.19: Statistical population distributions of product states sorted by their translational energy (a) or average impact parameter (b). Each bar represents the $L-$degenearcy of a particular $\{N_{K_2}, N_{Rb_2}\}$ pair, a quantity that is proportional to the population in that state under the statistical assumption. Blue curve in (a) is obtained by applying a Gaussian broadening of 0.5 cm^{-1} 1σ width to the underlying distribution to show the general trend in KE. In (b), state pairs that have average impact parameter significantly larger compared to the typical size of the intermediate complex are labeled by their rotational quantum numbers.

distribution as a function of said observable. To this end, we plot the $L-$ degeneracies of all 56 allowed $\{N_{K_2}, N_{Rb}\}$ pairs, sorted by their corresponding translational energy (KE) and average impact parameter (b_{avg}), in Fig. 7.19.

The blue curve overlaying the KE distribution in Fig. 7.19(a), obtained by applying a Gaussian broadening of 0.5 cm^{-1} 1σ width to every bar, represents the overall trend of the population as a function of KE. It shows gradual decays in population towards higher KE. By organizing the experimentally measured state distribution in a similar fashion and comparing it to the statistical outcome, we can look for any significant deviations which may suggest propensities in product KE.

The b_{avg} distribution in 7.19(b) shows that while the average impact parameter for most state pairs are within the extent of the complex ($4 - 8$ Å, see also Fig. 1.4), that of several others are considerably larger. Thus a manifestation of the second propensity rule proposed by Nesbitt would be significantly reduced population in these states compared to others with similar degeneracies but more reasonable b_{avg}. Comparing globally the measured distribution and the one in 7.19(b) may reveal a characteristic "cutoff" impact parameter, which will inform on the typical size of the intermediate complex prior to product pair separation.

Finally, we note that searching for any propensities in product state distribution becomes a much more challenging task if only separate distributions over N_{K_2} and N_{Rb_2} are available (*e.g.* Fig. 7.18(b)&(c)). In such a case, each N_{K_2} or N_{Rb_2} would, in general, correspond to a much wider range in value of experimental observables such as KE and b_{avg}. As a result, any trends in these observables would likely be washed out in the separate state distributions. As such, the pairwise distribution (*e.g.* Fig. 7.18(a)), despite requiring much longer data-taking to obtain, is the clearly superior option when it comes to studying state-to-state chemistry.

7.4.4 Conclusions and outlook

In this section, we have presented state-specific, coincidence product pair detection as a viable experimental technique to probe the dynamics of the ultracold KRb + KRb reaction with the highest level of details. We have discussed both statistical and non-statistical aspects of the product state distribution, the latter of which include possible propensities in the population distribution as functions of the product pair's translational energy and impact parameter upon departure. Effects such as these represent constraints placed upon product formation, not by conservation laws (section 7.1.4), but rather by the dynamics of the reaction. They essentially tell us how chemical bonds break – exactly what one hopes to learn from studying reaction dynamics. A comprehensive analysis of the complete pairwise state distribution that we eventually obtain may reveal other forces that guide product formation in this seemingly chaotic complex-forming reaction, providing better understanding of the energy landscape underlying the reaction.

Chapter 8

Conclusions and future directions

8.1 Conclusion

This thesis told the story of investigating the reaction KRb + KRb $\rightarrow$ K$_2$ + Rb$_2$ in the ultracold regime, understanding it with increasing levels of detail, and eventually gaining control over its various aspects. Probing the reaction required streamlined ultracold molecule production and reaction detection, which we realized by bringing techniques from ultracold physics and reaction dynamics together in a newly constructed experimental apparatus. The use of ion-based detection, including mass spectrometry and ion imaging, allowed direct identification of the reaction products, confirming the existence of the reaction first postulated by Ospelkaus *et al.* as seen through the loss of reactants. Surprisingly, we also identified K$_2$Rb$_2^+$ from the ion signal, which corresponds to the four-body intermediate complex of K$_2$Rb$_2^*$.

Direct observation of the complex using non-ultrafast lasers alluded to its extraordinarily long lifetime, the feature that we explored further in a subsequent study. There, we discovered strong photoexcitation of the K$_2$Rb$_2^*$ complex induced by the very light that is used to confine the KRb

molecules, and used this effect to steer the reaction from the ground PES onto an electronically excited one. The same effect also allowed us to create a well-defined time-zero for complex formation within the bulk gas, and make a time-domain measurement of the complex lifetime. The result of 360 ± 30 ns not only confirms that the complex is long-lived as we previously speculated, but also in good agreement with the result of an RRKM estimate, suggesting that the short-range dynamics is likely ergodic in nature.

Next, in an effort to further understand the dynamics of the KRb + KRb reaction, we studied the quantum state distribution of the reaction products. The measured occupations of K_2 and Rb_2 rotational states displayed strong and opposite parity preferences, which showed that the spins of the nuclei involved the reaction remained conserved throughout, and is decoupled from the rest of its dynamics. Exploiting this effect, we demonstrated continuous tuning of the product population in even and odd rotational states by manipulating the reactant nuclear spins via an external magnetic field. The thesis concludes with a discussion on the ongoing efforts towards a more comprehensive product state distribution, one that maps out the population in pairs of K_2 and Rb_2 rotational states rather than them separately. Such a measurement will be instrumental in examining both statistical and non-statistical aspects of the reaction dynamics.

Given all that we have learned about the ultracold KRb + KRb reaction, we can now address two questions raised in the introductory chapter of the thesis. One is that whether the ultracold nature of the reactants affect the short-range dyanmics, given that the system will get much "hotter" once it proceeds into the short-range well anyways. Our discovery of the long-lived complex that owes its existence to the ultracold preparation of the reactants answers "yes". Another question is whether the high degree of control afforded by the ultracold platform can be exploited to manipulate reaction pathways and outcomes. The answer is again affirmative, as we demonstrated optical steering of the reaction pathway, and tuning the final product state distribution using an external field – neither of which would have been possible in a higher temperature

266

setting. The hope here is that further explorations of this reaction reveal additional phenomena that are unique to the ultracold initial condition, and provide additional handles with which to control it.

8.2   Future work

Future directions on different aspects of the KRb + KRb reaction have been provided in sections 6.6, 7.3.4, and 7.4.4. Here, we discuss two other reactions that can be studied in the ultracold regime using the existing experimental infrastructure. These are the atom-molecule reactions

$$K + KRb \rightarrow K_2Rb^* \rightarrow K_2 + Rb, \tag{8.1}$$

$$\text{and} \quad Rb + KRb \rightarrow KRb_2^* \rightarrow Rb_2 + K. \tag{8.2}$$
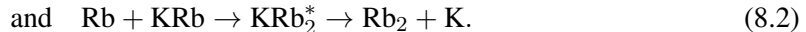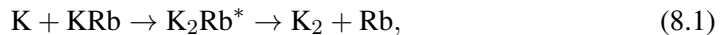
Similar to the KRb + KRb case, both reactions feature potential wells that support the formation of intermediate complexes, with depths of -1828 and -1607 cm^{-1}, respectively. The K + KRb reaction is exothermic with $\Delta E = -224.972(4) \text{ cm}^{-1}$. Evidence for its existence was provided in Ref.[162], which reported rapid loss of KRb molecules in the presence of K atoms. The Rb + KRb reaction, on the other hand, is endothermic with $\Delta E = 214.6(4) \text{ cm}^{-1}$. Thus when initiated at ultralow temperatures, the reaction is not allowed to proceed to products, but can return back into reactants.

From the perspective of intermediate complexes, the atom-molecule reactions can serve as comparative case studies to the molecule-molecule reaction. Recall from the RRKM theory (Eq. 6.1) that the complex lifetime is proportional to the DOS of the complex, ρ_c, and inversely proportional to the number of open channels, N_0. Compared to the four-atom complex, the ρ_c for the three-atom complexes are many orders of magnitude lower than that of the four-atom

complex. Ref.[55] estimates the DOS for the K_2Rb^* complex to be 28 K^{-1} near the K_2 + Rb collisional asymptote, compared at 2.6 μK^{-1} for the $K_2Rb_2^*$ complex. While a direct estimate for the DOS of the KRb_2^* complex is not available from literature, it is reasonable to assume it to be on the same order as K_2Rb^*. On the other hand, the number of exit channels in the three atom cases are much smaller than that in the four-atom case. Given ultracold, ground-state reactants, the exothermicity of the K + KRb reaction allows population of vibrational states $v = 0, 1$ and 2 and rotational states therein, and there exist a total of 141 allowed rovibrational channels[56]. The Rb + KRb reaction, on the other hand, will have a single exit channel that is identical to the entrance channel. Given the large differences in ρ_c and N_0 amongst the three reactions, will the atom-molecule reactions still ergodically explore the reaction phase space and display RRKM-consistent lifetimes, or would they find their exits much more quickly? Direct measurements of the three-atom complex lifetimes will help answer this question. Furthermore, all reactions can be initialized with rotationally and/or vibrationally excited reactants, providing controlled changes in ρ_c and N_0. Investigating the complex lifetime for different reactions as well as different initial conditions may allow us to establish a systematic understanding of how the dynamics of a complex-forming reaction changes as a function of basic system parameters.

For the K + KRb reaction, another interesting direction is to explore the product state distribution. The number of rovibrational channels ($N_0 = 141$) is not prohibitively large, and the reaction is ameanable to full product state mapping, using again the REMPI technique. More-over, numerically-exact quantum dynamics calculations have been reported for K + KRb[56], and our results will provide valuable benchmark to this state-of-the-art theory.

Appendix A

MOT cell heater placement

KRb MOT Cell heater placement diagram

Cell head

Up/btm*

Positive current
B-field direction:

shimX -> +X
shimY -> - Y
shimZ -> - Z
OP -> (+X, -Y)

Cell tail

Tube UR/LR

Window

Tube UL/LL

3% K source
(in use as of 08/12/2018)

7% K source
(unused as of 08/12/2018)
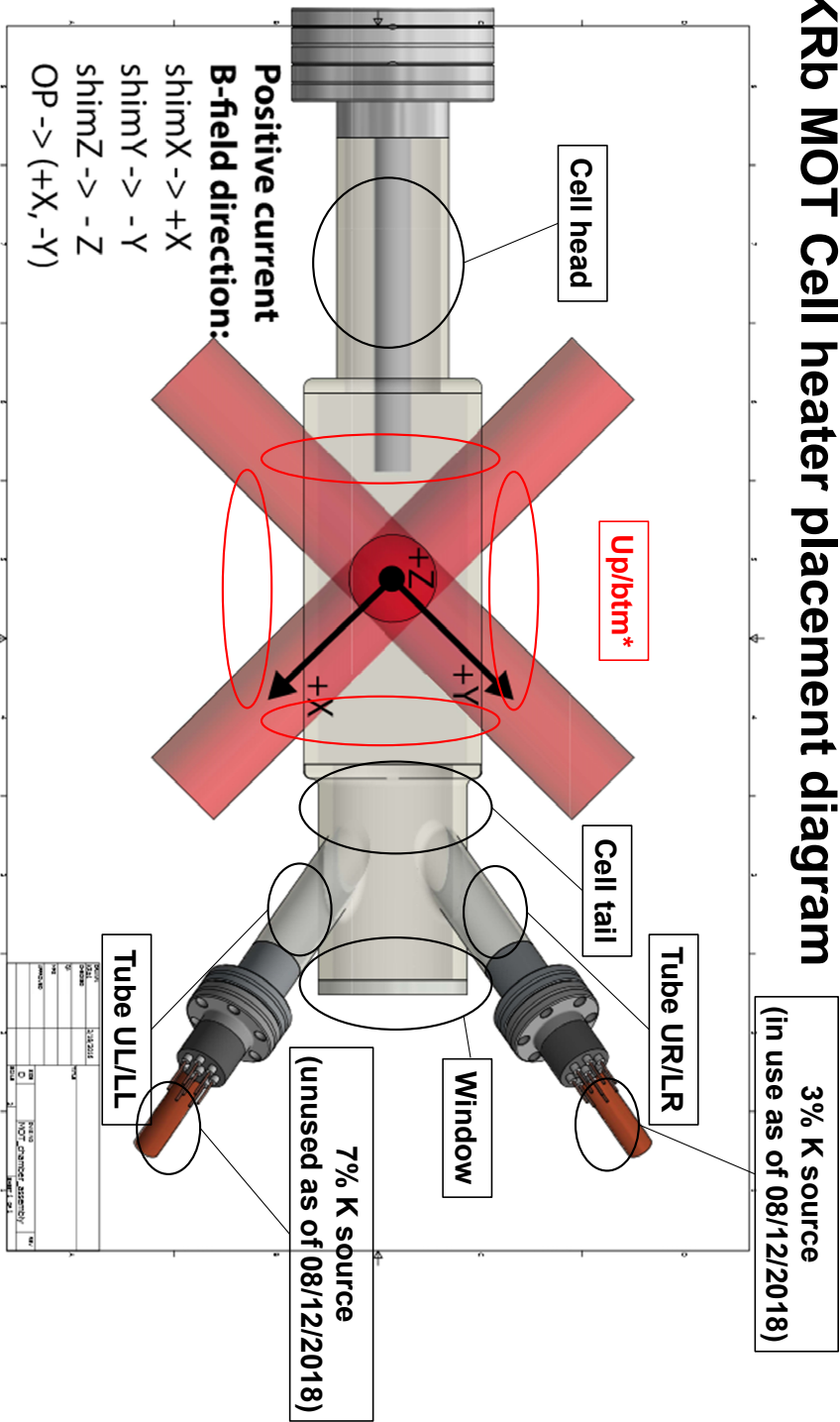
*Notes:
- These heaters are attached to the top and bottom sides of the MOT coil form;
- There are 4 heaters on top and 4 on the bottom;
- The top 4 heaters are connected in series, and so are the bottom 4;

Figure A.1

270

Appendix B

Magnetic coil constructions

Electromagnetic coils are used throughout our experiment to generate controllable magnetic fields for trapping, quantization, level shifting, etc. This Appendix documents the construction process for the two of the more specialized coil styles – the transfer coils (section 2.4.1) and the QUIC trap coils (section 2.4.2). Brief descriptions of the processes are offered in the figure captions below.
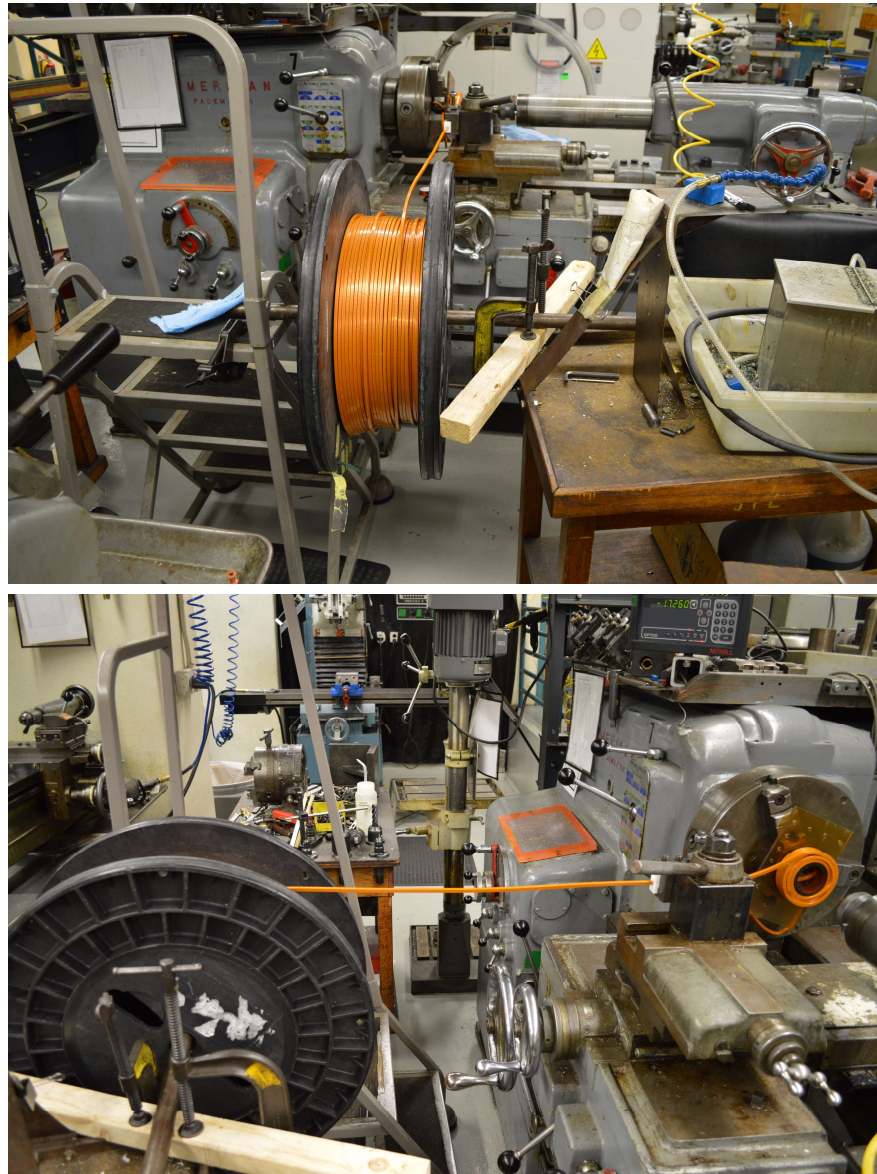
Figure B.1: Winding the transfer coil (Fig. 2.22) on a lathe (viewed from two different angles). Hollowed-cored copper wire (Fig. 2.22 inset) is fed from a spool to the coil mounted on a lathe. The lathe is run at a manually controlled low speed as the coil is wound turn by turn. During this process, epoxy is applied between adjacent turns to add mechanical strength. The same setup is used also to wind the Feshbach coils (Fig. 2.29).
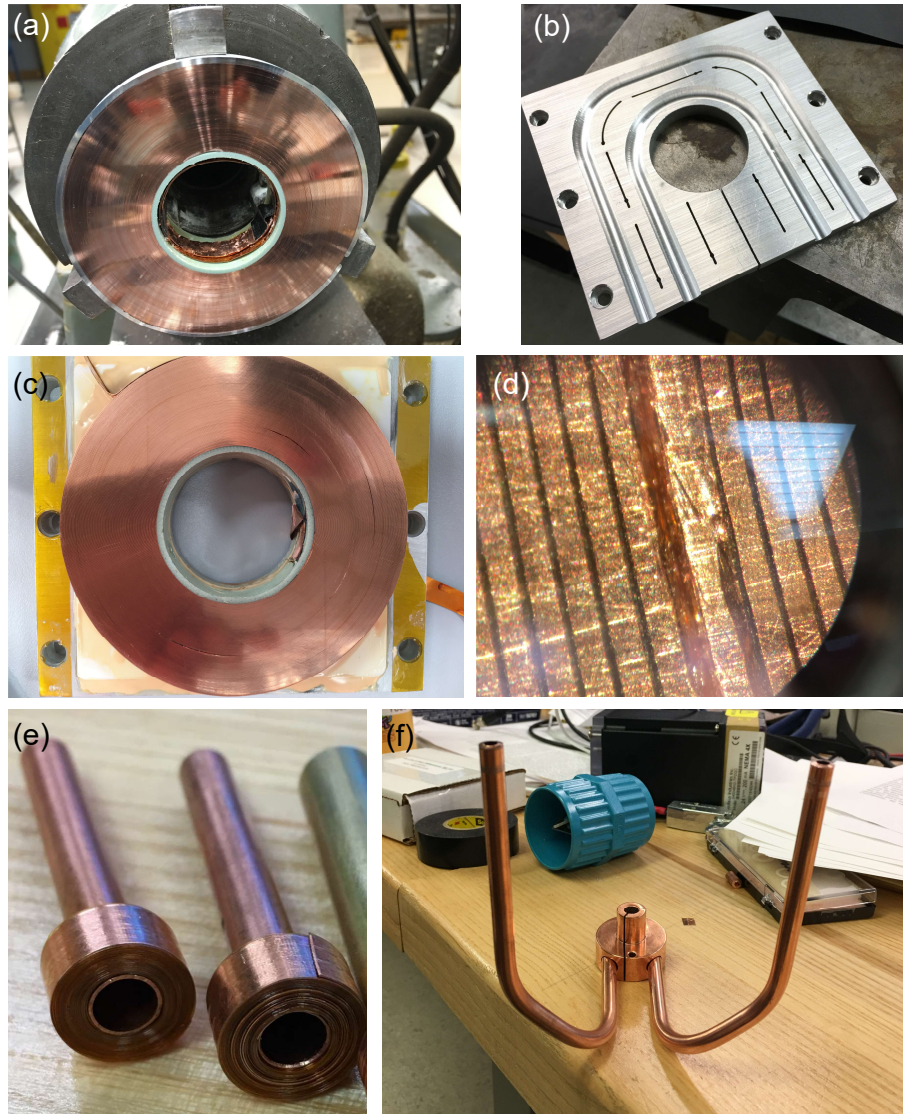
Figure B.2: Constructing the QUIC trap. (a) Facing off the quadrupole coil (QC) on a lathe. An aluminum ring bounds the perimeter of the coil to prevent the outermost layers of the coil from flaring out under the forces of machining. (b) QC cooling plate. Copper tubings are later pressed into the grooves to provide cooling. Thin slots are cut to minimize eddy currents. (c) After sanding off the lathed surface, the QC is epoxied via a thin sheet of alumina ceramic spacer to the backside of the cooling plate. (d) view of the QC surface under a microscope. Copper tapes (brown strips) are gaped by layers of Kapton lamination (thin black lines). The machining process introduces occasional shorts between layers. These shorts are removed via a surgical knife one by one, resulting in imperfections as such the valley-like feature at the center of the photo, which do not impede the functionality of the coil. (e) Ioffe coils (IC) wound on copper tubings before lathe work. Only one is used in the actual setup. (f) The IC cooling plate. Copper tubings feed cooling water through the center piece are attached to it via silver soldering. Purpose of the cut across half of the center piece is to minimize eddy currents.

273

Appendix C

Modeling the time-of-flight distributions of reaction products

To obtain the expected TOF distribution for ions generated in the ring portion of the hollow-bottle beams, we performed ion trajectory simulations in SIMION[69] with the realistic electric field created by considering the voltages and geometries of the VMI ion optics. For each product species, 10,000 ions are sampled according to the density distribution of the product as well as the ionization laser fluence distribution (see Fig. C.1). Each simulated TOF distribution is convolved with a Gaussian function (sigma = 4.2 ns) reflecting the time resolution of our MCP. The resulting TOF distribution is then fitted to the corresponding experimental data, with the overall amplitude as the only fitting parameter. The results are shown in Fig. 5.3 (b) and (c). The agreement between the widths and overall shapes of the experimental and simulated distributions supports our understanding for the spatial origins of the product ions. We speculate that the presence of the center peak, prominently seen in our data in figure 3E yet not captured by the simulated curve, is due to the non-zero intensity at the center of the hollow beams ionizing
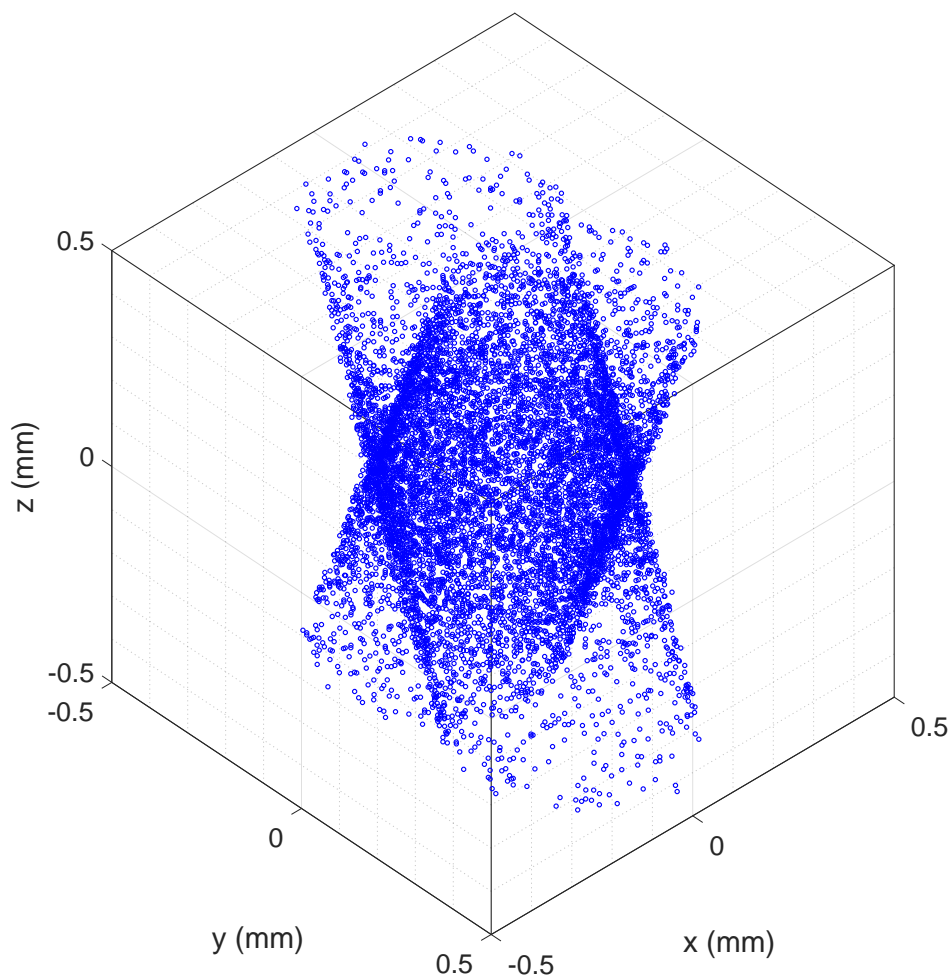
Figure C.1: Ion sampling for the TOF distribution simulation. 10,000 product ions (K_2^+ or Rb_2^+) are sampled according to the fluence distribution of the crossed hollow-bottle ionization beam (Fig. 2.32), as well as the steady-state density distribution of products (Eq. 4.3).

high density products at and around the center of the reactant KRb cloud. This center peak is less evident for K_2^+ because it has fewer ion counts and a narrower feature width, both of which make the center peak harder to resolve. The imperfections in the hollow beam are difficult to model exactly and are thus not included in the simulation.

Appendix D

Background ions in mass spectrometry

Figure D.1 shows the normalized mass spectra acquired at UV wavelengths of 285, 305, 335, and 356 nm, respectively, under otherwise similar experimental conditions. The 285 nm spectrum is the same as Fig. 5.2 save for a re-scaling of the y-axis to better show the low-mass noise peaks. While many of the same noise peaks can be identified in the different spectra, their amplitudes are quite different. As we vary the wavelength of UV ionization laser, we observe a general trend that the background level drops as the wavelength is increased, consistent with photoelectric behavior. We therefore speculate that these noise peaks are due to ions generated by photoelectrons, liberated by scattered UV light and accelerated by the VMI electric field, impacting on objects inside our vacuum chamber (e.g. chamber walls, electric field plates, supporting structures, etc.). Both 285 and 305 nm are above the ionization thresholds of the reaction products. Despite the significantly different levels of background ion counts in the two cases, the measured number of reaction products are roughly consistent with their wavelength-dependent ionization cross sections [195,53]. The ion images of products also show similar distributions for the two cases. We therefore conclude that the background ions present in our experiment does

276
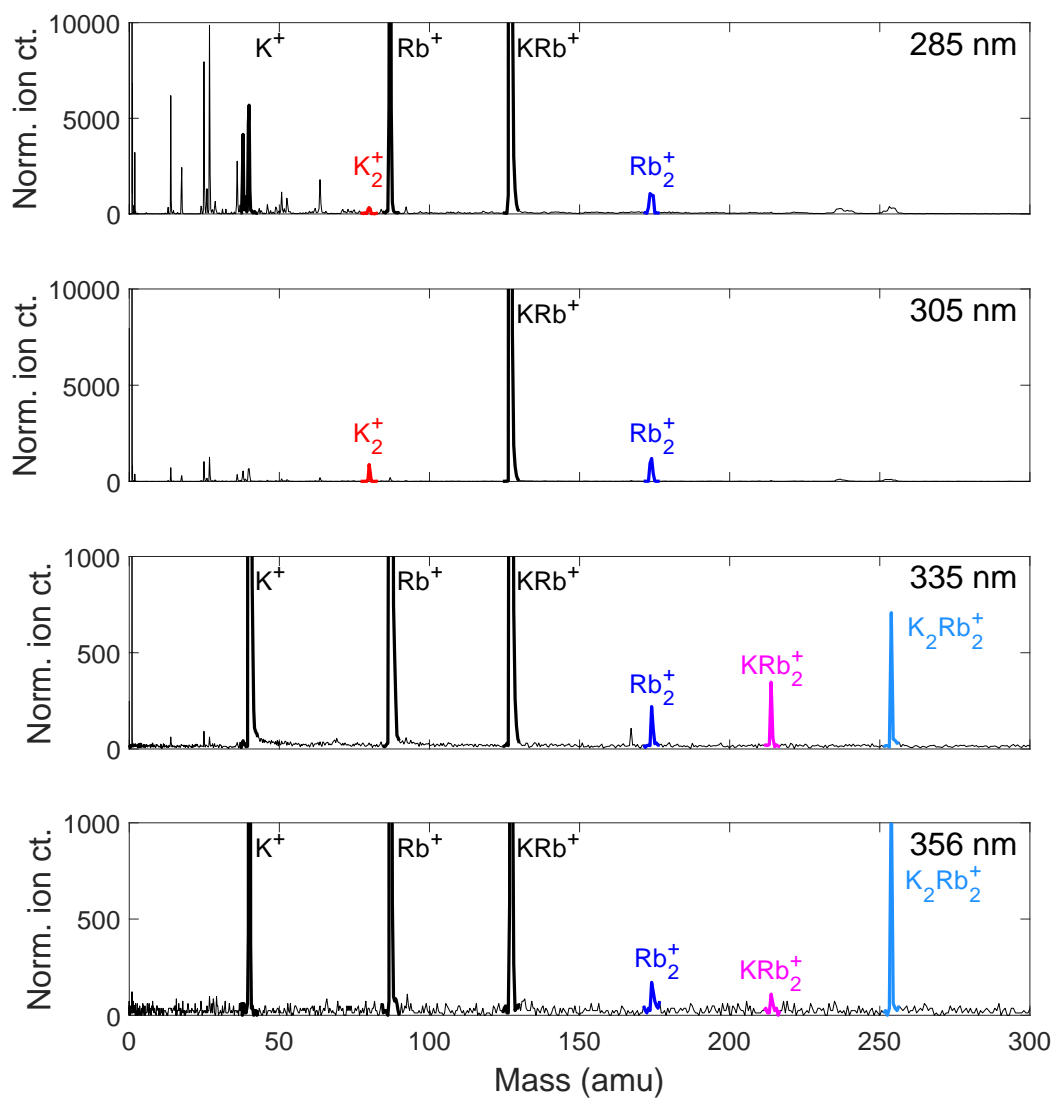
Figure D.1: Comparing the ion background at different ionization laser wavelengths. The four panels display the TOF mass spectra acquired at 285, 305, 335, and 356 nm UV wavelengths. Note the vertical scale change from the 305 nm panel to the 335 nm one. Ion counts in each spectrum is normalized by the pulse energy, repetition rate, and duration of the UV laser, as well as the number of experimental cycles over which the spectrum is accumulated. The masses corresponding to the detected species of interest are color-coded and labeled. The strengths of the background mass peaks decrease monotonically as the UV photon energy is reduced, consistent with a photoelectric behavior.

not confound the detection of the species of interest.

Appendix E

Bayesian analysis of ion images

Bayesian fits [188] are used to determine the signal radius in each velocity-map image for a model where a circular Gaussian (signal) is added to a constant background (noise). This model, although heuristic, appears to fit the data well.

Each fit has five parameters (background amplitude b; Gaussian amplitude A, horizontal center x_0, vertical center y_0, radius $\overline{R}$), collectively labeled $\boldsymbol{\theta} = (b, A, x_0, y_0, R) \in \mathbb{R}^5$. We calculate the probability of occurrence for a measured pixelated image pair (signal image and background image) as the product of individual pixel probabilities

$$P_{\text{images}}(\boldsymbol{\theta}) = \prod_{\substack{\text{pixels} \\ t \in 0,1}} P_{\text{pixel}}(x, y, t, n(x, y), \boldsymbol{\theta})$$

where $n(x, y)$ is the non-negative integer number of counts at location x, y in the measured image, $t = 0$ for signal and 1 for background and

$$P_{\text{pixel}}(x, y, t, n, \boldsymbol{\theta}) = \frac{\lambda(x, y, t, \boldsymbol{\theta})^n}{n!} e^{-\lambda(x, y, t, \boldsymbol{\theta})}$$

Table E.1: Number of KRb$_2^+$ ions used in the Bayesian analysis for Fig. 5.8.

Ionization laser wavelength (nm)	Ion number from signal image	Ion number from background image
285	79	17
296	44	15
300	25	7
330	8	2
335	281	78
338	102	18
340	17	3
342	34	9
344	21	5
346	18	4
348	54	9
352	18	5
354	55	17

is the Poisson probability of each individual pixel accumulating the measured counts n. The rate parameter λ for location x, y at time t and model parameters $\boldsymbol{\theta}$ is

$$\lambda(x, y, t, \boldsymbol{\theta}) = \begin{cases} b + \dfrac{A}{2\pi \overline{R}^2} e^{-\frac{(x-x_0)^2 + (y-y_0)^2}{2\overline{R}^2}}, & \text{if } t = 0, \\ b, & \text{if } t = 1. \end{cases}$$

At the beginning of the measurement ($t = 0$), the Poisson rate λ contains signal and background, while at the end of the measurement ($t = 1$), the signal source has been depleted by many repetitions of photoionization and only background remains.

Based on Bayes' theorem, the probabilities $P_{\text{images}}(\boldsymbol{\theta})$ together with uninformative priors ($\log(b), \log(A), \log(\overline{R}), x_0$, and y_0 are each uniformly distributed over all $\mathbb{R}$) for the fit parameters $\boldsymbol{\theta}$ yield the 5-D probability density $p(\boldsymbol{\theta})$. Numerical integration (marginalization) of this

function over the four other fit parameters leaves the probability density for the radius $\overline{R}$, from which the mean and the standard deviation of the mean (standard error) is calculated[188]. Figure 5.8 in Chapter 5 shows these values measured at different wavelengths and the ion number used for the Bayesian analysis is listed in table E.1.

Appendix F

Reaching a steady state following a change in the instantaneous ODT intensity

When the ODT intensity is switched from the I'-phase to the I-phase (Fig. 6.4) during a modulation, the rates at which the complexes and the products are generated experience a sudden increase, as the rate of complex photo-excitation is quenched. The density of the complex evolves into a new steady-state value on a timescale equal to or less than the complex lifetime τ_c, which we have measured to be 360 ± 30 ns (Fig. 6.6). Thus the 69 μs delay between ODT intensity switching and the UV ionization pulse used for the measurements shown in Fig. 6.4(b) leaves more than enough time for the complex population to reach a steady-state.

The products, on the other hand, take longer a time to re-establish their steady-state density distribution around the KRb cloud, due to the finite speed with which they escape the ODT and propagate to the region exposed by the cylinder-shaped UV ionization beam. The timescale

depends on the diameter of the cylinder (2.32) and the speeds of the products, which is up to 20.3 m/s for Rb_2 and 44.2 m/s for K_2 given the 9.53 cm^{-1} exothermicity. To probe the time for the product distribution to reach a steady state following the ODT intensity switching, we set up an experiment according to the timing scheme in Fig. F.1(a). We apply a 2 kHz, 1/4 duty-cycle square-wave modulation to the ODT intensity, and probe the products by UV ionization at different delay times with respect to the ODT turn off edge, t_{del}. The resulting ion counts per cycle as a function of t_{del} are shown in Fig. F.1(b) and Fig. F.1(c), for t_{del} in the range of $0 - 25$ μs and $0 - 400$ μs, respectively.

The results for both K_2^+ and Rb_2^+ show that the ion counts start increasing monotonically from the baseline after a short plateau* (Fig. F.1(a)), and reach saturation at $t_{del} \gtrsim 100\mu$s. The observed behaviors can be understood as follows. At $t_{del} = 0$, the ODT is switched off. The rate of product formation suddenly increases, and the newly formed products start to propagate outward. The sampled product ion counts starts to increase when the fastest products expand to a radius that matches the radius of the hollow UV beam, which will take 5 μs and 11 μs in the cases of K_2 and Rb_2, respectively (marked by dashed lines in Fig. F.1). The ion counts saturates when products of all velocity classes have reached the UV beam radius, at which point the product density distribution reaches a steady-state. Given the measured saturation timescale of $\sim 100\mu$s, the 165 μs delay between ODT intensity switching and the UV ionization pulse used for the measurements shown in Fig. 6.4(b) is sufficient to ensure that we are probing the products in its steady-state.

---

*This plateau is due to continued formation of products inspite of high ODT intensity (Appendix G), the origins of which remains unclear but are speculated in section 6.3.
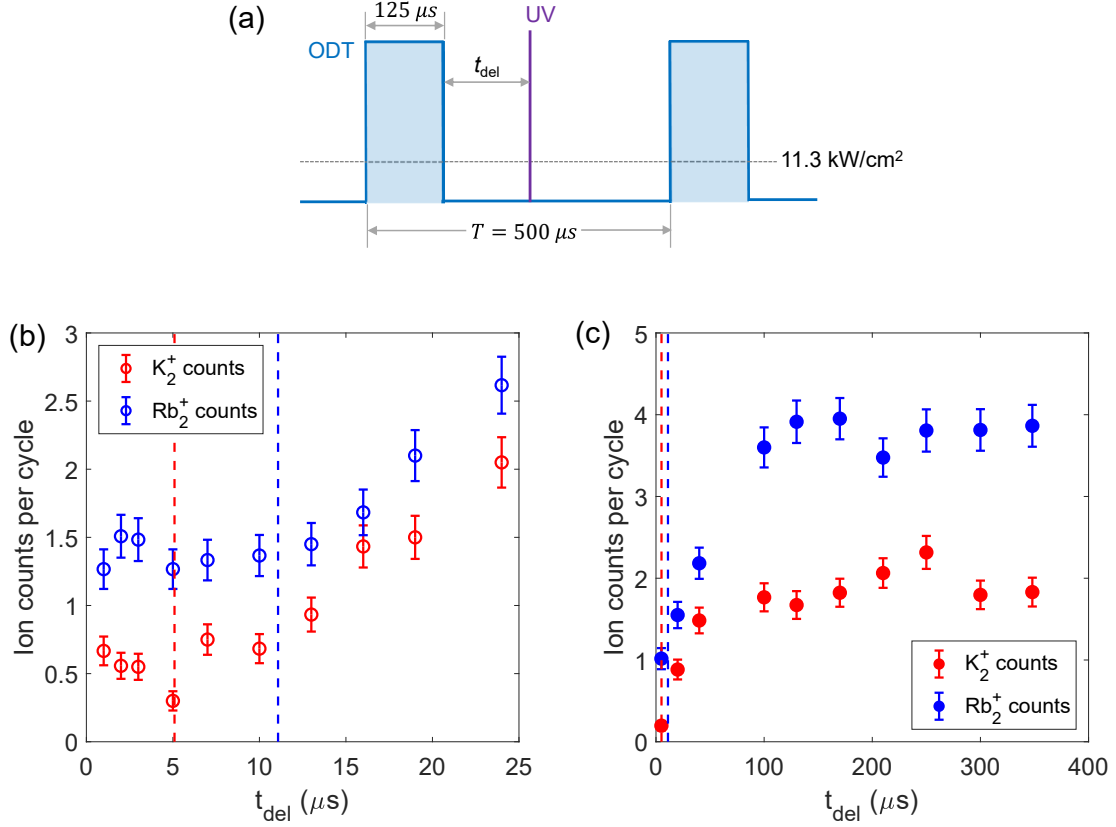
Figure F.1: Probing the time for the product density distribution to reach a steady-state. (a) Timing diagram for the experiment. We apply a 2 kHz, 1/4 duty-cycle square-wave modulation to the ODT intensity, and probe the products by UV ionization at different delay times with respect to the ODT turn off edge, t_{del}. The time-averaged ODT power is 11.3 kW/cm^2, as indicated by the gray dashed line. (b) K_2^+ and Rb_2^+ ion counts as functions of t_{del} for t_{del} in the range of $0 - 25$ μs. Error bars denote shot noise associated with ion counting. The red (blue) dashed line marks the time for the fastest-traveling K_2 (Rb_2) products to reach the ionization beam, which is 5 μs (11 μs). (c) Product ion counts for t_{del} in the range of $0 - 400$ μs, showing saturation at $t_{del} \gtrsim 100\mu$s.

Appendix G

Continued formation of products at high ODT intensities

We measure the dependence of the product ion counts on the ODT intensity in the 11.3 - 46.2 kW/cm^2 range, which partially overlaps with, but extends beyond the range probed in Fig. 2(a). For these measurements, the intensity of the ODT is modulated with full contrast, but with a variable duty cycle $D = t_{on}/T$, where the ODT is on for a duration of t_{on} within each cycle of period T, which is chosen to be 500 μs. The time-averaged ODT intensity, I_{avg}, is kept constant at 11.3 kW/cm^2. For a given duty cycle D, the intensity I during the on-phase is $I = I_{avg}/D$. The UV ionization pulses then probe the products shortly (2 μs) after the ODT is turned off. As this time is much shorter than the time it takes to perturb the product density distribution at the location of the ionization ring ($\sim$100 μs), the detected product density accurately reflects that during the on-phase of the ODT. The normalized product ion counts at different ODT intensities are shown in Extended Data Figure 1. The inset shows the timing diagram for the intensities of the ODT and the pulsed UV ionization laser. We observe plateaus in the ion counts for
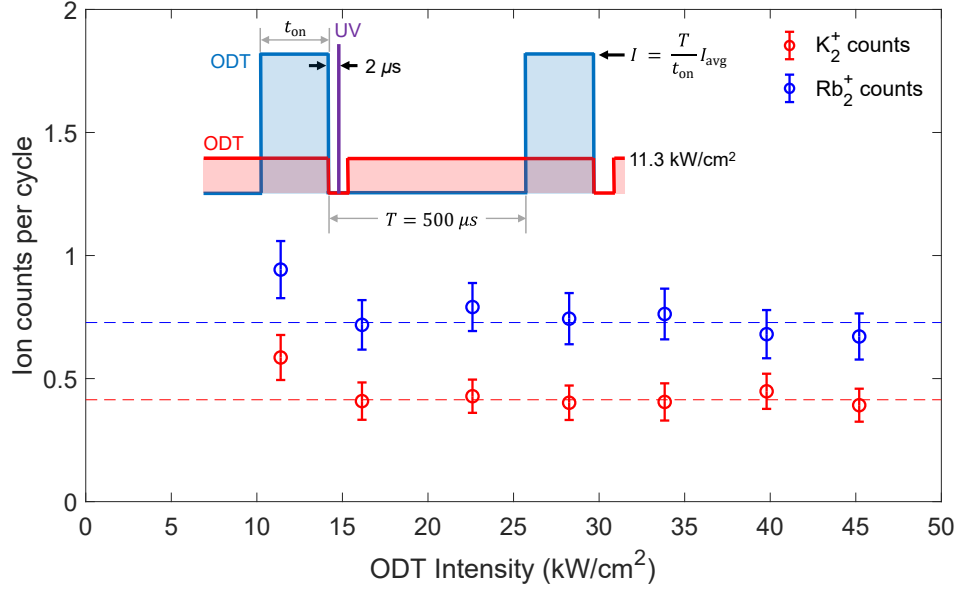
Figure G.1: **Extended Data Figure 1. Continued formation of products at high ODT intensities.** Steady-state K_2^+ (red circles) and Rb_2^+ (blue circles) ion counts at ODT light intensities in the 11.3 - 46.2 kW/cm^2 range, normalized by the number of experimental cycles (~ 80 for each data point). The error bars represent shot noise. The dashed lines indicate the levels to which the ion counts plateau, obtained by averaging, within each data set, the values of the points at ODT intensities larger than 15 kW/cm^2. (Inset) Timing schemes of the ODT (red and blue) and the pulsed UV ionization laser (purple) used for the measurements presented here. The red (blue) trace corresponds to a high (low) duty cycle modulation of the ODT. The instantaneous ODT intensity, I, is inversely proportional to the duty cycle, while the time-averaged ODT intensity, I_{avg} is constant for all measurements.

$I \geq 15$ kW/cm^2, indicating continued product formation despite the high ODT intensity. This plateau justifies our choice of using the average value of the high intensity data points in Fig. 2(a) to provide a baseline for the fitting.

Appendix H

Computer code for product state identification and counting

Initialize variables and define constants

```
StateCounter = 0; (*counter for all states including degeneracy*)
RotStateCounter = 0; (*counter for rotational states*)
DegeneracyCounter = 0; (*counter for state degeneracy*)
States = {};
DegeneracyStates = {};
Linit = 1; (*0 for s wave; 1 for p wave*)
vKRb1 = 0; (*KRb in ground vibrational state*)
vKRb2 = vKRb1;
NKRb1 = 0; (*KRb in ground rotational state*)
NKRb2 = NKRb1;
ωKRb = 75.87; (*[cm⁻¹], vibrational constant for KRb in the X¹Σ potential;
source: PRA 76 022511 2007*)
ωK2 = 90.58668; (*[cm⁻¹], vibrational constant for K₂ in the X¹Σ potential;
source: Chem Phys Lett 285 240-245 1998*)
ωRb2 = 57.121; (*[cm⁻¹], vibrational constant for Rb₂ in the X¹Σ potential;
source: J Chem Phys 113 3067 2000*)
BKRb = 0.037156; (*[cm⁻¹], rotational constant for KRb in v = 0 of the X¹Σ potential;
source: K.-K. Ni PhD thesis 2010*)
BK2 = 0.0546785; (*[cm⁻¹], rotational constant for K₂ in v = 0 of the X¹Σ potential;
source: Journal of Molecular Spectroscopy 147 2 370-382 1991 *)
BRb2 = 0.02188942; (*[cm⁻¹],  rotational constant for Rb₂ in v = 0 of the X¹Σ potential;
source: J Chem Phys 113 3067 2000*)
ΔE = 9.5; (*[cm⁻¹], reaction exothermicity*)
ETot = ΔE + (vKRb1 + vKRb2) * ωKRb + BKRb * NKRb1 * (NKRb1 + 1) + BKRb * NKRb2 * (NKRb2 + 1);
vK2max = Ceiling[x /. NSolve[ωK2 * x == ETot, x][[1]]];
(*highest vibrational state of K₂ allowed by energy conservation*)
vRb2max = Ceiling[x /. NSolve[ωRb2 * x == ETot, x][[1]]];
(*highest vibrational state of Rb₂ allowed by energy conservation*)
NK2max = Ceiling[x /. NSolve[BK2 * x * (x + 1) == ETot && x ≥ 0, x][[1]]];
(*highest rotational state of K₂ allowed by energy conservation*)
NRb2max = Ceiling[x /. NSolve[BRb2 * x * (x + 1) == ETot && x ≥ 0, x][[1]]];
(*highest rotational state of Rb₂ allowed by energy conservation*)
```

State identification and counting

```
For [ vK2 = 0, vK2 ≤ vK2max , vK2 = vK2 + 1,
 For [ vRb2 = 0, vRb2 < vRb2max , vRb2 = vRb2 + 1,
  For[NK2 = 0, NK2 < NK2max, NK2 = NK2 + 1,
   For[NRb2 = 0, NRb2 < NRb2max, NRb2 = NRb2 + 1,
    Llist = {};
    Eint = BK2 * NK2 * (NK2 + 1) + BRb2 * NRb2 * (NRb2 + 1) + ωK2 * vK2 + ωRb2 * vRb2;
    (*Energy imparted to the internal states of the products*)
    If[Eint ≤ ETot && (-1)^NK2 == 1 && (-1)^NRb2 == -1,
     (*Energy conservation and rotational state parity check*)
     DegeneracyCounter = 0;
     For[Nprod = Abs[NK2 - NRb2],
      Nprod ≤ Abs[NK2 + NRb2], Nprod++, (*Angular momentum conservation*)
      For[Nreac = Abs[NKRb1 - NKRb2], Nreac ≤ Abs[NKRb1 + NKRb2],
       Nreac = Nreac + 1, (*Angular momentum conservation*)
       For [ Jtot = Abs[Linit - Nreac], Jtot ≤ Abs[Linit + Nreac] ,
        Jtot = Jtot + 1, (*Angular momentum conservation*)
        For[L = Abs[Jtot - Nprod], L ≤ Abs[Jtot + Nprod], L++,
         (*Angular momentum conservation*)
         If[ (-1) ^ (NK2 + NRb2 + L) == (-1) ^ (NKRb1 + NKRb2 + Linit),
          (*Total parity conservation*)
          If[ (-1)^NK2 == 1 && (-1)^NRb2 == -1, (*Rotational state parity check*)
           StateCounter = StateCounter + 1;
           DegeneracyCounter = DegeneracyCounter + 1;
           Llist = Append[Llist, {Nprod, L}];
          ]
         ]
        ]]]
     ];
     States =
      Join[States, {{vK2, vRb2, NK2, NRb2, ETot - Eint, DegeneracyCounter, Llist}}];
     DegeneracyStates = Join[DegeneracyStates,
       {{vK2, vRb2, NK2, NRb2, ETot - Eint, DegeneracyCounter}}];
     If [DegeneracyCounter > 0,
      RotStateCounter = RotStateCounter + 1;
     ]
    ]
   ]
  ]
 ]]]
Print["Total number of exit channels: N₀=", StateCounter];
Print["Total number of Rot channels: N₀=", RotStateCounter];
MatrixForm[Join[{{"vK2", "vRb2", "NK2", "NRb2", "E_tran(cm⁻¹)", "Degeneracy{N_prod,L_prod}"}},
  SortBy[DegeneracyStates, #[[5]] &]]](*Print results into table,
states sorted in increasing order of the value in the 5th column,
which is the translational energy E_trans*)
```

Appendix I

Reaction exothermicity

In this appendix, we calculate the exothermicity of the reaction $^{40}\mathrm{K}^{87}\mathrm{Rb} + {}^{40}\mathrm{K}^{87}\mathrm{Rb} \rightarrow \mathrm{K}_2 + \mathrm{Rb}_2$, defined as

$$\Delta E = D_0(\mathrm{K}_2) + D_0(\mathrm{Rb}_2) - 2D_0(\mathrm{KRb}). \tag{I.1}$$

Here, D_0 is the dissociation energy, measured from the rovibrational ground-state of each species to the threshold of its dissociation into two free atoms (see Fig. 4.10(a) and 4.11(a)). Accurate knowledge of ΔE is important for determining the allowed rovibrational states of the products. To this end, we benefit from the high precision spectroscopy works previously performed on these bialkali molecules. In the case of $^{40}\mathrm{K}^{87}\mathrm{Rb}$, Ni *et al.*[154] obtained D_0 from the frequency difference between the lasers used to drive the STIRAP transitions (section 3.8), which were calibrated using a frequency comb to megahertz-level precision. In the cases of K_2 and Rb_2, large amounts of rovibronic transition frequencies were measured and used to fit the ground electronic potentials, yielding values for the well depth, D_e, that are accurate to better than 0.1 cm^{-1}. These fitted potentials also allowed for the calculation of the harmonic frequencies, ω_0. The dissociation energies of K_2 and Rb_2 are then obtained by adding the zero-point-energy to

Table I.1: Dissociation energy

Species	D_e (cm^{-1})	ω_0 (cm^{-1})	D_0 (cm^{-1})	Reference
^{40}K^{87}Rb			-4180.442	[154]
^{40}K$_2$	-4450.904(4)	91.032(1)	-4405.389(4)	[72]
^{87}Rb$_2$	-3993.53(6)	57.121(1)	-3964.97(6)	[185]

the well depth, *i.e.* $D_0 = D_e + \omega_0/2$.

The best known literature values for D_e, ω_0, and D_0 are summarized in Tab. I.1, along with their references. Using these values for D_0 and Eqn. I.1, we calculate an exothermicity of $\Delta E = -9.53(7)$ cm^{-1}. We note that this is lower in absolute value compared to the previously assumed -10.4(4) cm^{-1} calculated in Ref. [162], which used an earlier literature value for $D_0(\text{Rb}_2)$ [5].

Appendix J

Product rotational spectroscopy data

This appendix documents the frequencies for the rovibronic transitions of K_2 and Rb_2 that are relevant for product state detection (Chapter 7). We target rotational transitions within the $|X^1\Sigma_g^+, v = 0, N\rangle \rightarrow |B^1\Pi_u, v' = 4\rangle$ and $|X^1\Sigma_g^+, v = 0\rangle \rightarrow |B^1\Pi_u, v' = 6\rangle$ vibronic bands of Rb_2, and the $|X^1\Sigma_g^+, v = 0\rangle \rightarrow |B^1\Pi_u, v' = 1\rangle$ of K_2. Experimental searches for these transitions are guided by frequency calculations provided by O. Dulieu and coworkers, which are performed based on highly accurate ground and excited state potentials of K_2[68,72] and Rb_2[185,39,7] obtained from fits to large amounts of spectroscopic data on these molecules. We compare their results to spectroscopic measurements in Fig. 7.8, 7.6, and 7.7.

Both the calculated and measured frequencies, $f_{\text{calc.}}$ and $f_{\text{meas.}}$, contain sources of uncertainty. In our experiment, the diode lasers driving these transitions are frequency-referenced to a wavemeter (Bristol 771A), which is in turn (one-time) calibrated against well-known transitions such as the K and Rb D_2 lines (section 3.2). While we can typically trust the time-averaged wavemeter readings to within $1-2$ MHz, it occasionally jumps by $\pm 10 - 20$ MHz about the nominal center – a phenomenon for which the origin is not well-understood. Such changes appear to

be stochastic, and can occur during or in between data accumulation around at resonance. As a result, the absolute value of each $f_{\text{meas.}}$, as well as their relative differences, can only be trusted to within $\sim \pm 15$ MHz. The mean value of the entire set of $f_{\text{meas.}}$ (within a given vibronic band), however, should have much better accuracy, as these random fluctuations will be averaged out in this process. The opposite is true for $f_{\text{calc.}}$ – the relative differences between transition frequencies are know to greater precision than their mean. The reason is that the relative and the mean frequencies are determined, respectively, by the rotational and vibrational constants of the molecules, and the former is known with much better absolute accuracy than the latter (see, for example, Ref. [185]).

Given the complementary nature of the uncertainties associated with measurements and calculations, we adopt the following procedure to obtain the closest approximation to the actual transition frequencies. After correlating each measured resonance to a predicted line, we take the difference between the corresponding frequencies (i.e. $\Delta f = f_{\text{meas.}} - f_{\text{calc.}}$). The differences associated with all measured transitions are averaged to obtain $\overline{\Delta f}$, which is then applied to correct the set of $f_{\text{calc.}}$. The corrected frequencies, $f_{\text{corr.}} = f_{\text{calc.}} + \overline{\Delta f}$, represent our best knowledge of the transition frequencies, and are what we report in Tab. J.1–J.3. Note that while we report the frequencies for P-, Q-, and R- branch transitions, we measured primarily Q-branch transitions in the cases of $Rb_2 \, |v = 0\rangle \rightarrow |v' = 4\rangle$ (Tab. J.2) and $K_2 \, |v = 0\rangle \rightarrow |v' = 1\rangle$ (Tab. J.3), and P, Q-branch transitions in the case of $Rb_2 \, |v = 0\rangle \rightarrow |v' = 6\rangle$ (Tab. J.1). We do not, however, expect overall shifts in calculated transition frequencies between branches, as they occupy the same spectral region.

Table J.1: Frequencies for the P- ($N' = N - 1$), Q- ($N' = N$), and R- ($N' = N + 1$) branch rotational transitions within the $|X^1\Sigma_g^+, v = 0, \rangle \rightarrow |B^1\Pi_u, v' = 6, \rangle$ vibronic band of Rb$_2$, for $N = 0 - 21$. Values reported here are the corrected frequencies ($f_{\text{corr.}}$), obtained by adding to the set of calculated frequencies ($f_{\text{calc.}}$) an offset (Δf), which is found in this case to be - 2.16 GHz. See main text of this Appendix for details.

N_{Rb_2}	$f_{\text{corr.}}$ - 447000 (GHz)		
	P-branch	Q-branch	R-branch
0			753.56
1	751.13	752.25	754.50
2	749.63	751.88	755.25
3	747.95	751.31	755.80
4	746.07	750.56	756.17
5	744.01	749.62	756.36
6	741.76	748.49	756.35
7	739.32	747.18	756.16
8	736.69	745.67	755.78
9	733.88	743.98	755.21
10	730.87	742.10	754.45
11	727.68	740.03	753.50
12	724.30	737.77	752.37
13	720.73	735.33	751.05
14	716.98	732.70	749.54
15	713.04	729.88	747.84
16	708.90	726.87	745.96
17	704.59	723.67	743.88
18	700.08	720.29	741.62
19	695.38	716.71	739.17
20	690.50	712.95	736.53
21	685.43	709.00	733.71

Table J.2: Frequencies for the P- ($N' = N - 1$), Q- ($N' = N$), and R- ($N' = N + 1$) branch rotational transitions within the $|X^1\Sigma_g^+, v = 0,\rangle \rightarrow |B^1\Pi_u, v' = 4,\rangle$ vibronic band of Rb$_2$, for $N = 0 - 21$. Values reported here are the corrected frequencies ($f_{\text{corr.}}$), obtained by adding to the set of calculated frequencies ($f_{\text{calc.}}$) an offset (Δf), which is found in this case to be - 1.78 GHz. See main text of this Appendix for details.

| N_{Rb_2} | $f_{\text{corr.}}$ - 445000 (GHz) | | |
	P-branch	Q-branch	R-branch
0			37.24
1		35.93	38.19
2	33.31	35.57	38.96
3	31.64	35.03	39.55
4	29.78	34.30	39.95
5	27.75	33.40	40.18
6	25.54	32.31	40.22
7	23.14	31.05	40.09
8	20.56	29.60	39.77
9	17.81	27.97	39.27
10	14.87	26.17	38.60
11	11.75	24.18	37.74
12	8.45	22.01	36.70
13	4.97	19.66	35.47
14	1.30	17.12	34.07
15	-2.54	14.41	32.49
16	-6.56	11.52	30.73
17	-10.77	8.44	28.78
18	-15.15	5.19	26.66
19	-19.72	1.75	24.35
20	-24.46	-1.87	21.86
21	-29.39	-5.66	19.19

Table J.3: Frequencies for the P- ($N' = N - 1$), Q- ($N' = N$), and R- ($N' = N + 1$) branch rotational transitions within the $|X^1\Sigma_g^+, v = 0, \rangle \rightarrow |B^1\Pi_u, v' = 1, \rangle$ vibronic band of K$_2$, for $N = 0 - 14$. Values reported here are the corrected frequencies ($f_\text{corr.}$), obtained by adding to the set of calculated frequencies ($f_\text{calc.}$) an offset (Δf), which is found in this case to be - 8.30 GHz. See main text of this Appendix for details.

| N_{K_2} | $f_\text{corr.}$ - 462800 (GHz) | | |
	P-branch	Q-branch	R-branch
0			135.51
1		132.23	137.83
2	125.68	131.28	139.67
3	121.44	129.84	141.03
4	116.72	127.92	141.91
5	111.52	125.52	142.31
6	105.85	122.64	142.23
7	99.69	119.28	141.67
8	93.05	115.44	140.63
9	85.94	111.13	139.11
10	78.34	106.33	137.11
11	70.27	101.05	134.64
12	61.71	95.30	131.68
13	52.68	89.06	128.24
14	43.16	82.34	124.32

Appendix K

The nuclear spin states of KRb

The reactant KRb molecule consists of a spin-4 ^{40}K nucleus and a spin-3/2 ^{87}Rb nucleus, and therefore has a total of $(2 \times 4 + 1) \times (2 \times 3/2 + 1) = 36$ hyperfine* states in its ground rovibronic state. Prior works on KRb + KRb reactions were carried out in the presence of a 545.9 G magnetic field, which is near a ^{40}K-^{87}Rb Feshbach resonance[154,161]. At such a large field, the spins of the two nuclei are decoupled from one another, and the hyperfine eigenstates of the molecules can be expressed as $|i_{\mathrm{K}} = 4, i_{\mathrm{Rb}} = 3/2, m_i^{\mathrm{K}} = -4, m_i^{\mathrm{Rb}} = 1/2\rangle$, where i and m_i are the nuclear spins and their projections along the bias field, respectively[4] (see Fig. 1 of Ref.[161]).

Here, we apply the formalism developed in Ref.[4] to calculate the spin state of KRb under arbitrary external fields, with the particular goal of obtaining the coefficients α, β, and γ of the state-decomposition given in Eq. (7.18). To this end, we perform direct diagonalization of the molecular Hamiltonian for the ^{40}K^{87}Rb reactants using the basis of uncoupled hyperfine states. With the inclusion of the rotational degrees of freedom, these basis states are labeled as

---

*Since KRb lacks electronic spin in its ground electronic state ($X^1\Sigma^+$), the terms "hyperfine" and "nuclear spin" can be used interchangeably in this context.

by $\left| N, m_N, i_K, m_i^K, i_{Rb}, m_i^{Rb} \right\rangle$, where N represents the rotational angular momentum quantum number, m_N is its projection onto the z-axis, $i_{K,Rb}$ are the nuclear spins of the K and Rb atoms, and $m_i^{K,Rb}$ are the corresponding projections onto the z-axis. The direction of the z-axis here is defined by an externally applied magnetic field. In the vibronic ground state, the molecular Hamiltonian in the presence of external electric and magnetic fields can be expressed as[31,4],

$$H = H_{\text{rot}} + H_{\text{HF}} + H_{\text{S}} + H_{\text{Z}}. \tag{K.1}$$

Here,

$$H_{\text{rot}} = B_{\text{rot}} \boldsymbol{N}^2, \tag{K.2}$$

$$H_{\text{HF}} = -e \left(\boldsymbol{\nabla E} \right)_K \cdot \mathbf{Q}_K - e \left(\boldsymbol{\nabla E} \right)_{Rb} \cdot \mathbf{Q}_{Rb} + c_K \boldsymbol{N} \cdot \boldsymbol{I}_K + c_{Rb} \boldsymbol{N} \cdot \boldsymbol{I}_{Rb} + c_4 \boldsymbol{I}_K \cdot \boldsymbol{I}_{Rb}, \tag{K.3}$$

$$H_{\text{S}} = -\boldsymbol{\mu} \cdot \boldsymbol{E}, \tag{K.4}$$

$$H_{\text{Z}} = -g_r \mu_N \boldsymbol{N} \cdot \boldsymbol{B} - g_K \mu_N \left(1 - \sigma_K \right) \boldsymbol{I}_K \cdot \boldsymbol{B} - g_{Rb} \mu_N \left(1 - \sigma_{Rb} \right) \boldsymbol{I}_{Rb} \cdot \boldsymbol{B}, \tag{K.5}$$

where $\boldsymbol{N}$ is the rotational angular momentum operator, $\boldsymbol{I}_{K,Rb}$ are the nuclear spin operators for the K and Rb nuclei, respectively, $\left(\boldsymbol{\nabla E} \right)_{K,Rb}$ are the intramolecular electric field gradients at the K and Rb nuclei, respectively, $e\mathbf{Q}_{K,Rb}$ are the nuclear electric quadrupole moment operators for K and Rb, respectively, $\boldsymbol{\mu}$ is the molecular dipole moment, $\boldsymbol{E}$ is the external electric field, and $\boldsymbol{B}$ is the external magnetic field.

In this molecular Hamiltonian, Eq. (K.2) denotes the rotational contribution to the energy,

with corresponding rotational constant $B_{\mathrm{rot}}/h = 1.1139514\,\mathrm{GHz}$[161,152]. Eq. (K.3) represents the hyperfine energy, where $-e\,(\boldsymbol{\nabla}\mathbf{E})_i \cdot \mathbf{Q}_i$ describes the interaction between the intramolecular electric field gradient at nucleus i and the corresponding nuclear electric quadrupole moment, which is characterized by the electric quadrupole coupling constants $(eqQ)_{\mathrm{K}}/h = 0.452\,\mathrm{MHz}$ and $(eqQ)_{\mathrm{Rb}}/h = -1.308\,\mathrm{MHz}$[152]. The remaining three terms in Eq. (K.3) describe the interactions of the individual nuclear spins with the magnetic field associated with the rotation of the molecule, where the corresponding coupling constants are given by $c_{\mathrm{K}}/h = -24.1\,\mathrm{Hz}$ and $c_{\mathrm{Rb}}/h = 420.1\,\mathrm{Hz}$[4], as well as the scalar nuclear spin-spin interaction, with an associated coupling constant $c_4/h = -2030.4\,\mathrm{Hz}$[4]. The Stark Hamiltonian given by Eq. (K.4) describes the interaction between the permanent electric dipole moment of KRb, $\mu = 0.574\,\mathrm{Debye}$[?], and an external electric field. The Zeeman contribution to the energy (Eq. (K.5)), on the other hand, consists of three separate terms: the interaction between the external magnetic field and the magnetic moment arising from molecular rotation, with a corresponding rotational g-factor of $g_r = 0.014$[4], and the interactions between the magnetic moments of the individual nuclei, whose g-factors are given by $g_{\mathrm{K}} = -0.324$ and $g_{\mathrm{Rb}} = 1.834$[4], and the external magnetic field. The remaining parameters in Eq. (K.5), μ_N and $\sigma_{\mathrm{K,Rb}}$, represent the nuclear magneton and the nuclear shielding constants, respectively. For the K and Rb nuclei, the nuclear shielding constants are $\sigma_{\mathrm{K}} = 1321\,\mathrm{ppm}$ and $\sigma_{\mathrm{Rb}} = 3469\,\mathrm{ppm}$[4].

For the reactant state-decomposition calculations shown in Fig. 7.12a, we include rotational states up to $N_{\mathrm{max}} = 1$ when diagonalizing this Hamiltonian in the basis of uncoupled hyperfine states, $\left|N, m_N, i_{\mathrm{K}}, m_i^{\mathrm{K}}, i_{\mathrm{Rb}}, m_i^{\mathrm{Rb}}\right\rangle$, where $i_{\mathrm{K}} = 4$ and $i_{\mathrm{Rb}} = 3/2$. We also make use of the fact that the ground-state molecules are initially prepared at zero electric field and at a high magnetic field, $B \approx 544\,\mathrm{G}$, where the uncoupled basis states are a good representation of the eigenstates of the molecular Hamiltonian (Eq. (K.1)). In this configuration, the KRb molecules are produced in their rotational, vibrational, and electronic ground state, and in the hyperfine

state $\left|\psi_{\text{KRb}}^i\right\rangle \equiv \left|N = 0, m_N = 0, i_{\text{K}} = 4, m_i^{\text{K}} = -4, i_{\text{Rb}} = 3/2, m_i^{\text{Rb}} = 1/2\right\rangle$[137]. This corresponds to the situation where $\alpha \approx 1$ and $\beta = \gamma \approx 0$ in Eq. (7.18). As the electric and magnetic fields are changed adiabatically following the initial preparation of the reactant molecules, we obtain the coefficients α, β, and γ by diagonalizing the molecular Hamiltonian (Eq. (K.1)) at the desired values of the electric and magnetic fields, and selecting the eigenstate which is adiabatically connected to the initial hyperfine state, $\left|\psi_{\text{KRb}}^i\right\rangle$. The coefficients of the expansion of this eigenstate in terms of the uncoupled basis states are then α, β, and γ. For the calculations shown in Fig. 7.12a, we set $E = 0$ for simplicity, as the small electric field used in the experiment, $E = 18\,\text{V/cm}$, has a negligible effect on the state-decomposition, and we numerically calculate α, β, and γ as a function of the magnetic field.

Appendix L

Nuclear spin selection rules for the KRb + KRb reaction

Selection rules in chemical reactions arise when the S-matrix is diagonalizable in a basis made up of the eigenstates of some conserved quantity, also known as a collision constant[174]. Due to their weak couplings to other degrees of freedom, nuclear spins of molecules may be conserved in chemical reactions[159], and so their eigenstates may be used to derive one such selection rule. For ultracold reactions of bi-alkali molecules of the form, $AB + AB \rightarrow A_2 + B_2$, the nuclear spin states of the heteronuclear reactants can be described in the uncoupled basis, $\{|i_{A1}, i_{B1}, m_{A1}, m_{B1}\rangle \otimes |i_{A2}, i_{B2}, m_{A2}, m_{B2}\rangle\}$, while those of the homonuclear products are more naturally expressed in the coupled basis, $\{|I_{A_2}, M_{A_2}; i_{A1}, i_{A2}\rangle \otimes |I_{B_2}, M_{B_2}; i_{B1}, i_{B2}\rangle\}$, in which the states obey the exchange symmetry of identical nuclei. Here, A1 (A2) and B1 (B2) denote atomic nuclei from the 1st (2nd) AB molecules in the reaction. The total spin is defined as $\mathbf{I}_{A_2 (or\ B_2)} = \mathbf{i}_{A1(or\ B1)} + \mathbf{i}_{A2(or\ B2)}$ and its projection is $M_{A_2 (or\ B_2)} = m_{A1(or\ B1)} + m_{A2(or\ B2)}$. The coupled basis state $|I, M; i_1, i_2\rangle$ is symmetric under interchange of particles 1 and 2 if $i_1 + i_2 - I$

is even, and antisymmetric if $i_1 + i_2 - I$ is odd.

To obtain the probabilities for scattering into different channels, or product states, we can transform the reactant nuclear spin state from the uncoupled basis into the coupled basis. The coefficients of the reactant state in the coupled basis then provide the desired information regarding the branching into the different reaction channels. This basis transformation can be performed using the general formula for the addition of angular momentum,

$$|i_1, i_2, m_1, m_2\rangle = \sum_{I=|i_1-i_2|}^{i_1+i_2} \langle I, M; i_1, i_2 | i_1, i_2, m_1, m_2 \rangle | I, M; i_1, i_2 \rangle, \tag{L.1}$$

where $M = m_1 + m_2$ and $\langle I, M; i_1, i_2 | i_1, i_2, m_1, m_2 \rangle$ are the Clebsch-Gordan (CG) coefficients. Take the reactant state

$$\psi_{\text{KRb}} = \alpha \left| 4, \frac{3}{2}, -4, \frac{1}{2} \right\rangle + \beta \left| 4, \frac{3}{2}, -3, -\frac{1}{2} \right\rangle + \gamma \left| 4, \frac{3}{2}, -2, -\frac{3}{2} \right\rangle, \tag{L.2}$$

for example. Assuming that nuclear spins are spectators during the reaction, we can write the reactant nuclear spin state as,

$$
\begin{aligned}
\psi_{\text{KRb}} \otimes \psi_{\text{KRb}} &= \alpha^2 \left| 4, \frac{3}{2}, -4, \frac{1}{2} \right\rangle \otimes \left| 4, \frac{3}{2}, -4, \frac{1}{2} \right\rangle + \beta^2 \left| 4, \frac{3}{2}, -3, -\frac{1}{2} \right\rangle \otimes \left| 4, \frac{3}{2}, -3, -\frac{1}{2} \right\rangle \\
&\quad + \gamma^2 \left| 4, \frac{3}{2}, -2, -\frac{3}{2} \right\rangle \otimes \left| 4, \frac{3}{2}, -2, -\frac{3}{2} \right\rangle + \{\cdots\} \\
&= \alpha^2 \left| 4, 4, -4, -4 \right\rangle \otimes \left| \frac{3}{2}, \frac{3}{2}, \frac{1}{2}, \frac{1}{2} \right\rangle + \beta^2 \left| 4, 4, -3, -3 \right\rangle \otimes \left| \frac{3}{2}, \frac{3}{2}, -\frac{1}{2}, -\frac{1}{2} \right\rangle \\
&\quad + \gamma^2 \left| 4, 4, -2, -2 \right\rangle \otimes \left| \frac{3}{2}, \frac{3}{2}, -\frac{3}{2}, -\frac{3}{2} \right\rangle + \{\cdots\} \\
&= \alpha^2 |8, -8\rangle \otimes \left(\sqrt{\frac{3}{5}} |3, 1\rangle - \sqrt{\frac{2}{5}} |1, 1\rangle \right) \tag{L.3}
\end{aligned}
$$

$$+\beta^2 \left(-\sqrt{\frac{7}{15}}|6,-6\rangle + \sqrt{\frac{8}{15}}|8,-6\rangle \right) \otimes \left(\sqrt{\frac{3}{5}}|3,-1\rangle - \sqrt{\frac{2}{5}}|1,-1\rangle \right) \tag{L.4}$$

$$+\gamma^2 \left(\sqrt{\frac{45}{143}}|4,-4\rangle - \sqrt{\frac{14}{55}}|6,-4\rangle + \sqrt{\frac{28}{65}}|8,-4\rangle \right) \otimes |3,-3\rangle \tag{L.5}$$

$$+\alpha\beta|8,-7\rangle \otimes \left(\sqrt{\frac{9}{10}}|3,0\rangle - \sqrt{\frac{1}{10}}|1,0\rangle \right) \tag{L.6}$$

$$+\alpha\gamma \left(\sqrt{\frac{8}{15}}|6,-6\rangle + \sqrt{\frac{7}{15}}|8,-6\rangle \right) \otimes \left(\sqrt{\frac{3}{5}}|1,-1\rangle + \sqrt{\frac{2}{5}}|3,-1\rangle \right) \tag{L.7}$$

$$+\beta\gamma \left(\frac{2}{\sqrt{5}}|8,-5\rangle - \frac{1}{\sqrt{5}}|6,-5\rangle \right) \otimes |3,-2\rangle \tag{L.8}$$

$$+\alpha\beta|7,-7\rangle \otimes \sqrt{\frac{1}{2}} \left(|0,0\rangle - |2,0\rangle \right) \tag{L.9}$$

$$-\alpha\gamma|7,-6\rangle \otimes |2,-1\rangle \tag{L.10}$$

$$+\beta\gamma \left(\sqrt{\frac{9}{13}}|5,-5\rangle - \sqrt{\frac{4}{13}}|7,-5\rangle \right) \otimes |2,-2\rangle, \tag{L.11}$$

where we have used Eq. (L.1) to obtain the final equality, and $\{\cdots\}$ represents all additional terms. The last step gives the reactant state in the coupled basis, where we omit values of i_K and i_{Rb} for convenience. Each of the resulting tensor product states in Eqs. (L.3-L.11) corresponds to a possible scattered channel. Among them, the terms in Eqs. (L.9-L.11) are antisymmetric under the exchange of identical nuclei, while all others are symmetric. Therefore, the total probability for scattering into an antisymmetric nuclear spin state of the products is given by $P_A = |\alpha\beta|^2 + |\alpha\gamma|^2 + |\beta\gamma|^2$, whereas that for scattering into a symmetric state is $P_S = 1 - P_A$. Furthermore, based on the exchange symmetry of identical nuclei, the populations of even (odd) rotational states of the products are proportional to P_S (P_A) when the nuclei are bosonic, and

are proportional to P_A (P_S) when the nuclei are fermionic.

While this result was derived for a specific input state (Eq. (L.2)), the methodology does not depend on the particular form of this state, so that the formulae for P_A and P_S can be generalized to account for any initial states of the reactants. Additionally, as far as the summed probabilities are concerned, it is not strictly necessary to consider the CG coefficients of both reactant and product dressed states. Instead, it is sufficient, for the purposes of this work, to consider only the CG coefficients of the dressed reactant states. However, for a state-to-state measurement which resolves individual nuclear spin states, it is, strictly speaking, necessary to consider the CG coefficients of the dressed states. This subtlety will be discussed in another work by Goulven Quéméner.

References

[1] Aikawa, K., Akamatsu, D., Hayashi, M., Oasa, K., Kobayashi, J., Naidon, P., Kishimoto, T., Ueda, M., & Inouye, S. (2010). Coherent transfer of photoassociated molecules into the rovibrational ground state. *Physical Review Letters*, 105(20), 203001.

[2] Akerman, N., Karpov, M., Segev, Y., Bibelnik, N., Narevicius, J., & Narevicius, E. (2017). Trapping of molecular oxygen together with lithium atoms. *Physical Review Letters*, 119(7), 073204.

[3] Aldegunde, J. & Hutson, J. M. (2009). Hyperfine energy levels of alkali-metal dimers: Ground-state homonuclear molecules in magnetic fields. *Phys. Rev. A*, 79(1), 013401.

[4] Aldegunde, J., Rivington, B. A., Żuchowski, P. S., & Hutson, J. M. (2008). Hyperfine energy levels of alkali-metal dimers: Ground-state polar molecules in electric and magnetic fields. *Phys. Rev. A*, 78(3), 033434.

[5] Amiot, C. (1990). Laser-induced fluorescence of rb2: The (1) 1σ+ g (x),(2) 1σ+ g,(1) 1π u (b),(1) 1π g, and (2) 1π u (c) electronic states. *The Journal of chemical physics*, 93(12), 8591–8604.

[6] Amiot, C. (1991). The x1σg+ electronic state of k2. *Journal of Molecular Spectroscopy*, 147(2), 370–382.

[7] Amiot, C. & Vergès, J. (1997). Optical-optical double resonance and Fourier transform spectroscopy: The Rb_2 $B_1\Pi_u$ electronic state up to the quasibound energy levels. *Chem. Phys. Lett.*, 274(1-3), 91–98.

[8] Amiot, C. & Verges, J. (2000). The krb ground electronic state potential up to 10 å. *The Journal of Chemical Physics*, 112(16), 7068–7074.

[9] Anderegg, L., Augenbraun, B. L., Bao, Y., Burchesky, S., Cheuk, L. W., Ketterle, W., & Doyle, J. M. (2018). Laser cooling of optically trapped molecules. *Nature Physics*, 14(9), 890–893.

[10] Anderegg, L., Augenbraun, B. L., Chae, E., Hemmerling, B., Hutzler, N. R., Ravi, A., Collopy, A., Ye, J., Ketterle, W., & Doyle, J. M. (2017). Radio frequency magneto-optical trapping of caf with high density. *Physical Review Letters*, 119(10), 103201.

[11] Anderegg, L., Cheuk, L. W., Bao, Y., Burchesky, S., Ketterle, W., Ni, K.-K., & Doyle, J. M. (2019). An optical tweezer array of ultracold molecules. *Science*, 365(6458), 1156–1158.

[12] Anderson, B. P. & Kasevich, M. (2001). Loading a vapor-cell magneto-optic trap using light-induced atom desorption. *Physical Review A*, 63(2), 023404.

[13] Anderson, M. H., Ensher, J. R., Matthews, M. R., Wieman, C. E., & Cornell, E. A. (1995). Observation of bose-einstein condensation in a dilute atomic vapor. *science*, 269(5221), 198–201.

[14] Andreev, V. & Hutzler, N. (2018). Improved limit on the electric dipole moment of the electron. *Nature*, 562(7727), 355–360.

[15] Ashfold, M. N., Nahler, N. H., Orr-Ewing, A. J., Vieuxmaire, O. P., Toomes, R. L., Kitsopoulos, T. N., Garcia, I. A., Chestakov, D. A., Wu, S.-M., & Parker, D. H. (2006). Imaging the dynamics of gas phase reactions. *Physical Chemistry Chemical Physics*, 8(1), 26–53.

[16] Aveline, D. C., Williams, J. R., Elliott, E. R., Dutenhoffer, C., Kellogg, J. R., Kohel, J. M., Lay, N. E., Oudrhiri, K., Shotwell, R. F., Yu, N., et al. (2020). Observation of bose–einstein condensates in an earth-orbiting research lab. *Nature*, 582(7811), 193–197.

[17] Balakrishnan, N. (2016). Perspective: Ultracold molecules and the dawn of cold controlled chemistry. *The Journal of Chemical Physics*, 145(15), 150901.

[18] Baranov, M. A., Dalmonte, M., Pupillo, G., & Zoller, P. (2012). Condensed matter theory of dipolar quantum gases. *Chemical Reviews*, 112(9), 5012–5061.

[19] Baron, J., Campbell, W. C., DeMille, D., Doyle, J. M., Gabrielse, G., Gurevich, Y. V., Hess, P. W., Hutzler, N. R., Kirilov, E., Kozyryev, I., et al. (2014). Order of magnitude smaller limit on the electric dipole moment of the electron. *Science*, 343(6168), 269–272.

[20] Bell, M. T. & P. Softley, T. (2009). Ultracold molecules and ultracold chemistry. *Mol. Phys.*, 107(2), 99–132.

[21] Bergmann, K., Theuer, H., & Shore, B. (1998). Coherent population transfer among quantum states of atoms and molecules. *Reviews of Modern Physics*, 70(3), 1003.

[22] Bernath, P. F. (2016). *Spectra of Atoms and Molecules*. Oxford University Press.

306

[23] Beuc, R., Movre, M., Horvatic, V., Vadla, C., Dulieu, O., & Aymar, M. (2007). Absorption spectroscopy of the rubidium dimer in an overheated vapor: An accurate check of molecular structure and dynamics. *Physical Review A*, 75(3), 032512.

[24] Bjork, B. J., Bui, T. Q., Heckl, O. H., Changala, P. B., Spaun, B., Heu, P., Follman, D., Deutsch, C., Cole, G. D., Aspelmeyer, M., et al. (2016). Direct frequency comb measurement of od+ co→ doco kinetics. *Science*, 354(6311), 444–448.

[25] Black, E. D. (2001). An introduction to pound–drever–hall laser frequency stabilization. *American journal of physics*, 69(1), 79–87.

[26] Bohn, J., Avdeenkov, A., & Deskevich, M. (2002). Rotational feshbach resonances in ultracold molecular collisions. *Physical Review Letters*, 89(20), 203202.

[27] Bohn, J. L., Rey, A. M., & Ye, J. (2017). Cold molecules: Progress in quantum engineering of chemistry and quantum matter. *Science*, 357(6355), 1002–1010.

[28] Brif, C., Chakrabarti, R., & Rabitz, H. (2010). Control of quantum phenomena: past, present and future. *New J. Phys.*, 12(7), 075008.

[29] Brink, D. & Sukumar, C. (2006). Majorana spin-flip transitions in a magnetic trap. *Physical Review A*, 74(3), 035401.

[30] Brooks, P. R. (1988). Spectroscopy of transition region species. *Chemical Reviews*, 88(2), 407–428.

[31] Brown, J. M. & Carrington, A. (2003). *Rotational Spectroscopy of Diatomic Molecules*. Cambridge University Press.

[32] Broyer, M., Chevaleyre, J., Delacretaz, G., Martin, S., & Wöste, L. (1983). K2 rydberg state analysis by two-and three-photon ionization. *Chemical Physics Letters*, 99(3), 206–212.

[33] Büchler, H. P., Demler, E., Lukin, M., Micheli, A., Prokof'ev, N., Pupillo, G., & Zoller, P. (2007). Strongly correlated 2d quantum phases with cold polar molecules: controlling the shape of the interaction potential. *Physical Review Letters*, 98(6), 060404.

[34] Bui, T. Q., Bjork, B. J., Changala, P. B., Nguyen, T. L., Stanton, J. F., Okumura, M., & Ye, J. (2018). Direct measurements of doco isomers in the kinetics of od+ co. *Science advances*, 4(1), eaao4777.

[35] Bunker, D. L. & Hase, W.-L. (1973). On non-rrkm unimolecular kinetics: Molecules in general, and ch3nc in particular. *The Journal of Chemical Physics*, 59(9), 4621–4632.

[36] Byrd, J. N., Harvey Michels, H., Montgomery Jr, J. A., Côté, R., & Stwalley, W. C. (2012). Structure, energetics, and reactions of alkali tetramers. *The Journal of chemical physics*, 136(1), 014306.

[37] Byrd, J. N., Montgomery Jr, J. A., & Côté, R. (2010). Structure and thermochemistry of K_2Rb, KRb_2, and K_2Rb_2. *Physical Review A*, 82(1), 010502.

[38] Cairncross, W. B., Gresh, D. N., Grau, M., Cossel, K. C., Roussy, T. S., Ni, Y., Zhou, Y., Ye, J., & Cornell, E. A. (2017). Precision measurement of the electron's electric dipole moment using trapped molecular ions. *Physical Review Letters*, 119(15), 153001.

[39] Caldwell, C., Engelke, F., & Hage, H. (1980). High resolution spectroscopy in supersonic nozzle beams: The Rb_2 $B^1\Pi_u - X_1\Sigma_g^+$ band system. *Chem. Phys.*, 54(1), 21–31.

[40] Chabinyc, M. L., Craig, S. L., Regan, C. K., & Brauman, J. I. (1998). Gas-phase ionic reactions: dynamics and mechanism of nucleophilic displacements. *Science*, 279(5358), 1882–1886.

[41] Chatfield, D. C., Friedman, R. S., Schwenke, D. W., & Truhlar, D. G. (1992). Control of chemical reactivity by quantized transition states. *The Journal of Physical Chemistry*, 96(6), 2414–2421.

[42] Chen, G. K., Xie, C., Yang, T., Li, A., Suits, A. G., Hudson, E. R., Campbell, W. C., & Guo, H. (2019). Isotope-selective chemistry in the be+(2 s 1/2)+ hod→ beod+/beoh++ h/d reaction. *Physical Chemistry Chemical Physics*.

[43] Cheuk, L. W., Anderegg, L., Augenbraun, B. L., Bao, Y., Burchesky, S., Ketterle, W., & Doyle, J. M. (2018). λ-enhanced imaging of molecules in an optical trap. *Physical review letters*, 121(8), 083201.

[44] Cheuk, L. W., Anderegg, L., Bao, Y., Burchesky, S., Yu, S., Ketterle, W., Ni, K.-K., & Doyle, J. M. (2020). Observation of collisions between two ultracold ground-state caf molecules. *arXiv preprint arXiv:2002.00048*.

[45] Chin, C., Grimm, R., Julienne, P., & Tiesinga, E. (2010). Feshbach resonances in ultracold gases. *Reviews of Modern Physics*, 82(2), 1225.

[46] Christianen, A., Karman, T., & Groenenboom, G. C. (2019a). Quasiclassical method for calculating the density of states of ultracold collision complexes. *Physical Review A*, 100(3), 032708.

[47] Christianen, A., Zwierlein, M. W., Groenenboom, G. C., & Karman, T. (2019b). Photoinduced two-body loss of ultracold molecules. *Physical Review Letters*, 123(12), 123402.

[48] Chu, S. & Wieman, C. (1989). Laser cooling and trapping of atoms: Introduction. *JOSA B*, 6(11), 2020–2022.

[49] Comparat, D., Fioretti, A., Stern, G., Dimova, E., Tolra, B. L., & Pillet, P. (2006). Optimized production of large bose-einstein condensates. *Physical Review A*, 73(4), 043410.

[50] Continetti, R. E. & Guo, H. (2017). Dynamics of transient species via anion photodetachment. *Chemical Society Reviews*, 46(24), 7650–7667.

[51] Cooper, N. & Shlyapnikov, G. V. (2009). Stable topological superfluid phase of ultracold polar fermionic molecules. *Physical Review Letters*, 103(15), 155302.

[52] Cordonnier, M., Uy, D., Dickson, R., Kerr, K., Zhang, Y., & Oka, T. (2000). Selection rules for nuclear spin modifications in ion-neutral reactions involving H_3^+. *J. Chem. Phys.*, 113(8), 3181–3193.

[53] Creek, D. & Marr, G. (1968). Some ultraviolet cross-section measurements on molecular alkali-metal vapours. *Journal of Quantitative Spectroscopy and Radiative Transfer*, 8(7), 1431–1436.

[54] Crim, F. F. (1996). Bond-selected chemistry: vibrational state control of photodissociation and bimolecular reaction. *J. Phys. Chem.*, 100(31), 12725–12734.

[55] Croft, J., Balakrishnan, N., & Kendrick, B. (2017a). Long-lived complexes and signatures of chaos in ultracold k 2+ rb collisions. *Physical Review A*, 96(6), 062707.

[56] Croft, J., Makrides, C., Li, M., Petrov, A., Kendrick, B., Balakrishnan, N., & Kotochigova, S. (2017b). Universality and chaoticity in ultracold k+ krb chemical reactions. *Nature communications*, 8, 15897.

[57] Cumby, T. D., Shewmon, R. A., Hu, M.-G., Perreault, J. D., & Jin, D. S. (2013). Feshbach-molecule formation in a bose-fermi mixture. *Physical Review A*, 87(1), 012703.

[58] Davis, K. B., Mewes, M.-O., Andrews, M. R., van Druten, N. J., Durfee, D. S., Kurn, D., & Ketterle, W. (1995). Bose-einstein condensation in a gas of sodium atoms. *Physical review letters*, 75(22), 3969.

[59] de Jongh, T., Besemer, M., Shuai, Q., Karman, T., van der Avoird, A., Groenenboom, G. C., & van de Meerakker, S. Y. (2020). Imaging the onset of the resonance regime in low-energy no-he collisions. *Science*, 368(6491), 626–630.

[60] De Marco, L., Valtolina, G., Matsuda, K., Tobias, W. G., Covey, J. P., & Ye, J. (2019). A degenerate fermi gas of polar molecules. *Science*, 363(6429), 853–856.

[61] De Miranda, M., Chotia, A., Neyenhuis, B., Wang, D., Quéméner, G., Ospelkaus, S., Bohn, J., Ye, J., & Jin, D. (2011). Controlling the quantum stereodynamics of ultracold bimolecular reactions. *Nature Physics*, 7(6), 502.

[62] DeMille, D. (2002). Quantum computation with trapped polar molecules. *Physical Review Letters*, 88(6), 067901.

[63] Dribinski, V., Ossadtchi, A., Mandelshtam, V. A., & Reisler, H. (2002). Reconstruction of abel-transformable images: The gaussian basis-set expansion abel transform method. *Review of Scientific Instruments*, 73(7), 2634–2642.

[64] Dulieu, O. & Gabbanini, C. (2009). The formation and interactions of cold and ultracold molecules: new challenges for interdisciplinary physics. *Reports on progress in physics*, 72(8), 086401.

[65] Dulieu, O., Krems, R., Weidemüller, M., & Willitsch, S. (2011). Physics and chemistry of cold molecules. *Physical Chemistry Chemical Physics*, 13(42), 18703–18704.

[66] Edvardsson, D., Lunell, S., & Marian, C. M. (2003). Calculation of potential energy curves for Rb_2 including relativistic effects. *Molecular Physics*, 101(15), 2381–2389.

[67] Egorov, D., Lahaye, T., Schöllkopf, W., Friedrich, B., & Doyle, J. M. (2002). Buffer-gas cooling of atomic and molecular beams. *Physical Review A*, 66(4), 043401.

[68] Engelke, F., Hage, H., & Schühle, U. (1984). The K_2 $B^1\Pi_u - X^1\Sigma_g^+$ band system. Crossed laser-molecular-beam spectroscopy using doppler-free two-photon ionization. *Chem. Phys. Lett.*, 106(6), 535–539.

[69] Eppink, A. T. & Parker, D. H. (1997). Velocity map imaging of ions and electrons using electrostatic lenses: Application in photoelectron and photofragment ion imaging of molecular oxygen. *Review of Scientific Instruments*, 68(9), 3477–3484.

[70] Ernst, U., Marte, A., Schreck, F., Schuster, J., & Rempe, G. (1998). Bose-einstein condensation in a pure ioffe-pritchard field configuration. *EPL (Europhysics Letters)*, 41(1), 1.

[71] Esslinger, T., Bloch, I., & Hänsch, T. W. (1998). Bose-einstein condensation in a quadrupole-ioffe-configuration trap. *Physical Review A*, 58(4), R2664.

[72] Falke, S., Sherstov, I., Tiemann, E., & Lisdat, C. (2006). The a σ u+ 1 state of k 2 up to the dissociation limit. *The Journal of chemical physics*, 125(22), 224303.

[73] Faure, A., Hily-Blant, P., Le Gal, R., Rist, C., & Des Forêts, G. P. (2013). Ortho-para selection rules in the gas-phase chemistry of interstellar ammonia. *Astrophys. J. Lett.*, 770(1), L2.

[74] Fernandes, D. R., Sievers, F., Kretzschmar, N., Wu, S., Salomon, C., & Chevy, F. (2012). Sub-doppler laser cooling of fermionic 40k atoms in three-dimensional gray optical molasses. *EPL (Europhysics Letters)*, 100(6), 63001.

[75] Foster, P. J., Leckenby, R., & Robbins, E. J. (1969). The ionization potentials of clustered alkali metal atoms. *Journal of Physics B: Atomic and Molecular Physics*, 2(4), 478.

[76] Fröhlich, B., Lahaye, T., Kaltenhäuser, B., Kübler, H., Müller, S., Koch, T., Fattori, M., & Pfau, T. (2007). Two-frequency acousto-optic modulator driver to improve the beam pointing stability during intensity ramps. *Review of scientific instruments*, 78(4), 043101.

[77] Frye, M. D., Morita, M., Vaillant, C. L., Green, D. G., & Hutson, J. M. (2016). Approach to chaos in ultracold atomic and molecular physics: Statistics of near-threshold bound states for li+ cah and li+ caf. *Physical Review A*, 93(5), 052713.

[78] Fushitani, M. & Momose, T. (2002). Nuclear spin selection rule in the photochemical reaction of CH_3 in solid parahydrogen. *J. Chem. Phys.*, 116(24), 10739–10743.

[79] Garand, E., Zhou, J., Manolopoulos, D. E., Alexander, M. H., & Neumark, D. M. (2008). Nonadiabatic interactions in the cl+ h2 reaction probed by clh2-and cld2-photoelectron imaging. *Science*, 319(5859), 72–75.

[80] Gascooke, J. R., Gibson, S. T., & Lawrance, W. D. (2017). A "circularisation" method to repair deformations and determine the centre of velocity map images. *The Journal of chemical physics*, 147(1), 013924.

[81] Gillen, J. I., Bakr, W., Peng, A., Foelling, S., & Greiner, M. (2009). *The quantum gas microscope*. PhD thesis, Harvard University.

[82] Goldwin, J., Papp, S., DeMarco, B., & Jin, D. (2002). Two-species magneto-optical trap with 40 k and 87 rb. *Physical Review A*, 65(2), 021402.

[83] Goldwin, J. M. (2005). *Quantum degeneracy and interactions in the 87Rb-40K Bose-Fermi mixture*. PhD thesis, University of Colorado.

[84] Gong, J., Shapiro, M., & Brumer, P. (2003). Entanglement-assisted coherent control in nonreactive diatom–diatom scattering. *J. Chem. Phys.*, 118(6), 2626–2636.

[85] González-Martínez, M. L., Dulieu, O., Larrégaray, P., & Bonnet, L. (2014). Statistical product distributions for ultracold reactions in external fields. *Physical Review A*, 90(5), 052716.

[86] Greene, C. H. & Zare, R. N. (1983). Determination of product population and alignment using laser-induced fluorescence. *The Journal of Chemical Physics*, 78(11), 6741–6753.

[87] Gregory, P. D., Blackmore, J. A., Bromley, S. L., & Cornish, S. L. (2020). Loss of ultracold rb 87 cs 133 molecules via optical excitation of long-lived two-body collision complexes. *Physical Review Letters*, 124(16), 163402.

[88] Gregory, P. D., Frye, M. D., Blackmore, J. A., Bridge, E. M., Sawant, R., Hutson, J. M., & Cornish, S. L. (2019). Sticky collisions of ultracold rbcs molecules. *Nature communications*, 10(1), 1–7.

[89] Griffiths, D. J. & Schroeter, D. F. (2018). *Introduction to quantum mechanics*. Cambridge University Press.

[90] Grimm, R., Weidemüller, M., & Ovchinnikov, Y. B. (1999). Optical dipole traps for neutral atoms. *arXiv preprint physics/9902072*.

[91] Gruebele, M., Sims, I., Potter, E., & Zewail, A. (1991). Femtosecond probing of bimolecular reactions: The collision complex. *The Journal of chemical physics*, 95(10), 7763–7766.

[92] Grussie, F., Berg, M. H., Crabtree, K., Gärtner, S., McCall, B., Schlemmer, S., Wolf, A., & Kreckel, H. (2012). The low-temperature nuclear spin equilibrium of H_3^+ in collisions with H_2. *Astrophys. J.*, 759(1), 21.

[93] Gunthardt, C. E., Aardema, M. N., Hall, G. E., & North, S. W. (2019). Evidence for lambda doublet propensity in the UV photodissociation of ozone. *J. Chem. Phys.*, 151(22), 224302.

[94] Guo, H. (2012). Quantum dynamics of complex-forming bimolecular reactions. *International Reviews in Physical Chemistry*, 31(1), 1–68.

[95] Guo, M., Ye, X., He, J., González-Martínez, M. L., Vexiau, R., Quéméner, G., & Wang, D. (2018). Dipolar collisions of ultracold ground-state bosonic molecules. *Physical Review X*, 8(4), 041044.

[96] Guo, M., Zhu, B., Lu, B., Ye, X., Wang, F., Vexiau, R., Bouloufa-Maafa, N., Quéméner, G., Dulieu, O., & Wang, D. (2016). Creation of an ultracold gas of ground-state dipolar na 23 rb 87 molecules. *Physical Review Letters*, 116(20), 205303.

[97] Hall, F. H. & Willitsch, S. (2012). Millikelvin reactive collisions between sympathetically cooled molecular ions and laser-cooled atoms in an ion-atom hybrid trap. *Physical Review Letters*, 109(23), 233202.

[98] Han, D., Wynar, R., Courteille, P., & Heinzen, D. J. (1998). Bose-einstein condensation of large numbers of atoms in a magnetic time-averaged orbiting potential trap. *Physical Review A*, 57(6), R4114.

[99] Hardwidge, E. A., Rabinovitch, B., & Ireton, R. C. (1973). Test of rrkm theory. rates of decomposition in the series of chemically activated 2-n-alkyl radicals from c4 to c16. *The Journal of Chemical Physics*, 58(1), 340–348.

[100] Henson, A. B., Gersten, S., Shagam, Y., Narevicius, J., & Narevicius, E. (2012). Observation of resonances in penning ionization reactions at sub-kelvin temperatures in merged beams. *Science*, 338(6104), 234–238.

[101] Herschbach, D. (1973). Reactive scattering. *Faraday Discussions of the Chemical Society*, 55, 233–251.

[102] Hess, H. F. (1986). Evaporative cooling of magnetically trapped and compressed spin-polarized hydrogen. *Physical Review B*, 34(5), 3476.

[103] Hess, H. F., Kochanski, G. P., Doyle, J. M., Masuhara, N., Kleppner, D., & Greytak, T. J. (1987). Magnetic trapping of spin-polarized atomic hydrogen. *Physical review letters*, 59(6), 672.

[104] Hickstein, D., Yurchak, R., Das, D., Shih, C., & Gibson, S. (2016). Pyabel (v0. 7): A python package for abel transforms.

[105] Hickstein, D. D., Gibson, S. T., Yurchak, R., Das, D. D., & Ryazanov, M. (2019). A direct comparison of high-speed methods for the numerical abel transform. *Review of Scientific Instruments*, 90(6), 065115.

[106] Hoffmann, R. (1968). Transition state for the hydrogen–iodine and the hydrogen exchange reactions. *The Journal of Chemical Physics*, 49(8), 3739–3740.

[107] Hu, M.-G., Liu, Y., Grimes, D., Lin, Y.-W., Gheorghe, A., Vexiau, R., Bouloufa-Maafa, N., Dulieu, O., Rosenband, T., & Ni, K.-K. (2019). Direct observation of bimolecular reactions of ultracold krb molecules. *Science*, 366(6469), 1111–1115.

[108] Hu, M.-G., Liu, Y., Nichols, M. A., Zhu, L., Quéméner, G., Dulieu, O., & Ni, K.-K. (2020). Product-state control of ultracold reactions via conserved nuclear spins. *arXiv preprint arXiv:2005.10820*.

[109] Huber, K.-P. (2013). *Molecular spectra and molecular structure: IV. Constants of diatomic molecules*. Springer Science & Business Media.

[110] Hudson, E. R., Bochinski, J., Lewandowski, H., Sawyer, B. C., & Ye, J. (2004). Efficient stark deceleration of cold polar molecules. *The European Physical Journal D-Atomic, Molecular, Optical and Plasma Physics*, 31(2), 351–358.

[111] Hudson, E. R. & Campbell, W. C. (2018). Dipolar quantum logic for freely rotating trapped molecular ions. *Physical Review A*, 98(4), 040302.

[112] Hudson, R. & Carter, V. (1965). Absorption of light by potassium vapor between 2856 and 1150 å. *Physical Review*, 139(5A), A1426.

[113] Hummon, M. T., Tscherbul, T. V., Kłos, J., Lu, H.-I., Tsikata, E., Campbell, W. C., Dalgarno, A., & Doyle, J. M. (2011). Cold n+ nh collisions in a magnetic trap. *Physical Review Letters*, 106(5), 053201.

[114] Jagutzki, O., Mergel, V., Ullmann-Pfleger, K., Spielberger, L., Spillmann, U., Dörner, R., & Schmidt-Böcking, H. (2002). A broad-application microchannel-plate detector system for advanced particle or photon detection tasks: large area imaging, precise multi-hit timing information and high detection rate. *Nuclear Instruments and Methods in Physics Research Section A: Accelerators, Spectrometers, Detectors and Associated Equipment*, 477(1-3), 244–249.

[115] Kappes, M. M., Schaer, M., & Schumacher, E. (1985). Generation of all homo-and heteronuclear alkali dimers in supersonic nozzle beams. ionization potential measurements. *The Journal of Physical Chemistry*, 89(8), 1499–1504.

[116] Kendrick, B., Hazra, J., & Balakrishnan, N. (2015). The geometric phase controls ultracold chemistry. *Nature communications*, 6(1), 1–7.

[117] Ketterle, W., Durfee, D. S., & Stamper-Kurn, D. (1999). Making, probing and understanding bose-einstein condensates. *arXiv preprint cond-mat/9904034*.

[118] Kilaj, A., Gao, H., Rösch, D., Rivero, U., Küpper, J., & Willitsch, S. (2018). Observation of different reactivities of para and ortho-water towards trapped diazenylium ions. *Nature communications*, 9.

[119] Klein, A., Shagam, Y., Skomorowski, W., Żuchowski, P. S., Pawlak, M., Janssen, L. M., Moiseyev, N., van de Meerakker, S. Y., van der Avoird, A., Koch, C. P., et al. (2017). Directly probing anisotropy in atom–molecule collisions through quantum scattering resonances. *Nature Physics*, 13(1), 35.

[120] Kokish, M. G., Stollenwerk, P. R., Kajita, M., & Odom, B. C. (2018). Prospects for a polar-molecular-ion optical probe of varying proton-electron mass ratio. *Physical Review A*, 98(5), 052513.

[121] Kondov, S., Lee, C.-H., Leung, K., Liedl, C., Majewska, I., Moszynski, R., & Zelevinsky, T. (2019). Molecular lattice clock with long vibrational coherence. *Nature Physics*, 15(11), 1118–1122.

[122] Korek, M., Younes, G., & Allouche, A. (2003). Theoretical study of the low-lying electronic states of the molecular ion krb+. *International journal of quantum chemistry*, 92(4), 376–380.

[123] Krems, M., Zirbel, J., Thomason, M., & DuBois, R. D. (2005). Channel electron multiplier and channelplate efficiencies for detecting positive ions. *Review of Scientific Instruments*, 76(9), 093305.

[124] Kulin, S., Aubin, S., Christe, S., Peker, B., Rolston, S. L., & Orozco, L. A. (2001). A single hollow-beam optical trap for cold atoms. *Journal of Optics B: Quantum and Semiclassical Optics*, 3(6), 353–357.

[125] Lang, F., Winkler, K., Strauss, C., Grimm, R., & Denschlag, J. H. (2008). Ultracold triplet molecules in the rovibrational ground state. *Physical Review Letters*, 101(13), 133005.

[126] Lavert-Ofir, E., Shagam, Y., Henson, A. B., Gersten, S., Kłos, J., Żuchowski, P. S., Narevicius, J., & Narevicius, E. (2014). Observation of the isotope effect in sub-kelvin reactions. *Nature chemistry*, 6(4), 332.

[127] León, I., Yang, Z., Liu, H.-T., & Wang, L.-S. (2014). The design and construction of a high-resolution velocity-map imaging apparatus for photoelectron spectroscopy studies of size-selected clusters. *Review of Scientific Instruments*, 85(8), 083106.

[128] Léonard, J., Lee, M., Morales, A., Karg, T. M., Esslinger, T., & Donner, T. (2014). Optical transport and manipulation of an ultracold atomic cloud using focus-tunable lenses. *New Journal of Physics*, 16(9), 093028.

[129] Levine, R. D. (2009). *Molecular reaction dynamics*. Cambridge University Press.

[130] Levinsen, J., Cooper, N. R., & Shlyapnikov, G. V. (2011). Topological p x+ ip y superfluid phase of fermionic polar molecules. *Physical Review A*, 84(1), 013603.

[131] Li, J. & Kais, S. (2019). Entanglement classifier in chemical reactions. *Sci. Adv.*, 5(8), eaax5283.

[132] Lifshitz, C. (2001). Some recent aspects of unimolecular gas phase ion chemistry. *Chemical Society Reviews*, 30(3), 186–192.

[133] Light, J. C. (1967). Statistical theory of bimolecular exchange reactions. *Discussions of the Faraday Society*, 44, 14–29.

[134] Lique, F., Honvault, P., & Faure, A. (2014). Ortho–para-H_2 conversion processes in astrophysical media. *Int. Rev. Phys. Chem.*, 33(1), 125–149.

[135] Lique, F., Willitsch, S., Ye, J., Sims, I., Bergeat, A., Vilesov, A., Lepers, M., Koch, C., Quemener, G., Tscherbul, T., et al. (2017). *Cold Chemistry: Molecular Scattering and Reactivity Near Absolute Zero*. Royal Society of Chemistry.

[136] Liu, L., Hood, J., Yu, Y., Zhang, J., Hutzler, N., Rosenband, T., & Ni, K.-K. (2018). Building one molecule from a reservoir of two atoms. *Science*, 360(6391), 900–903.

[137] Liu, Y., Grimes, D. D., Hu, M.-G., & Ni, K.-K. (2020). Probing ultracold chemistry using ion spectrometry. *Physical Chemistry Chemical Physics*.

[138] Marcus, R., Hase, W. L., & Swamy, K. (1984). Rrkm and non-rrkm behavior in chemical activation and related studies. *The Journal of Physical Chemistry*, 88(26), 6717–6720.

[139] Mayle, M., Quéméner, G., Ruzic, B. P., & Bohn, J. L. (2013). Scattering of ultracold molecules in the highly resonant regime. *Physical Review A*, 87(1), 012709.

[140] Mayle, M., Ruzic, B. P., & Bohn, J. L. (2012). Statistical aspects of ultracold resonant scattering. *Physical Review A*, 85(6), 062712.

[141] McDonald, M., McGuyer, B., Apfelbeck, F., Lee, C.-H., Majewska, I., Moszynski, R., & Zelevinsky, T. (2016). Photodissociation of ultracold diatomic strontium molecules with quantum state control. *Nature*, 535(7610), 122.

[142] McKay, D., Jervis, D., Fine, D., Simpson-Porco, J., Edge, G., & Thywissen, J. (2011). Low-temperature high-density magneto-optical trapping of potassium using the open 4 s→ 5 p transition at 405 nm. *Physical Review A*, 84(6), 063420.

[143] Mewes, M.-O., Andrews, M., Van Druten, N., Kurn, D., Durfee, D., & Ketterle, W. (1996). Bose-einstein condensation in a tightly confining dc magnetic trap. *Physical Review Letters*, 77(3), 416.

[144] Meyrath, T. (2005). *Experiments with Bose-Einstein condensation in an optical box*. PhD thesis.

[145] Micheli, A., Brennen, G., & Zoller, P. (2006). A toolbox for lattice-spin models with polar molecules. *Nature Physics*, 2(5), 341.

[146] Molony, P. K., Gregory, P. D., Ji, Z., Lu, B., Köppinger, M. P., Le Sueur, C. R., Blackley, C. L., Hutson, J. M., & Cornish, S. L. (2014). Creation of ultracold rb 87 cs 133 molecules in the rovibrational ground state. *Physical Review Letters*, 113(25), 255301.

[147] Momose, T., Fushitani, M., & Hoshina, H. (2005). Chemical reactions in quantum crystals. *Int. Rev. Phys. Chem.*, 24(3-4), 533–552.

[148] Moses, S. A. (2016). A quantum gas of polar molecules in an optical lattice.

[149] Mukherjee, N. & Zare, R. N. (2011). Stark-induced adiabatic raman passage for preparing polarized molecules. *The Journal of chemical physics*, 135(2), 024201.

[150] Naik, D. & Raman, C. (2005). Optically plugged quadrupole trap for bose-einstein condensates. *Physical Review A*, 71(3), 033617.

[151] Nesbitt, D. J. (2012). Toward state-to-state dynamics in ultracold collisions: Lessons from high-resolution spectroscopy of weakly bound molecular complexes. *Chemical Reviews*, 112(9), 5062–5072.

[152] Neyenhuis, B., Yan, B., Moses, S. A., Covey, J. P., Chotia, A., Petrov, A., Kotochigova, S., Ye, J., & Jin, D. S. (2012). Anisotropic polarizability of ultracold polar $^{40}K^{87}Rb$ molecules. *Phys. Rev. Lett.*, 109, 230403.

[153] Ni, K.-K. (2009). *A quantum gas of polar molecules*. PhD thesis, Citeseer.

[154] Ni, K.-K., Ospelkaus, S., De Miranda, M., Pe'Er, A., Neyenhuis, B., Zirbel, J., Kotochigova, S., Julienne, P., Jin, D., & Ye, J. (2008). A high phase-space-density gas of polar molecules. *science*, 322(5899), 231–235.

[155] Ni, K.-K., Ospelkaus, S., Nesbitt, D. J., Ye, J., & Jin, D. S. (2009). A dipolar gas of ultracold molecules. *Physical Chemistry Chemical Physics*, 11(42), 9626–9639.

[156] Ni, K.-K., Ospelkaus, S., Wang, D., Quéméner, G., Neyenhuis, B., De Miranda, M., Bohn, J., Ye, J., & Jin, D. (2010). Dipolar collisions of polar molecules in the quantum regime. *Nature*, 464(7293), 1324.

[157] Ni, K.-K., Rosenband, T., & Grimes, D. D. (2018). Dipolar exchange quantum logic gate with polar molecules. *Chemical science*, 9(33), 6830–6838.

[158] Noll, R. J., Yi, S. S., & Weisshaar, J. C. (1998). Bimolecular ni+ (2d5/2)+ c3h8 reaction dynamics in real time. *The Journal of Physical Chemistry A*, 102(2), 386–394.

[159] Oka, T. (2004). Nuclear spin selection rules in chemical reactions by angular momentum algebra. *J. Mol. Spectrosc.*, 228(2), 635–639.

[160] Osborn, D. L. (2017). Reaction mechanisms on multiwell potential energy surfaces in combustion (and atmospheric) chemistry. *Annual Review of Physical Chemistry*, 68, 233–260.

[161] Ospelkaus, S., Ni, K.-K., Quéméner, G., Neyenhuis, B., Wang, D., De Miranda, M., Bohn, J., Ye, J., & Jin, D. (2010a). Controlling the hyperfine state of rovibronic ground-state polar molecules. *Phys. Rev. Lett.*, 104(3), 030402.

[162] Ospelkaus, S., Ni, K.-K., Wang, D., De Miranda, M., Neyenhuis, B., Quéméner, G., Julienne, P., Bohn, J., Jin, D., & Ye, J. (2010b). Quantum-state controlled chemical reactions of ultracold potassium-rubidium molecules. *Science*, 327(5967), 853–857.

[163] Pan, H., Wang, F., Czakó, G., & Liu, K. (2017). Direct mapping of the angle-dependent barrier to reaction for cl+ chd 3 using polarized scattering data. *Nature chemistry*, 9(12), 1175.

[164] Papp, S. B. (2007). *Experiments with a two-species Bose-Einstein condensate utilizing widely tunable interparticle interactions*. PhD thesis, Ph. D. thesis, University of Colorado.

317

[165] Park, J. W., Will, S. A., & Zwierlein, M. W. (2015). Ultracold dipolar gas of fermionic na 23 k 40 molecules in their absolute ground state. *Physical Review Letters*, 114(20), 205302.

[166] Park, J. W., Yan, Z. Z., Loh, H., Will, S. A., & Zwierlein, M. W. (2017). Second-scale nuclear spin coherence time of ultracold 23na40k molecules. *Science*, 357(6349), 372–375.

[167] Perreault, W. E., Mukherjee, N., & Zare, R. N. (2017). Quantum control of molecular collisions at 1 kelvin. *Science*, 358(6361), 356–359.

[168] Polanyi, J. & Wong, W. (1969). Location of energy barriers. i. effect on the dynamics of reactions a+ bc. *The Journal of Chemical Physics*, 51(4), 1439–1450.

[169] Polanyi, J. C. (1972). Concepts in reaction dynamics. *Accounts of Chemical Research*, 5(5), 161–168.

[170] Polanyi, J. C. & Zewail, A. H. (1995). Direct observation of the transition state. *Accounts of Chemical Research*, 28(3), 119–132.

[171] Pretzier, G. (1991). A new method for numerical abel-inversion. *Zeitschrift für Naturforschung A*, 46(7), 639–641.

[172] Puri, P., Mills, M., Simbotin, I., Montgomery, J. A., Côté, R., Schneider, C., Suits, A. G., & Hudson, E. R. (2019). Reaction blockading in a reaction between an excited atom and a charged molecule at low collision energy. *Nature chemistry*, 11(7), 615.

[173] Qiu, M., Ren, Z., Che, L., Dai, D., Harich, S. A., Wang, X., Yang, X., Xu, C., Xie, D., Gustafsson, M., et al. (2006). Observation of Feshbach resonances in the F + $H_2 \rightarrow$ HF + H reaction. *Science*, 311(5766), 1440–1443.

[174] Quack, M. (1977). Detailed symmetry selection rules for reactive collisions. *Mol. Phys.*, 34(2), 477–504.

[175] Rosi, S., Burchianti, A., Conclave, S., Naik, D. S., Roati, G., Fort, C., & Minardi, F. (2018). λ-enhanced grey molasses on the d 2 transition of rubidium-87 atoms. *Scientific reports*, 8(1), 1301.

[176] Rvachov, T. M., Son, H., Sommer, A. T., Ebadi, S., Park, J. J., Zwierlein, M. W., Ketterle, W., & Jamison, A. O. (2017). Long-lived ultracold molecules with electric and magnetic dipole moments. *Physical Review Letters*, 119(14), 143001.

[177] Sansonetti, J. E. (2006). Wavelengths, transition probabilities, and energy levels for the spectra of rubidium (rb i through rb xxxvii). *Journal of physical and chemical reference data*, 35(1), 301–421.

[178] Sansonetti, J. E. (2008). Wavelengths, transition probabilities, and energy levels for the spectra of potassium (ki through k xix). *Journal of Physical and Chemical Reference Data*, 37(1), 7–96.

[179] Santos, L., Shlyapnikov, G., Zoller, P., & Lewenstein, M. (2000). Bose-einstein condensation in trapped dipolar gases. *Physical Review Letters*, 85(9), 1791.

[180] Sato, H. (2001). Photodissociation of simple molecules in the gas phase. *Chemical Reviews*, 101(9), 2687–2726.

[181] Scherer, N., Sipes, C., Bernstein, R., & Zewail, A. (1990). Real-time clocking of bimolecular reactions: Application to h+ co2. *The Journal of Chemical Physics*, 92(9), 5239–5259.

[182] Schinke, R., Engel, V., & Staemmler, V. (1985). Rotational state distributions in the photolysis of water: influence of the potential anisotropy. *The Journal of chemical physics*, 83(9), 4522–4533.

[183] Schramm, B., Bamford, D., & Moore, C. B. (1983). Nuclear spin state conservation in photodissociation of formaldehyde. *Chem. Phys. Lett.*, 98(4), 305–309.

[184] Scoles, G., Bassi, D., Buck, U., & Laine, D. (1988). *Atomic and molecular beam methods*, volume 1. Oxford university press New York.

[185] Seto, J. Y., Le Roy, R. J., Verges, J., & Amiot, C. (2000). Direct potential fit analysis of the x 1 σ g+ state of rb 2: Nothing else will do! *The Journal of Chemical Physics*, 113(8), 3067–3076.

[186] Shapiro, M. & Brumer, P. (2003). Coherent control of molecular dynamics. *Rep. Prog. Phys.*, 66(859–942), 224302.

[187] Sims, I., Gruebele, M., Potter, E., & Zewail, A. (1992). Femtosecond real-time probing of reactions. viii. the bimolecular reaction br+ i2. *The Journal of chemical physics*, 97(6), 4127–4148.

[188] Sivia, D. & Skilling, J. (2006). *Data analysis: a Bayesian tutorial*. OUP Oxford.

[189] Soley, M. B. & Heller, E. J. (2018). Classical approach to collision complexes in ultracold chemical reactions. *Physical Review A*, 98(5), 052702.

[190] Steck, D. A. (2001). Rubidium 87 d line data.

[191] Steele, R. (1983). Optical phase-locked loop using semiconductor laser diodes. *Electronics Letters*, 19(2), 69–71.

[192] Strauss, C., Takekoshi, T., Lang, F., Winkler, K., Grimm, R., Denschlag, J. H., & Tiemann, E. (2010). Hyperfine, rotational, and vibrational structure of the a 3 σ u+ state of rb 87 2. *Physical Review A*, 82(5), 052514.

[193] Stwalley, W. C. & Wang, H. (1999). Photoassociation of ultracold atoms: a new spectroscopic technique. *Journal of molecular spectroscopy*, 195(2), 194–228.

[194] Su, Y.-T., Huang, Y.-H., Witek, H. A., & Lee, Y.-P. (2013). Infrared absorption spectrum of the simplest criegee intermediate CH_2OO. *Science*, 340(6129), 174–176.

[195] Suemitsu, H. & Samson, J. A. (1983). Relative photoionization cross sections of cs, cs 2, rb, and rb 2. *Physical Review A*, 28(5), 2752.

[196] Takekoshi, T., Reichsöllner, L., Schindewolf, A., Hutson, J. M., Le Sueur, C. R., Dulieu, O., Ferlaino, F., Grimm, R., & Nägerl, H.-C. (2014). Ultracold dense samples of dipolar RbCs molecules in the rovibrational and hyperfine ground state. *Physical Review Letters*, 113(20), 205301.

[197] Tannor, D. J. (2007). *Introduction to quantum mechanics: a time-dependent perspective*. University Science Books.

[198] Tiecke, T. (2010). Properties of potassium. *University of Amsterdam, The Netherlands, Thesis*, (pp. 12–14).

[199] Toscano, J., Lewandowski, H., & Heazlewood, B. R. (2020). Cold and controlled chemical reaction dynamics. *Physical Chemistry Chemical Physics*, 22(17), 9180–9194.

[200] Troe, J. (1994). The Polanyi Lecture. The colourful world of complex-forming bimolecular reactions. *Journal of the Chemical Society, Faraday Transactions*, 90(16), 2303–2317.

[201] Tscherbul, T., Barinovs, Ğ., Kłos, J., & Krems, R. (2008). Formation of slow molecules in chemical reactions in crossed molecular beams. *Physical Review A*, 78(2), 022705.

[202] Tscherbul, T., Suleimanov, Y. V., Aquilanti, V., & Krems, R. (2009). Magnetic field modification of ultracold molecule–molecule collisions. *New Journal of Physics*, 11(5), 055021.

[203] Uy, D., Cordonnier, M., & Oka, T. (1997). Observation of ortho-para H_3^+ selection rules in plasma chemistry. *Phys. Rev. Lett.*, 78(20), 3844.

[204] Vadla, C., Beuc, R., Horvatic, V., Movre, M., Quentmeier, A., & Niemax, K. (2006). Comparison of theoretical and experimental red and near infrared absorption spectra in overheated potassium vapour. *The European Physical Journal D-Atomic, Molecular, Optical and Plasma Physics*, 37(1), 37–49.

[205] Vager, Z., Naaman, R., & Kanter, E. (1989). Coulomb explosion imaging of small molecules. *Science*, 244(4903), 426–431.

[206] Vande Linde, S. R. & Hase, W. L. (1990). Non-rrkm kinetics in gas-phase sn2 nucleophilic substitution. *Journal of Physical Chemistry*, 94(16), 6148–6150.

[207] Vitanov, N. V., Rangelov, A. A., Shore, B. W., & Bergmann, K. (2017). Stimulated raman adiabatic passage in physics, chemistry, and beyond. *Reviews of Modern Physics*, 89(1), 015006.

[208] Wang, T., Chen, J., Yang, T., Xiao, C., Sun, Z., Huang, L., Dai, D., Yang, X., & Zhang, D. H. (2013). Dynamical resonances accessible only by reagent vibrational excitation in the f+ hd→ hf+ d reaction. *Science*, 342(6165), 1499–1502.

[209] Webb, A. D., Dixon, R. N., & Ashfold, M. N. (2007). Imaging studies of the photodissociation of H_2S^+ cations. I. Illustrations of the role of nuclear spin. *J. Chem. Phys.*, 127(22), 224307.

[210] Werner, H.-J., Knowles, P. J., Knizia, G., Manby, F. R., Schütz, M., et al. (2019). Molpro, version 2019.2, a package of ab initio programs. see www.molpro.net.

[211] Westerberg, L., Hjörvarsson, B., Wallén, E., & Mathewson, A. (1997). Hydrogen content and outgassing of air-baked and vacuum-fired stainless steel. *Vacuum*, 48(7-9), 771–773.

[212] Whittaker, E. A., Gehrtz, M., & Bjorklund, G. C. (1985). Residual amplitude modulation in laser electro-optic phase modulation. *JOSA B*, 2(8), 1320–1326.

[213] Womack, C. C., Martin-Drumel, M.-A., Brown, G. G., Field, R. W., & McCarthy, M. C. (2015). Observation of the simplest criegee intermediate ch2oo in the gas-phase ozonolysis of ethylene. *Science advances*, 1(2), e1400105.

[214] Woodward, R. B. & Hoffmann, R. (2013). *The conservation of orbital symmetry*. Elsevier.

[215] Wu, X., Gantner, T., Koller, M., Zeppenfeld, M., Chervenkov, S., & Rempe, G. (2017). A cryofuge for cold-collision experiments with slow polar molecules. *Science*, 358(6363), 645–648.

[216] Yang, D., Zuo, J., Huang, J., Hu, X., Dawes, R., Xie, D., & Guo, H. (2020). A global full-dimensional potential energy surface for the k2rb2 complex and its lifetime. *The Journal of Physical Chemistry Letters*, 11, 2605–2610.

[217] Yang, H., Zhang, D.-C., Liu, L., Liu, Y.-X., Nan, J., Zhao, B., & Pan, J.-W. (2019a). Observation of magnetically tunable feshbach resonances in ultracold 23na40k+ 40k collisions. *Science*, 363(6424), 261–264.

[218] Yang, T., Huang, L., Xiao, C., Chen, J., Wang, T., Dai, D., Lique, F., Alexander, M. H., Sun, Z., Zhang, D. H., et al. (2019b). Enhanced reactivity of fluorine with para-hydrogen in cold interstellar clouds by resonance-induced quantum tunnelling. *Nature Chemistry*, 11(8), 744–749.

[219] Yao, N. Y., Zaletel, M. P., Stamper-Kurn, D. M., & Vishwanath, A. (2018). A quantum dipolar spin liquid. *Nature Physics*, 14(4), 405–410.

[220] Ye, X., Guo, M., González-Martínez, M. L., Quéméner, G., & Wang, D. (2018). Collisions of ultracold ^{23}Na^{87}Rb molecules with controlled chemical reactivities. *Science advances*, 4(1), eaaq0083.

[221] Yelin, S., Kirby, K., & Côté, R. (2006). Schemes for robust quantum computation with polar molecules. *Physical Review A*, 74(5), 050301.

[222] Zare, R. N. & Herschbach, D. R. (1963). Doppler line shape of atomic fluorescence excited by molecular photodissociation. *Proceedings of the IEEE*, 51(1), 173–182.

[223] Zewail, A. H. (2000). Femtochemistry: Atomic-scale dynamics of the chemical bond. *The Journal of Physical Chemistry A*, 104(24), 5660–5694.

[224] Zhang, J. T., Yu, Y., Cairncross, W. B., Wang, K., Picard, L. R., Hood, J. D., Lin, Y.-W., Hutson, J. M., & Ni, K.-K. (2020). Forming a single molecule by magnetoassociation in an optical tweezer. *arXiv preprint arXiv:2003.07850*.

[225] Zhou, J., Lin, J. J., & Liu, K. (2003). Mode-correlated product pairs in the f+ chd 3→ df+ chd 2 reaction. *The Journal of chemical physics*, 119(16), 8289–8296.

[226] Zirbel, J. (2008). *Ultracold fermionic Feshbach molecules*. PhD thesis, University of Colorado at Boulder.

[227] Żuchowski, P. S. & Hutson, J. M. (2010). Reactions of ultracold alkali-metal dimers. *Physical Review A*, 81(6), 060703.